MAE Center Report No. 11-01

MULTI-OBJECTIVE OPTIMAL SEISMIC DESIGN OF BUILDINGS USING ADVANCED ENGINEERING MATERIALS

by

Bora Gencturk and Amr S. Elnashai

Department of Civil and Environmental Engineering
University of Illinois at Urbana-Champaign
Urbana, Illinois

July 2011

Mid-America Earthquake Center

ABSTRACT

Although seismic safety remains a major concern of society--and unfortunately this observation has been underpinned by recent earthquakes--economy and sustainability in seismic design are growing issues that the engineering community must face due to increasing human population and excessive use of the earth's nonrenewable resources. Previous studies have addressed the design and assessment of buildings under seismic loading considering a single objective, namely, safety. Seismic design codes and regulations also center on this objective.

The goal of this study is to develop a framework that concurrently addresses the societal-level objectives of safety, economy and sustainability using consistent tools at every component of the analysis. To this end, a high-performance material; namely, engineered cementitious composites (ECC) is utilized. ECC is classified under the general class of fiber-reinforced concrete (FRC); however, ECC is superior to conventional FRC in many aspects, but most importantly in its properties of energy absorption, shear resistance and damage tolerance, all of which are utilized in the proposed procedure. The behavior of ECC is characterized through an experimental program at the small-scale (scale factor equal to 1/8). ECC mixtures with different cost and sustainability indices are considered. It is seen that all ECC mixtures outperform concrete to different extents of stiffness, strength, ductility and energy absorption under cyclic loading conditions. Under simulated earthquake motion, ECC shows significant damage tolerance resulting from increased shear and spalling resistance and reduced interstory drifts.

Numerical modeling of ECC is also performed to carry out structural level simulations to complement the experimental data. A constitutive model is developed for ECC and validated at the material, component and system levels. The numerical tool is utilized in the experimental program for hybrid simulation and life-cycle cost (LCC) optimization as described briefly below. Additionally, a parametric study of ECC columns is performed to investigate the effect of material tensile properties on the structural level response metrics. It is observed that the material properties have a major effect on member strength, ductility and energy absorption capacity, while the member stiffness is relatively insensitive.

Reducing the LCC of buildings (through reductions in material usage and seismic damage cost) is required to achieve the objectives of economy and sustainability. A rigorous LCC formulation that uses advanced analysis for structural assessment, and that takes into account all sources of uncertainty, is used along with an efficient search algorithm to compare the optimal design solutions. A novel aspect of this work is that three different structural frames are considered, RC, ECC and a multi-material frame in which ECC is deployed only at the critical locations (e.g. plastic hinges) to improve seismic performance. It is found that both the initial and LCC of frames that use ECC are lower due to savings in material and labor cost of transverse reinforcement for the former and due to increased capacity and reduced demand for the latter.

By considering the inelastic behavior of structures and incorporating all the required components, the proposed framework is generic and applicable to other types of construction such as bridges, to other innovative materials such as high performance steels, and to other extreme loading scenarios such as wind and blast.

ACKNOWLEDGEMENTS

This research was funded by the Mid-America Earthquake (MAE) Center and the George E. Brown, Jr. Network for Earthquake Engineering Simulation (NEES), a facility in the Department of Civil and Environmental Engineering at the University of Illinois at Urbana-Champaign. The MAE Center is a graduated National Science Foundation (NSF) Engineering Research Center, funded under NSF Grant EEC-9701785. Funding from NEES was through an Illinois site grant from NSF, reference CMMI-0927178, and the NSF NEES-SG Seismic Simulation and Design of Bridge Columns under Combined Actions and Implications on System Response, reference CMMI-0530737. Material-level test data were provided by Professor Sarah Billington and Dr. Hiroshi Fukuyama. The engineered cementitious composites (ECC) were prepared, and the ECC columns were cast, at Stanford University in collaboration with Professors Michael Lepech and Sarah Billington.

TABLE OF CONTENTS

LIST OF FIGURES

LIST OF TABLES

LIST OF ABBREVIATIONS

A	
α-OS	alpha- Operator Splitting
ABCB	Australian Building Codes Board
ACI	American Concrete Institute
AISC	American Institute of Steel Construction
ATC	Applied Technology Council
B	
BIA	Building Industry Authority
C	
CA	California
CSM	Capacity Spectrum Method
CUREe	California Universities for Research in Earthquake Engineering
CP	Collapse Prevention
CPU	Central Processing Unit
D	
DBD	Displacement-Based Design
DFRCC	Ductile Fiber Reinforced Cementitious Composites
DOF	Degrees-Of-Freedom
DSHA	Deterministic Seismic Hazard Analysis
E	
EA	Evolutionary Algorithms
ECC	Engineered Cementitious Composites
ES	Exhaustive Search
F	
FEMA	Federal Emergency Management Agency
FRC	Fiber Reinforced Concrete
FRCC	Fiber Reinforced Cementitious Composites
FRP	Fiber Reinforced Polymer
G	
GA	Genetic Algorithms
H	
HAZUS	HAZard U.S.

HPFRCC	High Performance Fiber Reinforced Cementitious Composites
I	
ICBO	International Conference of Building Officials
IO	Immediate Occupancy
ISO	International Organization for Standardization
J	
JSCE	Japan Society of Civil Engineers
L	
LBCB	Load and Boundary Condition Box
LBCB OM	Load and Boundary Condition Box Operations Manager
LCC	Life-Cycle Cost
LS	Life Safety
LVDT	Linear Variable Differential Transformer
M	
MCS	Monte Carlo Simulation
MSI	Material Sustainability Index
N	
NEES	Network for Earthquake Engineering Simulation
NGA	*N*ext *G*eneration of Ground-Motion *A*ttenuation Models
NKB	Nordiska Komitten for Byggbetammelser
NSF	National Science Foundation
O	
OC	Optimality Criteria
P	
PBD	Performance-Based Design
PBEE	Performance-Based Earthquake Engineering
PBSD	Performance-Based Seismic Design
PE	Polyethylene
PEER	Pacific Earthquake Engineering Research
PGA	Peak Ground Acceleration
PGD	Peak Ground Displacement
PGV	Peak Ground Velocity
PP	Polypropylene
PSHA	Probabilistic Seismic Hazard Analysis

PVA	Polyvinyl Alcohol
PVC	PolyVinyl Chloride
R	
RC	Reinforced Concrete
RECC	Reinforced Engineered Cementitious Composite
S	
SA	Simulated Annealing
SAC	*S*EAOC, *A*TC, *C*UREe
SCWB	Strong Column-Weak Beam
SDOF	Single-Degree-Of-Freedom
SEAOC	Structural Engineers Association of California
SI	Standard International
SIFCON	Slurry Infiltrated Fiber CONcrete
SIMCON	Slurry Infiltrated Mat CONcrete
T	
TS	Taboo Search
U	
UBC	Uniform Building Code
UHS	Uniform Hazard Spectrum/Spectra
UHMWPE	Ultra-High Molecular Weight Polyethylene
US	United States
USGS	United States Geological Survey
W	
WCSB	Weak Column-Strong Beam
Y	
Y-R	Yankelevsky-Reinhardt
YRP	Years Return Period

LIST OF SYMBOLS

a = Constant defining reloading curve in ECC model

a_{RS} = Constant in Ramber-Osgood model

A_{ch} = Cross-sectional area of the member measured to the outside edges of transverse reinforcement

A_e = Effective tensile stress area of threaded rods

A_g = Gross area of concrete section

A_{sh} = Total cross-sectional area of shear reinforcement

A_v = Total cross-sectional area of shear reinforcement

b = Constant defining reloading curve in ECC model

b_c = Cross-sectional dimension of confined section

b_{RS} = Constant in Ramber-Osgood model

b_w = Width of the member

c = Constant defining reloading curve in ECC model

c_1-c_3 = Constants defining the mean of earthquake demand

c_4-c_6 = Constants defining the logarithmic standard deviation of earthquake demand

c_7-c_{10} = Constants defining the hazard curve

C_i = Repair cost of damage for the ith limit state

C_{SD} = Seismic damage cost

C_0 = Initial cost of a structure

d = Constant defining reloading curve in ECC model or depth of section to calculate shear strength

d_b = Nominal diameter of threaded rods

$\boldsymbol{dA}$ = Vector of incremental cross-sectional areas in fiber-based finite element model

E = Elastic (Young's) modulus

$E[\cdot]$ = Expected value

E_{cvar} = Tangent stiffness used to define reloading curves in ECC model in compression

E_{sec} = Secant stiffness defining the transition curves in ECC model

E_{tc} = Tangent stiffness defining the transition curves in ECC model

E_{tvar} = Tangent stiffness defining the reloading curves in ECC model in tension

$f_{C,i}$ = Probability density function for structural capacity for the ith damage state

f_{vd} = Design tensile yield strength of ECC

f_{yt} = Yield strength of shear reinforcement

F = Axial force in parametric analysis of ECC columns

F_{max} = Peak lateral force resistance

F_y = Yield force

h_1 = Larger cross-sectional dimension of experimental columns

h_2 = Smaller cross-sectional dimension of experimental columns

IM = Intensity measure

k_c = Parameter defining the rate of strength and stiffness degradation in ECC model in compression

k_{cmax} = Maximum rate of strength and stiffness degradation in ECC model in compression

k_{cmin} = Minimum rate of strength and stiffness degradation in ECC model in compression

k_t = Parameter defining the rate of strength and stiffness degradation in ECC model in tension

k_{tmax} = Maximum rate of strength and stiffness degradation in ECC model in tension

k_{tmin} = Minimum rate of strength and stiffness degradation in ECC model in tension

l = Element length in finite element model

L = Service life of a structure

n = Parameter defining the post-peak response of the compression envelope in ECC model

N = Total number of limit states

n_{RS} = Constant in Ramber-Osgood model

P = mm per thread for threaded rods

P_i = Total probability that the structure will be in the ith damage state throughout its lifetime

R = Parameter defining the transition curves in ECC model

s = Spacing of stirrups

V_c = Nominal shear capacity provided by concrete

V_{cd} = Design shear capacity provided by mortar

V_{fd} = Design shear capacity provided by reinforcing fibers

V_n = Nominal shear capacity

V_{ped} = Design shear capacity provided by prestressing steel

V_s = Nominal shear capacity provided by shear reinforcement

V_{sd} = Design shear capacity provided by shear reinforcement

V_{yd} = Total design shear capacity

α = Discount factor

α_c = Parameter controlling the rate of unloading in ECC model in compression

α_{cmax} = Maximum rate of unloading in ECC model in compression

α_{cmin} = Minimum rate of unloading in ECC model in compression

α_t = Parameter controlling the rate of unloading in ECC model in tension

α_{tmax} = Maximum rate of unloading in ECC model in tension

α_{tmin} = Minimum rate of unloading in ECC model in tension

β_C = Uncertainty term for structural capacity

β_D = Uncertainty term for earthquake demand

β_u = Angle of diagonal crack to calculate shear capacity

$\Delta_{C,i}$ = Structural capacity defining the ith damage state

Δ_D = Earthquake demand

Δ_m = Displacement at peak force

Δ_u = Ultimate displacement

Δ_y = Yield displacement

ε = Strain (generic)

ε_{cp} = Strain corresponding to compressive strength of ECC

ε_{cmin} = Minimum ever experienced compressive strain in ECC model

ε^*_{cmin} = Adjusted minimum ever experienced compressive strain in ECC model

ε_{cprl} = Strain defining the starting point of unloading curve in ECC model in compression

ε_{cpul} = Strain defining the starting point of reloading curve in ECC model in compression

ε_{cu} = Strain defining the post-peak response of the compression envelope in ECC model

ε_{cul} = Plastic strain in ECC model in compression

ε_{cvar} = Strain defining starting point of unloading curve in ECC model in compression

ε_{tmax} = Maximum ever experienced tensile strain in ECC model

ε^*_{tmax} = Adjusted maximum ever experienced tensile strain in ECC model

ε_{tp} = Strain in ECC corresponding to ultimate strength in tension

ε_{tprl} = Strain defining the starting point of unloading curve in ECC model in tension

ε_{tpul} = Strain defining the starting point of reloading curve in ECC model in tension

ε_{tvar} = Strain defining starting point of unloading curve in ECC model in tension

ε_{tu} = Tensile strain capacity of ECC

ε_{tul} = Plastic strain in ECC model in tension

ε_{t0} = Cracking strain of ECC in tension

γ_b = Member factor to calculate shear capacity

λ = Annual discount rate

λ_D = Natural logarithm of the mean of the earthquake demand

μ = Material ductility

μ_D = Mean of earthquake demand

μ_m = Component ductility at peak load

μ_u = Component ductility at failure

ρ = Reinforcement ratio

$\Phi[\cdot]$ = Standard normal cumulative distribution

σ = Stress (generic)

σ_c = Stress on compression envelope in ECC model

σ_{cmin} = Stress corresponding to minimum ever experienced compressive strain in ECC model

σ^*_{cmin} = Stress corresponding to adjusted minimum ever experienced compressive strain in ECC model

σ_{cr} = Stress defining the post-peak response of the compression envelope in ECC model

σ_{cp} = Compressive strength of ECC

σ_{cprl} = Stress defining the starting point of unloading curve in ECC model in compression

σ_{cpul} = Stress defining the starting point of reloading curve in ECC model in compression

σ_{cvar} = Stress defining the starting point of unloading or reloading curve in ECC model in compression

σ_t = Stress on tension envelope in ECC model

σ_{tmax} = Stress corresponding to maximum ever experienced tensile strain in ECC model

σ^*_{tmax} = Stress corresponding to adjusted maximum ever experienced tensile strain in ECC model

σ_{tp} = Ultimate strength of ECC in tension

σ_{tprl} = Stress defining the starting point of unloading curve in ECC model in tension

σ_{tpul} = Stress defining the starting point of reloading curve in ECC model in tension

σ_{tvar} = Stress defining the starting point of unloading curve in ECC model in tension

σ_{t0} = Cracking stress of ECC

ν = Annual frequency of exceedance

1

INTRODUCTION

"The technical man must not be lost in his own technology. He must be able to appreciate life; and life is art, drama, music, and most importantly, people."

Fazlur Khan

The motivation for the research presented in this thesis is to reduce the social and economic consequences of earthquakes through improved seismic design of buildings in terms of the three fundamental societal-level objectives of today's world: safety, economy and sustainability. Details are described in this chapter.

1.1. PREAMBLE

Recent incidents of earthquakes have shown that there is still need for a considerable amount of research to reduce the consequences of seismic hazards to acceptable levels. The extent and severity of the problem varies depending on the location; thus, the solution is not unique. Whereas loss of life, injuries and homelessness are priority issues for developing countries where the seismic design codes are not strictly enforced, reduction of direct and indirect economic losses is the main objective for mitigating the consequences of earthquakes in developed countries. Basic design guidance can significantly ameliorate the situation in developing countries; however, more advanced tools are required to develop a comprehensive understanding of the consequences of earthquakes and to devise novel solutions.

The science and engineering community learns something new after each natural hazard. As examples, the Northridge earthquake (1994) showed that the current seismic design guidance in the United States (US) is satisfactory to limit the loss of life and injuries. On the other hand, monetary losses were major, causing significant burden to the economy. As a consequence, PBEE concepts (where the design of structures for multiple objectives is considered) gained popularity. The Sumatra (2004) and the recent Tōhoku (2011) earthquakes showed that proper design for strong ground shaking is not sufficient when communities are vulnerable to secondary effects such as tsunamis, soil liquefaction and the failure of hazardous facilities. Therefore, earthquake preparedness and related research efforts must go beyond improving the seismic

resistance of structures and enforcement of seismic design codes. There is a need for developing frameworks that are comprehensive, uniform (throughout their components), robust and applicable to different scenarios. The efforts should be concentrated, the objectives should be well defined, prioritizing the welfare of communities, and the outcomes should be a product of a group of knowledgeable people from backgrounds covering all related fields from sciences to engineering and business.

1.2. DEFINITION OF THE PROBLEM

The goal of all engineering efforts is to benefit society and reduce or eliminate human problems. The huge problems resulting from earthquake damage threaten society in terms of human life, health and social infrastructure, so to meet the challenges posed by earthquake events, both problems and objectives must be defined at the societal level. The protection of human life and health is certainly the first priority, but despite tremendous advancements in science and technology, the satisfactory realization of this goal still eludes us. Although the rates of fatality and injury from earthquakes are relatively low, unfortunately they are not yet at acceptable levels. Major obstacles to the safety of communities in earthquake-prone areas are the enforcement of appropriate design codes and the lack of education in earthquake preparedness—problems of human will and organization. While it is not possible to account for and prevent all sources of risk to human safety, engineers can play a huge role in fulfilling the objective of seismic risk reduction by designing damage tolerant and forgiving structures.

Human safety, however, is obviously not the only concern of societies. The earth's human population is growing at an increasing rate, and the availability of resources will be a major problem in the near future. Thus, sustainability is one of the grand challenges for engineering in the 21st century. From an engineering perspective, this translates into a more economical usage of materials to reduce the burden on the economy, and sustainable design that aims for long term reduced environmental impacts and resiliency. Obviously these two objectives, economical and sustainable design, are interrelated.

More specifically, in terms of seismic design, performance objectives can be satisfied via several possible structural designs. Best earthquake engineering practice selects the most fit-for-purpose design, often on the basis of economy. However, present seismic design practice does not provide direct and clear guidance on how to select the optimum solution amongst many and currently the only objective is to satisfy the required performance. As a result, it has been confirmed that structures designed based on the current seismic codes exhibit excessive overstrength (e.g. Jain and Navin, 1995; Kappos, 1999; Elnashai and Mwafy, 2002). Such unnecessary over-design is not just economically wasteful but also environmentally unfriendly. Moreover, structural overstrength does not necessarily correspond to safer design. Structural components might be stronger than required yet may have insufficient ductility (e.g. Repapis et al., 2006), or while having excessive ductility they might not have the required stiffness to satisfy the serviceability limit states. It is clear that different components of a system call for different characteristics, distributed differently. Therefore, for an optimal design in which the construction material is fully utilized, the structural system should be analyzed on a component basis, critical

regions requiring a specific combination of the three behavioral characteristics (stiffness, strength and ductility) should be identified, and these requirements should be satisfied through optimal material distribution, reinforcement detailing and section dimensioning.

To address the above stated problems, seismic design must be tuned, and the match between supply and demand in terms of stiffness, strength and ductility must be controlled using reliable analysis tools and design guidance. Use of advanced materials with improved energy absorption, damage tolerance and reduced life-cycle cost (LCC) is needed to enhance human safety and increase long term sustainability. New seismic design criteria should be developed taking into account the behavior of new materials and improved design concepts. Clear relationships between material-level considerations and whole life-cycle assessment (taking into account multiple objectives), including post-earthquake rehabilitation, are also needed.

1.3. OBJECTIVES AND SCOPE

The objectives of this study derive from, and map onto the problems defined in the preceding section: to address the consequences of earthquakes by considering safety, economy and sustainability in seismic design of buildings. A significant amount of literature focuses on these objectives individually, but the novelty of the work presented in this thesis mainly stems from its proposed approach to the problem where the three main societal level objectives are addressed in a unified framework. For this purpose a seismic design framework is developed using an advanced material, namely, engineered cementitious composites (ECC), a type of fiber-reinforced concrete (FRC) with damage tolerant characteristics to enhance seismic safety. Additionally, not only the initial but also the life-cycle cost of buildings due to post-earthquake rehabilitation is taken into account to address the economy and sustainability objectives. The use of ECC along with optimization tools results in savings in the LCC of buildings.

The proposed seismic design framework is illustrated in Figure 1.1. The main societal-level objectives are safety, economy and sustainability, and a number of tools are developed and used to achieve these objectives. (1) An experimental program is needed to characterize the behavior of ECC at the component and system levels. The experimental program helps better understand the advantages of ECC in achieving the objectives in seismic design of buildings. (2) A numerical tool is developed to complement the experimental data and investigate the system behavior under simulated earthquake motion. (3) Through structural level simulation, the developed numerical tool is validated, and the performance enhancement with the use of ECC is further investigated. (4) The developed numerical tool is also used for structural optimization and LCC analysis to reduce the initial and LCC of buildings. These components of the framework are also depicted in Figure 1.1 with brief objectives assigned to each of them.

The framework is proposed as a compressive assessment of buildings, subjected to seismic loads, from material- to system-level with due consideration to the three main societal objectives of safety, economy and sustainability. The strength of the framework stems from its use of consistent tools and rigorous procedures at every stage of the assessment. By considering the inelastic behavior of structures in all the tools mentioned above, the framework is applicable to other structural types such as bridges and other extreme loading scenarios such as wind and blast.

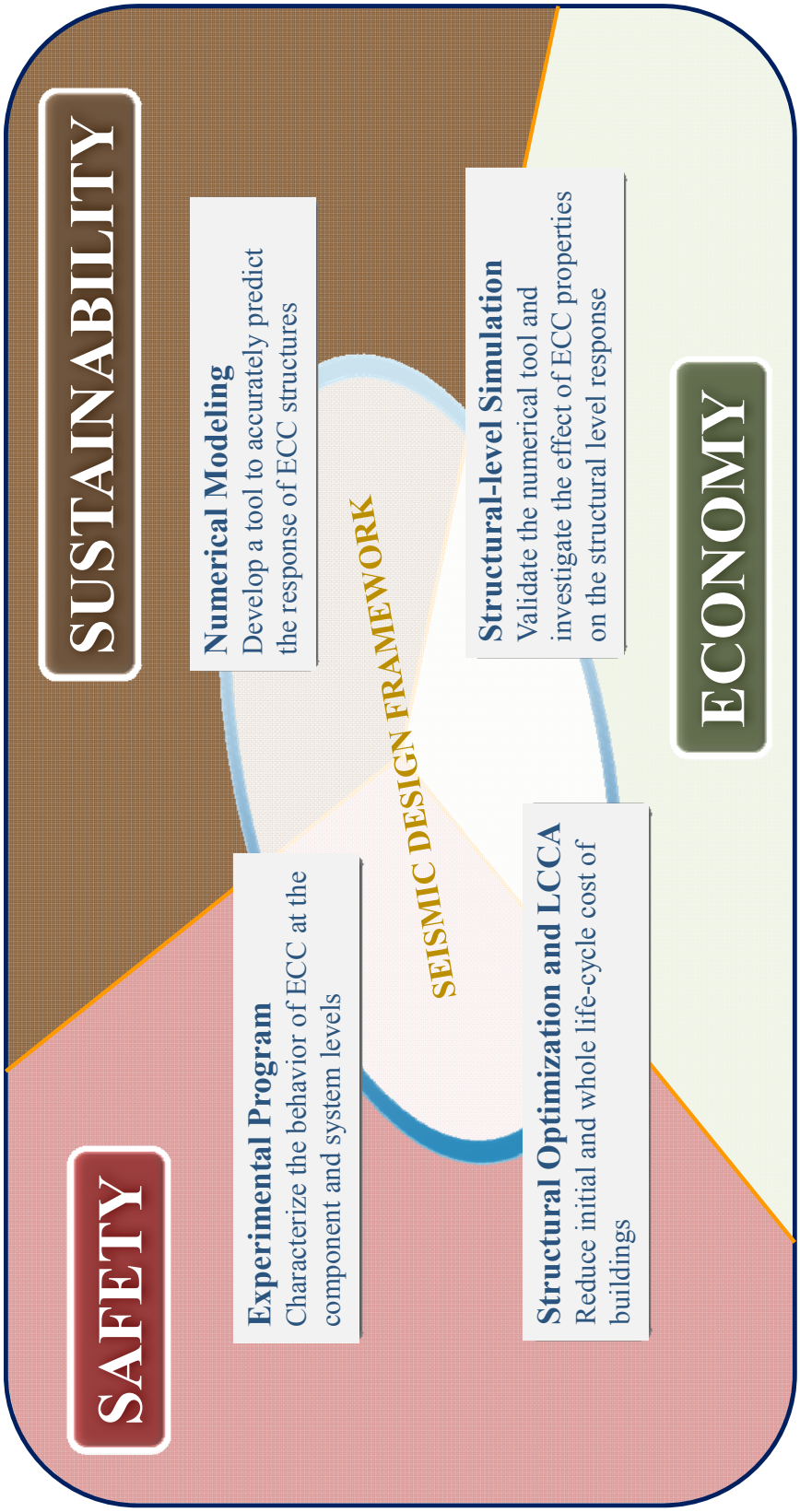

Figure 1.1. Framework for improved seismic design and assessment of buildings

1.4. ORGANIZATION OF THE THESIS

One chapter is dedicated to each of the tools of the seismic design framework mentioned above and depicted in Figure 1.1. No separate chapter is provided for literature review; rather, an extensive review of relevant previous work is provided at the beginning of each chapter along with other necessary background information required for the reader to fully comprehend the presented information. In the following a brief review of each chapter is provided.

Chapter 2 focuses on the development of a numerical tool for assessing the structural capacity of, and earthquake demand on, ECC structures. Background information covers the evolution of fiber reinforced cementitious materials, previous work on the testing of ECC at the material level, and constitutive modeling of ECC. An empirical, uniaxial constitutive relationship is developed for ECC based on existing stress-strain level data. The constitutive model features nonlinear unloading/reloading relationships in addition to a plastic strain model. The model is validated at the stress-strain level and implemented into fiber-based finite element analysis software for structural-level simulation.

Chapter 3 describes the experimental program developed at the small-scale (with a scale factor of 1/8) for the testing of reinforced concrete (RC) and ECC columns and frames. The background information covers the motivation for conducting small-scale testing, the pros and cons of small-scale testing, and a description of pseudo-dynamic and hybrid testing procedures. Additionally, existing literature on small-scale testing and testing of ECC structural members is reviewed. The design of experimental columns and the structural frame is performed, and the procedures used in preparing materials for small-scale testing and fabrication of specimens are described. The testing and simulation framework is presented which includes details on the testing equipment, experimental setup and software environment. Different input motions are developed to simulate earthquake motion. Using the logistical and financial advantages of small-scale testing, a large number of test parameters are investigated. Finally, the results are analyzed and interpreted in terms of the most commonly used seismic design parameters: stiffness, strength, ductility and energy absorption capacity.

Chapter 4 deals with the structural-level simulation of RC and ECC components and systems. The background information covers the modeling of ECC structural members, additional advantages of ECC that contribute to the sustainability objective of the seismic design framework, and structural applications of and code regulations on ECC. Thenceforth, the numerical tool developed for ECC in Chapter 2 is validated at the structural level using the experimental data from Chapter 3. Validation is performed using both cyclic test data from component level testing and results from hybrid simulation of ECC frames under earthquake excitation. A parametric analysis of ECC columns is performed using the validated numerical tool to investigate the effect of ECC tensile properties on the structural level response metrics: stiffness, strength, ductility and energy absorption capacity. The chapter concludes with recommended research on developing seismic design guidelines for ECC structures.

Chapter 5 addresses the optimal seismic design of buildings considering the LCC. The background information covers the definition of terminology used throughout the chapter,

description of approaches for seismic hazard assessment and selection and scaling of earthquake ground motions. The historical evolution of performance-based seismic design (PBSD) is also included. An extensive review of literature is performed in order to identify and address the shortcomings in existing approaches on structural optimization and LCC analysis. For relevance to the application study in this chapter, previous studies on testing of multi-material structural elements are also reviewed in the background section. The earthquake ground motions that are used in LCC optimization are derived consistently for different hazard levels by considering site-specific hazard. An LCC formulation is presented that takes into account all sources of uncertainty with rigorous evaluation of failure probabilities. An optimization algorithm that caters the requirements of multi-objective combinatorial problems with discrete variables is validated and used. The presented formulation is applied to three structural frames (RC, ECC and a multi-material frame) to demonstrate that it is required for an LCC assessment of structures to achieve the economy and sustainability objectives of the seismic design framework.

The thesis concludes with a reiteration of main findings from each chapter and recommendations for future research. As supplementary documentation, test results from Chapter 3 are archived in Appendix A, the design drawings of the formwork that is used for fabrication of small-scale specimens is provided in Appendix B, and the disaggregation results (related to the derivation of seismic hazard) and plots of spectra and time histories of ground motions are given in Appendix C.

Before going into the main body of the thesis, it is important to note the following:

- The term “ECC” is used to refer both to the material and the reinforced structural components and frames. The reader may easily deduct the meaning from the context in which it is used;
- Standard International (SI) units are used consistently throughout the entire document. In certain cases English equivalents are provided in parentheses;
- Acronyms are defined once in each chapter as they appear the first time;
- A list of abbreviations and a list of symbols are provided at the beginning;
- If a single legend is provided in figures with multiple plots (a, b and so on), the legend relates to the data in both plots;
- References and citations are organized almost exclusively according the author-date system of the Chicago Manual of Style (2010).

2

ANALYTICAL MODELING OF ECC

"All analyses are based on some assumptions which are not quite in accordance with the facts. From this, however, it does not follow that the conclusions of the analysis are not close to the facts."

Hardy Cross

Chapter 2 deals with analytical modeling of engineered cementitious composites (ECC). Background information related to the development and evolution of ECC is provided, and structurally related characteristics of the material are described. A uniaxial cyclic constitutive model for ECC is developed and validated at the material level. The uniaxial model is implemented into fiber-based finite element software ZEUS NL for structural level simulations. The objective of this chapter to develop a numerical tool to be utilized in the seismic design framework (described in Chapter 1) for hybrid simulation in Chapter 3, for parametric study of ECC columns in Chapter 4, and for life-cycle cost (LCC) optimization of reinforced concrete (RC) and ECC frames in Chapter 5.

2.1. BACKGROUND

Section 2.1 provides a detailed review of previous work related to development and characterization of ECC as well as testing at the material level and modeling of ECC structural members.

2.1.1. Evolution of Fiber Reinforced Cementitious Composites and Development of ECC

Fiber-reinforced cementitious composites (FRCC), which also comprise Fiber-reinforced concrete (FRC), is a broad classification of materials including ductile fiber-reinforced cementitious composites (DFRCC) and high-performance fiber-reinforced cementitious composites (HPFRCC). ECC, slurry infiltrated fiber concrete (SIFCON), and slurry infiltrated mat concrete (SIMCON) are classified under HPFRCC. More detailed information regarding the categorization of FRCC is available in Matsumoto and Mihashi (2002) and Stang and Li (2004).

The idea of employing fibers in concrete dates back to the 1800's (Berard, 1874), and the first testing of steel fibers as secondary (dispersed) reinforcement in concrete was performed by Romualdi and Batson (1963) and Romualdi and Mandel (1964). However, the first detailed study of the tensile characteristics of FRC was conducted by Naaman (1972). In these tests, tensile strain hardening or multiple cracking behaviors were not observed. Several other studies were performed on FRC (e.g. Kelly, 1972; Hannant, 1978; Lankard, 1985) where the ultimate goal was to improve the tensile characteristics of the material. Further details on the historical evolution of FRCC may be found in Naaman (2007) and Brandt (2008).

Li and co-workers introduced the concept of ECC with strain hardening and multiple-cracking (or diffused cracking properties, which increases energy dissipation and avoids abrupt fracture) properties through a series of papers (Li, 1992b, a; Li and Leung, 1992; Li and Wu, 1992). As mentioned earlier, ECC is categorized under HPFRC. However, ECC differs from other types of HPFRC in that the microstructures are optimized using micromechanical models to achieve ultra-high ductility, with crack widths limited to below 100μm and ultimate tensile strain capacity as high as five percent (Li et al., 2001). Figure 2.1 illustrates the crack widths and distribution of cracks for conventional concrete and ECC. Distributed cracks with small crack widths are observed in ECC while concrete develops large, localized cracks. With proper tailoring of the fiber, matrix and the fiber-matrix interface strain hardening behavior can be achieved with fiber content typically less than two percent by volume. The relatively small amount of fiber in ECC makes it feasible for construction project execution with regular construction equipment. Polyvinyl alcohol (PVA) fibers--specifically developed for ECC and with a special oiling agent to achieve strain hardening--are usually preferred in ECC. Polyethylene (PE) and polypropylene (PP) fibers are among several other alternatives.

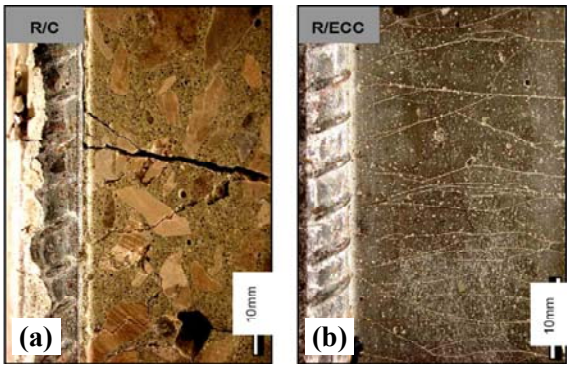

Figure 2.1. Crack widths and distribution of cracks for (a) concrete and (b) ECC (Li, 2003b)

2.1.2. Testing of ECC at the Material Level

Several researchers have investigated the behavior of ECC at the stress-strain level. Chandrangsu and Naaman (2003) conducted monotonic tensile tests on HPFRCC materials with three different types of fibers: Spectra, PVA and steel; and two types of matrices: mortar and concrete. Improved tensile response (over conventional concrete) in terms of exhibiting strain hardening, higher strain capacity and strength was observed for all the test cases. Ahmed et al.

(2006) and Yun et al. (2007) investigated using hybrid fibers (combinations of fibers with different aspect ratios, or mixing steel fibers with synthetic fibers). It was shown that the performance of the material, in terms of tensile strength, ductility, and multiple cracking, could be improved by utilizing hybrid fibers.

For ECC the most comprehensive testing at the stress-strain level was conducted by Kesner and Billington (2004). Monotonic tension and compression tests in addition to cyclic tests with different loading protocols were performed. Through monotonic tension tests, curing and drying periods, specimen geometry, and different fibers in ECC were evaluated. It was found that a longer wet curing period could increase the tensile strain capacity, and that a sufficient drying period was essential. Dog-bone shaped specimens exhibited higher tensile strain capacity when compared to cylinder and prism specimens, and cylinder specimens had a lower peak tensile strength. Three different types of fibers, two made of ultra-high molecular weight polyethylene (UHMWPE) and one from PVA were tested in mixtures of different proportions with and without aggregates. It was confirmed that the type of fibers and the existence of aggregates significantly influence the tensile response characteristics of the material, and that by changing the bond strength between the fibers and the matrix, the aspect ratio of fibers and the content of aggregate and other admixtures, ECC with different properties could be produced based on the micromechanical principles. Monotonic compressive testing conducted by Kesner and Billington (2004) revealed that inclusion of fibers drastically increased the ductility of the material. Cyclic compressive testing indicated that the presence of fibers maintained the integrity of the material, and stable hysteresis loops were observed without any notable reduction from the backbone curve obtained from monotonic compressive testing. Reversed cyclic tension-compression tests showed that the tensile strain hardening characteristics of the material was preserved under load reversal unless softening in compression occured. The occurrence of compression softening was found to cause strength degradation in tension. These findings were also confirmed by a study on cyclic response of ECC which investigated a relatively limited number of parameters (Fukuyama et al., 1999).

2.1.3. Constitutive Relationships for ECC

Geng and Leung (1997) developed a micromechanics based constitutive model to predict the cracking behavior of FRCC beams under bending. Reasonable agreement was observed between finite element simulation and experimental data. It was shown that micro-parameters of the developed constitutive model such as fiber length, volume fraction, and yield strength could be used to optimize the material design, and it was concluded that a micromechanics based analytical tool was important to investigate the effect of micro-parameters on the mechanical properties of the material. Chuang and Ulm (2002) proposed a two phase (matrix and the composite fibers) constitutive model for predicting the material behavior of HPFRCC which could also be used for material design and optimization. One of the important findings from this study was that the ductility of the material was independent of structural dimensions and related only to mixture (i.e. no size effects on ductility). Yang and Fischer (2006) simulated multiple cracking and strain hardening behaviors of ECC under uniaxial tension using a model based on

experimental data on the fiber bridging stress-crack opening relationships of the material. The model parameters included fiber tensile strength and matrix flaw size amongst others. The results were in good agreement with experimental data, but more importantly the model could predict the stress-strain behavior based on the stress-crack opening relationship. Dick-Nielsen et al. (2006) also developed a damage mechanics based model to simulate the uniaxial tensile response characteristics of ECC. Ahmed et al. (2007c) developed prediction equations for the first cracking and ultimate fiber bridging strength of ECC which could also be used to determine the minimum volume fraction of fibers required for the material to exhibit strain hardening and multiple-cracking behaviors in tension. It was found that the properties of the fibers and the interfacial bond strength greatly affected the minimum volume fraction and the first-crack and ultimate bridging strengths.

All the above-cited work relates to characterization of the material behavior, and no attempt was made to predict the response of FRC at the structural level. Only in a limited number of studies proposed constitutive relationships that could be used to simulate structural components (Kabele, 2002; Han et al., 2003). Kabele (2002) developed a constitutive model based on the micromechanics of an equivalent continuum of identical macro mechanical characteristics with the real cracked material and successfully demonstrated the predictive capabilities of the model. Although accurate, the applicability of constitutive models based on continuum damage theory and the theory of plasticity are generally limited due to the large number of parameters required for model definition and the inaptness of the models for structural scale simulations where the global behavior is of interest. The constitutive relationship proposed by Han et al. (2003) was based on cyclic loading/unloading behavior observed in experimental testing of ECC at the stress-strain level. The uniaxial model was generalized to 2-D plane stress analysis based on a total strain rotating crack model. Han et al. (2003) showed that the model could simulate experimental behavior with reasonable accuracy. A modification to compression envelope of the ECC model by Han et al. (2003) is reported in Lee and Billington (2008). The ECC model developed by Han et al. (2003) is also used for fiber based finite element analysis of post-tensioned bridge piers in Lee (2007).

2.2. DEVELOPMENT OF A UNIAXIAL CONSTITUTIVE MODEL FOR ECC

In this section, a macroscopic cyclic constitutive model for ECC is developed based on the response of material at the stress-strain level under different loading regimes. Various features specific to ECC including unloading and reloading characteristics, different backbone curves in tension and compression, and residual strains are taken into account in the model development. Input parameters are limited to those that can be obtained from conventional monotonic compression and tension tests, thus facilitating the model's use with minimum information. With its sensitivity to the main features of ECC response, its simplicity and sufficient accuracy, the model is suited to use in predicting the behavior of ECC structures under monotonic, cyclic and general dynamic loading scenarios. The model is first validated at the stress-strain level and then implemented into fiber-based finite element analysis software. The component and system level validation of the model is performed in Chapter 4, and the model is subsequently used to

investigate the effect of ECC properties on structural level response metrics. The numerical tool developed in this chapter is also utilized for LCC analysis of RC and ECC frames in Chapter 5.

The ECC cyclic constitutive model presented in this thesis builds on the study by Han et al. (2003), and various improvements are proposed to the existing model. These improvements include: higher order reloading relationships in tension and compression, plastic strain model based on regression analysis, and transition curves from tension to compression and vice versa. There is a need for a simplified (yet accurate) ECC constitutive model that can be easily implemented in (fiber based or equivalent) finite element software for structural-scale analysis. The work presented here is proposed as a tool for transition from material level to structural level simulations. The applications of ECC are increasing rapidly (Li, 2006) and for an in-depth understanding of the material behavior, extensive computational simulation should accompany (and partly substitute for) expensive structural testing. The analytical tools developed here are embedded in the proposed framework for the optimal design of buildings.

2.2.1. Overview of the Cyclic Constitutive Model for ECC

The ECC cyclic constitutive model presented here is developed based on experimental observations from two independent studies (Fukuyama et al., 2002; Kesner and Billington, 2004) where testing at the stress-strain level was performed under different loading regimes. Extensive monotonic tension and compression, and cyclic testing of ECC that was conducted by Kesner and Billington (2004) constitute the majority of the experimental data used in this study to develop the various segments of cyclic behavior. Experimental results from Fukuyama et al. (2002) are utilized to verify the ability of the constitutive model to capture the material response exhibited by an independent mixture, that is to say, to compare against data not used in calibrating the model.

Data from three out of four ECC mixtures tested by Kesner and Billington (2004) are used in this study, and the relevant properties for these mixtures are outlined in Table 2.1. The naming convention in Kesner and Billington (2004) is also adopted here. For further details the reader is referred to the original study. In addition to monotonic tension and compression tests, Kesner and Billington (2004) performed cyclic testing under three different loading schemes: cyclic compression, Yankelevsky-Reinhardt (Y-R), and cyclic balanced loading. Three cylindrical specimens were tested for each mixture and for each loading condition in order to investigate the reproducibility of the results. Data from all these tests are utilized here for the model development. Due to the high strain capacity and strain hardening behavior of ECC in tension, the response under cyclic loading is significantly different from that of conventional concrete. Therefore, in order to fully understand the unloading and reloading characteristics in tension and compression as well as transition curves from tension to compression and vice versa, the previously listed loading regimes were employed by Kenser and Billington (2004).

In cyclic compressive testing the specimens were subjected to increasing levels of compressive strain, and full unloading was performed such that the specimens returned to their original lengths. The Y-R loading was adopted from Yankelevsky and Reinhardt (1989) where the material was subjected to increasing levels of tensile strain. At each cycle, in order to ensure

the complete closure of tensile cracks, the specimens were loaded in compression until a similar stiffness to the elastic stiffness in compression was achieved. The results from cyclic compression and Y-R loading herein are utilized to develop empirical relationships for unloading and reloading curves in compression and in tension, respectively. In cyclic balanced loading the material was subjected to alternately increasing levels of strain in compression and tension. The balanced loading scheme helps understand the nature of transition behavior from tension to compression and vice versa and to develop the pertinent relationships for the material model.

Table 2.1. Properties of different ECC mixtures (material ratio by mass)

Material ratio \ Mixture Design	**SP**	**SP-A**	**RECS-A**
Water/Cement	0.35	0.35	0.39
Silica Fume/Cement	0.1	0.1	0
Fly Ash/Cement	0	0	0.3
Aggregate/Cement	0	0.5	0.5
Fiber Volume Fraction	2%	2%	2%
Property \ Mix Design	**SP**	**SP-A**	**RECS-A**
Compressive Strength (MPa)	63	38	41
Comp. Modulus of Elasticity (GPa)	13.8	11.2	12.1
Max. Compressive Strain	0.50%	0.40%	0.40%
Fiber Property \ Fiber Type	**UHMWPE**	**UHMWPE**	**PVA**
Modulus (GPa)	73	73	39
Diameter (μm)	38	38	40
Length (mm)	12.7	12.7	12.7
Interfacial Bond Strength (GPa)	0.5 – 1.0	0.5 – 1.0	3.8

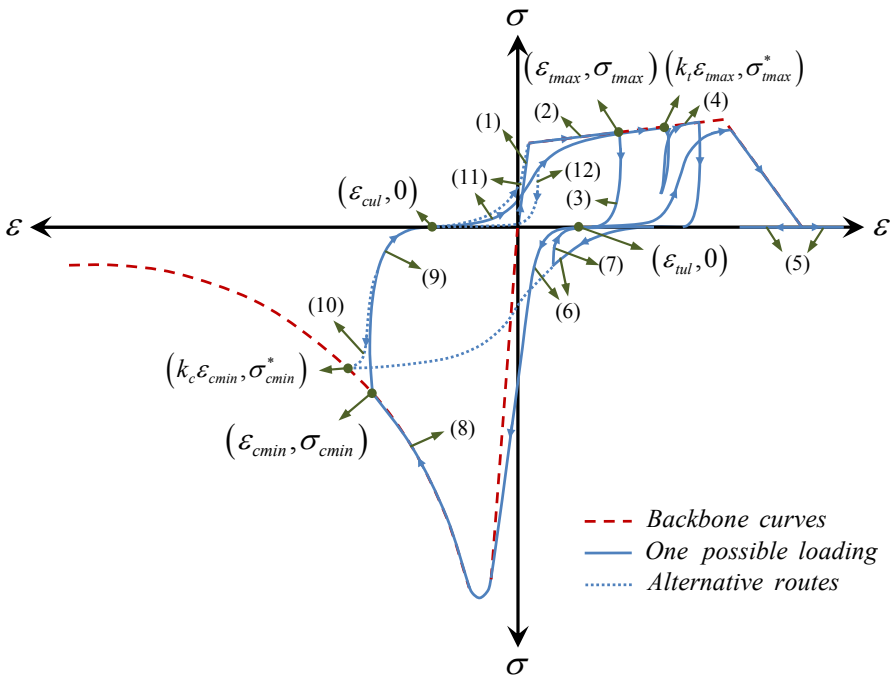

Figure 2.2. ECC cyclic constitutive model (the numbering indicates the different segments)

The loading and unloading segments for the proposed constitutive model are shown in Figure 2.2. The following sections refer to the numbered segments indicated in Figure 2.2. Due to similarities between the two approaches, the notation of Han et al. (2003) is partly followed in the derivation of the constitutive model presented here.

2.2.2. Envelope Curves (Segments 1, 2, 5 and 8)

An envelope (backbone) curve is constructed by joining the points that have maximum absolute value of stress at every strain value in the loading history. Envelope curves, as for most construction materials, are dependent on the loading history and are not unique. As a matter of fact, experimental evidence indicates that conventional concrete exhibits higher strength degradation under load reversal (Karsan and Jirsa, 1969). However, due to its simplicity and ease in determining the model parameters, the monotonic curve is adopted as the envelope curve in several studies (Sinha et al., 1964; Mander et al., 1988; Yankelevsky and Reinhardt, 1989; Bahn and Hsu, 1998, amongst others); recent modeling approaches tend to include the effect of load reversal on the backbone curves (Martínez-Rueda and Elnashai, 1997; Palermo and Vecchio, 2003; Sakai et al., 2006; Sima et al., 2008, amongst others).

Monotonic tests by Kesner and Billington (2004) indicate that ECC tensile behavior is characterized by three distinct regions as shown in Figure 2.3(a). The material exhibits linear elastic behavior until it reaches the cracking strain, ε_{t0}. With the formation of multiple-cracking, the stiffness of the material is significantly reduced (to a value between 1/20 to 1/50 of the elastic stiffness); nevertheless, the material undergoes pseudo strain-hardening and is capable of carrying increasing stresses until the ultimate strength of the material, σ_{tp}, is reached. As the tensile strain goes beyond ε_{tp} (the strain corresponding to ultimate strength in tension), crack localization occurs, and the material starts to soften. Once the ultimate tensile strain, ε_{tu}, is exceeded, the material is unable to carry any tensile stress. The representation of the tension envelope as shown in Figure 2.3(a) was deemed adequate by several researchers (Fischer and Li, 2002; Kabele, 2002; Han et al., 2003; amongst others) in that it well represents the material response observed in monotonic tension tests while providing simplicity in modeling. The mathematical representation of the tension envelope illustrated in Figure 2.3(a) is

$$\sigma_t = \begin{cases} E\varepsilon & \text{for} \quad 0 \le \varepsilon \le \varepsilon_{t0} \\ \sigma_{t0} + \left(\sigma_{tp} - \sigma_{t0}\right)\left(\dfrac{\varepsilon - \varepsilon_{t0}}{\varepsilon_{tp} - \varepsilon_{t0}}\right) & \text{for} \quad \varepsilon_{t0} < \varepsilon \le \varepsilon_{tp} \\ \sigma_{tp}\left(1 - \dfrac{\varepsilon - \varepsilon_{tp}}{\varepsilon_{tu} - \varepsilon_{tp}}\right) & \text{for} \quad \varepsilon_{tp} < \varepsilon \le \varepsilon_{tu} \\ 0 & \text{for} \quad \varepsilon_{tu} < \varepsilon \end{cases} \tag{2.1}$$

where σ_t represents stress on the tension envelope, ε denotes strain, E is the elastic modulus, σ_{t0} is the cracking strength, and the remaining parameters are explained above. The model envelope in Figure 2.3(a) is compared to experimental data in Figure 2.4(a).

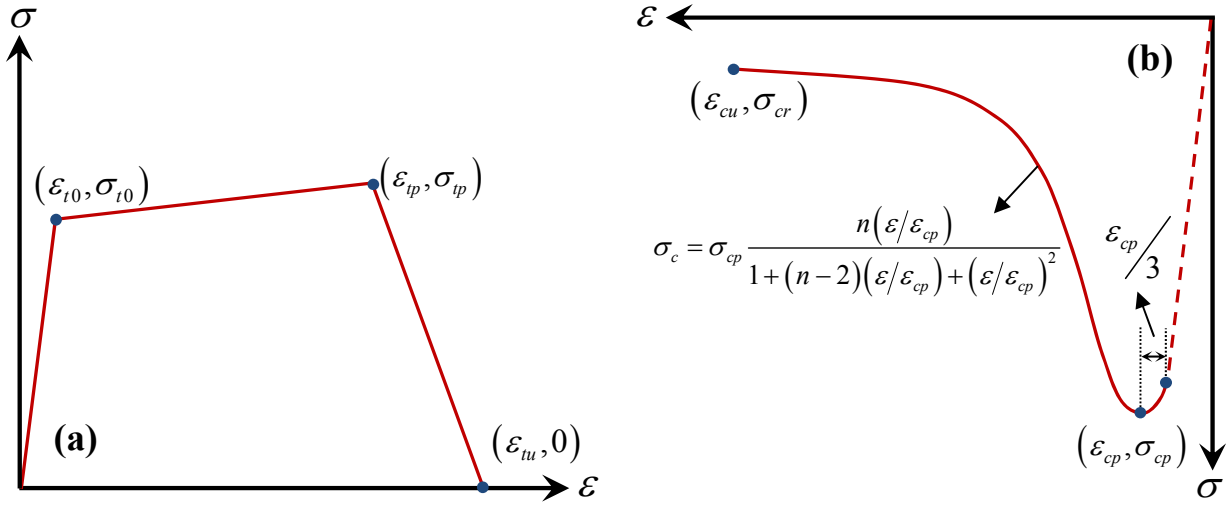

Figure 2.3. (a) Tension and (b) compression envelope curves (drawings not to scale)

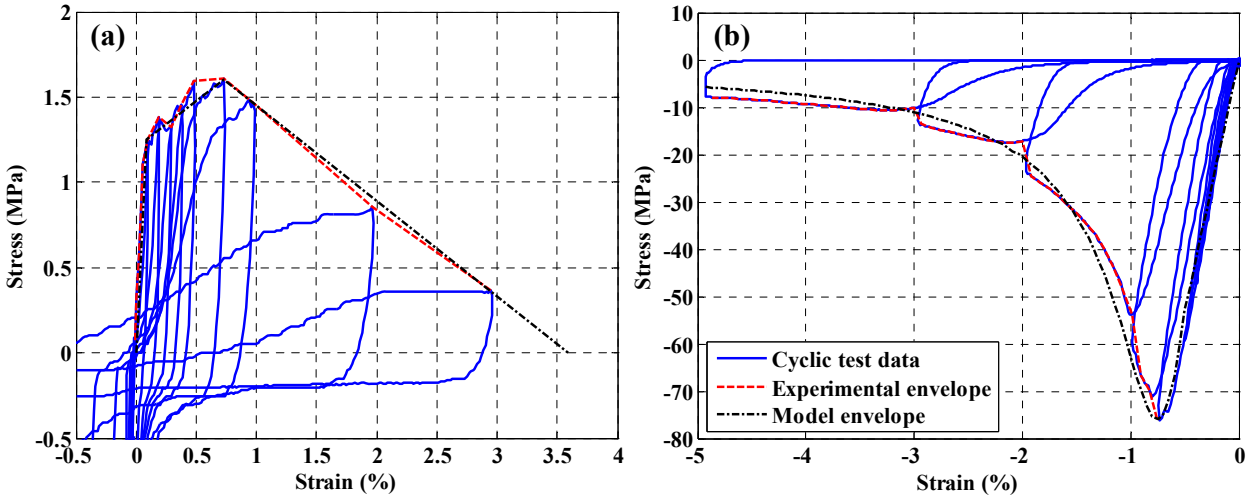

Figure 2.4. SP mixture, comparison of experimental and model (a) tension and (b) compression backbone curves

Test results suggest that load reversals do not induce further degradation to compression envelope, and the stress-strain relationship obtained from monotonic compressive testing could be accurately used as the backbone curve for cyclic modeling of the material. The experimental data indicated a certain amount of disagreement between the monotonic compression curves and the cyclic backbone curves; however, the amount of variation between the monotonic curves alone and the cyclic envelopes alone were similar to that between the monotonic curves and cyclic envelopes. Therefore this variation is mainly attributed to differences in specimen

preparation and imperfections rather than the effect of load reversals on the monotonic curves. Furthermore, the shape of the compression envelope for post-peak response is found to be similar to that observed in conventional concrete. However, the pre-peak response of the ECC is observed to be better represented by a linear elastic relationship up to 2/3 of the strain corresponding to peak stress as shown in Figure 2.3(b). For higher strain values the equation proposed by Saenz (1964) is used to represent the compression envelope for the ECC constitutive model proposed here. It is important to note that the strain is taken to be negative in compression and positive in tension for the derivations presented in Chapter 2. The mathematical representation of the compression envelope is

$$\sigma_c = \begin{cases} E\varepsilon & \text{for } \varepsilon \le \dfrac{2}{3}\varepsilon_{cp} \\ \sigma_{cp}\dfrac{n\left(\varepsilon/\varepsilon_{cp}\right)}{1+\left(n-2\right)\left(\varepsilon/\varepsilon_{cp}\right)+\left(\varepsilon/\varepsilon_{cp}\right)^2} & \text{for } \varepsilon > \dfrac{2}{3}\varepsilon_{cp} \end{cases} \tag{2.2}$$

$$n = -\sigma_{cr}\frac{\varepsilon_{cp}^2 - 2\varepsilon_{cu}\varepsilon_{cp} + \varepsilon_{cu}^2}{\varepsilon_{cu}\varepsilon_{cp}\left(\sigma_{cr} - \sigma_{cp}\right)} \tag{2.3}$$

where σ_c is the stress on the compression envelope, σ_{cp} is the compressive strength and ε_{cp} is the strain corresponding to compressive strength, n is defined by Eqn. (2.3), and ε_{cu} and σ_{cr} are defined by any point on the descending branch of the envelope curve. The schematic representation of the compression envelope is shown in Figure 2.3(b). Although ε_{cu} is depicted as the ultimate strain that the material is expected to undergo in compression (and σ_{cr} as the corresponding stress), in calculation of n, any point on the descending branch that is available can replace this point. Figure 2.4(b) compares the experimental and the model backbone curve given by Eqn. (2.2).

2.2.3. Unloading Curves (Segments 3 and 9)

Figure 2.5 shows the response of ECC for a complete cycle under balanced loading. Starting with tensile unloading: as the elastic strains in the fibers that bridge the cracks are recovered, the material exhibits crack closing with almost zero stiffness (also known as the pinching behavior). As the cracks are fully closed and the material starts to bear compressive stresses, increase in stiffness is observed. Imposing further compressive strains on the material results in stress that reaches and follows the envelope curve. Unloading in compression shows similar behavior to that in tension where stiffness is reduced with crack opening; the material starts to attain higher stiffness in tension as the fibers straighten to bridge the cracks and start to carry the tensile forces. The tensile backbone curve is reached with further increase in strains, and the cycle is completed.

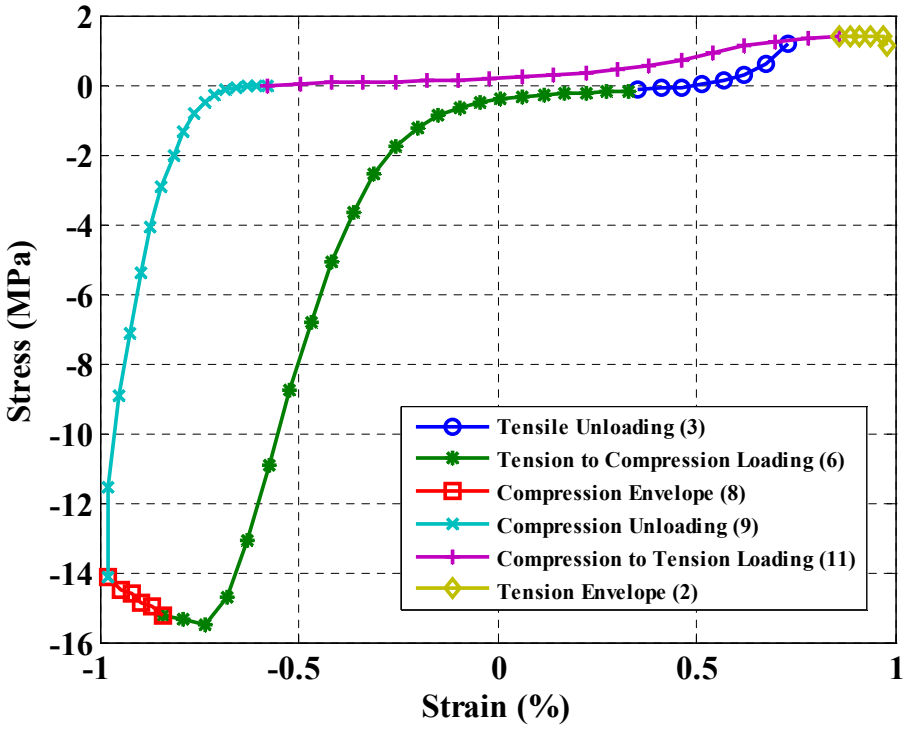

Figure 2.5. A typical cycle of ECC under balanced loading [values in parenthesis are the corresponding segments of the model; data are from Kesner and Billington (2004)]

The unloading curves in tension and compression (schematically shown in Figure 2.6) are represented with a power law as

$$\sigma = \begin{cases} \sigma_{tvar}\left(\dfrac{\varepsilon-\varepsilon_{tul}}{\varepsilon_{tvar}-\varepsilon_{tul}}\right)^{\alpha_t} & \text{tension} \\ \sigma_{cvar}\left(\dfrac{\varepsilon-\varepsilon_{cul}}{\varepsilon_{cvar}-\varepsilon_{cul}}\right)^{\alpha_c} & \text{compression} \end{cases} \tag{2.4}$$

where ε_{tul} and ε_{cul} are shown in Figure 2.6, and α_t and α_c control the rate of unloading as discussed below. Unloading is allowed to start from the envelope curves or from partial reloading preceded by partial unloading. ε_{tvar}, ε_{cvar}, σ_{tvar} and σ_{cvar} are given by

$$\varepsilon_{tvar} = \begin{cases} \varepsilon_{tmax} & \text{unloading from envelope} \\ \varepsilon_{tprl} & \text{otherwise} \end{cases} \tag{2.5}$$

$$\varepsilon_{cvar} = \begin{cases} \varepsilon_{cmin} & \text{unloading from envelope} \\ \varepsilon_{cprl} & \text{otherwise} \end{cases} \tag{2.6}$$

$$\sigma_{tvar} = \begin{cases} \sigma_{tmax} & \text{unloading from envelope} \\ \sigma_{tprl} & \text{otherwise} \end{cases} \tag{2.7}$$

$$\sigma_{cvar} = \begin{cases} \sigma_{cmax} & \text{unloading from envelope} \\ \sigma_{cprl} & \text{otherwise} \end{cases} \tag{2.8}$$

where ε_{tprl}, ε_{cprl}, ε_{tmax}, ε_{cmin}, σ_{tmax} and σ_{cmin} are shown in Figure 2.6. It is deducted from experimental observations that the slope of the unloading curve decreases much faster as the maximum ever experienced strain in tension and compression increases. Therefore, the controlling parameters in Eqn. (2.4), i.e. α_t and α_c, are made linear functions of ε_{tmax} and ε_{cmin}

$$\begin{aligned} \alpha_t &= \alpha_{tmin} + \left(\alpha_{tmax} - \alpha_{tmin}\right)\left(\frac{\varepsilon_{tmax} - \varepsilon_{t0}}{\varepsilon_{tu} - \varepsilon_{t0}}\right) \\ \alpha_c &= \alpha_{cmin} + \left(\alpha_{cmax} - \alpha_{cmin}\right)\left(\frac{\varepsilon_{cmin} - 2/3\varepsilon_{cp}}{\varepsilon_{cu} - 2/3\varepsilon_{cu}}\right) \end{aligned} \tag{2.9}$$

where α_{tmin}, α_{cmin} and α_{tmax}, α_{cmax} are evaluated using experimental data, and two and 40 (for minimum and maximum values, respectively) are found to provide the best fit to the experimentally observed response. The minimum and maximum values for α_t and α_c are determined based on experimental data. Other variables given in Eqn. (2.9), i.e. ε_{t0}, ε_{tu}, ε_{cp}, and ε_{cu}, are parameters defining the envelope curves, and they are previously defined (shown in Figure 2.3).

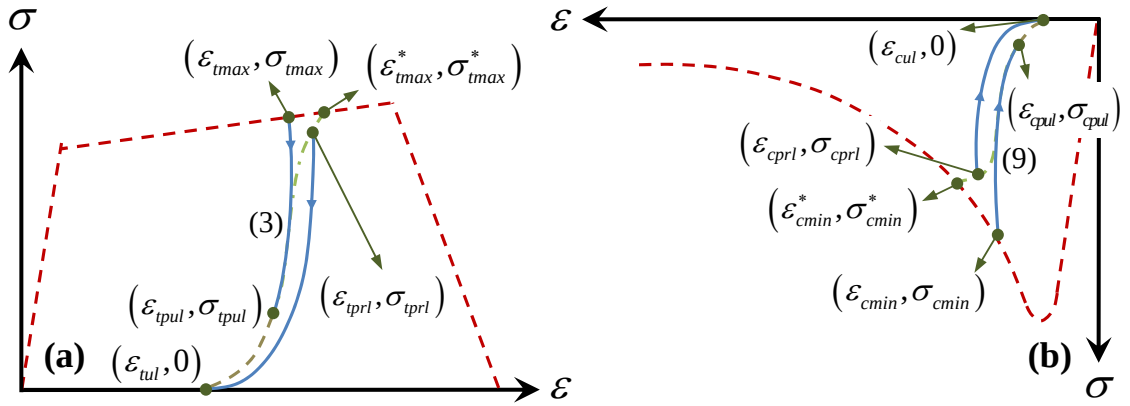

Figure 2.6. Unloading curves in (a) tension and (b) compression (dashed lines: envelope curves, solid lines: unloading segments, dash-dot: example reloading curves)

ε_{tul} and ε_{cul} are the plastic (irrecoverable) strains. Using the available experimental data a plastic strain model is developed for the ECC. Plastic strains in tension and compression are found for each unloading point on the envelope curves, ε_{tmax} and ε_{cmin}, and model parameters

are determined using regression analysis. A plot of data points is provided in Figure 2.7 along with the predictions of the regression models. The plastic strains are given by

$$\varepsilon_{tul} = 0.4583 \cdot \left(\varepsilon_{tmax}\right)^{0.9737}$$
$$\varepsilon_{cul} = \begin{cases} 0 & \varepsilon_{cmin} > -0.00422 \\ -5.5148 \cdot \varepsilon_{cmin}^2 + 0.5940 \cdot \varepsilon_{cmin} + 2.611 \times 10^{-3} & \text{otherwise} \end{cases} \quad (2.10)$$

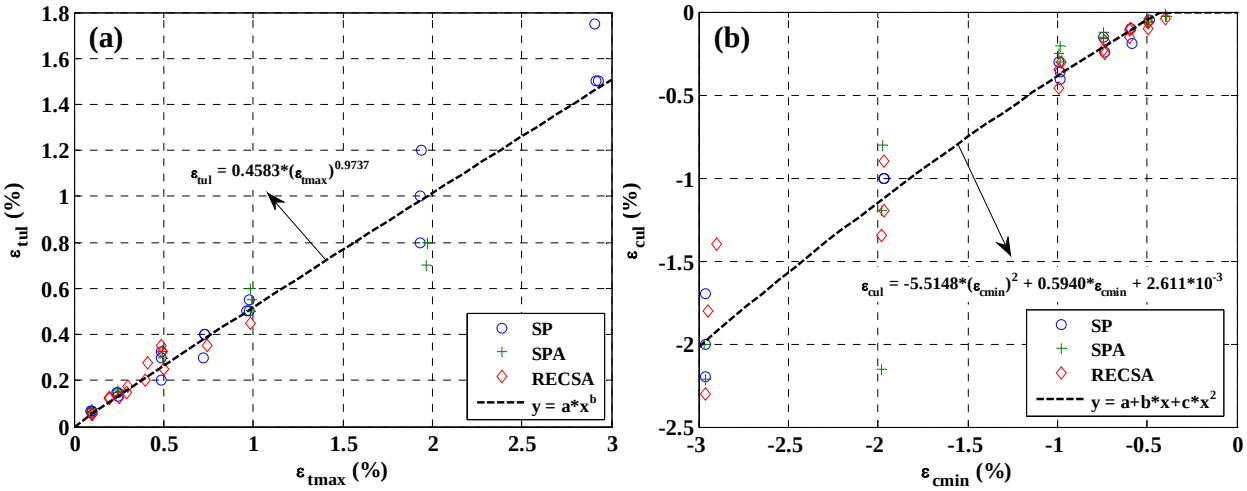

Figure 2.7. Plastic strain models for ECC (a) tension and (b) compression

2.2.4. Reloading Curves (Segments 4 and 10)

As shown in Figure 2.8 the reloading can start from a partial unloading originated in tension or from complete unloading in tension or in compression. Reloading behaviors in tensile and compressive regions are represented using third order polynomials in the form of

$$\sigma = a + b\varepsilon + c\varepsilon^2 + d\varepsilon^3 \quad (2.11)$$

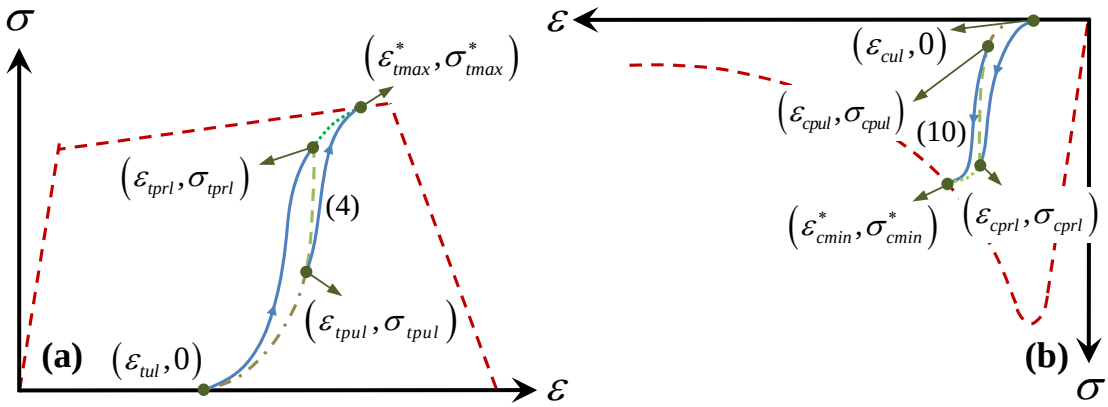

Figure 2.8. Reloading curves in (a) tension and (b) compression (dashed lines: envelope curves, solid lines: reloading segments, dash-dot: example unloading curves)

The coefficients a, b, c and d in Eqn. (2.11) are determined from the initial conditions

$$\left.\begin{aligned}&\sigma\left(\varepsilon_{tvar}\right)=\sigma_{tvar};\ \sigma\left(\varepsilon^{*}_{tmax}\right)=\sigma^{*}_{tmax}\\&\sigma'\left(\varepsilon_{tvar}\right)=E_{tvar};\ \sigma'\left(\varepsilon^{*}_{tmax}\right)=E_{tvar}\end{aligned}\right\}\ \text{tension}$$
$$\left.\begin{aligned}&\sigma\left(\varepsilon_{cvar}\right)=\sigma_{cvar};\ \sigma\left(\varepsilon^{*}_{cmin}\right)=\sigma^{*}_{cmin}\\&\sigma'\left(\varepsilon_{cvar}\right)=E_{cvar};\ \sigma'\left(\varepsilon^{*}_{cmin}\right)=0\end{aligned}\right\}\ \text{compression} \tag{2.12}$$

where the points $(\varepsilon^{*}_{tmax}, \sigma^{*}_{tmax})$ and $(\varepsilon^{*}_{cmin}, \sigma^{*}_{cmin})$, shown in Figure 2.8, are evaluated only when the model goes into the segments two and eight (envelope curves). These points on the envelope curves define the location towards which the reloading occurs. ε^{*}_{tmax} and ε^{*}_{cmin} are given by

$$\begin{aligned}\varepsilon^{*}_{tmax}&=k_t\varepsilon_{tmax}\\\varepsilon^{*}_{cmin}&=k_c\varepsilon_{cmin}\end{aligned} \tag{2.13}$$

where k_t and k_c are linear functions of the maximum ever experienced strains in tension and compression (similar to α_t and α_c)

$$\begin{aligned}k_t&=k_{tmin}+\left(k_{tmax}-k_{tmin}\right)\left(\frac{\varepsilon_{tmax}-\varepsilon_{t0}}{\varepsilon_{tu}-\varepsilon_{t0}}\right)\\k_c&=k_{cmin}+\left(k_{cmax}-k_{cmin}\right)\left(\frac{\varepsilon_{cmin}-2/3\varepsilon_{cp}}{\varepsilon_{cu}-2/3\varepsilon_{cu}}\right)\end{aligned} \tag{2.14}$$

where recommended values for k_{tmin}, k_{tmax}, k_{cmin}, and k_{cmax} are 1.03, 1.1, 1.05 and 1.1, respectively, and the remaining parameters are previously defined. For tension, ε_{tvar}, σ_{tvar} and E_{tvar} depend on whether the reloading starts from full or partial unloading, and the value of ε^{*}_{tmax}

$$\varepsilon_{tvar}=\begin{cases}\varepsilon_{tul} & \text{for reloading from full unloading}\\\varepsilon_{tpul} & \text{for reloading from partial unloading}\end{cases} \tag{2.15}$$

$$\sigma_{tvar}=\begin{cases}0 & \text{for reloading from full unloading}\\\sigma_{tpul} & \text{for reloading from partial unloading}\end{cases} \tag{2.16}$$

$$E_{tvar} = \begin{cases} 0 & \text{for} \quad \varepsilon_{tvar} = \varepsilon_{tul} \\ \dfrac{\sigma^*_{tmax} - \sigma_{tpul}}{\varepsilon^*_{tmax} - \varepsilon_{tpul}} & \text{for} \quad \varepsilon_{tvar} = \varepsilon_{tpul} \\ \dfrac{\sigma_{tp} - \sigma_{t0}}{\varepsilon_{tp} - \varepsilon_{t0}} & \text{for} \quad \varepsilon_{t0} < \varepsilon^*_{tmax} \leq \varepsilon_{tp} \\ 0 & \text{for} \quad \varepsilon_{tp} < \varepsilon^*_{tmax} < \varepsilon_{tu} \end{cases} \tag{2.17}$$

where ε_{tpul} and σ_{tpul} are shown in Figure 2.8 and the remaining parameters are defined previously. For compression ε_{cvar}, σ_{cvar} and E_{cvar} are determined using the same equations, i.e. Eqn. (2.15) through Eqn. (2.17), by replacing ε_{tul}, ε_{tpul} and σ_{tpul} with their equivalents in compression, i.e. ε_{cul}, ε_{cpul} and σ_{cpul}. However, the slope, E_{cvar}, at the point $(\varepsilon^*_{cmin}, \sigma^*_{cmin})$ is not a function of ε^*_{cmin} and is always taken to be zero on the envelope curve in compression.

2.2.5. Transition Curves from Tension to Compression and Vice Versa (Segments 6, 7, 11 and 12)

The cyclic ECC constitutive model presented here does not pass through the origin after the material yields either in tension or in compression. Therefore it is necessary to define loading and unloading segments for the transition regions from tension to compression and vice versa.

The unloading and reloading behavior is shown in Figure 2.2 with segments numbered as 6, 7, 11 and 12 for the transition curves. The unloading curves follow exactly the same derivation described in Section 2.2.3. For unloading from (re)loading in tension to compression, the compression region relation in Eqn. (2.4) is used with ε_{cul} replaced by ε_{tul} and ε_{cvar} equal to ε_{cprl}. The point $(\varepsilon_{cprl}, \sigma_{cprl})$ has the same definition with that shown in Figure 2.6(b) and Figure 2.8(b). Similarly, for unloading from (re)loading in compression to tension, the tension region relation in Eqn. (2.4) is used with ε_{tul} replaced by ε_{cul} and ε_{tvar} equal to ε_{tprl}. The point $(\varepsilon_{tprl}, \sigma_{tprl})$ has the same definition with that shown in Figure 2.6(a) and Figure 2.8(a).

If the material is loading from tension to compression, and the maximum ever experienced strain in compression is less than $2/3\varepsilon_{cp}$, or the material is loading from compression to tension and the maximum ever experienced strain in tension is greater than ε_{t0}, the same reloading curves defined by Eqn. (2.11) in Section 2.2.4 are used, subject to initial conditions provided in Eqn. (2.12). For (re)loading from tension to compression, compression region initial conditions apply, and ε_{cul} and ε_{cpul} are replaced with ε_{tul} and ε_{tpul}. Similarly, for (re)loading from compression to tension, tension region initial conditions apply, and ε_{tul} and ε_{tpul} are replaced by ε_{cul} and ε_{cpul}.

If the material is (re)loading from tension to compression, and ε_{cmin} is greater than $2/3\varepsilon_{cp}$, i.e. the material has not yet yielded in compression, the functional form of Chang and Mander (1994) is utilized

$$\sigma = \sigma_{tvar} + \left(\varepsilon - \varepsilon_{tvar}\right)\left[E_{tc} + A\left|\varepsilon - \varepsilon_{tvar}\right|^{R}\right] \tag{2.18}$$

where ε_{tvar} and σ_{tvar} are given in Eqn. (2.15) and Eqn. (2.16), respectively. E_{tc} (which is only a function of ε_{tvar} in this case) is equal to E_{tvar} as given by Eqn. (2.17) where ε^*_{tmax} and σ^*_{tmax} are replaced by σ^*_{cmin} and $2/3\varepsilon_{cp}$, respectively. R and A are obtained as

$$\begin{aligned} R &= \frac{E - E_{sec}}{E_{sec} - E_{tc}} \\ A &= \frac{E_{sec} - E_{tc}}{\left|2/3\,\varepsilon_{cp} - \varepsilon_{tvar}\right|^{R}} \end{aligned} \tag{2.19}$$

where E_{sec} is

$$E_{sec} = \frac{E\left(2/3\,\varepsilon_{cp}\right) - \sigma_{tvar}}{2/3\,\varepsilon_{cp} - \varepsilon_{tvar}} \tag{2.20}$$

If the material is (re)loading from compression to tension, the above derivations hold; however, each of the variables is replaced with its reciprocal in tension or in compression (with the reciprocal of $2/3\varepsilon_{cp}$ being ε_{t0}).

2.2.6. Summary of the Model

The cyclic ECC constitutive model proposed here is comprised of a total of 12 segments that define the unloading and (re)loading behaviors in tension, compression and the transition regions. These segments are summarized in Figure 2.2. The (re)loading curves incorporate the strength and stiffness degradation as well as the pinching phenomenon observed as a result of crack opening and closing. Quasi-static material test results are used, and rate dependency, creep and fatigue effects are neglected in the derivation of the model. The current model does not take into account degradation due to partial looping. In other words, in order to observe degradation in stiffness and strength it is required that the strains reach or exceed the maximum ever experienced strain either in tension or in compression.

The model parameters are limited to those that define the tension and compression envelopes in order to render the model functional, solely depending on the values that may be determined by monotonic tension and monotonic compression tests, which are relatively effortless to conduct when compared to cyclic tests. Table 2.2 lists the parameters that need to be defined as well as the author's recommended values based on the analyses carried out in this study. During implementation of the model, the following parameters should be stored at each step of the analysis: ε_{tmax}, ε_{cmin}, ε^*_{tmax}, σ^*_{tmax}, ε^*_{cmin}, σ^*_{cmin}, ε_{tul}, ε_{cul}, ε_{tpul}, σ_{tpul}, ε_{cpul}, σ_{cpul}, ε_{tprl}, σ_{tprl}, ε_{cprl}, σ_{cprl}, α_t, α_c, k_t and k_c.

Table 2.2. Parameters of the ECC constitutive model

#	Symbol	Definition	Notes
1	E	Young's Modulus	Parameters defining the tension envelope.
2	ε_{t0}	First cracking strain	
3	σ_{t0}	First cracking stress	
4	ε_{tp}	Strain at peak stress in tension	
5	σ_{tp}	Strength in tension	
6	ε_{tu}	Tensile strain capacity	
7	ε_{cp}	Strain at peak stress in compression	Parameters defining the compression envelope.
8	σ_{cp}	Strength in compression	
9	ε_{cu}	Ultimate strain in compression expected during analysis	
10	σ_{cr}	Stress corresponding to ε_{cu} on the compression envelope	
11	α_{tmin}, α_{tmax} α_{cmin}, α_{cmax}	Parameters defining the minimum and maximum rate of unloading. 2 and 40 are the recommended values for minimum and maximum, respectively.	Parameters defining the unloading and (re)loading segments.
12	k_{tmin}, k_{tmax} k_{cmin}, k_{cmax}	Parameters defining the strength and stiffness degradation. 1.03, 1.1, 1.05 and 1.1 are the recommended values, respectively.	

In conclusion, an empirical macroscopic cyclic constitutive model for ECC is developed. Simple mathematical functions are employed to represent loading and unloading segments of the material behavior. A plastic strain model is developed by regression analysis from experimental data. Transition curves from tension to compression and vice versa are defined such that they do not necessarily pass through the origin after yielding either in tension or in compression.

2.3. VALIDATION OF THE ECC CONSTITUTIVE MODEL AT THE MATERIAL LEVEL

The validation of the ECC constitutive model presented in Section 2.2 is performed at three levels: material, component and system, by comparisons with experimental data. The material level validation is presented in this section while the structural level validation, i.e. component and system, is presented in Chapter 4.

Figure 2.9 compares experimental data from the testing of RECSA mixture (see Table 2.1) under cyclic compressive loading (Kesner and Billington, 2004) with the prediction from the constitutive model. In order to further illustrate the agreement between experiment and simulation, loading and unloading curves are plotted separately in Figure 2.10.

In Figure 2.11, the ECC constitutive model is compared against experimental data (Kesner and Billington, 2004) for SPA mixture (see Table 2.1) under balanced loading conditions. The tension and compression regions are plotted separately to allow for a better comparison.

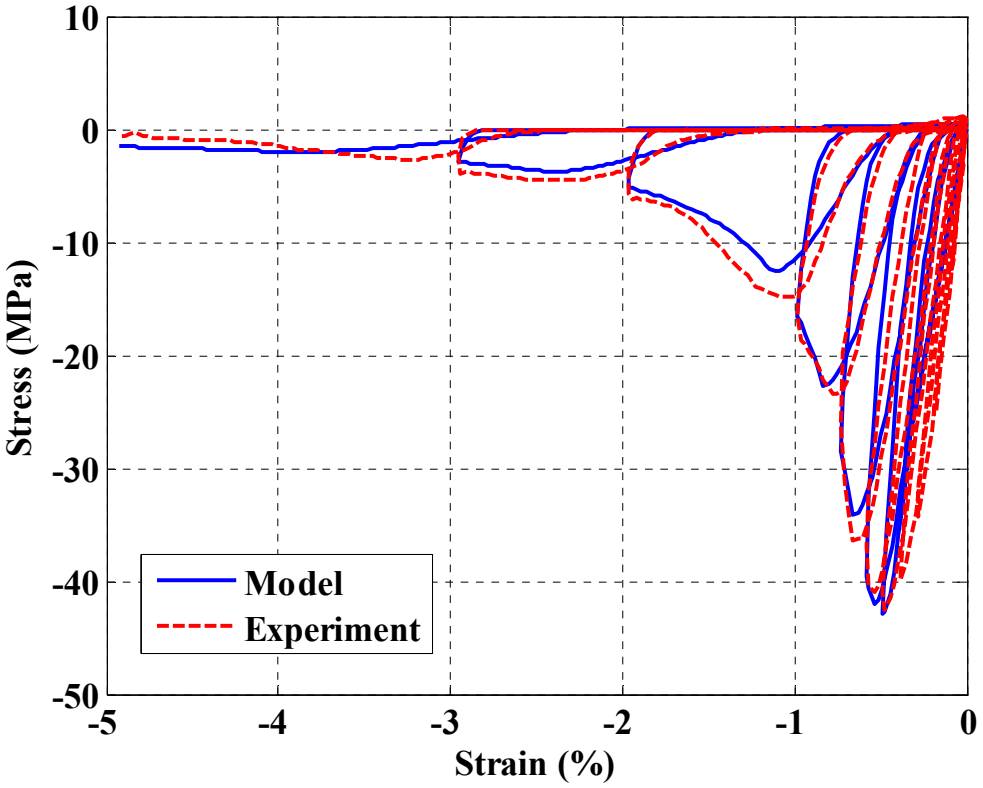

Figure 2.9. Comparison of experiment (Kesner and Billington, 2004) and prediction by the constitutive model for RECSA mixture under cyclic compressive loading

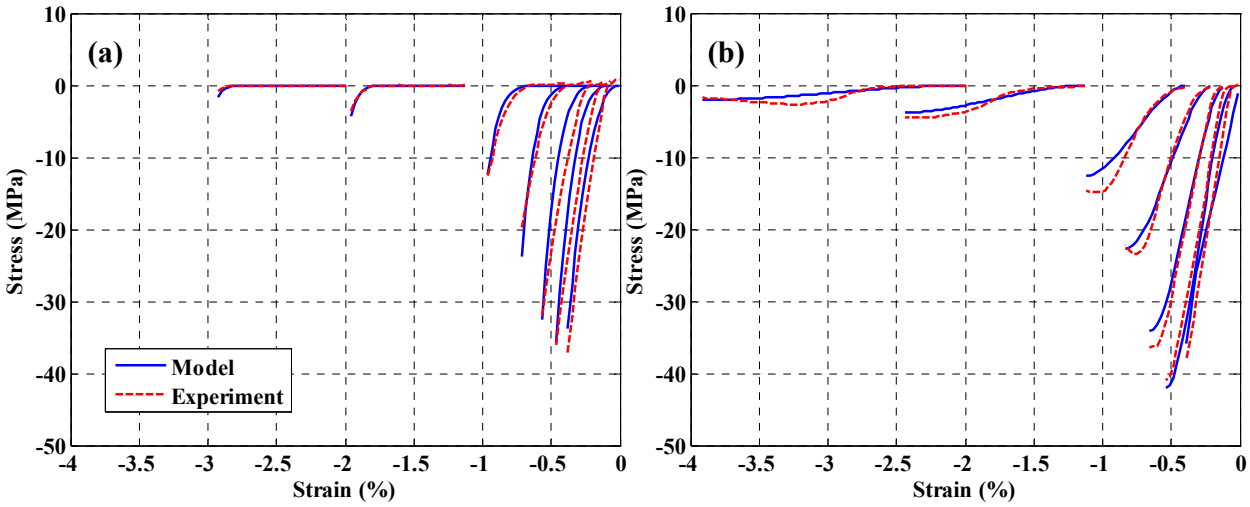

Figure 2.10. Comparison of experiment (Kesner and Billington, 2004) and prediction by the constitutive model for RECSA mixture under cyclic compressive loading, (a) unloading and (b) reloading curves

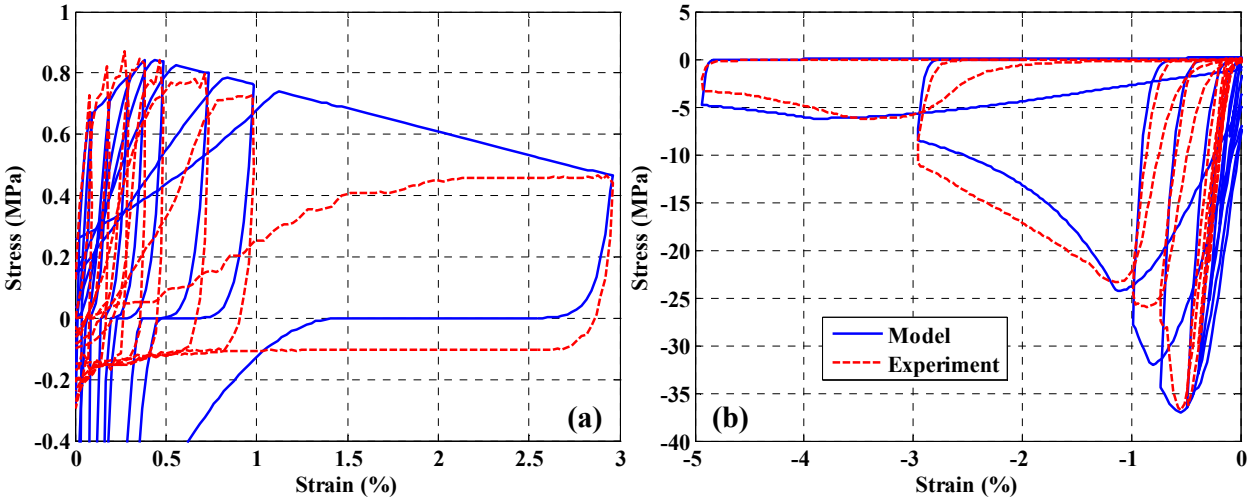

Figure 2.11. Comparison of experiment (Kesner and Billington, 2004) and ECC constitutive model for SPA mixture under balanced loading (a) compression and (b) tension regions

The ECC constitutive model is also validated under cyclic tensile loading. Fukuyama et al. (2002) tested two different ECC mixtures. The loading in these tests was similar to the previously described Y-R loading where material was mainly subjected to cycles in tension. For further details regarding this loading protocol the reader is referred to Sato et al. (2001). One percent PE fibers, and one percent PE fibers and one percent steel cords by volumetric ratio were used for the two mixtures pertaining to comparisons shown in Figure 2.12(a) and Figure 2.12(b), respectively. Figure 2.12 also illustrates that the ECC constitutive model is capable of capturing the experimentally observed behavior for Y-R loading regime also and for mixtures to which it is not specifically calibrated. Although not being reported here, the model is also tested under arbitrary loading cases with no unreasonable behavior observed.

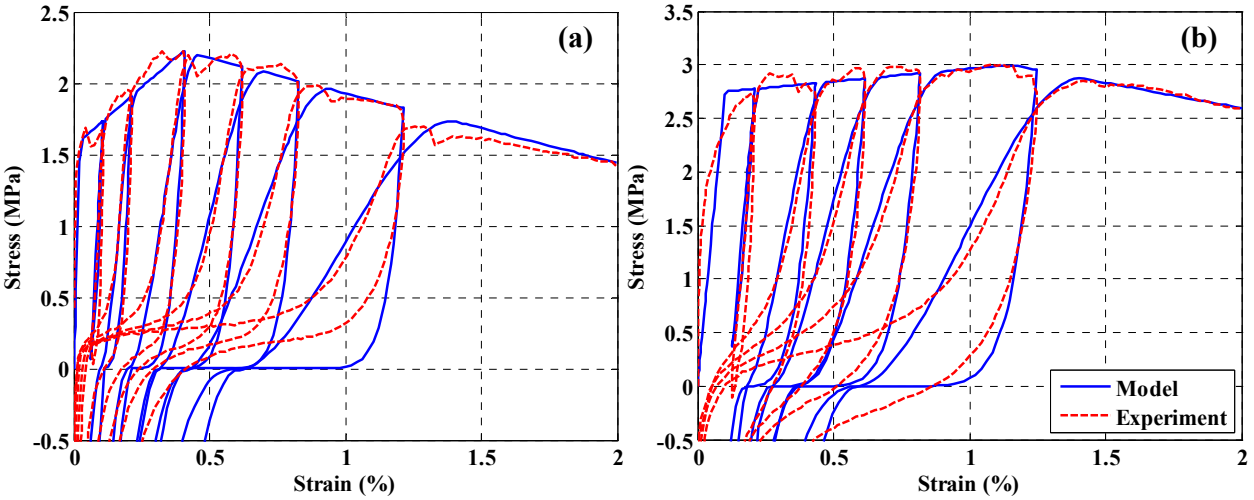

Figure 2.12. Comparison of experiment and ECC constitutive model for two mixtures tested by Fukuyama et al. (2002) under cyclic tensile loading

In addition to the comparative stress-strain plots provided in this section, various response metrics important in the evaluation of a material model are assessed. Strains at different stress levels (i.e. 25 and 50 percent of the compressive and tensile strengths of the material) are computed from both experimental data and model simulation and compared. It is observed that the mean of error ranges between 5-20 percent depending on the loading scheme and mixture. Additionally, peak-to-peak stiffness of the material, which is defined as the slope of the line joining the peak tensile stress and peak compressive stress within a cycle, is compared. The mean of error is found to vary between 5-15 percent. Noting that, the variation between the experimental data from the testing of different specimens of the same mixture is of the same order as the error in the proposed constitutive relationships. It may thus be concluded that the ECC model has acceptable accuracy.

As summarized in Table 2.2, other than the parameters that define the envelope curves in tension and compression, the proposed model has eight additional variables (i.e. α_{tmin}, α_{tmax}, α_{cmin}, α_{cmax}, k_{tmin}, k_{tmax}, k_{cmin}, and k_{cmax}) that control the unloading and reloading segments. Recommended values for these additional parameters are already provided in the preceding sections, and it is advised that users adopt these values unless experimental evidence to the contrary exists. It is informative to demonstrate the effect of these parameters on model behavior and illustrate the sensitivity of the model. To this end, a sensitivity study is conducted and the results are provided in Figure 2.13. With model parameters selected as indicated in Table 2.3, a sinusoidal loading with increasing amplitude is utilized to obtain the results shown in Figure 2.13. As shown in the figure, the parameters k_{tmin}, k_{tmax}, and k_{cmin}, k_{cmax} control the reloading curves towards the tension and compression regions, respectively. Minimum and maximum values allow the user to control stiffness and strength degradation at low and high strain levels, respectively. Increasing values result in increasing stiffness and strength degradation. On the other hand, α_{tmin}, α_{tmax} and α_{cmin}, α_{cmax}, control the steepness of unloading curves in tensile and compressive regions, respectively. Minimum and maximum values serve the same purpose as in the reloading segments. Although the effect of these parameters on the simulated response might be different depending on loading history and envelope curves, it is observed that the model is not very sensitive to these parameters. The insensitivity of the model is desirable because in most cases the experimental data required to determine these parameters is not readily available, and an incorrect selection might lead to inaccurate simulation of structural response.

Table 2.3. Model parameters for sensitivity analysis

Parameter	E	ε_{t0}	σ_{t0}	ε_{tp}	σ_{tp}	ε_{tu}	ε_{cp}	σ_{cp}	ε_{cu}	σ_{cr}
Value	16000 (MPa)	2.5×10^{-4}	4 (MPa)	0.038	5.5 (MPa)	0.06	-0.005	-30 (MPa)	-0.1	-0.5 (MPa)

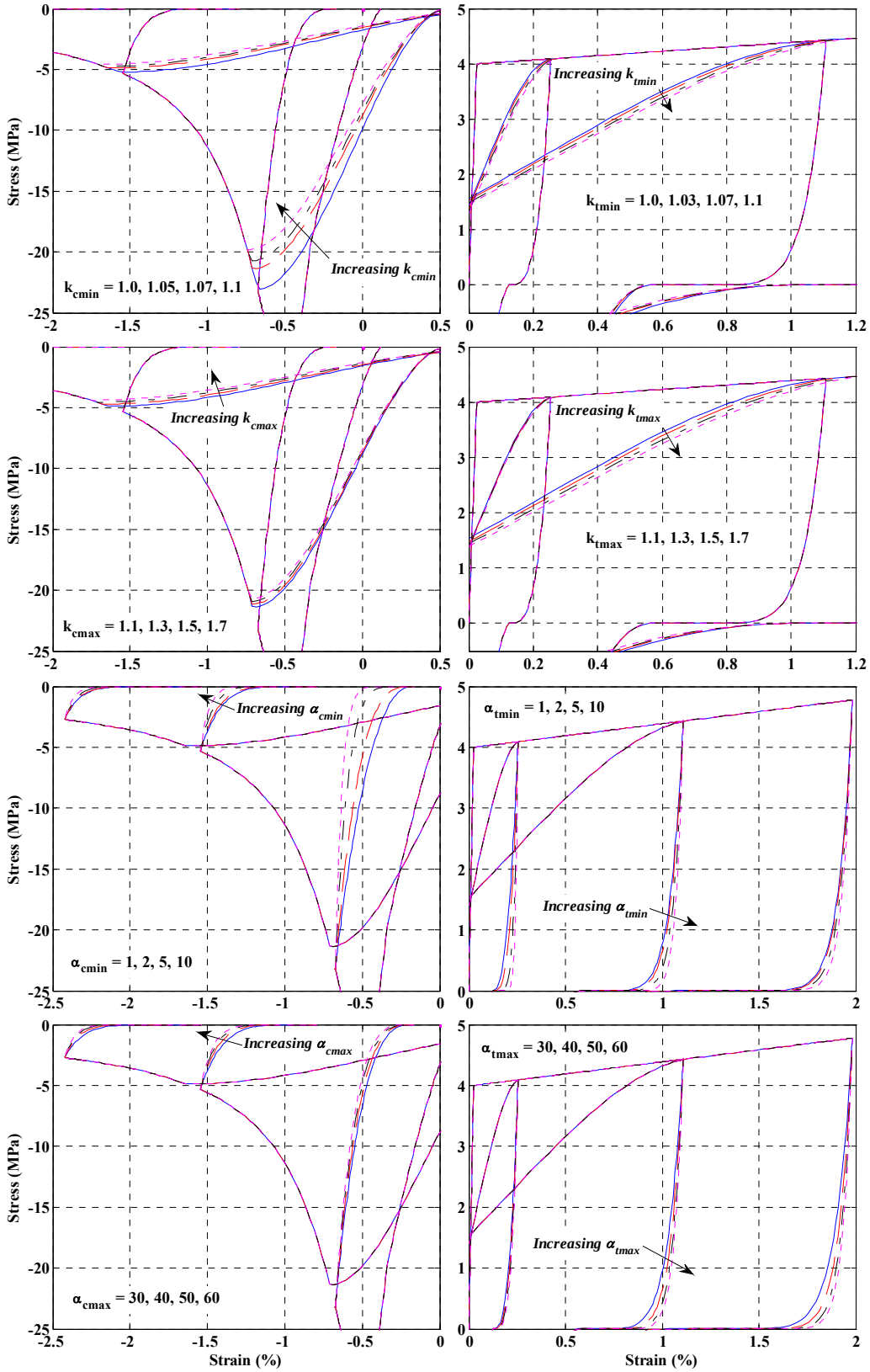

Figure 2.13. Sensitivity of the ECC constitutive relationship to model parameters

Based on the comparisons provided in this section, it is concluded that the ECC constitutive model simulates the experimental behavior with reasonable accuracy. It is important to note that it is possible to obtain more accurate results from simulation by calibrating the parameters of the model specifically to each specimen tested for each mixture; however, for comparison purposes in this section, the model that is described in Section 2.2 is used with the recommended values in Table 2.2 and without data specific calibration. The author believes that such an approach for comparison is a more realistic assessment of the validity of the model. This argument is particularly true when constitutive models are used in structure-level finite element analyses of components and systems. In such cases, which are the main use of macroscopic constitutive relationships, it is rare that material level data will be available for fine calibration prior to structural analysis.

The constitutive model is compared against experimental data from cyclic tension, cyclic compression and cyclic tension-compression tests, and it is observed that the model captures with reasonable accuracy the required characteristics of the material response such as irrecoverable strains, pinching due to crack opening and closing, peak-to-peak stiffness within a cycle, and levels of stiffness and strength degradation. The only major drawback of the current model is that it does not take into account degradation due to partial looping. No experimental data are available to characterize the degradation due to partial loops, and improvements to the model are contingent on further testing.

The constitutive relationship presented here is utilized as a tool for structural-level simulation under monotonic, cyclic and earthquake loading in Chapters 3, 4, and 5.

2.4. IMPLEMENTATION OF THE ECC CONSTITUTIVE MODEL

This section describes the implementation of the ECC constitutive model (developed and validated at the material level in Sections 2.2 and 2.3) into the finite element software package ZEUS NL (Elnashai et al., 2010) to conduct structural level simulations. As explained further in the following, ZEUS NL is a fiber-based finite element analysis program that employs beam-column elements to represent the geometry of structures.

Fiber-based finite element modeling is a very efficient and accurate tool for simulating the response of complete structural systems under static and/or dynamic loading conditions, schematically illustrated in Figure 2.14. Members of the structural frame are represented with beam-column elements that follow the Euler-Bernoulli formulation. As shown in Figure 2.14, each element has two nodes. For 2-D analysis, two displacements and one rotation at each node define the deformation of the elements. In ZEUS NL, evaluation of the element stiffness matrix is performed at two Gauss points located at a distance of $l/2\sqrt{3}$ from the mid-point of the member. Further details regarding the formulation of elasto-plastic beam-column elements in ZEUS NL can be found in Izzuddin and Elnashai (1993a, b). The section at each integration point is further divided into fibers that form the basis of distributed inelasticity models. Section stiffness is evaluated at each of the Gauss points based on the contribution of each fiber. Integration of the stiffness at the Gauss points (along the element length) yields the tangent stiffness matrix for the member. The global stiffness matrix is then populated from the element

stiffness matrices and is used to perform the time integration. A Eulerian formulation is employed to account for the geometric nonlinearities.

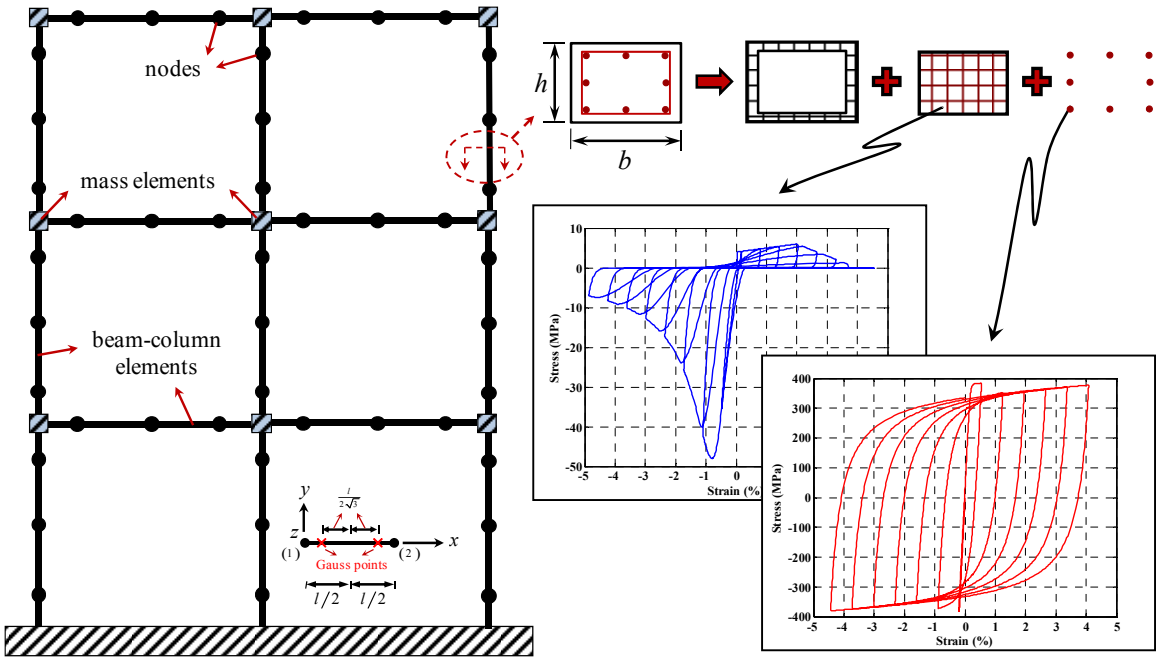

Figure 2.14. Illustration of fiber-based finite element analysis

Sections for the frame member are shown to have a rectangular shape in Figure 2.14; however, other section types are also available in ZEUS NL including I- and T-shaped and circular geometries. It is required to define the locations of reinforcing bars (if present) and the properties for each of the materials on the cross-section. For the example cross-section in Figure 2.14, material properties for unconfined and confined concrete regions as well as reinforcing bars are defined. The program then divides the section into finite regions with areas $\boldsymbol{dA}$ and defines the location of each fiber in the local coordinate system. These finite areas are referred to as "monitoring points." As the number of fibers increases, both the degree of accuracy and the computational time increase. Therefore, a reasonable value should be selected based on the requirements of the section and the type of analysis being conducted. The constitutive relationships used to define each of the materials on the cross-section is fundamental to fiber-based finite element modeling because the accuracy of the results strongly relies on the validity of the material models. Through proper selection of stress-strain relationships, fiber-based modeling allows for representation of various material behaviors including the concrete cracking, crushing and post-peak softening, and the tension stiffening effect. Discretization of the section into fibers makes it possible to define different material models for different regions, e.g. confined and unconfined concrete regions and reinforcing bars.

The strain at each of the monitoring points is calculated based on the nodal translations and rotations. The evaluated strain values are then input to the uniaxial stress-strain relationships corresponding to the material models that are assigned to each of the fibers (as illustrated in Figure 2.14). Implementation of the constitutive relationships in fiber-based modeling is

straightforward. Once the uniaxial stress-strain relationship is defined, say the ECC model described in the previous sections, subroutines with the following functionalities are added to ZEUS NL to allow for structural level simulations:

- Provide stress as a function of strain and the history dependent parameters;
- Provide material tangent stiffness as a function of strain and the history dependent parameters;
- Update history dependent parameters at each iteration;
- Initialize values for history dependent parameters.

Fiber-based finite element analysis, being computationally efficient and accurate in capturing the response of large structures, is used for structural-level simulation in this study.

2.5. CONCLUSIONS

Extensive experimental work related to ECC is available both at material and member levels. However, for a complete understanding of the structural behavior and to further promote ECC applications for improved seismic design, analytical modeling should accompany (and partly substitute for) experimentation. For this purpose, a numerical tool for assessing the behavior of ECC structures has been developed in this chapter. A review of relevant literature on the evolution of FRCC (specifically ECC), testing of ECC at the stress-strain level, and constitutive relationships for ECC has been provided and an empirical macroscopic constitutive model for ECC proposed.

The model was compared against experimental data at the stress strain level and observed to capture with reasonable accuracy the most distinct characteristics of the material response such as irrecoverable strains, pinching due crack opening and closing, peak-to-peak stiffness within a cycle, and stiffness and strength degradation. The only major drawback of the model is that it does not take into account the degradation due partial looping. No experimental data are available to characterize the degradation due to partial loops, and improvements to the model are contingent upon further testing of material at the stress-strain level. The model was first validated at the material level through comparisons with experimental data covering different loading protocols and ECC mixtures. The model was then implemented into ZEUS NL, a fiber-based finite element analysis package, for structural-level simulations. Validation of the model at the structural level is provided in Chapter 4.

The fiber-based analysis technique is selected because this approach provides accurate estimations of the global response of complete structural systems with manageable computational demand. The numerical tool developed in this chapter is utilized for hybrid simulation in Chapter 3, for parametric study of ECC columns in Chapter 4 and for LCC optimization of RC and ECC frames in Chapter 5. The computational efficiency of the fiber-based finite element simulation also allows for the large number of analyses required for structural optimization.

3

EXPERIMENTAL PROGRAM

"If you find that you're spending almost all your time on theory, start turning some attention to practical things; it will improve your theories. If you find that you're spending almost all your time on practice, start turning some attention to theoretical things; it will improve your practice."

Donald Knuth

The objective of Chapter 3 is to build on the information presented in Chapter 2 regarding the behavior of engineered cementitious composites (ECC) at the material level and to characterize the response of ECC at the component and system levels. All testing is conducted at small-scale (with a scale factor of 1/8). Rigorous procedures are employed to achieve realistic similitude for material properties. A concrete mixture that has been developed and verified elsewhere is used. The reinforcing steel is selected with due consideration to stress-strain behavior and bond characteristics with the surrounding matrix. The specimens are fabricated using durable Polyvinyl chloride (PVC) forms to achieve consistency and precision in dimensions. The tests are performed in a well-controlled environment with very high precision in imposed displacements and forces. This experimental program is completed in two phases. In the first phase, reinforced concrete (RC) and reinforced ECC columns are tested under monotonic and cyclic loading. In the second phase the response of RC and ECC structural frames is simulated using sub-structured pseudo dynamic testing (or hybrid simulation). The numerical tool developed for ECC structures in Chapter 2 is utilized in modeling the analytical component of the hybrid simulation where earthquake ground motions are applied to structural systems. The objective of the experimental program is to assess the performance of ECC at the component and system levels and to guide material selection. The results from these tests are also used to validate the constitutive model developed for ECC at the structural level.

3.1. BACKGROUND

Experimental investigations have been fundamental to earthquake engineering research, with results being considered as the basis of several theories, and many of the seismic design

guidelines derived from the experimental observations. In this section, a review of previous studies on small-scale testing, testing of ECC structural members and hybrid simulation is first provided and the motivation for conducting small-scale tests is then described.

3.1.1. Small-Scale Testing

The trend in the civil engineering community in the recent years has been to build larger, more complex laboratories that allow for testing of full-scale specimens under loading and boundary conditions that represent more realistically the real life conditions. Thousands of such tests are being conducted successfully every year in the U.S. and around the world. The major impediment to large-scale testing of structures is the requirement of significant amounts of time and resources for the construction and testing of specimens. Investigating a large number of test variables also requires a significant amount of funding, which is in most cases not available.

As an alternative to large-scale testing, researchers have focused on working with reduced scale specimens (with varying scale factors) and developed test setups that accommodate these models. In an early study, Gilbertsen and Moehle (1980) tested small-scale columns (with cross sectional dimensions of 51 mm x 38 mm) under axial and shear force reversals. Micro-concrete and rusted smooth wires were used to model concrete and reinforcement respectively. It was concluded that the behavior of small-scale columns closely matched that of full-scale members. Kim et al. (1989) conducted a series of experiments on RC beams to develop suitable techniques to model small-scale RC behavior for earthquake simulations. In the same study the performance of different model reinforcement was investigated, and it was concluded that threaded rods best represent the behavior of prototype reinforcement. In a more recent study, Lu et al. (1999) investigated the effect of level of scaling on the cyclic behavior of RC columns. Three scales were considered: 1/2, 1/3 and 1/5.5. Although a more concentrated cracking pattern was noticed in the smaller scale columns, in general, similar behavior was observed on all scales, which is attributed to procedures followed in construction of the specimens that enhanced the similarity between the scales. Several other studies investigated RC behavior at a reduced scale (Caccese and Harris, 1990; Panahshahi et al., 1991; Kim et al., 2009, amongst others). A common finding of these studies was that good correlations could be obtained between the scales if careful procedures were followed in preparation of materials and construction of specimens. It was also found that the discrepancies resulting from the use of materials such as mortar and smooth wires to represent concrete and longitudinal reinforcement respectively and observed at highly inelastic stages in some of the earlier studies (Abrams, 1976), could be avoided.

Some researchers have rightly approached reduced scale testing with caution due to the phenomenon known as size effects (here used as the failure that is related to some characteristic length). Theoretically, scaling is a valid approach. However, scaling requires achieving identical stress-strain relationships for materials in both scales while also scaling other properties such as aggregate size and voids. Even if these requirements are achieved, the similitude is guaranteed only if the model is linear elastic or the failure is governed by plasticity. If the model fails by some other mechanism, such as fracture, size effects could be expected. Researchers have shown that lightly or unreinforced concrete elements fail in shear display size effects (e.g. Bažant and

Kazemi, 1991; Collins and Kuchma, 1999) due to the quasi-brittle nature of concrete. A detailed investigation of size effects is outside the scope of this thesis, but an in-depth treatment of size effects and the ensuing consequences for the strength of materials is available in Bažant (2005).

3.1.2. Pseudo-Dynamic Testing and Hybrid Simulation

Shake table testing is the most direct way of experimentally investigating the behavior of structures since the dynamic loading effects are naturally taken into account. Although extensive shake table testing facilities have been built in recent years (e.g. University of California San Diego Outdoor Shake Table and E-defense facility in Japan) to allow for testing of full-scale structures, such facilities are rare due to very high construction and operation costs. Furthermore, there are still limitations in terms of dimension, payload and dynamic capacity, especially for the testing of horizontally extending structures such as bridges.

An alternative approach is pseudo-dynamic testing where the inertial and dynamic forces are analytically computed thereby eliminating the dynamic load requirements on the testing equipment and at the same time overcoming the load path issues associated with quasi-static testing. Pseudo-dynamic testing was first introduced in Japan (Hakuno et al., 1969; Hakuno et al., 1972; Takanashi et al., 1975). Since then, this powerful method has been successfully used in various experiments around the world (e.g. Mahin and Shing, 1985; Nakashima and Kato, 1987; Elnashai et al., 1990; Jeong and Elnashai, 2005).

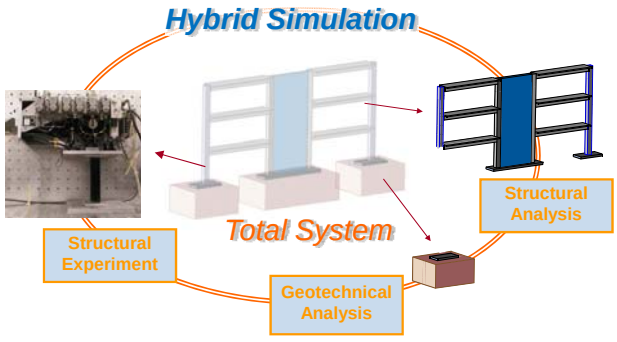

Figure 3.1. Illustration of sub-structure technique for pseudo-dynamic testing

In sub-structured pseudo-dynamic testing (or hybrid simulation), which is an extension of the existing method, the complete structural system is sub-structured into components (see illustration in Figure 3.1). This technique was first introduced by Dermitzakis and Mahin (1985). Sub-structured pseudo dynamic testing allows for a more realistic simulation of the response of the entire system by making use of the advantages of both physical testing and numerical analysis. The well-understood regions of the system are analyzed computationally, while regions of particular interest (usually those that exhibit high inelasticity) are tested in the laboratory. Hybrid simulation has also been extended to span multiple facilities (distributed sub-structured pseudo-dynamic testing) to utilize the unique capabilities of different testing equipment (e.g. Wanatabe et al., 1999; Spencer et al., 2004; Stojadinovic et al., 2006; Mosqueda et al., 2008). Hybrid simulation also allows for utilization of multiple structural analysis software to capitalize

on the different capabilities of each numerical tool, and having an experimental component is not a requirement. Hybrid simulation has been successfully used for assessing the performance of buildings (e.g. Seible et al., 1996; Molina et al., 1999; Tsai et al., 2004) and bridges (e.g. Nagata et al., 2004; Pinto et al., 2004; Kwon and Elnashai, 2007; Kim and Elnashai, 2008).

3.1.3. Previous Experimental Work on ECC Structural Members

Several experimental studies have been performed on ECC structural members. These studies show enhanced structural characteristics of ECC over conventional concrete. Below, previous experimental work is categorized under titles based on structural behavioral characteristics, and the major findings are outlined.

3.1.3.a. Damage Tolerance

Fukuyama (2002) proposed using a short column with very high strength, stiffness and ductility for retrofitting structures that are prone to soft story failure. This device is proposed as a cost effective damage mitigation strategy, and high-performance fiber-reinforced cementitious composites (HPFRCC) are employed in place of concrete to achieve high energy dissipation and ductility. Xia and Naaman (2002) proposed using a new seismic shear wall. Through testing, it was shown that improved strength, displacement and rotation ductility, and shear deformation and energy dissipation capacities could be achieved by using HPFRCC in certain wall layouts. Fischer and Li (2003a) tested fiber-reinforced polymer (FRP) reinforced ECC cantilever column elements and showed that large tensile strain capacity of ECC resulted in compatible deformations between the FRP reinforcement and the ECC matrix which reduced residual deflections. Another study by the same researchers (Fischer and Li, 2003b) on ECC portal frames with FRP reinforced columns and steel reinforced beams showed that the inelastic deformations could be trapped at beam plastic hinges, and large drift levels could be achieved without plastic hinge formation at the column bases. The latter helped the structure to sustain its load carrying capacity without any sign of overall instability, and the system suffered very small permanent drifts. Very small residual deflections and no concrete cover spalling were observed, which allowed for retrofitting members at a lower cost in a post-earthquake situation.

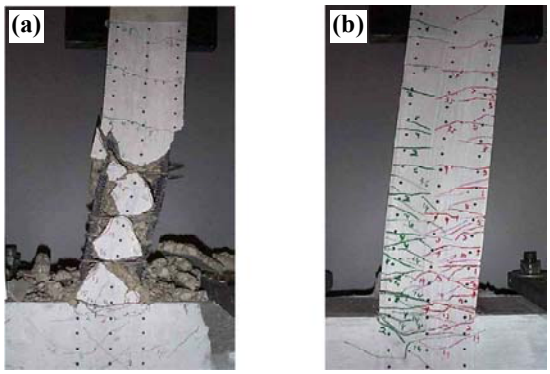

Figure 3.2. Illustration of higher damage tolerance observed in ECC members, (a) RC (b) reinforced ECC (Fischer and Li, 2002)

Testing of ECC and concrete columns conducted by Fischer and Li (2002) indicated higher damage tolerance by ECC (Figure 3.2). Parra-Montesinos and Chompreda (2007) demonstrated that the existence of an ECC matrix in flexural members prevented buckling of longitudinal reinforcement up to plastic hinge rotations of four percent or greater for members with no web reinforcement, and no rebar buckling was observed for specimens with web reinforcement spaced at half the member depth. In most cases, occurrence of rebar buckling caused irreparable damage, so elimination of this phenomenon would substantially decrease the retrofitting costs. Fukuyama et al. (1999; 2000) tested polyvinyl alcohol (PVA) ECC beams and columns under Ohno-type cyclic loading. It was observed that brittle failure modes such as shear failure and bond-splitting could be effectively mitigated by using ECC instead of ordinary concrete. Additionally, very small shear crack widths were observed (even below the durability limit state) at excessively high drift ratios, exemplifying the damage tolerance characteristic of the ECC specimens.

3.1.3.b. Shear Resistance

It was shown by several researches that the ductile nature of ECC could be used effectively to improve the performance of shear critical structural components such as beam-column connections, walls, deep beams and short columns, and brittle failure modes could be avoided (Kanda et al., 1998). Fischer and Li (2002), Parra-Montesinos and Chompreda (2007) and Li and Wang (2002) amongst several others showed that when ECC was employed due to high shear resistance and self-confining features, shear reinforcement could be effectively reduced or completely eliminated. Studies performed on shear critical components such as coupling beams (Canbolat et al., 2005; Yun et al., 2008), energy dissipation devices (Fukuyama and Suwada, 2003; Nagai et al., 2004) and beam-column connections (Parra-Montesinos et al., 2005) confirmed findings on increased ductility and load sustainability at excessive deformations, high shear resistance with reduced (or no) shear reinforcement, and high damage tolerance and energy absorption characteristics achieved when HPFRCC was employed in place of conventional concrete. Van Zijl (2007) proved through pure shear testing at the stress-strain level that ECC exhibited high shear resistance and ductility, and Shimuzu et al. (2004) and Fukuyama (2000) showed increased shear resistance of ECC beams through a series of tests under Ohno type loading (Figure 3.3).

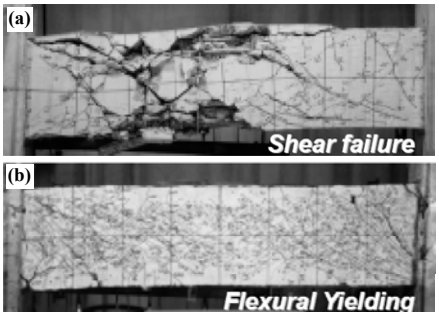

Figure 3.3. (a) Shear failure in RC and (b) flexure yielding in ECC members (Fukuyama et al., 2000)

3.1.3.c. Energy Absorption

Billington and Yoon (2004) proposed using a precast segmental concrete pier system with ductile fiber-reinforced cementitious composites (DFRCC) in potential plastic hinge regions. Through testing, it was proven that the existence of DFRCC considerably increased the hysteretic energy absorption capacity and damage tolerance of the pier up to drift levels of three to six percent. Specimens with conventional concrete at the plastic hinge regions exhibited localized cracking resulting in spalling of concrete cover and exposure of mild reinforcement. On the other hand, DFRCC material showed multiple cracking without any crack localization or cover spalling, even though no additional transverse reinforcement was provided to that required for shear strength. Energy absorption capacity of columns with DRFCC was observed to increase by around 50 percent on average when compared to columns with conventional concrete. Fischer and Li (2002) tested cantilever column elements under flexural cyclic loading. It was observed that steel reinforced ECC members could absorb three times more energy than RC members (Figure 3.4). Although the majority of the absorbed energy was due to plastic deformations of the steel reinforcement, the ductile stress-strain behavior of ECC allowed for high deformations in reinforcement, while this mode of energy dissipation could not be fully utilized in RC members due to shear and compression failure of concrete.

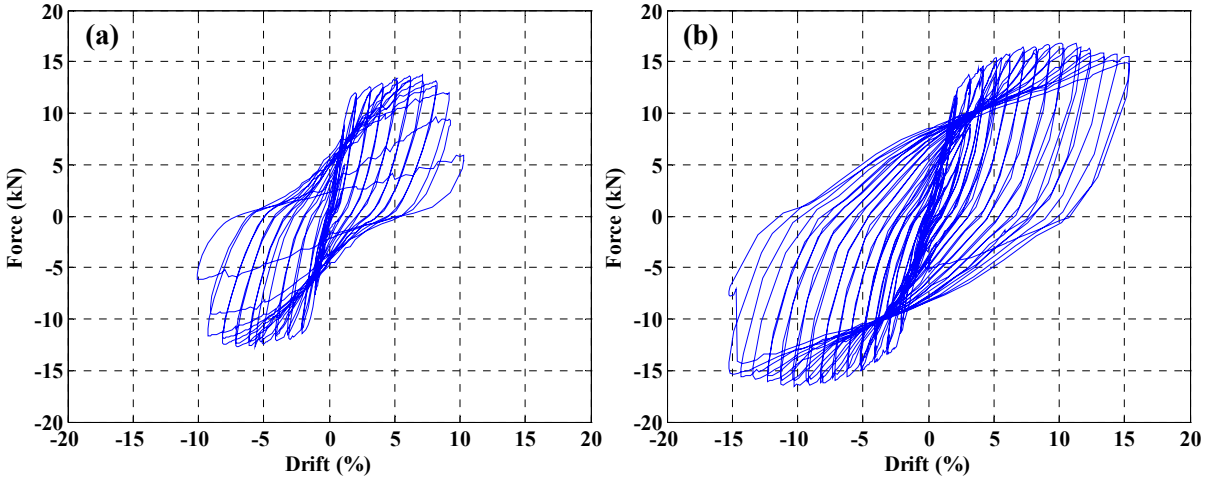

Figure 3.4. Higher energy absorption observed in (b) ECC members when compared to (a) conventional concrete (Fischer and Li, 2002)

3.1.3.d. Bond Strength, Spalling Resistance and Deformability

Testing showed that high tensile strain capacity of ECC resulted in continuous deformation of the matrix and the reinforcing bar, reduced the strain localization and improved bonding (Fantilli et al., 2005; Mihashi et al., 2007). Fischer and Li (2002) showed that the high tensile strain capacity of ECC results in compatible deformations between the reinforcement and the ECC matrix, even at excessive levels. Compatible deformations prevented local damage induced by bond slip and large interfacial bond stresses. Bond-splitting failure was eliminated when ECC was employed in place of concrete, as demonstrated in Figure 3.5. Improved response could be

achieved in terms of tensile strength, energy absorption, and level of damage at large deformations.

As opposed to conventional concrete, ECC did not disintegrate due to fiber bridging. Therefore cover spalling caused by factors such as expansion of concrete due to corrosion debris or excessive deformations was eliminated (Fukuyama and Suwada, 2003; Li and Stang, 2004). A comparison of the spalling resistance of ECC and RC members is shown in Figure 3.6. This feature of ECC prevented exposure and buckling of reinforcing bars. Qian and Li (2006) demonstrated that improved response in terms of load carrying capacity and ductility could be achieved at steel anchorages to concrete through utilizing the inelastic straining capacity of the ECC. Kurihashi et al. (2006) showed through testing of slabs under static and projectile loading that using ECC increased the spalling and impact resistance.

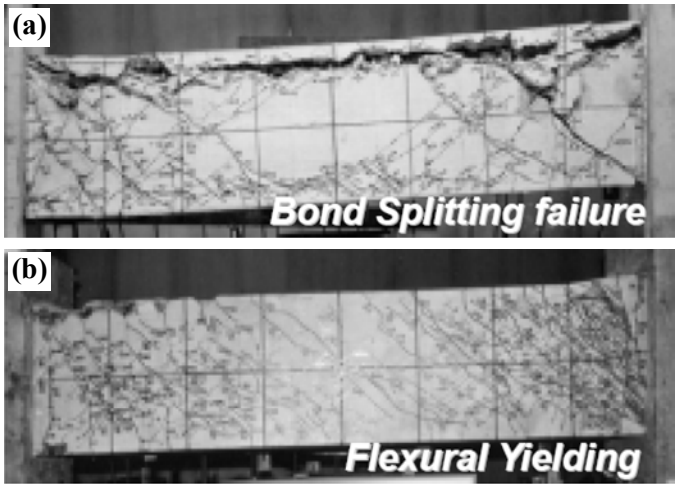

Figure 3.5. Higher bond-splitting resistance observed in (b) ECC members when compared to (a) conventional concrete (Fukuyama et al., 2000)

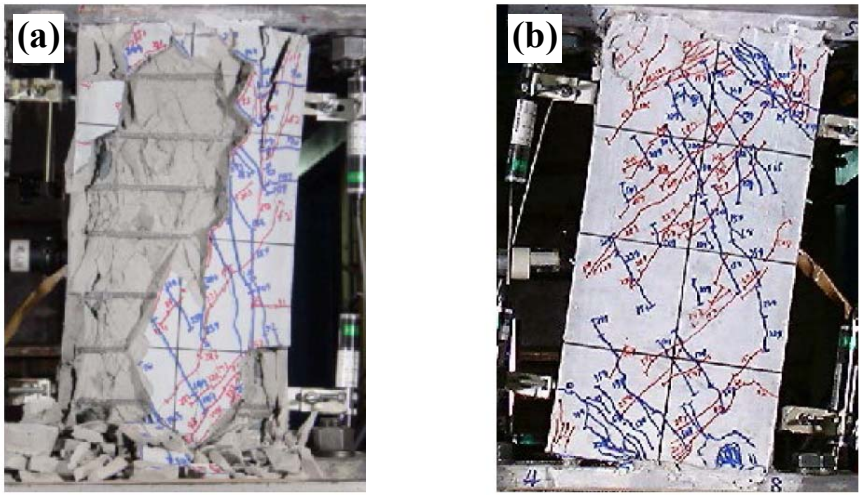

Figure 3.6. Higher spalling resistance observed in (b) ECC members when compared to (a) conventional concrete (Fukuyama and Suwada, 2003)

3.1.3.e. Retrofitting

Maalej and Leong (2005) tested the effectiveness of external FRP strengthening for beams with ECC as a ductile layer around the main flexural reinforcement. It was shown that the existence of an ECC layer delays debonding of FRP. Testing and analysis by Habel et al. (2007) indicated that the existence of a layer material with strain hardening and high ductility features in tensile regions of beams increased the stiffness and reduced crack widths and crack spacing. It was observed that when two percent reinforcing bars by volume were included in this layer, the composite beams' hardening magnitude could be increased three times.

Kesner and Billington (2005) proposed using precast infill panels made with DFRCC for retrofitting steel framed hospital structures. Testing indicated that using DFRCC material was favorable for achieving the desired strength, drift capacity and energy dissipation over conventional concrete. Krstulovic-Opara and Al-Shannag (1999) demonstrated that 25 mm thick HPFRCC jacketing could prevent brittle shear failure and eliminate the shear reinforcement requirement for beams. These observations signify the potential for using HPFRCC in retrofitting applications of structures with poor seismic detailing. Dogan and Krstulovic-Opara (2003) investigated using HPFRCC for jacketing column lap splices and joint regions to increase the confinement and hence the flexural column capacity, and to improve the anchorage of discontinuous bottom beam reinforcement. HPFRCC was found to be effective in achieving these retrofitting objectives.

3.1.4. Motivation for Small-Scale Testing

In a recent study, Holub (2009) investigated the effect of variable axial load on the response of RC bridge piers through a set of large- (1/2 scale factor) and small-scale (1/20 scale factor) tests. The experiments were conducted at the NEES@Illinois facility using the same testing equipment as for the test undertaken here (further details about the testing framework is given in Section 3.5). The size of the specimens did not allow for the measurement of local response (e.g. strains); however, when global response measures, such as drift and lateral force resistance, were considered, excellent correlations were obtained between the scales. Figure 3.7 compares the lateral force vs. drift response of large- and small-scale piers under cyclic loading with constant axial tension. The successful series of small-scale tests performed by Holub (2009) has been the main motivating factor in developing the experimental program described in this thesis. The main reasons that led to successful experiments at the small-scale (and which were missing in some of the earlier work), are summarized as follows: (i) materials are prepared carefully based on behavior and not on direct scaling; (ii) stringent guidelines are established and followed in specimen construction to assure consistency among specimens; (iii) the testing equipment is an exact replica of that is used for large-scale testing and allows for very precise execution and measurement of displacements and forces; and (iv) the specimens are designed to fail by plastic yielding that to a large extent avoids size effects.

It is also important to mention that, as described in detail in the subsequent sections, in the development of this experimental program, the materials that are used in construction of small-

scale specimens are carefully prepared in order to mimic the stress-strain response exhibited by the prototype materials. Furthermore, the specimens are designed to fail in flexure, which is governed by the laws of plasticity; thus, size effects are minimized. The specimens are fabricated with attention to precision in small-scale dimensions to achieve consistency across specimens, and the tests are performed using high precision testing equipment.

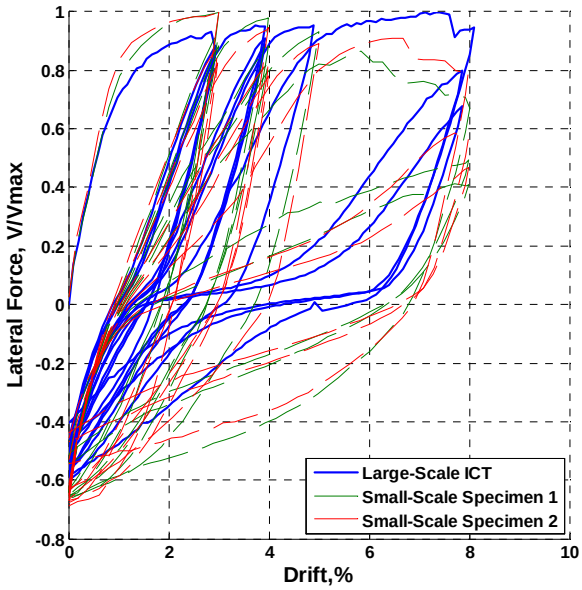

Figure 3.7. Lateral force vs. drift response of large- and small-scale bridge piers tested at the NEES@Illinois facility (Holub, 2009)

The logistical and financial requirements of small-scale testing are much less than those of the large-scale. Small-scale specimens can be quickly constructed and tested at a fraction of the cost of one large-scale specimen. As a comparison, as far as the experimental program presented in this thesis is concerned, the cost associated with the construction and testing of a small-scale specimen is approximately $500 versus $10,000 for a large-scale specimen. Furthermore, the small-scale laboratory at the NEES@Illinois facility is an exact replica of the large-scale counterpart that limits the scaling problems often associated with experimental setups. To conclude, based on the recent experience with small-scale testing at the NEES@Illinois facility, to best utilize the resources and study a large number of test variables, a small-scale experimental program is developed to investigate the seismic behavior of concrete and ECC structures, details of which are given in the subsequent sections.

3.2. MATERIALS USED IN THE CONSTRUCTION OF SPECIMENS

Three different materials are used in the construction of specimens: micro-concrete, ECC and steel. The conventional materials available for full-scale construction could not be used in the small-scale due to unavailability of steel and large aggregates in concrete. ECC mixtures do not comprise large aggregates; therefore, ECC did not require any scaling. The preparation and properties of micro-concrete, ECC and reinforcing steel is described in this section.

3.2.1. Micro-concrete

Preparing a concrete mixture for small-scale testing is a challenging task due to similitude considerations. Most often, this design is required to mimic full-scale material behavior at small-scale which necessitates the scaling of concrete constituents such as the aggregates, which is impractical to achieve most of the time. Thus, researchers have used the concept of micro-concrete with an aggregate gradation scaled to partially fulfill the similitude requirements. In other words, instead of exactly duplicating the prototype material, stress-strain response is imitated. Holub (2005) studied the development of micro-concrete in detail. In Holub (2005), ultimate compressive and tensile strength, strain at ultimate strength, and modulus of elasticity were selected as the parameters to link the two scales. Two main problems were identified in the production of the micro-concrete: (1) due to size effects, micro-concrete of a specified compressive strength exhibited a higher ultimate strain and a lower modulus of elasticity; and (2) due to an increase in the aggregate surface area and bond between the aggregate and cement paste, the tensile strength of micro-concrete tended to be higher when compared to a similar prototype mixture. Furthermore, use of higher aggregate content to increase the modulus of elasticity resulted in unworkable mixtures.

No specific prototype material behavior is considered in the present study. Thus, the behavior of concrete is of little concern as long as the material represents the response of a commonly used prototype concrete. The mixture proposed by Holub (2005) is utilized here. To overcome the above listed difficulties, Holub (2005) developed the detailed guidelines for preparation of mixtures which are also adopted here. To summarize: (1) Type III cement is used to accelerate the construction and testing of small-scale specimens; (2) for aggregate, the material below the #100 sieve [United States (US) size] is removed to limit the amount of fines in the mixture. Thus, the tensile strength was reduced and a more desirable compressive to tensile strength ratio is achieved; (3) to achieve uniformity between mixtures prepared at different times, a large stock of sand is graded into sizes and stored for recombination later. As recommended by Holub (2005), the aggregate gradation provided in Table 3.1 is used here (also shown in Figure 3.8). This selected grading results in a maximum aggregate size of 2 mm, which corresponds to a 16 mm aggregate in the full-scale. The water to cement (W/C) and aggregate to cement (A/C) ratios, based upon weight, are 0.65 and 3.25, respectively. It was observed that the material properties were not strongly dependent on the age of the concrete. Through testing of large- and small-scale specimens, Holub (2009) demonstrated that the materials presented herein were suitable for achieving significantly good correlations between the two scales (see Section 3.1.4 for more details).

Table 3.1. Aggregate gradation for micro-concrete (Holub, 2005)

Sieve Size	Percent Retained	Percent Passing
No. 10 (2.00 mm)	0	100
No. 16 (1.18 mm)	7.87	92.13
No. 30 (0.60 mm)	7.8	84.33
No. 50 (0.36 mm)	65.49	18.84
No. 100 (0.15 mm)	18.84	0

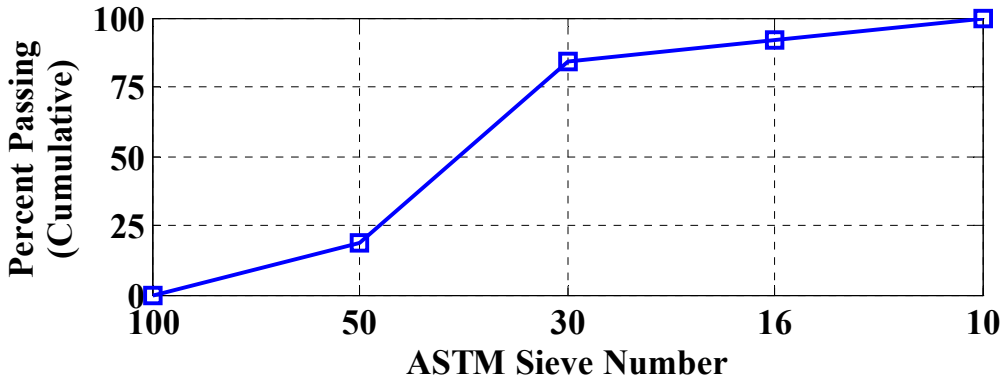

Figure 3.8. Aggregate gradation for micro-concrete (Holub, 2005)

To quantify the characteristics of micro-concrete, 50 x 100 mm (2 x 4 in) cylinders are used as recommended by ACI (1979). The use of 2 x 4 in cylinders also facilitated the testing procedure, since capping equipment and plastic disposable molds with these dimensions are commercially available. Well-controlled compressive and split cylinder tests were conducted to determine the material behavior (see Figure 3.9). The mean compressive and tensile strengths of the micro-concrete are determined as 37.5 MPA and 2.9 MPa with standard deviations of 1.93 MPa and 0.48 MPa, respectively. The typical material response under compression is plotted in Figure 3.10, and the properties of micro-concrete are summarized in Table 3.2 (alongside the properties of ECC mixtures). Note that in Figure 3.10, instead of the initial material stiffness, an effective modulus is shown since it is more relevant to the small-scale testing conducted here. Testing of 76 x 152 mm (3 x 6 in) cylinders is also performed, and their mean compressive and tensile strengths are found to be 28.1 MPa and 1.93 MPa, respectively. It is known that the size of the cylinders has an effect on strength (Burggrabe, 1972). Results from the testing of 50 x 100 mm cylinders are utilized since they are the relevant size for the small-scale experimental program presented here.

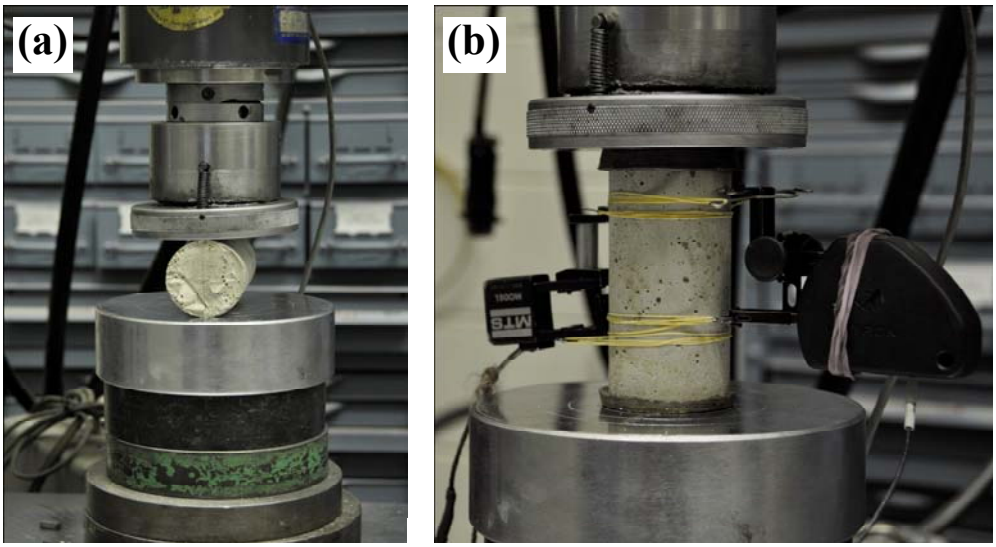

Figure 3.9. (a) Tensile and (b) compressive testing of micro-concrete

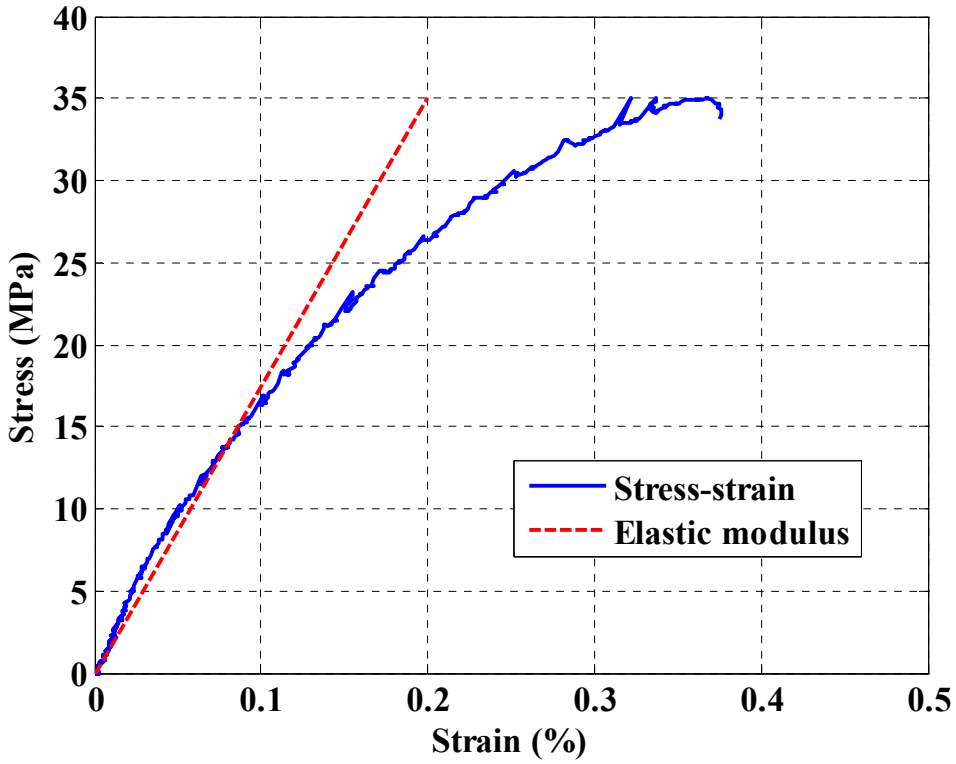

Figure 3.10. A typical stress-strain response and effective elastic modulus for micro-concrete

3.2.2. Engineered Cementitious Composites

The procedures described for developing micro-concrete are also needed for ECC. However, there is no concern of aggregate scaling because the maximum aggregate size for the ECC mixtures considered here is workable in the small-scale. Four different ECC mixtures with different cost and material sustainability indices (MSI) are investigated. As stated earlier, one of the objectives of the experimental program detailed here is to study the performance of different materials at the structural level and derive guidelines for materials selection that favor more sustainable and economical design.

The mixture proportions for the designs are given in Table 3.2. The mixture designated as M45 is the most commonly used ECC design. HFA mixture is considered because it is greener than the other mixtures with its high fly ash content. PPF mixture uses a low cost fiber and it is considerably more economical than others. Finally, SF mixture includes very fine particles only and it is considered as a trial mixture to investigate potential improvements in tensile properties.

To quantify the greenness of ECC mixtures, four MSI are considered: material and energy flow during production process (expressed in terms of primary energy consumption), water usage, the amount of solid waste generation, and the amount of carbon dioxide release. The primary energy consumption is associated with global warming and is considered as an overall indicator of the environmental impact resulting from the production of the material. Freshwater

resources are being depleted at an increasing rate as the total human population increases; hence it has become important to limit water usage during material production processes. Proper treatment of solid waste is costly and requires additional use of resources. Carbon dioxide is a greenhouse gas whose excessive release aggravates global warming.

Cost and MSI for ECC mixtures considered here are given in Table 3.2, and values for a typical concrete mixture are also provided for comparison. MSI are calculated based on the information in Keoleian et al. (2005). The cost of each mixture is estimated based on the unit costs of the constituents (for large purchases) obtained from the main suppliers of the materials in North America. The cost for each ECC mixture is given relative to the cost of concrete. The costs associated with the preparation of the mixtures are not included in the calculations since they might vary depending on the project and other factors such as the cost of electricity. The relative costs of mixtures are intended to be used only in the material selection process.

As seen in Table 3.2, conventional concrete is more environmentally friendly than ECC mixtures when total primary energy, water usage or carbon dioxide release are considered. The amount of solid waste produced by HFA, M45 and PPF mixtures is negative because fly ash and silica fume (silica fume is used only in SF mixture) are considered as waste products, and their usage increases the greenness of the material (Lepech, 2006; Yang et al., 2007). The coal fly ash slurry spill at the TVA Kingston Fossil Plant in 2008 caused debates as to whether fly ash should be classified as a hazardous waste. However, the concerns are related to the storage of the material and not its use in concrete applications. The increased usage of fly ash in concrete production helps reduce the problems related to storage and undesired landfill. Moreover, the greenness of the resulting mixtures is increased by cement replacement. The SF mixture is the least green amongst all due to high use of cement and little cement replacement (with silica fume). As seen in Table 3.2, ECC mixtures can be up to 3.3 times more expensive than conventional concrete. The main contributor to the cost is the existence of fibers. PPF mixture is less costly than the others because it uses PP fibers, which cost approximately half the cost of PVA fibers. In order to justify the use of more expensive and less environmental friendly ECC mixtures, it is necessary to quantify the potential benefits that could be obtained at the structural level. Life-cycle cost (LCC) analysis of RC and ECC structures (subjected earthquake excitation) is investigated in Chapter 5.

The material properties of ECC mixtures are also shown in Table 3.2. Compressive strength is evaluated through testing, while, due to lack of data, the tensile properties are back-calculated from the flexural response of the columns that are tested as a part of the experimental program. The tensile properties provided in Table 3.2 do not directly correlate to the values obtained from direct tensile tests where the fibers are aligned in the direction of loading. In such tests, tensile strength values as high as 5 MPa were obtained for similar mixtures (Wang and Li, 2007; Lepech et al., 2008).

Table 3.2. Mixture constituents, sustainability indices and relative costs, and mechanical properties of considered micro-concrete and ECC mixtures (mixture proportions are in terms of weight and fiber content is two percent by volume for all mixtures, PVA: Polyvinyl alcohol, PP: Polypropylene)

Mix Constituents	Concrete	HFA	M45	PPF	SF
Cement	1.0	1.0	1.0	1.0	1.0
Fly Ash	0	2.0	1.2	2.0	0
Silica Fume	0	0	0	0	0.1
Sand	3.25	0.8	0.8	0.8	0
Water	0.65	0.57	0.55	0.65	0.28
High-range water reducer	0	0.01	0.01	0.013	0.006
Cellulose	0	0.00112	0.00112	0.00112	0.005
Fiber	---	PVA	PVA	PP	PVA
Sustainability Indices and Cost	**Concrete**	**HFA**	**M45**	**PPF**	**SF**
Total Energy (MJ/L)	2.46	5.39	5.96	4.51	10.95
Water Used (L/L)	0.4	0.93	1.0	0.93	1.07
Solid Waste (kg/L)	0.2	-0.76	-0.46	-0.73	0.33
CO2 (g/L)	373.28	532.98	623.5	511.85	1,431.29
Unit Cost (1/L)	1.0	2.53	2.6	1.55	3.29
Mechanical Properties	**Concrete**	**HFA**	**M45**	**PPF**	**SF**
Compressive Strength (MPa)	37.5	58.6	55.2	54.5	56.2
Strain at Compressive Strength (%)	0.3	0.3	0.3	0.3	0.3
Cracking Strength (MPa)	2.9	1.75	1.50	1.00	1.00
Tensile Strength (MPa)	2.9	3.25	2.5	1.75	1.75
Strain at Tensile Strength (%)	0.0091	2	1.75	1.75	1.75
Ultimate Tensile Strain (%)	0.0091	4.50	4.25	4.00	4.00
Young's Modulus (MPa)	17,500	25 000	25 000	25 000	25 000

3.2.3. Steel

3.2.3.a. Longitudinal Reinforcement

The bond between the reinforcing bars and the concrete is a critical feature of the prototype behavior. Therefore, instead of smooth wire, threaded rods are used as longitudinal reinforcement. Improved bond characteristics are achieved due to existence of threads when compared to smooth materials. An 8-32 size threaded rod is selected for this study (see Figure 3.11). The rods have a nominal major diameter and an effective tensile stress area of 4.17 mm and 9.03 square mm, respectively. Based on the AISC specifications (2005), the effective tensile stress area, A_e, is calculated as

$$A_e = 0.7854\left(d_b - 0.9382P\right)^2 \tag{3.1}$$

where d_b is the nominal diameter in mm, and P is mm per threads (0.794 for the rods considered here). For an 8-32 size threaded rod, the effective diameter is calculated from the effective tensile stress area as 3.4 mm. The threaded bars correspond to a metric #25-29 bar in large-scale.

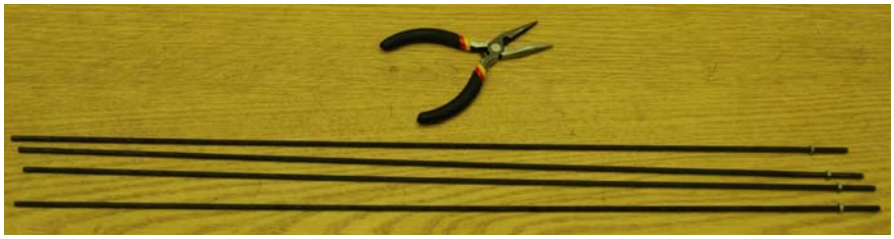

Figure 3.11. 8-32 size threaded rods

The threaded rods are made of general-purpose steel (1018 mild, low-carbon steel), and as obtained from the manufacturer, they have a round stress-strain response as a result of cold processing. In order to achieve a reasonable behavior, normalizing through heat treatment is performed. The stress-strain response of the material after heat treatment is dependent on the diameter of the rods, heat treatment duration and temperature. Here, the variable is chosen as the temperature, and the resulting stress-strain relationships are investigated. During the heat treatment procedure, the rods are raised to specified temperature levels and kept there for one hour, then air cooled (approximately 38 °C per min) to room temperature. Heat treatment is performed using high quality furnaces and methods at a local metal working facility.

To obtain the stress-strain response, the specimens are tested using a 90 kN servo-hydraulic MTS loading frame (see Figure 3.12). An Instron and an MTS extensometer (with ranges of ±10 and ±25 percent strain, respectively) are used to measure the strains. The threaded rods are obtained in lengths of 610 mm (24 inches) from the manufacturer and are cut in half before testing. Displacement control is utilized and the loading rate is adjusted such that the yielding is achieved within approximately one minute. Seven heat treatment temperatures are investigated ranging from 510 °C (950 °F) to 675 °C (1250 °F) with ~28 °C (50 °F) increments. Stress-strain relationships at different temperatures are shown in Figure 3.13(a). The yield and maximum strengths versus the heat treatment temperature are plotted in Figure 3.13(b). The stress-strain relationship obtained from heat treatment at 593 °C (1100 °F) is deemed suitable for the purposes of this study. After the heat treatment temperature is determined, a large batch of threaded rods is purchased and the heat treatment is performed at once in order to ensure uniform material properties of threaded rods in all specimens. The material response after the final heat treatment is plotted in Figure 3.15(a). As seen in Figure 3.15(a), nearly the same stress-strain curves are obtained for specimens of the same batch. After the heat treatment, the material has yield and ultimate strengths of 310 MPa and 362 MPa, respectively. Yielding is observed at a strain level of 0.16 percent from which the Young's modulus is calculated as 189.61 GPa. The properties of heat-treated threaded rods are summarized in Table 3.3 (alongside the properties of the transverse reinforcement described in the next section). The stress-strain response of the selected bar is a reasonable replication of the prototype material behavior, and the properties are similar to a grade 280 bar in ASTM A615 / A615M (2009).

Figure 3.12. Uniaxial testing of threaded rods using servo-hydraulic loading frame

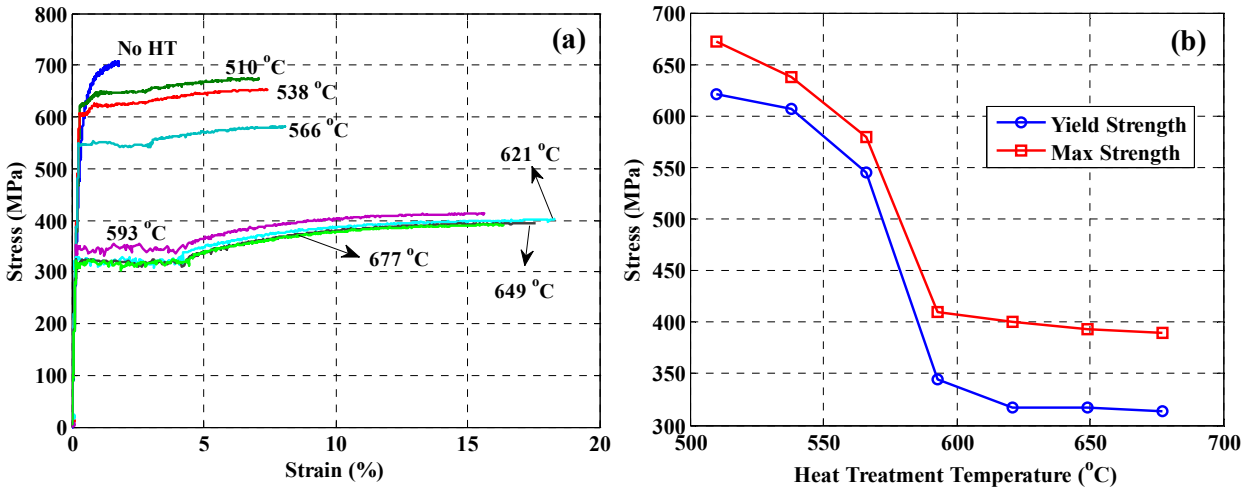

Figure 3.13. (a) Stress-strain curves and (b) yield and maximum strengths for threaded rods at different heat treatment temperatures

3.2.3.b. Transverse Reinforcement

Bond is not a critical feature of the transverse reinforcement used for confinement in small-scale columns. Therefore, a smooth black annealed wire (1008 carbon steel, zinc galvanized) is utilized. The material is commercially available in continuous rolls, and the wire is cut and bent to be used as transverse reinforcement in the small-scale columns as shown in Figure 3.14. The diameter of the smooth bar selected for this study is 1.22 mm with a tensile stress area of 1.16 square mm (corresponds to a metric #10 bar at the full-scale). No heat treatment is applied to the material because it is already annealed and shows a ductile behavior. The stress-strain response

after straightening is shown in Figure 3.15(b). The same equipment used for testing of longitudinal reinforcement (described in Section 3.2.3.a) is used to measure the uniaxial stress-strain response. The yield and the ultimate strengths of the material are obtained as 275 MPa (at 0.2 percent offset) and 448 MPa, respectively. The properties of the smooth black annealed wire used as transverse reinforcement are summarized in Table 3.3.

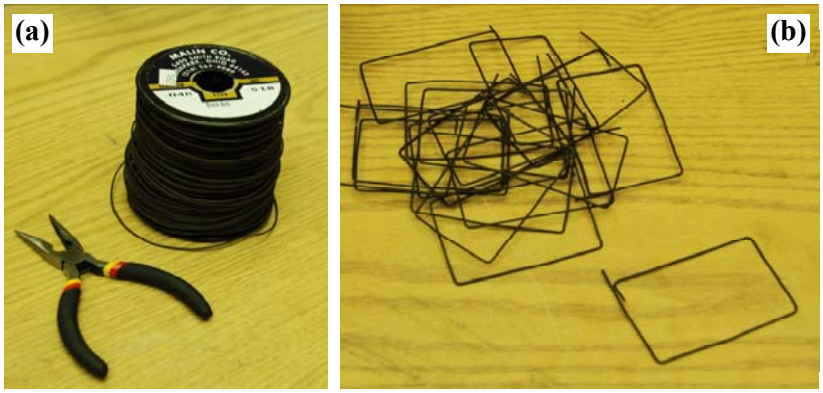

Figure 3.14. (a) Smooth black annealed wire in continuous rolls and (b) rectangular stirrups prepared as transverse reinforcement for small-scale columns

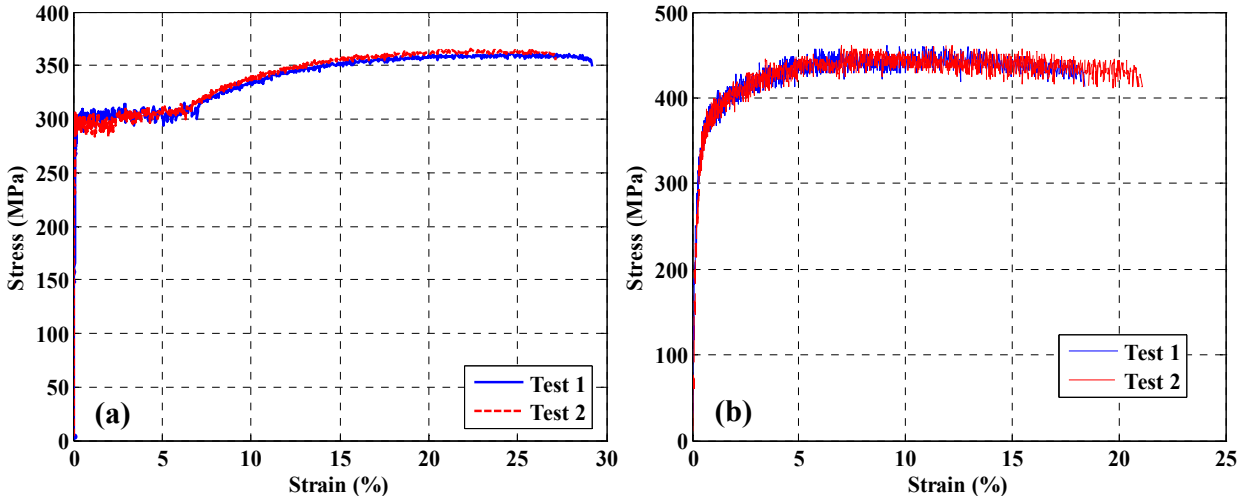

Figure 3.15. Stress-strain response of (a) threaded rods after heat treatment at 593 °C (1100 °F) for one hour and (b) smooth black annealed wire

Table 3.3. Properties of heat treated threaded rods (longitudinal reinforcement) and smooth black annealed wire (transverse reinforcement) used in the construction of small-scale specimens

Property	Long. Reinf.	Trans. Reinf.
Yield Strength (MPa)	310	275
Ultimate Strength (MPa)	362	448
Yield Strain (%)	0.16	0.2
Young's Modulus (GPa)	190	200

3.3. DESIGN OF EXPERIMENTAL COLUMNS AND THE STRUCTURAL FRAME

The two-story two-bay frame shown in Figure 3.17 is selected as the reference structure. The left exterior column of the first story is chosen as the experimental member. First, the design of the experimental member is performed taking into account the limitations imposed by workability at the small-scale and the capacity of the testing equipment. The column height is taken equal to the clear story height, i.e. 381 mm (15 inches) in small-scale (scale factor is 1/8). The ranges for cross-sectional dimensions and the reinforcement ratio are constrained by several factors. These are

- Flexural mode of failure is sought to achieve high energy absorption before failure; thus, the minimum allowed aspect ratio for the columns is taken as four, thus the maximum cross-sectional dimension, h_1 in Figure 3.16(a), is 95.25 mm in small-scale.
- The minimum cross-sectional dimension is determined by workability constraints in small-scale. The minimum cross-sectional dimension, h_2 in Figure 3.16(a), is taken as 50 mm, which is determined based on experience with casting micro-concrete and placement of longitudinal and transverse reinforcement (see Section 3.2 for material properties).
- Sequential yielding occurs if all the reinforcing bars are not located at the same distance from the section edges. Shifting of neutral axis during testing further complicates the behavior. In order to better understand ECC behavior, longitudinal bars are placed only at the extreme tension or compression fiber.
- As described in Section 3.2.3, the reinforcing bars used in the construction of specimens are prepared through involved procedures; hence, only a single diameter bar is used, and the reinforcement ratio is adjusted by changing the number of bars on the cross-section [see Figure 3.16(a)]. However, since all the bars are placed on the same line, the maximum number of bars in the section is limited to prevent congestion during concrete casting and to allow for proper bonding. The minimum clear distance between the bars is selected as two times the maximum aggregate size, which is ~2.5 mm in small-scale.
- The clear cover is taken as approximately 3.2 mm in small-scale.

Based on the requirements listed above, two structural configurations as shown in Figure 3.17 are selected. Finite element modeling of the configuration in the test matrix (see Section 3.7.1 for test matrix), which is expected to show the maximum lateral force resistance (i.e. higher reinforcement ratio, higher axial load and stronger material ECC) is performed using ZEUS NL. The material properties are determined based on the actual material data from Section 3.2. Pushover analysis is conducted with a constant axial load equal to 10 percent of the axial strength of columns, determined based on the gross cross-sectional properties. The pushover curve is shown in Figure 3.16(b). The required axial load and lateral strength of the column (determined from pushover analysis) are compared against the capacity of the testing equipment. Comparing the values in Figure 3.16(b) to those in Table 3.4, it is seen that the testing equipment has the required force and displacement capacities in both axial and lateral directions.

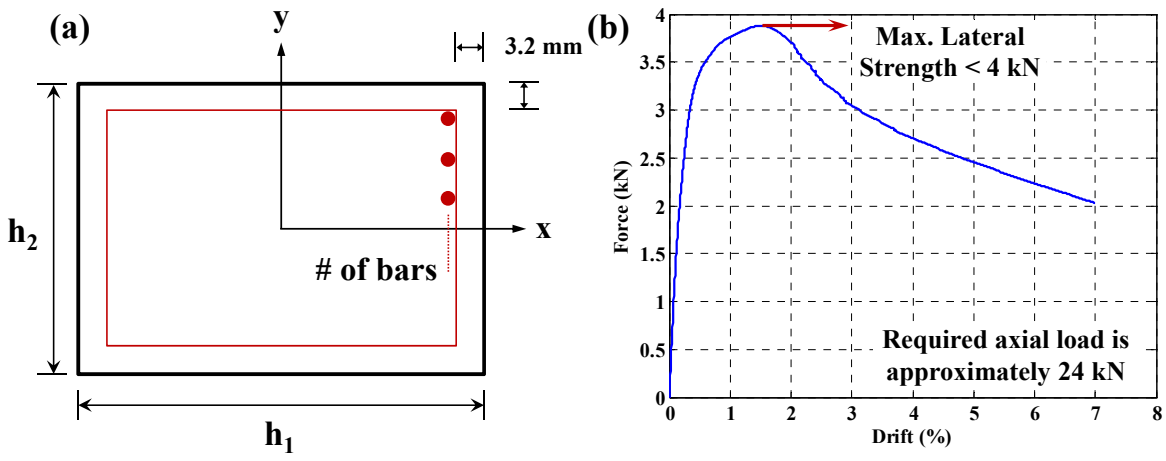

Figure 3.16. (a) Variables considered in design of experimental columns: cross-sectional dimensions and number of reinforcing bars, (b) pushover curve of the strongest configuration obtained from finite element analysis

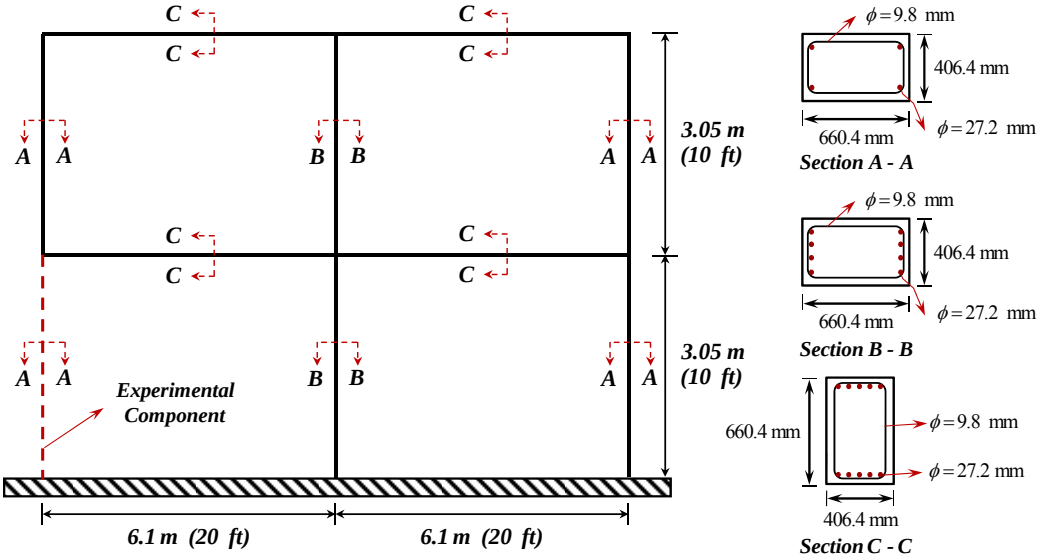

Figure 3.17. Reference structural frame for design of experimental columns

Once the properties of the exterior columns are determined, the interior columns are assumed to have the same cross-sectional dimensions and a higher reinforcement ratio (see Figure 3.17). The rest of the frame is then designed according to the weak column-strong beam (WCSB) principle so that the columns (experimental member) fail before the beams do. The section sizes and rebar dimensions are shown in Figure 3.17. The exterior columns are deliberately designed to have a low reinforcement ratio (two configurations: 0.87 and 1.29 percent) in order to highlight the effect of ECC tensile properties on the response of the structure.

The relatively high aspect ratio (approximately 4.6) of the columns and the adequate shear reinforcement guarantees the flexural mode of failure expected to minimize the size effects. Distributed loads are applied on the beams such that the exterior columns develop axial load

levels equal to 5, 7.5 and 10 percent (three configurations) of the axial strength of an equivalent concrete column in compression. These three levels of gravity loading can be considered to represent three frames with different height to width ratios. A higher level of gravity load corresponds to a more slender structure where the column axial loads are higher due to increased overturning under lateral loading. Design checks are made according to ACI 318-08 (2008) for the extreme loading case. The frame satisfied all design criteria except for the minimum reinforcement ratio requirement of one percent in the columns, which is violated by the configuration that has 0.87 percent longitudinal reinforcement. This criterion is neglected in order to highlight the ECC tensile properties as mentioned above. Section A-A in Figure 3.17 shows (at full-scale) one of the two configurations of columns that are tested. As noted earlier, the other configuration has six longitudinal bars (one additional bar is added on each side) as shown in Figure 3.18. In small-scale, the dimensions of the experimental columns are 82.55 x 50.8 x 381 mm (3.25 x 2 x 15 in), and the materials described in Section 3.2 are used for fabrication. The cross-sectional dimensions and reinforcement detailing of the small-scale columns are shown in Figure 3.18.

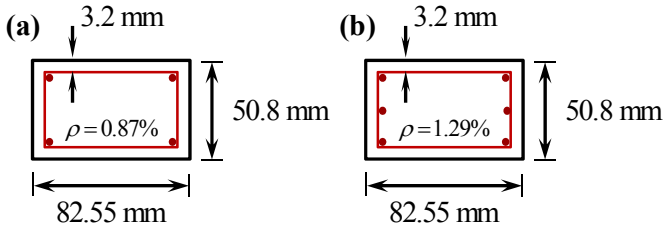

Figure 3.18. Cross-sectional dimensions and reinforcement detailing of small scale columns [with a scale factor of 1/8], (a) configuration 1, (b) configuration 2 (ρ denotes reinforcement ratio)

3.4. FABRICATION OF SPECIMENS

A total of 18 ECC and nine RC specimens are fabricated. In order to achieve consistency between the specimens, rigorous procedures are followed from design of formwork to connection of specimens to testing apparatus. The details are described in the following sections.

3.4.1. Formwork Design

Once the cross-sectional dimensions, the reinforcement topology and the height of specimens are determined, reusable formwork is designed and manufactured from PVC material. PVC material is selected for being inexpensive and having enhanced durability under multiple uses. The forms are designed to allow for easy assembly and disassembly, expediting the fabrication of specimens. Assembly and disassembly of a form could be completed in less than 30 minutes. The formwork design is illustrated in Figure 3.19. Each set is composed of 21 pieces that are connected with standard hex head cap screws. A total of nine sets of forms are manufactured to allow for the simultaneous casting of specimens. The design drawing for each piece in the form is provided in Appendix B.

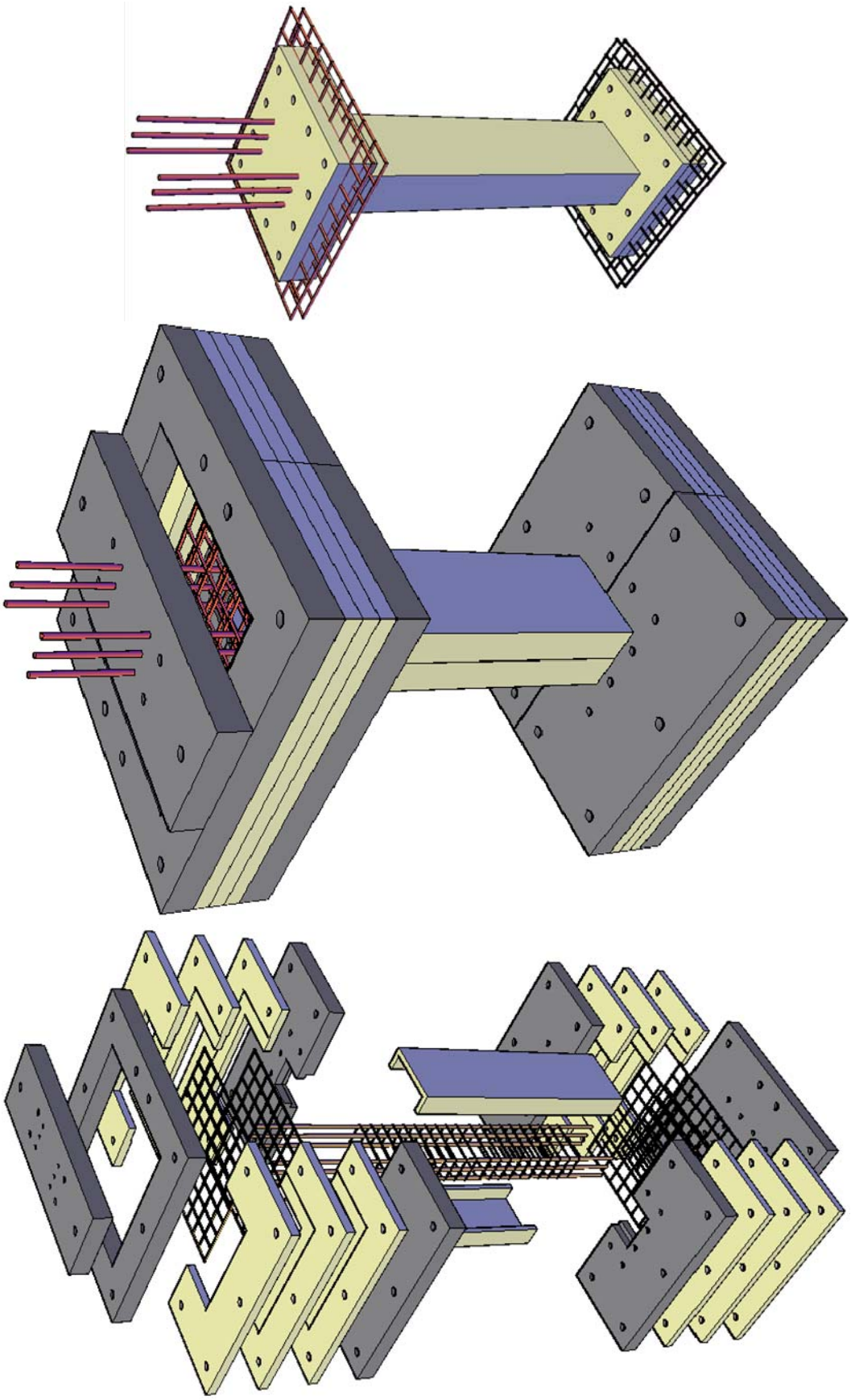

Figure 3.19. Illustration of formwork designs for small-scale specimen fabrication

3.4.2. Preparation of Reinforcement and Formwork

The most laborious part of specimen fabrication is the preparation of the reinforcement. First, the continuous roll of smooth wire used as the transverse reinforcement is cut, straightened and bent into ties (Figure 3.14). The ties are carefully connected to the longitudinal bars and secured into place with wires in order to prevent dislocation during casting (Figure 3.20). Reinforcement detailing guidelines for full-scale RC members are closely followed to ensure similarity between the scales. The end-caps of the specimens used to connect the specimen to the adapter plates (which are in turn connected to the testing apparatus) are also cast from the same material (concrete or ECC) to provide realistic boundary conditions and prevent stress concentrations. Two layers of mesh reinforcement (with 25 x 25 mm spacing) are placed in the end-caps to prevent failures in these regions [Figure 3.21(a)]. The longitudinal and transverse reinforcement are connected to the end-caps as shown in Figure 3.21(b). The rest of the form is assembled and the specimens are prepared as shown in Figure 3.22.

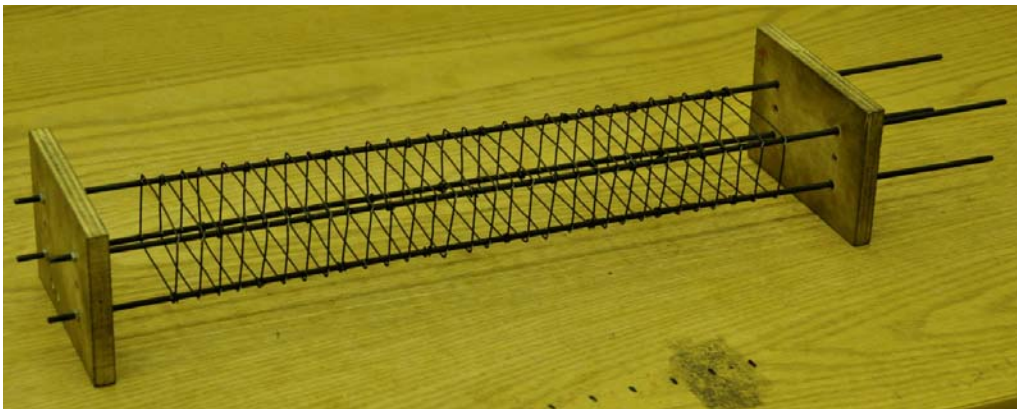

Figure 3.20. Preparation of the reinforcement detailing

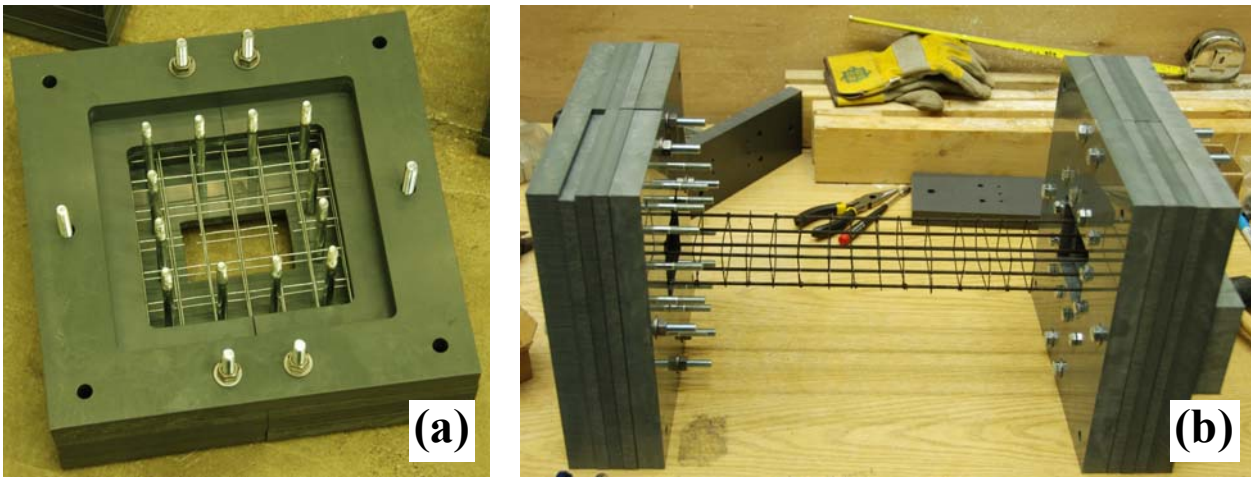

Figure 3.21. (a) Mesh reinforcement inside the end-caps, and (b) connecting the reinforcement to formwork

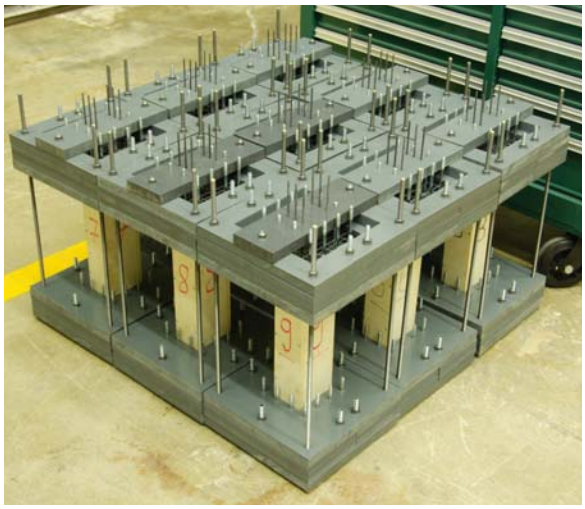

Figure 3.22. Forms at the final stage of preparation

3.4.3. Casting and Curing

Similar procedures are used in preparation of concrete and ECC mixtures. First the dry materials are placed in the mixing bowl and mixed until a homogeneous distribution of different size grains is achieved. This step is followed by the gradual addition of water at 3-4 increments. In the case of ECC mixtures, the fibers are added after the mixture is wetted with some water. The mixing is continued for another 5-10 min until the material becomes homogeneous. Finally, the material is poured into the forms from the openings on top that are visible in Figure 3.22. The preparation of ECC mixture is shown in Figure 3.23(a). The specimens are covered with plastic bags to prevent immediate loss of water from surfaces exposed to air [Figure 3.23(b)].

Figure 3.23. (a) Preparation of ECC mixture, and (b) curing of specimens after casting

3.4.4. Removal of Formwork and Preparation for Testing

The forms are removed from casting after at least 21 days, small dents on the specimens are patched, and the specimens are painted. The top surfaces of the top end-caps are finished with white gypsum cement (also known as hydrocal) to create a level surface. The adapter plates are connected to both ends to finalize the specimen fabrication. Specimen surface preparation and one of the specimens ready for testing are shown in Figure 3.24.

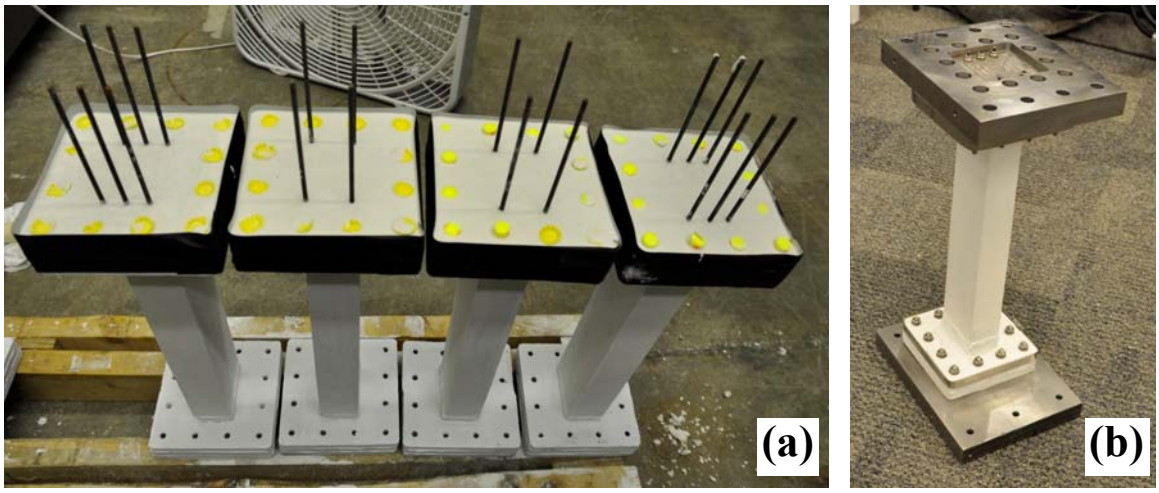

Figure 3.24. (a) Specimen surface preparation, (b) one of the specimens ready for testing

3.5. TESTING AND SIMULATION ENVIRONMENT

Advanced testing equipment and control software are used in order to realize the complex tests conducted here. The capabilities of the testing facility and the software environment are described in the following sections.

3.5.1. NEES@Illinois Facility

The NEES@Illinois facility is one of the fifteen sites in the George E. Brown Jr. Network for Earthquake Engineering Simulation (NEES). It is funded by the National Science Foundation (NSF) and provides distributed experimental-computational simulation capabilities to the earthquake engineering community. The facility is equipped with a large and a 1/5th scale model laboratory, which is equivalently functional as large-scale. The unique feature of the NEES@Illinois facility is the loading capability provided by load and boundary condition boxes (LBCBs). Each LBCB is a self-reacting assembly of actuators and swivel joints, with control software capable of imposing any combination of six actions (forces and moments) and six deformations (displacements and rotations) to test specimens connected to its loading platform. Each actuator is equipped with a servo-valve, a displacement transducer and a load cell for control and measurement. Large- and small-scale LBCBs are shown in Figure 3.25. The capabilities of LBCBs enable complex testing configurations using substructure schemes or multiple loading points on test specimens. The large- and small-scale LBCBs are identical except for their force and displacement limits. Moreover, the same control software is utilized at both scales. Thus, very good correlations are obtained between laboratories and scales. LBCBs are mounted on L-shaped reaction walls at different locations and orientations based on the testing configuration. The large- and small-scale reaction walls are shown in Figure 3.25.

Additionally, a portable and self-reacting LBCB (pLBCB) is available at the small-scale facility. This pLBCB is used for the tests described here due to its higher force capacity. The force and displacement capacities of the pLBCB are given in Table 3.4.

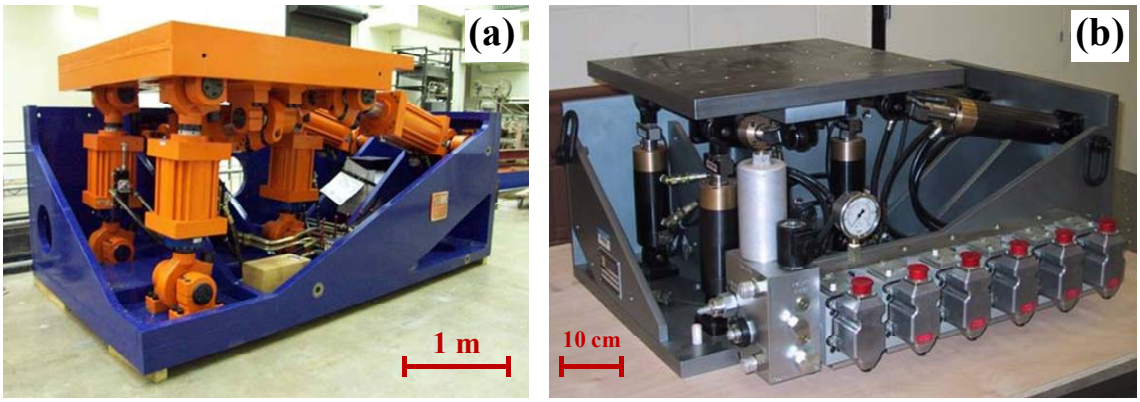

Figure 3.25. (a) Large- and (b) small-scale LBCBs

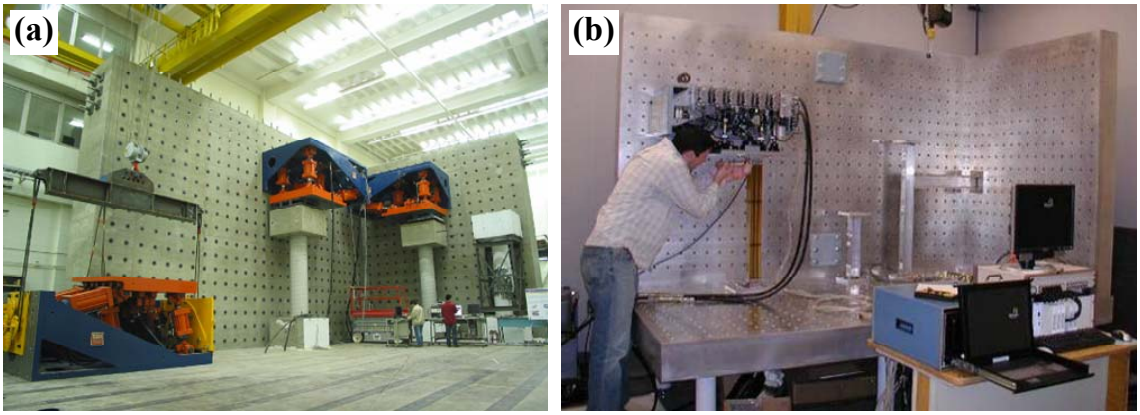

Figure 3.26. (a) Large- and (b) small-scale reaction walls

Table 3.4. Force and displacement capacities of the pLBCB (note that the values provided here do not reflect the interaction between different degrees-of-freedom of the loading platform)

Type	Axis	Capacity	Type	Axis	Capacity
Displacement (mm)	X	± 50.8	**Rotation (degree)**	X	± 11.7
	Y	± 25.4		Y	± 9.7
	Z	± 25.4		Z	± 22.6
Force (kN)	X	± 26.7	**Moment (kN-mm)**	X	± 3 265
	Y	± 13.3		Y	± 6 643
	Z	± 40		Z	± 3 265

3.5.2. Experimental Setup, Testing Configuration, Instrumentation, Control Considerations, and Data Acquisition

The overall experimental setup is shown in Figure 3.27(a). As shown in the same figure, the LBCB platen is attached to the base of the column, and the top is attached to the surrounding steel reaction frame. Since the platen is at the bottom, the specimen is in an upside-down position during testing.

From the LBCB, six actuator displacements, six actuator forces, six Cartesian displacements, and six Cartesian forces are recorded. The displacements of interest for the test are those that occur between the end caps of the specimen. Therefore, six additional external transducers, as shown in Figure 3.27(b), are installed, and feedback displacements are collected. A nonlinear Jacobian based algorithm is used to transform the six individual transducer measurements into Cartesian displacements with geometric nonlinearities handled in the transformation. The feedback Cartesian coordinate displacements are then compared against the target commands. For the tests conducted here, the difference between the target and the measured displacements is found to be negligible. Had the stiffness of the reaction frame (or the platen) been close to that of the specimen, additional correction steps would have been executed to account for the elastic deformations of the external components. High-resolution photos of the specimens are automatically taken from three different angles at each load step, and a walk-around hand camera is used to take detailed photos when needed. The data are collected through a custom LabVIEW program in both continuous and stepwise (numerical integration step) manner. Still photos are also automatically collected and stored using camera plugin software developed at the NEES@Illinois site.

Due to the large number of specimens and the reduced scale, no additional measurements, such as rebar strain, are collected. This decision was made because the small-scale tests are not intended to provide detailed behavioral information but rather to obtain global member or system response. Thus, the detailed local instrumentation is not warranted.

At the bottom connection point, designated as the control point in Figure 3.27(b), lateral displacement (Δ_x) and rotation (θ_y) are varied depending on the testing protocol. The axial degree-of freedom (DOF) is controlled in displacement (Δ_z) for the hybrid simulation tests and in force (F_z) for monotonic, cyclic and static time history tests (STH) [see Section 3.6 for different types of tests]. The remaining DOFs are constrained to zero for the planar problem studied here.

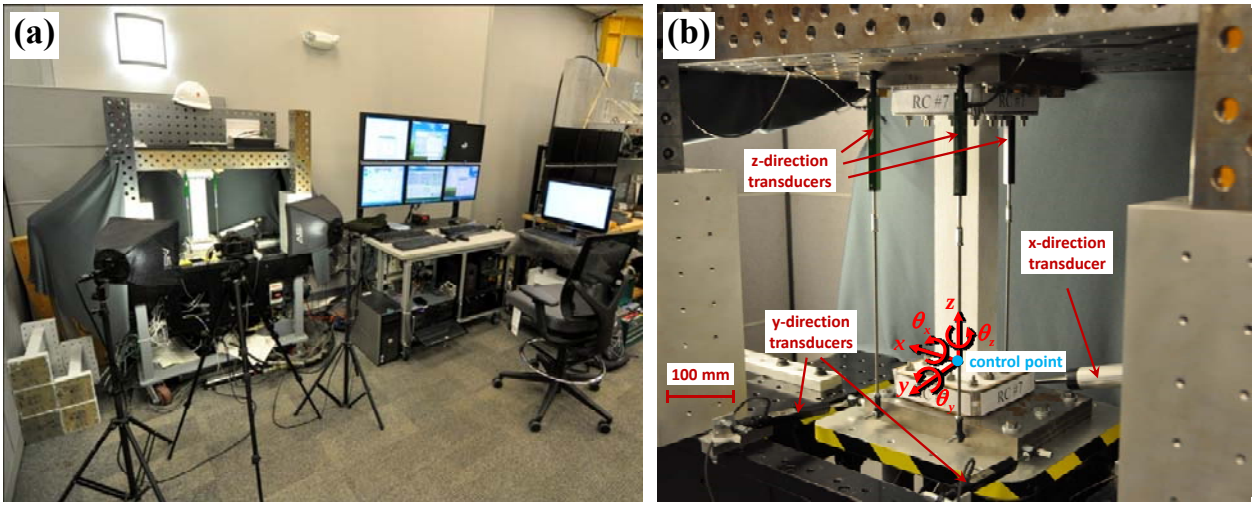

Figure 3.27. (a) Overall view of the experimental setup, and (b) testing configuration and instrumentation

3.5.3. Software Environment

The sub-structured pseudo-dynamic (hybrid simulation) tests have several advantages over conventional pseudo-dynamic tests. Most importantly, it is not necessary that the entire structure be constructed; the well-behaved regions are identified and analyzed computationally, while components of particular interest or high complexity are tested in the lab. Hybrid simulation requires the combined use of several software programs for controlling the testing equipment, receiving and storing data from data acquisition devices, and running the analysis for computational parts of the structure. The schematic representation of the hybrid testing framework at the NEES@Illinois facility is illustrated in Figure 3.28, and the key software in conducting the tests is described below.

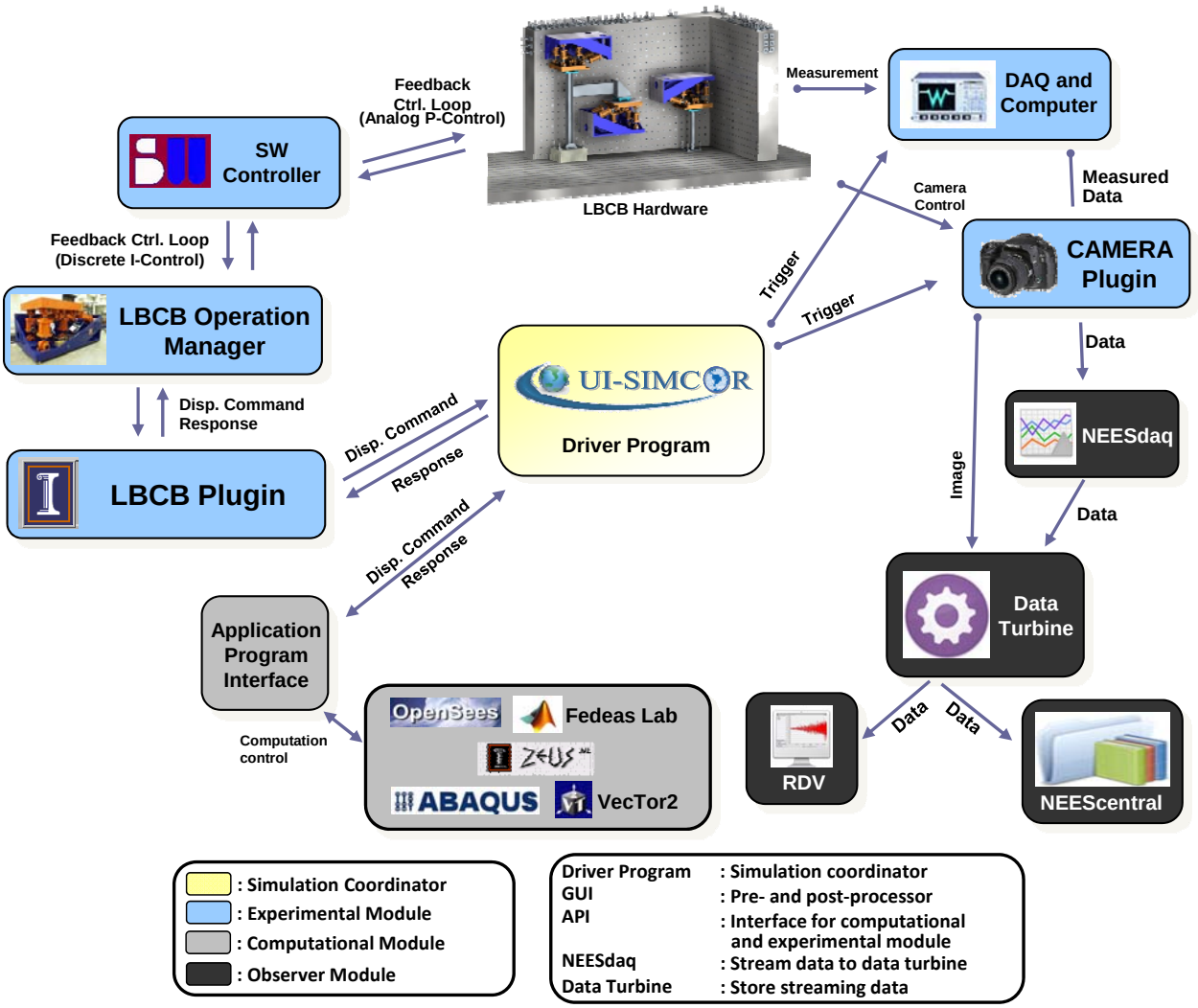

Figure 3.28. Schematic representation of hardware and software environment for hybrid testing at the NEES@Illinois facility (courtesy of Dr. Oh-Sung Kwon)

3.5.3.a. UI-SIMCOR

UI-SIMCOR is the master control program developed at the University of Illinois for hybrid testing (Kwon et al., 2005). It is responsible for communication between the experimental and analytical modules of the simulation. The software is also capable of controlling and synchronizing data collected from the data acquisition program and the camera plugin software that automatically takes and stores still pictures at every time step. UI-SIMCOR handles both the static and dynamic loading of all sub-structured components. The alpha-Operator Splitting (α-OS) method is used as the time integration scheme for dynamic analysis (Combescure and Pegon, 1997). α-OS is a non-iterative, linearly implicit and non-linearly explicit method that only requires measurements from the current time step, and it is preferred for its feature of numerically damping out spurious oscillations. The α-OS method requires determination of the initial stiffness of the structure for the controlled DOFs prior to conducting the simulation. For the experimental module, the initial stiffness is determined by sequentially imposing a small-amplitude cyclic loading to each of the DOFs of interest while keeping the others fixed. The slope of the line obtained through linear regression analysis of the measured forces gives the experimental stiffness. The stiffness of the analytical module is assembled by UI-SIMCOR by sending predefined displacement values to the control DOFs in the analytical module and receiving the restoring forces.

3.5.3.b. LBCB-Plugin

The LBCB Plugin serves as intermediate software between UI-SIMCOR and the LBCB Operations Manager (LBCB OM) described below. It is used as the master program for tests other than hybrid. As a result, it has the capability of triggering auxiliary hardware such as the data acquisition and cameras (through the camera plugin). The coordinate transformation of the displacement command is performed in the LBCB Plugin before it is sent to the LBCB OM. The coordinate transformation for the external feedback control (mentioned in Section 3.5.2) is also done in the LBCB Plugin. It is possible to do limit checks on force, displacement and increments through the LBCB Plugin to prevent execution of an unexpected command. Monotonic, cyclic and STH tests are conducted by importing displacement histories from text files and using the LBCB Plugin as the master software.

3.5.3.c. LBCB Operations Manager

The LBCB OM serves as the main controlling software for the LBCBs at the NEES@Illinois facility. It can be operated in displacement, force or mixed mode control in either Cartesian or actuator space. It incorporates various control loops including auto-balance feedback, digital integrator technique, and mixed load and displacement feedbacks. The program launches with an auto-balance process to determine the position of the LBCB platen and to prevent damage to a possibly connected specimen. It has several additional control capabilities such as function generator and step-wise ramp generator. Although a single LBCB is used for the tests conducted here, it is capable of synchronously controlling two LBCBs.

3.5.3.d. Shore Western Controller

The Shore Western control software receives the signal in digital form from the LBCB OM, converts it to an analog signal, applies gain, and sends it to the actuators. This software was developed by the manufacturer.

3.5.3.e. ZEUS NL

UI-SIMCOR is capable of communicating with a number of finite element analysis software programs and can be used to model the analytical components. For the hybrid tests conducted here (see Section 3.6.3 for more details), the analytical part of the frame described in Section 3.3 is modeled using ZEUS NL (Elnashai et al., 2010). ZEUS NL is a fiber-based finite element analysis package specifically developed for earthquake engineering applications (more information is available in Section 2.4). Fiber-based finite element modeling is chosen here for being computationally efficient, robust and accurate in capturing the global response of complete structures. The masses are lumped at the beam-column connections, and the gravity loads are applied through UI-SIMCOR before starting the dynamic load steps.

3.6. INPUT MOTIONS

The specimens are tested under four different loading conditions, namely, monotonic, cyclic, STH loading, and sub-structured pseudo dynamic loading (hybrid simulation). The testing and simulation environment used here is capable of applying desired loading and boundary conditions in mixed mode as described in Section 3.5.1. The developed input motions are described in the following sections.

3.6.1. Monotonic Loading

The monotonic tests are carried out under a fixed-pinned boundary condition as shown in Figure 3.29(a).

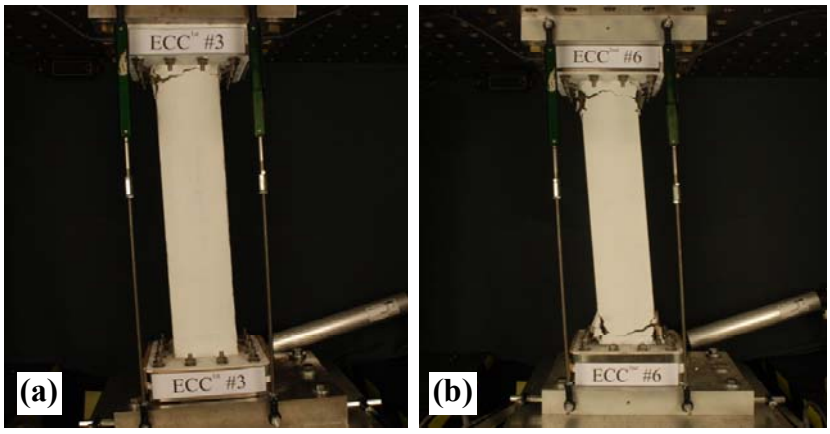

Figure 3.29. (a) Fixed-pinned, and (b) fixed-fixed boundary conditions (note the rotation at the bottom of the specimen on the left)

Displacements are increasingly applied at a rate of 0.01 percent drift per step. Ramp (step execution) and hold (stabilization) times are selected high enough not to introduce any dynamic effects (quasi-static test). A constant axial compressive load equal to 7.5 percent of the axial capacity of the columns is applied in all monotonic tests. Tests are stopped when a complete loss of load resistance is observed.

3.6.2. Cyclic Loading

The cyclic tests are carried under two different boundary conditions: fixed-pinned and fixed-fixed as shown in Figure 3.29. The loading history is shown in Figure 3.30. Two cycles are applied at drift levels of 0.15, 0.25, 0.5, 0.75, 1, 1.5, 2, and up to 10 percent, with one percent increments, or until complete loss of load resistance. The selected loading history is in accordance with the recommendations in FEMA 461 (2007). Similar to monotonic tests, a constant axial compressive load equal to 7.5 percent of the gross capacity of the column is applied in cyclic tests. In both monotonic and cyclic tests a loading rate of approximately 1 mm/min is used to ensure quasi-static testing.

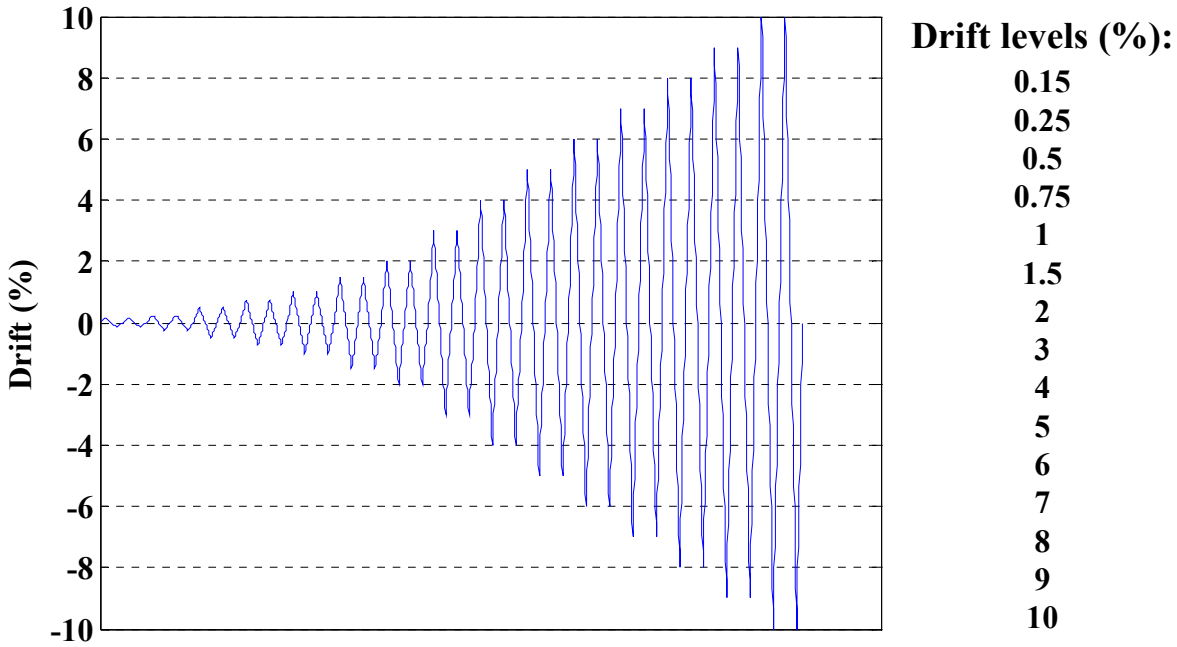

Figure 3.30. Loading history for cyclic tests (x-axis label is not shown because time is not a relevant parameter of static tests)

3.6.3. Static Time History Loading and Hybrid Simulation

In order to better represent the loading and boundary conditions that a member would be subjected to under earthquake excitation, two additional types of tests are conducted: STH and hybrid simulation. In STH tests, the displacements (translations and rotations) at the control point (top of the columns) are determined from inelastic dynamic analysis. The structural frames described in Section 3.3 are modeled using ZEUS NL and subjected to earthquake excitation.

The displacements at the top of the column chosen to be the experimental module are extracted, scaled and applied to the specimens using the testing equipment. In hybrid simulation, the frame is subjected to the same earthquake excitation; however, the experimental module (left-exterior first story column) is tested in the lab, and the rest of the frame is simulated numerically in ZEUS NL. Details regarding the testing and simulation framework are given in Section 3.5. A spectrum-compatible earthquake ground motion developed to represent an event with 2475 years return period (YRP) at a selected site is used for STH tests and hybrid simulation as shown in Figure 3.31. Detailed derivation of the ground motions used in this study is provided in Section 5.2.

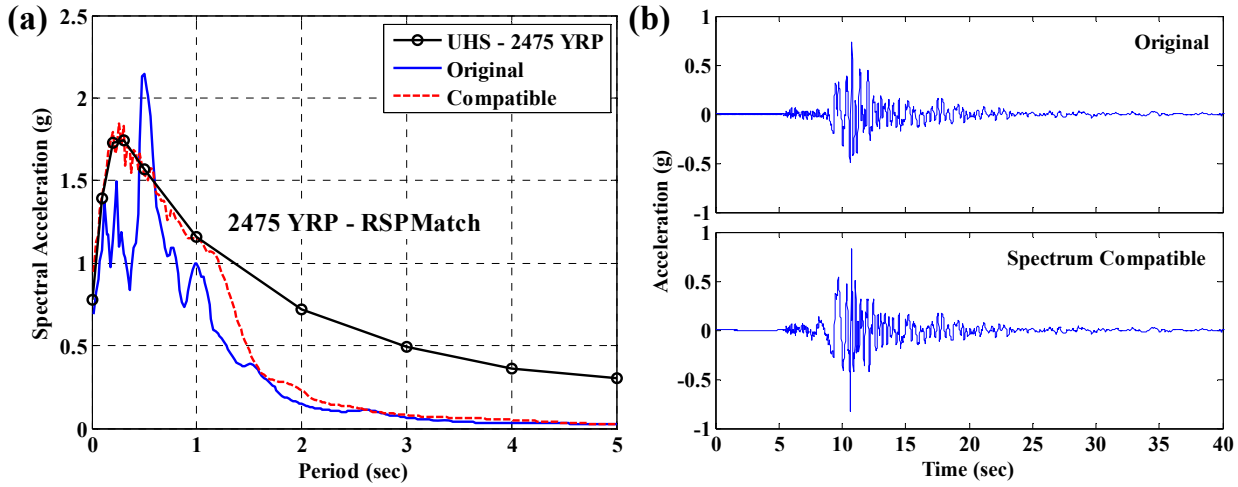

Figure 3.31. (a) Response spectrum and (b) acceleration time history of the ground motion before and after spectrum matching

3.7. ATTRIBUTES OF TESTS

3.7.1. Test Matrix

The test matrix is provided in Table 3.5. Four different variables are considered: longitudinal and transverse reinforcement ratios, mixture design and level of axial load. Two longitudinal reinforcement ratios are considered: 0.87 and 1.29 percent (as shown in Figure 3.18). The transverse reinforcement ratio is varied from 0.36 percent to 0 percent (no stirrups). Four ECC mixtures and a concrete mixture are considered as previously described in Section 3.2. Four different tests are conducted: monotonic, cyclic (with two different boundary conditions: fixed-pinned and fixed-fixed), STH, and hybrid simulation. The axial load is kept constant at 7.5 percent of the column axial strength for monotonic and cyclic tests, and three different axial load levels are considered for the STH and hybrid tests (5, 7.5 and 10 percent). More than one test is conducted in some cases to check the repeatability of the tests. As mentioned in Section 3.4, a total of 27 specimens are fabricated. 26 tests are conducted as indicated in Table 3.5; one specimen is used to validate the control algorithm.

Table 3.5. Test matrix (axial load is in percentage of the axial strength of columns; for the transverse reinforcement ratio, N/A indicates that the stirrup spacing is not a relevant parameter for the conducted test)

Long. Reinf. Ratio (%)	Trans. Reinf. Ratio (%)	Mix Design	Type of Test	Axial Load (%)	Number of Specimens
0.87	0.36	Concrete	Monotonic	7.5	1
1.29	0.36	Concrete	Monotonic	7.5	2
0.87	0.12	ECC-HFA	Monotonic	7.5	1
1.29	0	ECC-HFA	Monotonic	7.5	1
0.87	0.36	Concrete	Cyclic	7.5	1
1.29	0.36	Concrete	Cyclic	7.5	3
0.87	0.12	ECC-HFA	Cyclic	7.5	1
1.29	0	ECC-HFA	Cyclic	7.5	1
1.29	0.12	ECC-HFA	Cyclic	7.5	1
1.29	0.18	ECC-HFA	Cyclic	7.5	1
1.29	0.12	ECC-M45	Cyclic	7.5	1
1.29	0.12	ECC-PPF	Cyclic	7.5	1
1.29	0.12	ECC-SF	Cyclic	7.5	1
1.29	0.12	ECC-HFA	Cyclic-Fixed	7.5	1
1.29	0.12	ECC-M45	Cyclic-Fixed	7.5	1
1.29	0.12	ECC-PPF	Cyclic-Fixed	7.5	1
1.29	0.12	ECC-SF	Cyclic-Fixed	7.5	1
1.29	N/A	ECC-HFA	STH	5	1
1.29	N/A	ECC-HFA	STH	10	1
0.87	0.36	Concrete	Hybrid	7.5	1
0.87	0.12	ECC-HFA	Hybrid	7.5	1
1.29	N/A	ECC-HFA	Hybrid	5	1
1.29	N/A	ECC-HFA	Hybrid	10	1

3.7.2. Validation of Applied Loading

In order to validate the accuracy of applied displacements, external measurement devices, i.e. linear variable differential transformers (LVDTs), are mounted on the specimens as shown in Figure 3.27(b). The main objectives in taking the external measurements are first to check whether there is any significant difference between the imposed (command) and measured displacements due to elastic deformations of external components or any other source, and second, to prevent out-of-plane motion (if any) for the planar tests.

The applied and measured actions on a specimen during a STH test where the lateral displacement, rotation and axial force are obtained from finite element simulation (as described in Section 3.6.3) are compared in Figure 3.32 and Figure 3.33. It is observed that the error between applied and measured lateral drift, rotation and axial force is negligible for any practical purpose. The out-of-plane motion of the loading platform results from cross-talk between different DOF. It is seen that the out-of-plane drift is too small (less than 0.1 percent) to have any significant effect on the results [see Figure 3.32(b)]. A STH test is intentionally selected for the validation of loading because the loading and boundary conditions are harder to achieve compared to a monotonic or cyclic test.

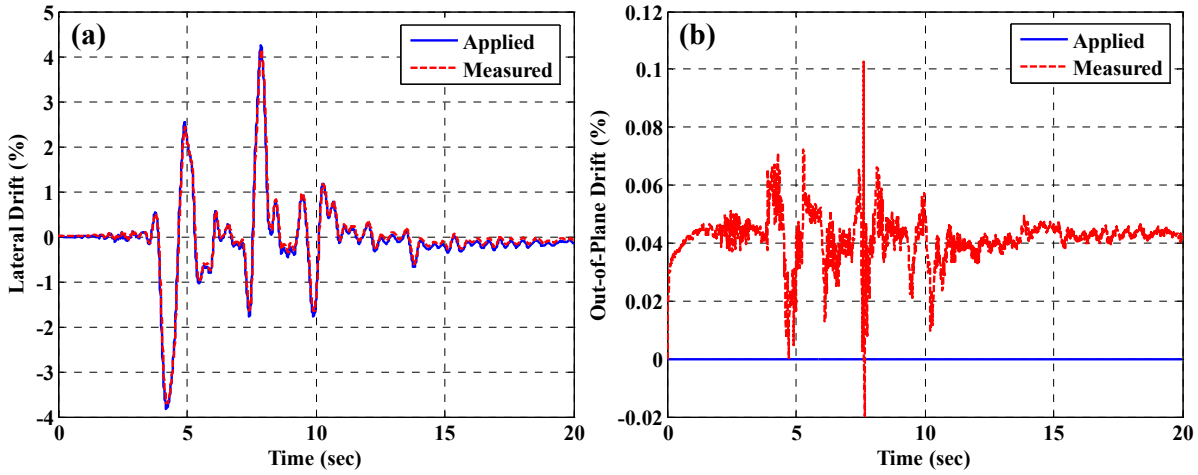

Figure 3.32. Comparison of applied and measured (a) lateral drift (b) out-of-plane drift

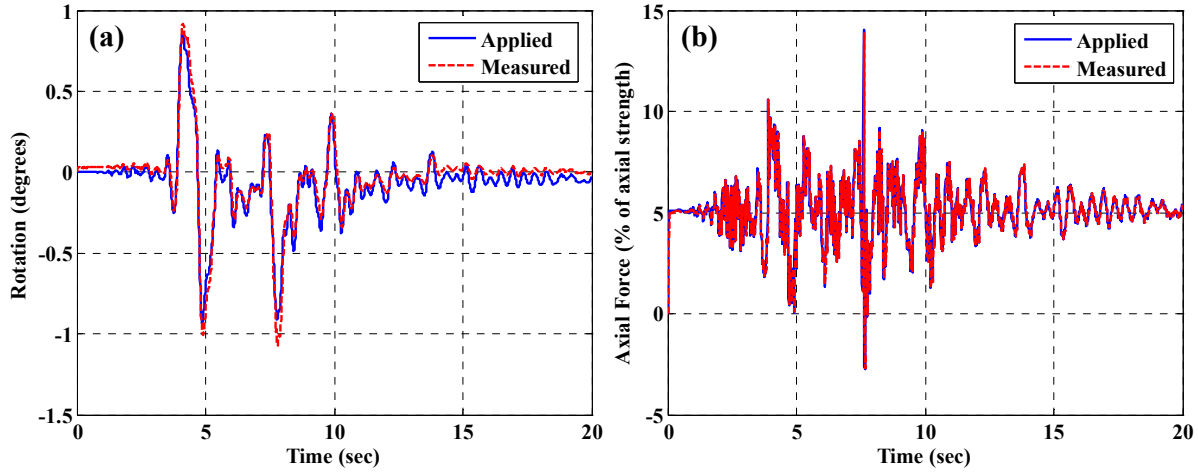

Figure 3.33. Comparison of applied and measured (a) rotation (b) axial force

3.8. ANALYSIS AND INTERPRETATION OF RESULTS

Section 3.8 presents the results from the experimental program. First, the reproducibility of the tests is illustrated. The tests are then divided into two categories: monotonic and cyclic tests, and STH tests and hybrid simulation and the results are analyzed in terms of structural level response metrics: stiffness, strength, ductility and energy absorption capacity, the most commonly used parameters in seismic design of buildings.

3.8.1. Reproducibility of Tests

Reproducibility of tests has been a major concern in small-scale testing due to inconsistency across specimens and inaccuracy in applying displacements and forces on the test specimens through the testing equipment. As described in Sections 3.4 and 3.5, rigorous procedures are followed in the fabrication of specimens, and the testing equipment used here is capable of imposing displacements and forces with high precision (see comparisons in Section 3.7.2).

Figure 3.34(a) compares the responses of two identical RC specimens with 1.29 percent longitudinal reinforcement under cyclic loading with fixed-pinned boundary conditions. It is observed that the force-displacement relationships match very well. Another comparison is made in Figure 3.34(b) between the monotonic and cyclic tests of ECC specimens with 0.87 percent longitudinal reinforcement. It is seen that the monotonic curve envelopes the cyclic response. Due to reversed loading, higher strength and stiffness degradation is observed in cyclic tests at high drift levels. These results confirm the reproducibility of the tests conducted here.

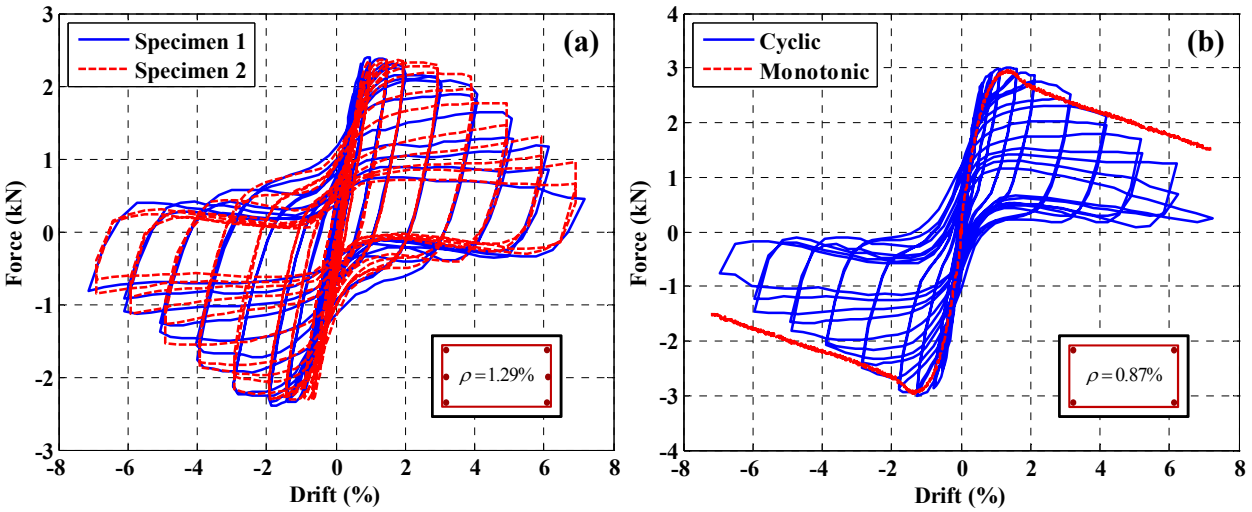

Figure 3.34. Repeatability of tests: (a) RC specimens with 1.29 percent longitudinal reinforcement, comparison of cyclic tests, (b) ECC specimens with 0.87 percent longitudinal reinforcement, comparison of cyclic and monotonic tests

3.8.2. Monotonic and Cyclic Tests

Table 3.6 summarizes the results for the cyclic tests. All parameters in Table 3.6 (except for those related to energy) are calculated on the mean envelope curves obtained by averaging the envelope curves for the positive and negative drift regions. An example cyclic test result alongside the evaluated envelope curves is shown in Figure 3.35(a). The calculation of the yield, maximum and ultimate (corresponding to 10 percent reduction in load carrying capacity) points according to Park (1988), as well as the definition of ductility μ_m and μ_u are illustrated in Figure 3.35(b). These points are associated with the three socio-economic limit states for structures under seismic events: immediate occupancy (IO), life safety (LS), and collapse prevention (CP), respectively. The initial stiffness of the specimens is defined as the ratio of the force corresponding to 20 percent of the peak lateral force resistance to the drift at this point. The peak lateral force resistance is defined as the lateral strength of the specimen. The energy absorption capacities up to peak and failure are defined as the sum of areas within complete cycles up to the attainment of the peak and ultimate drifts, respectively. In Table 3.7 for each of the groups (i.e. cyclic six bars, cyclic four bars, and cyclic-fixed six bars) the differences with respect to a baseline case are provided in percentages. The groups named with the number of bars refer to the specimens with reinforcement designs shown in Figure 3.18. Each of the structural level

response parameters evaluated from the experimental data is discussed in detail in the following sections. The results here are compared in terms of structural performance; the material sustainability and cost for different ECC mixtures are compared in Section 3.2.

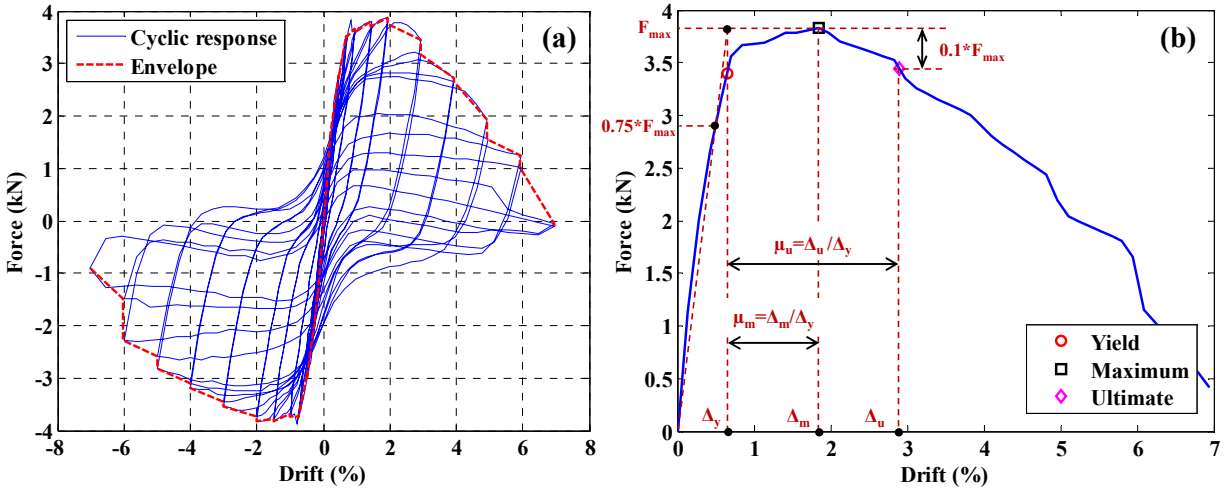

Figure 3.35. (a) An example cyclic response and the envelope curve, (b) definitions of yield, maximum and ultimate points, and the ductility on a typical envelope curve

3.8.2.a. Initial Stiffness and Stiffness Degradation

The initial (elastic) stiffness of the specimens is defined as the ratio of the force corresponding to 20 percent of the peak lateral force resistance to the drift at this point. The elastic stiffness depends on several other factors such as the member dimensions, reinforcement ratio and the boundary conditions; however, it is still possible to compare the stiffness of RC specimens with that of different ECC specimens. It is observed that (for fixed-pinned boundary conditions) the initial stiffness of ECC specimens is significantly higher than that of concrete specimens ranging from 20 to 120 percent depending on the mixture design (see Table 3.7 and Figure 3.36). The higher strength might be expected since the compressive strength of ECC mixtures is significantly higher than that of concrete. However, the higher compressive strength of ECC is not the only source since the variation in the compressive strengths of ECC mixtures is significantly less. The HFA mixture exhibited the highest initial stiffness. The stiffness increase achieved with ECC for the configuration with 0.87 percent longitudinal reinforcement is significantly less when compared to the case with 1.29 percent reinforcement. It is also seen that the fixed-fixed boundary condition during the test increases the stiffness of specimens twice when compared to the fixed-pinned boundary condition (see Table 3.7 and Figure 3.37, the asymmetry in envelope curves for fixed-fixed condition is explained in Appendix A); theoretically the stiffness increase should be four times. This theoretical result is based on perfect fixity; however, the end caps do not restrain the columns to achieve this condition, which is similar to actual conditions at structural assemblages such as beam-column connections.

The secant stiffness of the specimens is calculated as a function of drift level, and the stiffness degradation curves for concrete and different ECC mixtures are shown in Figure 3.38.

The highest degradation is observed in HFA and M45 mixture designs while the SF and PPF mixture designs and RC showed a lower degradation. The stiffness degradation observed in cyclic and monotonic tests is compared in Figure 3.39. Significantly lower stiffness degradation is observed in the monotonic tests. For instance, at a drift level of one percent the stiffness reduces to 46 percent of the initial stiffness during the cyclic test while the stiffness is equal to 61 percent of initial stiffness at the same drift level during the monotonic test (for reinforcement ratio equal to 1.29 percent). Another parameter that is investigated in the experimental program is the effect of the transverse reinforcement ratio in ECC specimens. It is seen that the transverse reinforcement ratio has no significant effect on the initial stiffness or the stiffness degradation of ECC specimens which is attributed to internal confinement provided by the ECC as discussed further in the next section on strength and strength degradation.

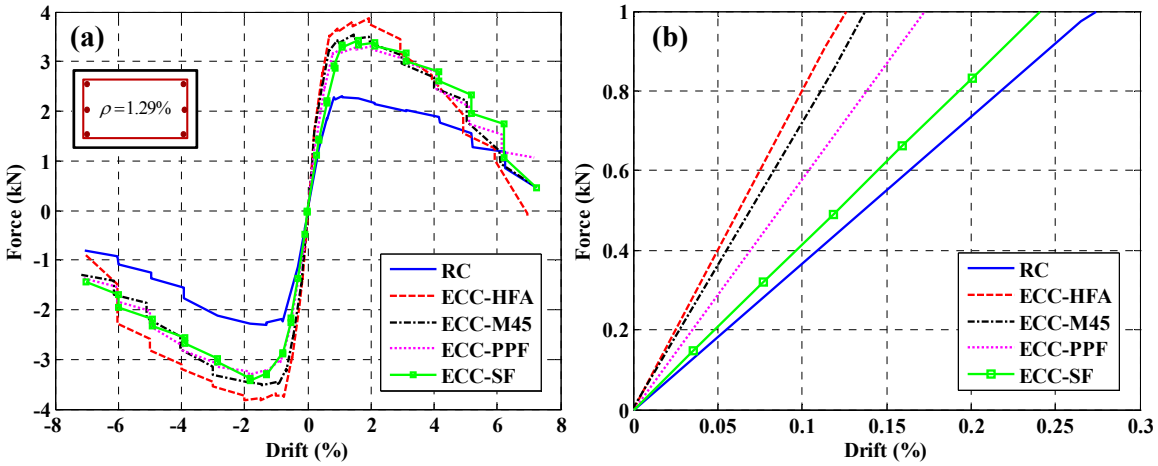

Figure 3.36. (a) Envelope curves from testing of RC and ECC specimens with a reinforcement ratio of 1.29 percent and fixed-pinned boundary condition, (b) initial stiffness obtained from envelope curves

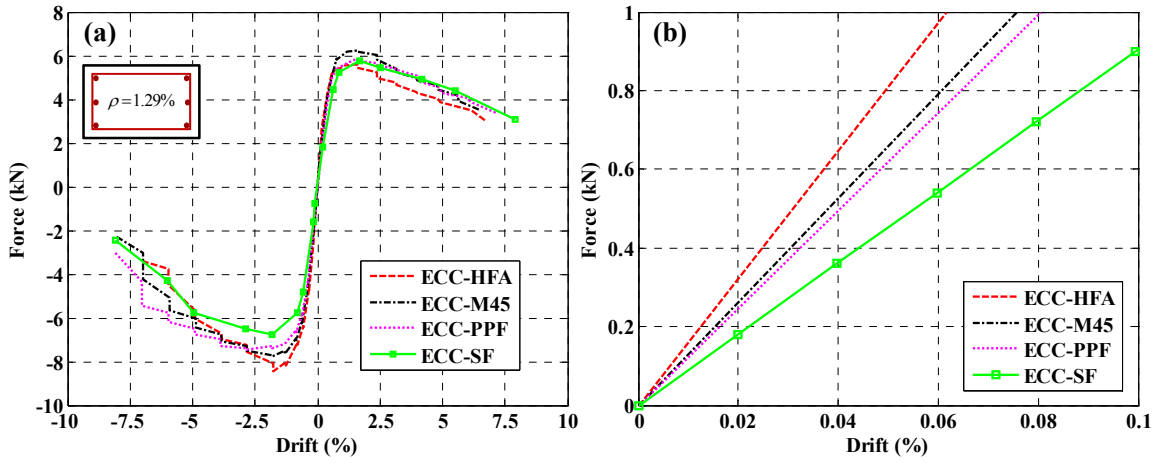

Figure 3.37. (a) Envelope curves from testing of RC and ECC specimens with a reinforcement ratio of 1.29 percent and fixed-fixed boundary condition, (b) initial stiffness obtained from envelope curves

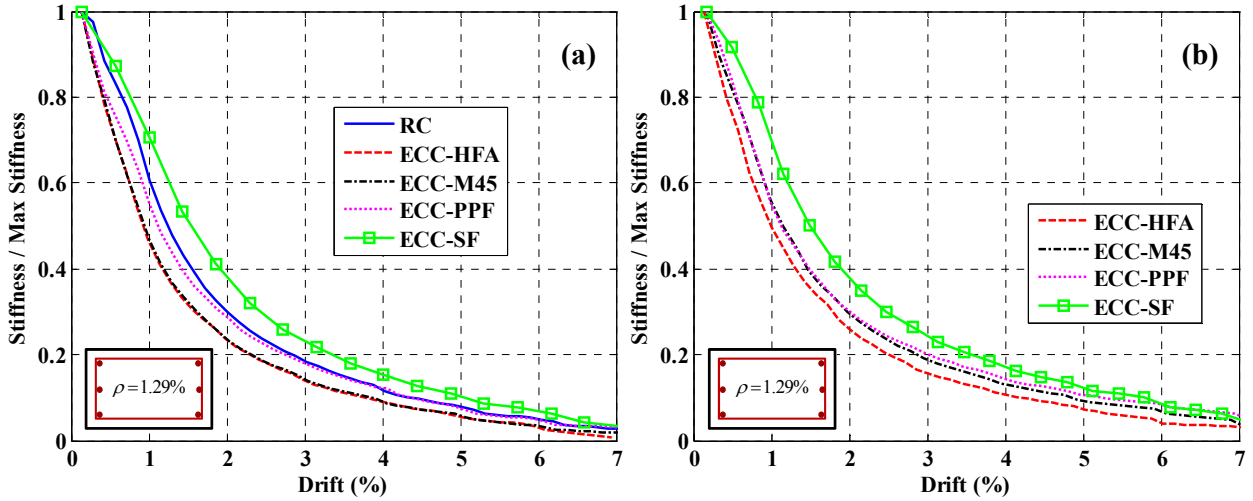

Figure 3.38. Stiffness degradation of concrete and ECC specimens with a reinforcement ratio of 1.29 percent: (a) fixed-pinned and (b) fixed-fixed boundary conditions

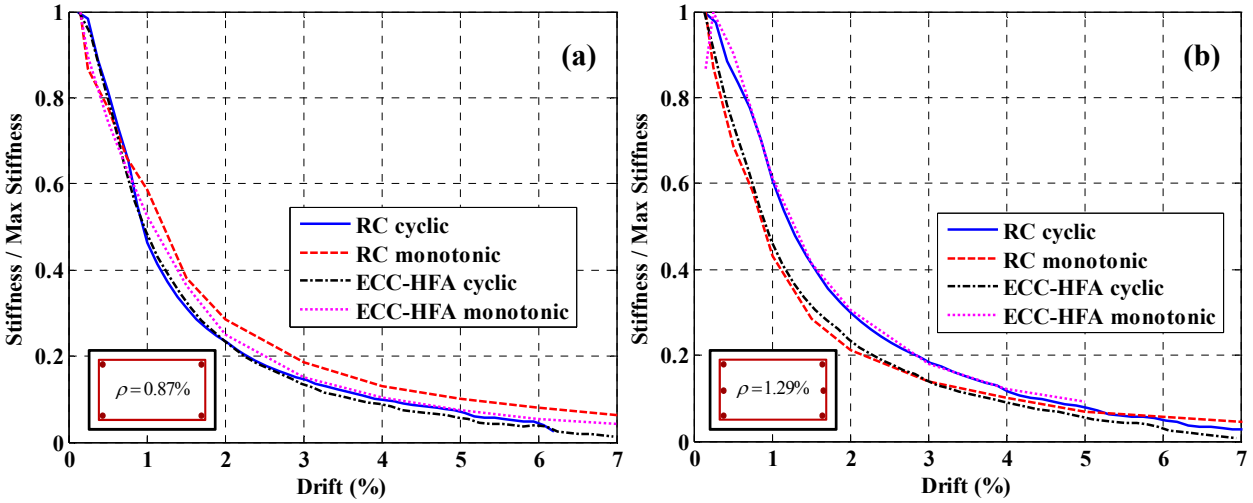

Figure 3.39. Comparison of stiffness degradation between monotonic and cyclic tests, and concrete and ECC specimens (a) 0.87 percent and (b) 1.29 percent reinforcement ratio

3.8.2.b. Strength and strength degradation

The strength of the specimens is defined as the peak load resistance, shown as in Figure 3.35(b). It is observed that the strength of ECC specimens is significantly higher than that of concrete specimens and ranges from 43 to 67 percent depending on the mixture design. The strength increase by replacing concrete with ECC-HFA is higher (68 percent) for the case with 1.29 percent longitudinal reinforcement when compared to the case with 0.87 percent reinforcement (46 percent) [see Figure 3.40]. The higher strength increase for the 1.29 percent longitudinal reinforcement case is mainly due to the high tensile strain capacity of ECC, which results in compatible deformations between the matrix and the longitudinal reinforcement, hence

preventing debonding and increasing the contribution of longitudinal reinforcement in the member response. It is important to note that both the concrete and the ECC specimens failed in flexure, meaning that higher compressive strength of ECC mixtures is not a major source of higher member strength of ECC columns.

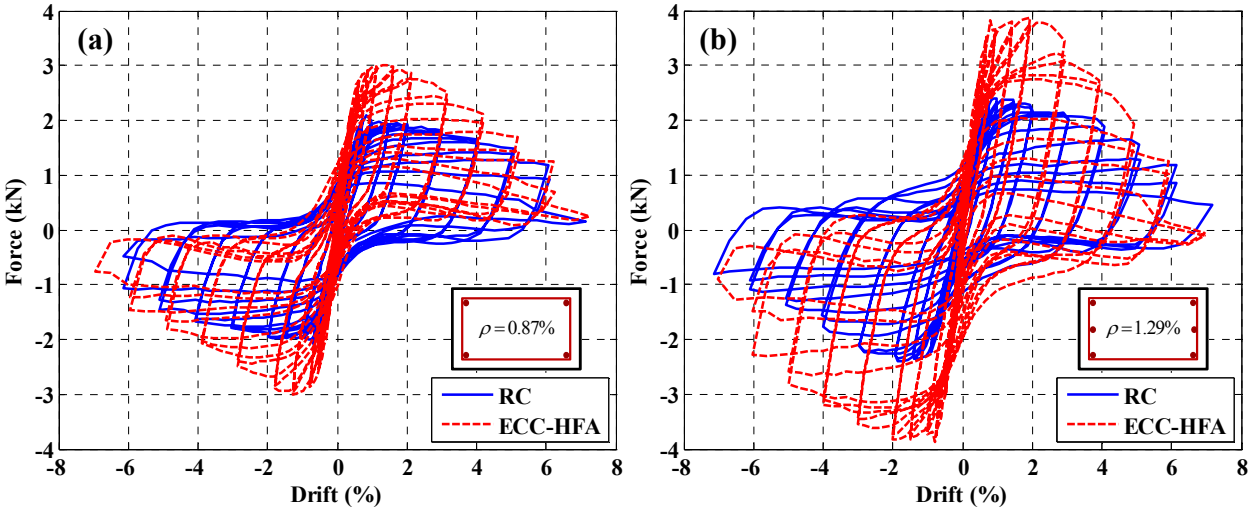

Figure 3.40. Cyclic response of RC and ECC specimens: (a) 0.87 percent and (b) 1.29 percent longitudinal reinforcement

The effect of stirrup spacing on the response of ECC specimens is illustrated in Figure 3.41. The data pertains to the configuration with 1.29 percent longitudinal reinforcement ratio and HFA mixture. As seen in Figure 3.41(a), no significant difference in the performance of the member with no transverse reinforcement is observed in comparison to the member with 0.18 percent transverse reinforcement. The six percent increase in strength is attributed to slight variation between the specimens. The same conclusion is confirmed in Figure 3.41(b) by looking at the envelope curves obtained from cyclic tests for the different transverse reinforcement ratios considered here. Due to the existence of secondary reinforcement (fibers), ECC has internal confinement. It is observed as long as the shear capacity of ECC (which is significantly higher compared to mixtures without fibers) is not exceeded, the transverse reinforcement does not have a significant effect on the flexural behavior. These same conclusions are also drawn elsewhere (Fischer and Li, 2002).

The comparison of envelope curves in Figure 3.36(a), see also Table 3.6, for different ECC mixtures indicate that the HFA mixture yields the highest force resistance amongst the four considered ECC mixtures, and the difference between the HFA and PPF mixtures is around 18 percent (for fixed-pinned boundary condition). As introduced in Section 3.2.2, the PPF mixture is the cheapest and most environment-friendly followed by the HFA mixture. Based on the results obtained here, it can be concluded that the HFA mixture is superior to M45 and SF mixtures in terms of cost, sustainability and performance. Although having a relatively lower performance, PPF mixture might be preferred over the HFA mixture due to its lower cost and higher level of greenness.

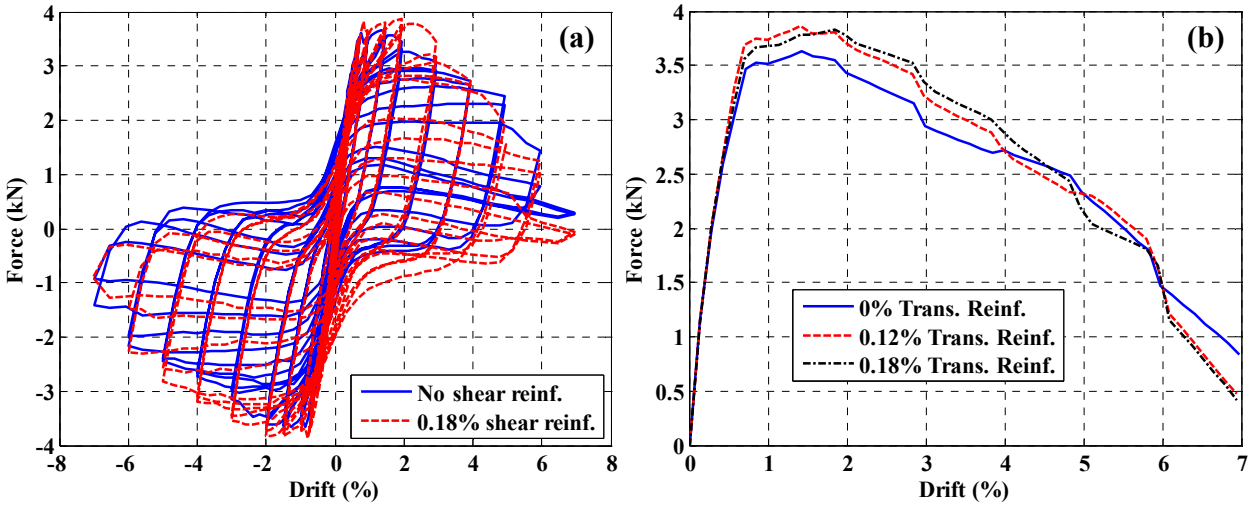

Figure 3.41. (a) Effect of stirrup spacing, ECC specimens with no stirrups and 0.18 percent transverse reinforcement ratio (b) envelope curves from cyclic tests for ECC specimens with different transverse reinforcement ratios

The monotonic test results and envelopes from the cyclic tests are compared in Figure 3.42. Very good correlations are observed between monotonic and cyclic tests in terms of strength. As expected, the strength degradation is higher in the cyclic tests correlating directly with the stiffness degradation observation earlier.

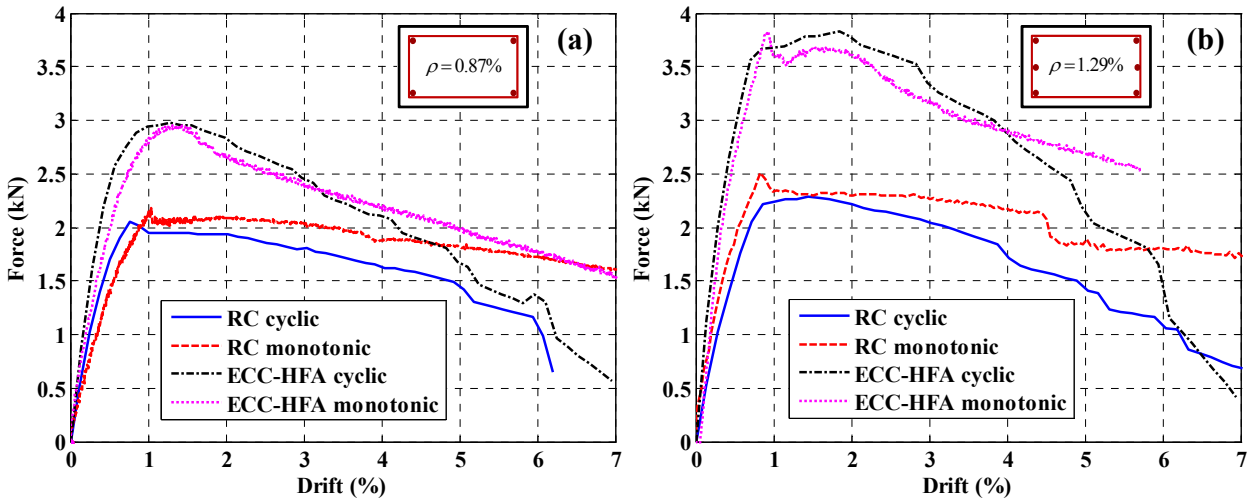

Figure 3.42. (a) Comparison of monotonic curves and envelopes from cyclic tests: (a) 0.87 percent and (b) 1.29 percent longitudinal reinforcement

The mean envelope curves are obtained from those shown in Figure 3.36(a) and Figure 3.37(a), normalized by the individual maximum lateral force resistances, and plotted in Figure 3.43 to illustrate the strength degradation. Although the normalized envelope curves for different ECC mixtures and concrete are similar for fixed-pinned boundary conditions, the ECC columns are tested under a higher axial compressive load to achieve a constant ratio for all specimens.

ECC specimens would have exhibited higher strength degradation due to second order effects if the performance of ECC had not been superior. It is observed that the strength degradation of the HFA mixture is higher compared to other mixtures under fixed-fixed boundary conditions [see Figure 3.43(b)]. Strength degradation is found to be lower for the fixed-fixed boundary conditions when compared to fixed-pinned tests [compare Figure 3.43(a) and Figure 3.43(b)].

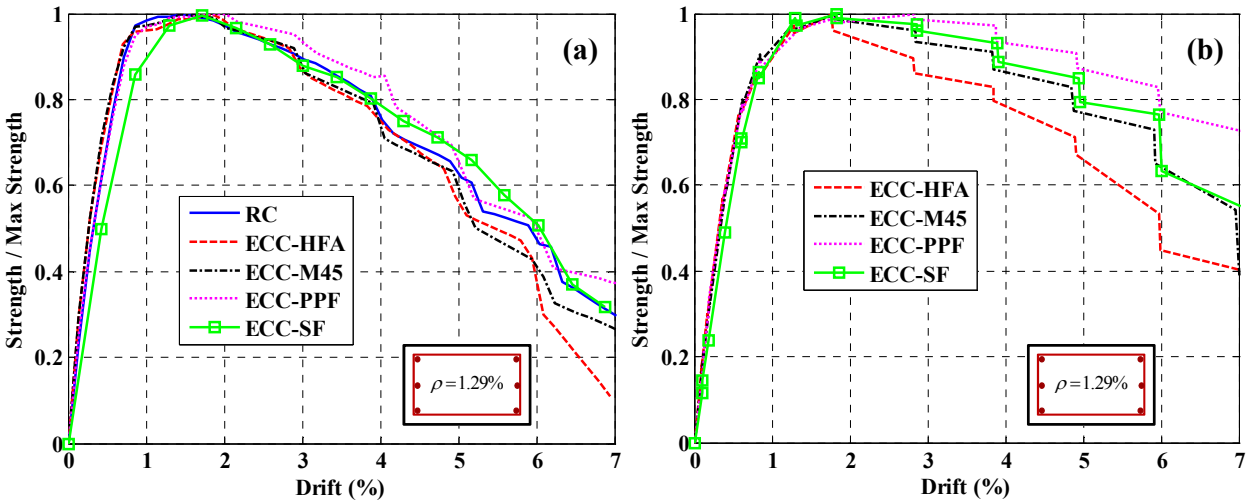

Figure 3.43. Normalized envelope curves (a) fixed-pinned (b) fixed-fixed boundary conditions

3.8.2.c. Ductility

Two ductility definitions are adopted here based on the drifts corresponding to the strength and failure point of the specimens, μ_m and μ_u respectively. The specimens are assumed to have failed at a drift level that corresponds to 10 percent reduction in load carrying capacity as shown in Figure 3.35(b). Two different ductility definitions are used here due to the fact that the ductility based on peak and ultimate points is associated with two different structural limit states: life safety and collapse prevention respectively. The calculation of the yield point is also illustrated in Figure 3.35(b). The drift values at yield, peak and 10 percent reduction are provided in Table 3.6. It is seen that, although drift values at the peak load resistance are higher for ECC specimens, the drift corresponding to yield and ultimate points is similar. This finding results in higher μ_m values for ECC specimens compared to concrete and μ_u values that are similar. The similarity in μ_u values across all specimens is attributed to higher second order effects in the ECC specimens, which would otherwise be expected to have greater μ_u values, as discussed in the previous section. Thus, it is concluded that the ECC specimens perform better in terms of ductility since they are subjected to higher axial loads which erode member ductility.

3.8.2.d. Energy Absorption Capacity

Another parameter significant to the seismic design of structural members is the energy absorption capacity. The higher the energy absorption capacity of a structure without significant

reduction in load carrying capacity, the lower the chance of collapse under sustained displacement reversals during an earthquake.

The elastic energy (estimated as $1/2 \cdot \Delta_y \cdot F_y$ where F_y is the force corresponding to yield drift Δ_y) and the energy absorption capacities up to peak and ultimate drifts (equal to the sum of the areas within complete cycles up to the peak and ultimate points) are summarized in Table 3.6. The energy absorption capacities of ECC mixtures are significantly higher than concrete ranging from 20 to 220 percent (see Table 3.7). The gain in energy absorption capacity by using ECC instead of concrete is more significant when the peak point is considered. As mentioned previously, due to second order effects the reduction in load carrying capacity of ECC and concrete specimens, and hence the drift corresponding to ultimate points, are similar. Thus the gain is limited to the increase in load resistance exhibited by the ECC specimens. The cumulative energy absorption as a function of drift is plotted in Figure 3.44(a) for concrete and considered ECC mixtures under fixed-pinned boundary conditions. The difference in energy absorption capacities of the ECC specimens when compared to the concrete specimen is provided in Figure 3.44(b). It is seen that the difference in energy absorption capacities between the concrete and ECC specimens reduces with increasing drift. Nevertheless the increase in energy absorption capacity in the ECC specimens relative to the concrete specimen ranges from 20 to 50 percent.

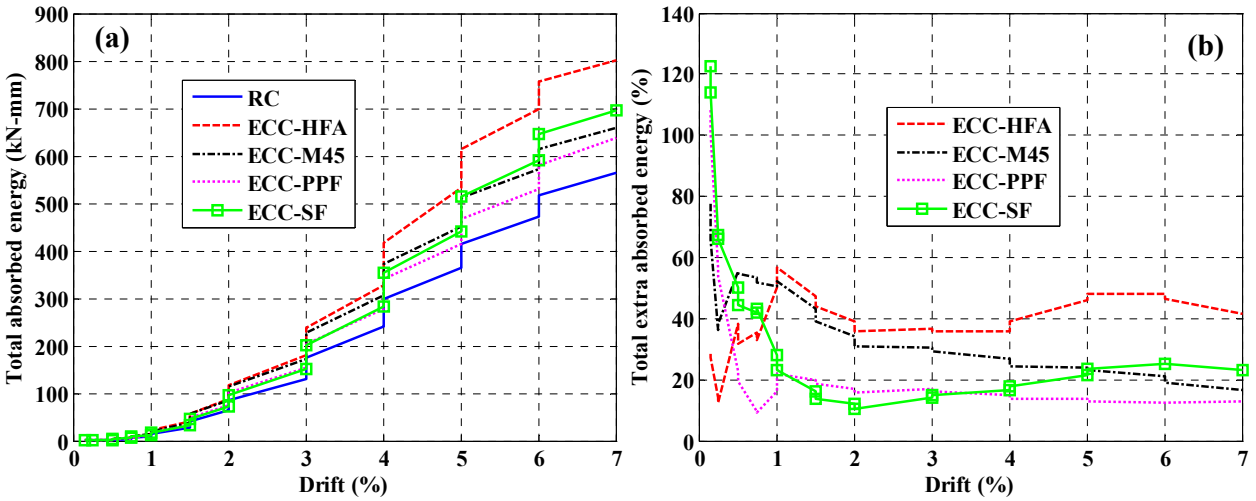

Figure 3.44. (a) Total energy absorption of concrete and ECC specimens, (b) difference in energy absorption of ECC mixtures with respect to concrete

Table 3.6. Summary of results for cyclic tests

	Mix	Stiffness (kN/mm)	Strength (kN)	Drift at Yield (%)	Drift at Peak (%)	Drift at 10% reduction	Ductility (Δ_m/Δ_y)	Ductility (Δ_u/Δ_y)	Energy Elastic (kN-mm)	Energy up to Peak (kN-mm)	Energy up to 10% Red. (kN-mm)
Cyclic 6 bars	RC	0.963	2.281	0.742	1.438	2.955	1.937	3.981	2.935	30.694	142.489
	ECC-HFA	2.091	3.829	0.650	1.841	2.895	2.831	4.452	4.203	95.756	194.438
	ECC-M45	1.895	3.514	0.644	1.449	2.948	2.251	4.579	3.760	92.462	185.554
	ECC-PPF	1.493	3.272	0.759	1.736	3.292	2.286	4.336	4.241	80.895	293.647
	ECC-SF	1.149	3.398	0.933	1.577	2.823	1.690	3.025	5.363	35.163	162.965
Cyclic 4 bars	RC	1.085	2.047	0.584	0.759	2.630	1.299	4.503	2.033	13.383	124.702
	ECC-HFA	1.584	2.982	0.592	1.278	2.367	2.159	3.998	2.939	42.544	153.973
Cylic-fixed 6 bars	ECC-HFA	4.192	8.428	0.755	1.770	2.770	2.343	3.668	10.055	240.410	420.649
	ECC-M45	3.431	7.780	0.777	1.811	3.838	2.331	4.940	10.016	241.506	643.665
	ECC-PPF	3.453	7.473	0.792	2.829	4.913	3.572	6.203	9.716	441.017	1107.701
	ECC-SF	2.424	6.774	0.889	1.825	3.907	2.054	4.398	9.947	233.765	656.805

Table 3.7. Summary of results for cyclic tests (differences in percentage)

	Mix	Stiffness	Strength	Drift at Yield	Drift at Peak	Drift at 10% reduction	Ductility (Δ_m/Δ_y)	Ductility (Δ_u/Δ_y)	Energy Elastic	Energy up to Peak	Energy up to 10% Red.
Cyclic 6 bars	RC	0.000	0.000	0.000	0.000	0.000	0.000	0.000	0.000	0.000	0.000
	ECC-HFA	117.048	67.867	-12.408	27.999	-2.044	46.130	11.832	43.178	211.976	36.458
	ECC-M45	96.722	54.081	-13.280	0.753	-0.240	16.182	15.038	28.106	201.244	30.223
	ECC-PPF	55.026	43.441	2.276	20.706	11.411	18.020	8.933	44.487	163.556	106.083
	ECC-SF	19.247	48.979	25.706	9.666	-4.477	-12.760	-24.010	82.714	14.562	14.370
Cyclic 4 bars	RC	0.000	0.000	0.000	0.000	0.000	0.000	0.000	0.000	0.000	0.000
	ECC-HFA	46.003	45.696	1.380	68.466	-9.983	66.172	-11.208	44.619	217.891	23.473
Cylic-fixed 6 bars	ECC-HFA	0.000	0.000	0.000	0.000	0.000	0.000	0.000	0.000	0.000	0.000
	ECC-M45	-18.147	-7.689	2.875	2.348	38.529	-0.513	34.657	-0.381	0.456	53.017
	ECC-PPF	-17.630	-11.331	4.874	59.868	77.330	52.437	69.088	-3.368	83.444	163.331
	ECC-SF	-42.177	-19.618	17.652	3.120	41.041	-12.351	19.881	-1.071	-2.764	56.141

3.8.3. Static Time History Tests and Hybrid Simulation

As indicated in Table 3.5, two STH tests and four hybrid simulations are conducted. Descriptions of STH tests and hybrid simulation are provided in Sections 3.3 and 3.6.3. Four different cases are considered, and the properties of the frames in each case are summarized in Table 3.8. The frames are either made entirely of concrete or ECC. The longitudinal reinforcement ratios in Table 3.8 relate to the experimental columns, which are selected as the left-exterior first story columns of the frames as described earlier. The gravity loads are applied (as distributed loading) to the beams such that the columns develop an axial compressive load equal to the desired percentages of the axial strength of an equivalent concrete column. The same ground excitation (with a PGA of 0.8 g) is used in all cases. The ground motion is developed by spectrum matching to represent an earthquake with a return period of 2475 years at a specific site (see Figure 3.31). The record with the selected return period is associated with the collapse prevention socio-economic limit state for buildings. Although the monotonic and cyclic tests are very useful in terms of deriving several structural level response metrics, results from the STH tests and hybrid simulation are important because they are more realistic descriptions of the input motion that a structure would undergo during an earthquake.

Table 3.8. Summary of results from STH tests and hybrid simulation

	Description of Cases			Test Results				
Case	**Material**	**Long. Reinf. Ratio (%)**	**Gravity Loads (%)**	**Initial Stiffness (kN/mm)**	**Final Stiffness (kN/mm)**	**Max Force (kN)**	**Max Drift (%)**	**Energy dissipation (kN-mm)**
1 Hybrid	Concrete	0.87	7.5	1.551	1.239	4.906	4.180	189.461
2 Hybrid	ECC-HFA	0.87	7.5	2.109	1.462	6.429	3.593	231.387
3 STH	ECC-HFA	1.29	5	1.575	1.066	6.538	4.143	229.571
3 Hybrid	ECC-HFA	1.29	5	1.421	0.984	6.149	4.513	326.017
4 STH	ECC-HFA	1.29	10	2.245	1.812	8.158	2.856	162.513
4 Hybrid	ECC-HFA	1.29	10	2.539	1.855	8.111	3.231	224.711

The initial and final (post-earthquake) stiffness, maximum force, maximum drift and the energy absorption of the experimental column are summarized in Table 3.8 for all cases. It is seen that the initial stiffness of the specimens is similar to that obtained in the cyclic tests and somewhere between the stiffness obtained from the fixed-pinned and fixed-fixed boundary conditions. It is thus concluded that cyclic tests with considered boundary conditions give a good estimation of the initial stiffness. The stiffness of the ECC specimen is observed to be significantly higher than that of the concrete specimen (approximately 35 percent). Stiffness reduction is observed to be similar for all cases independent of the material, reinforcement ratio and axial load level. At the end of ground excitation the stiffness of the specimens is reduced to 67-80 percent of the original values. This level of stiffness reduction occurs at a drift level of 0.5-1.25 percent (depending on the mixture design) under cyclic loading. This observation indicates that cyclic tests erode stiffness at a much faster rate than actual earthquake excitation (mainly due to several small amplitude cycles). It is seen that the ECC column develops a higher maximum force resistance than the concrete column, and the ECC column (hence the frame) undergoes a lower maximum drift (~15 percent reduction in drift) [see Figure 3.45(a) and Figure

3.46(a)]. The energy absorption of the ECC column is observed to be 22 percent higher than that of the concrete column [see Figure 3.48(a)].

The responses of the columns obtained during STH tests and hybrid simulation are shown in Figure 3.45 through Figure 3.50. The maximum drifts in the hybrid simulations are observed to be higher than those in STH tests [see Figure 3.45(b)]. These higher drifts are due to the interaction between the experimental column and the numerically modeled frame (or the analytical module) during hybrid simulations. The good correlation between STH and hybrid simulation tests is a result of the predictive capabilities of the numerical model. It is seen that the axial force varies significantly under simulated earthquake motion (Figure 3.47). The column is always in compression during hybrid simulations while it is subjected to axial tension during STH test for case 3. As seen in Figure 3.48 and mentioned earlier, the drift and rotation demand is reduced for the ECC specimen, resulting in reduced damage for ECC frames. A comparison of cases 3 and 4 (Figure 3.49 and Figure 3.50) indicates that higher axial load on the columns increases the lateral force and moment demands; however, it significantly reduces the drift and rotation demands. Since ECC columns have very high axial force and shear capacity, higher axial load is found to be beneficial in reducing the deformation demands on vertical members.

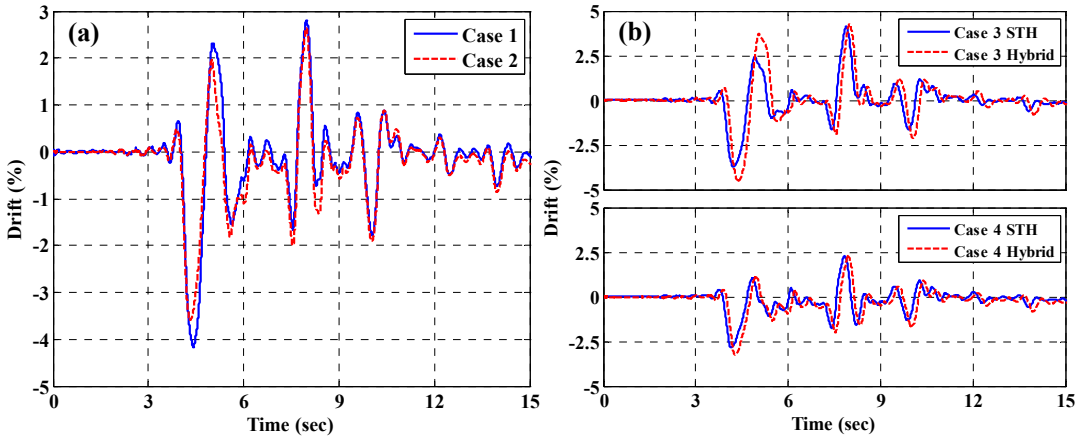

Figure 3.45. Drift response of columns in STH tests and hybrid simulation

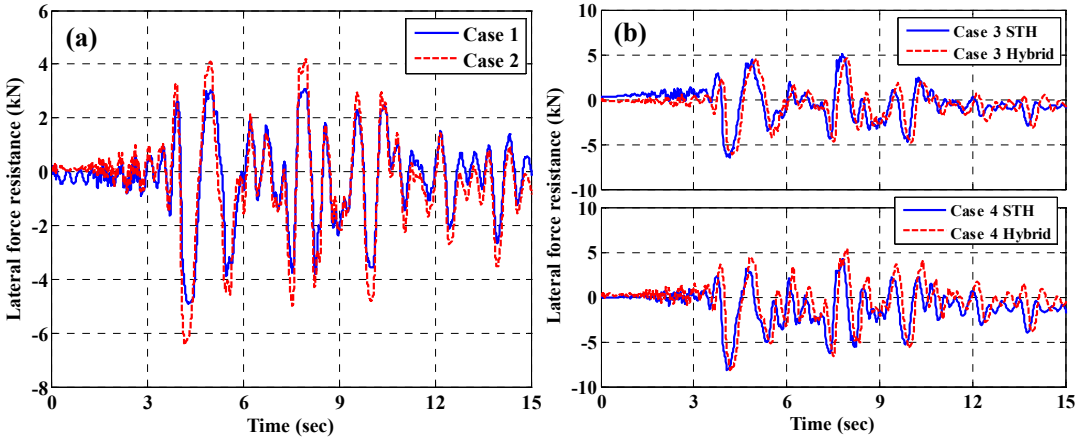

Figure 3.46. Lateral force resistance of columns in STH tests and hybrid simulation

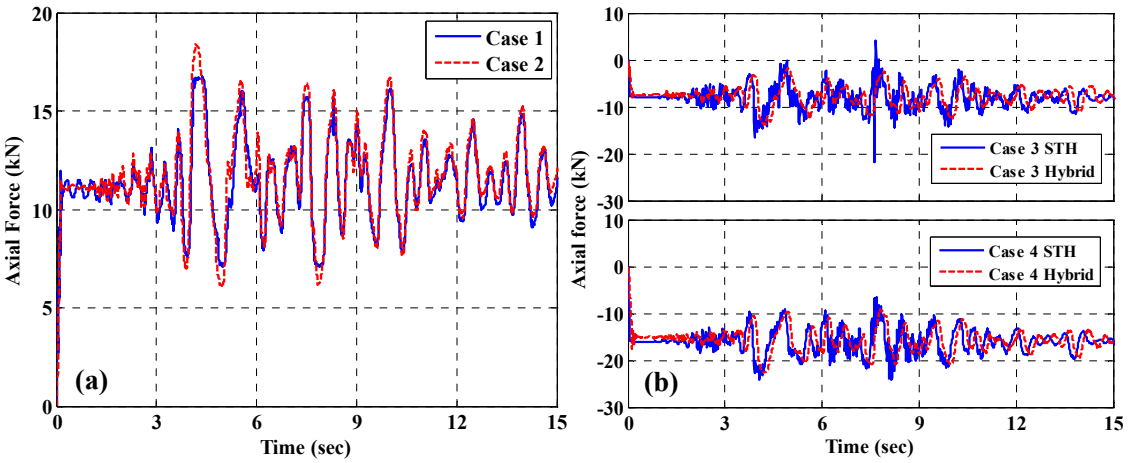

Figure 3.47. Axial force imposed on columns during STH tests and hybrid simulation

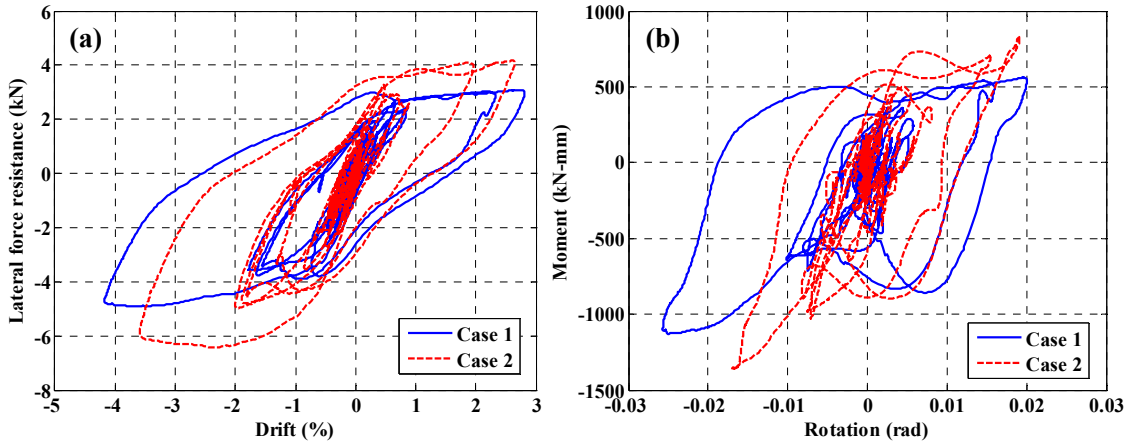

Figure 3.48. (a) Lateral force vs. drift and (b) moment vs. rotation responses of columns during hybrid simulation for cases 1 and 2

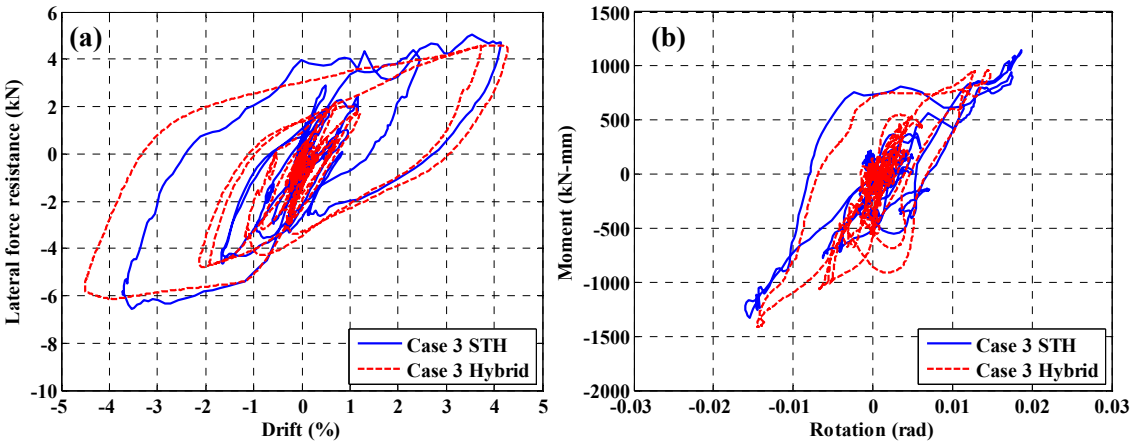

Figure 3.49. (a) Lateral force vs. drift, and (b) moment vs. rotation responses of columns during STH tests and hybrid simulation for case 3

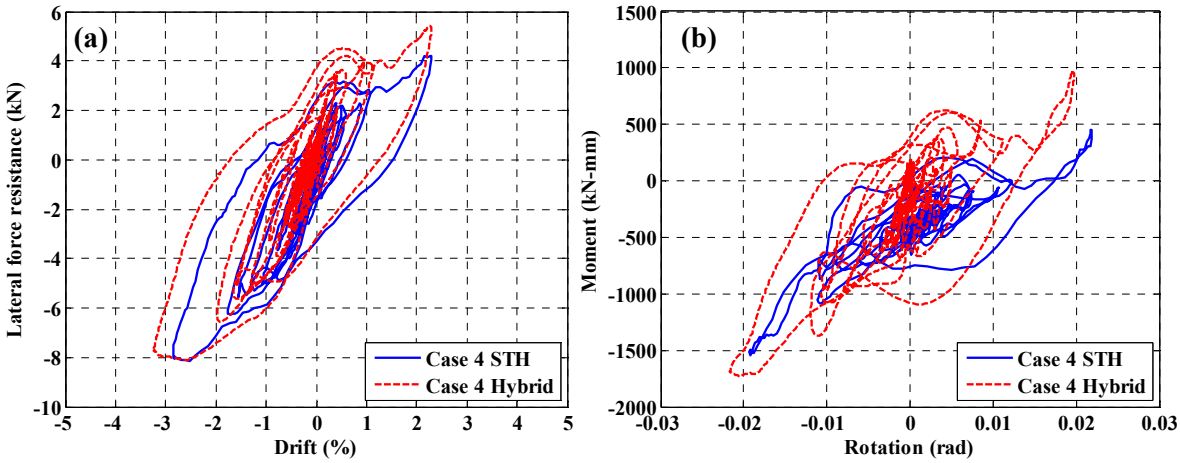

Figure 3.50. (a) Lateral force vs. drift, and (b) moment vs. rotation responses of columns during STH tests and hybrid simulation for case 4

3.9. CONCLUSIONS

Chapter 3 has presented an experimental program at the small-scale (with a scale factor of 1/8). Small-scale testing is chosen to investigate a large-number of test parameters by utilizing logistical and financial advantages. Based on a detailed review of existing literature, the following are identified as critical for the success of small-scale testing: careful preparation of materials to match prototype behavior, consistency across specimens, and high precision testing equipment capable of imposing desired loading and boundary conditions. These requirements are achieved in this study and the author is further motivated by the findings from a recent study that developed a similar experimental program and achieved very good correlations between large-scale and small-scale tests (Holub, 2009). Through the experimental program, the performance of ECC is characterized at the component and system levels and is compared against RC behavior. Component behavior is investigated under monotonic and cyclic loading, while to investigate the system behavior, sub-structured pseudo-dynamic testing (or hybrid simulation) is used.

Making use of the logistical and financial advantages of small-scale testing, a range of parameters is investigated. It is demonstrated that the tests are repeatable, and different loading scenarios correlate well with each other. Important conclusions are made regarding material selection by comparing the performance of concrete and ECC mixtures with different costs and sustainability indices. It is observed that ECC specimens have a significantly higher initial stiffness compared to concrete specimens, ranging from 20 to 120 percent depending on the properties of the ECC mixture. The stiffness degradation of the two materials however, is similar. There is also a significant amount of increase in lateral strength with ECC ranging from 43 to 68 percent. The ECC member ductility is significantly higher than that of concrete when the LS limit state is considered, while similar values are obtained for the CP limit state. ECC also outperforms concrete with respect to energy absorption capacity. The increase in energy absorption is approximately 150 and 50 percent for LS and CP limit states, respectively. Hybrid

simulation of concrete and ECC frames under a ground motion representative of an earthquake associated with the CP socio-economic limit state indicates that the cyclic test under fixed-pinned and fixed-fixed conditions are the lower and upper bounds for the response of columns in terms of initial stiffness, strength, and energy absorption capacity. On the other hand, it is seen that stiffness and strength degradation under cyclic loading are significantly higher and do not correlate well with results obtained from hybrid simulation.

It is also important to mention that small-scale testing has certain limitations. First, the size of the specimens tested here does not allow for measurement of local response quantities such as strains in longitudinal reinforcement and the matrix (concrete or ECC). Furthermore, a more concentrated crack pattern is observed at small-scale which is difficult to relate to prototype specimens. Due to size effects, the results would not have been as reliable if specimen failure had been governed by fracture rather than by plastic yielding. Notwithstanding these limitations, small-scale testing is an accurate alternative to large-scale testing when global structural response measures are of interest. The inter-correlation of the small-scale tests in this study provides strong evidence in support of the use of ECC for seismic design applications. The experimental results provided in this thesis lend weight to focusing future efforts on the large scale testing of ECC members and structures to provide data for the derivation of design guidelines and to encourage the use of ECC in earthquake resistant construction.

The findings described quantitatively above satisfy the main societal-level objectives mentioned in Chapter 1. Specifically, the safety, economy and sustainability in seismic design of buildings are all supported with use of ECC. These advantages result from the better utilization of longitudinal reinforcement, reduction in material usage and workmanship costs (due to higher shear resistance and confinement), reduced deformational demand on structural members and higher damage tolerance that prevents structural damage are in line with the societal level objectives safety, economy and sustainability in seismic design of buildings.

4

STRUCTURAL LEVEL SIMULATION

"In dealing with earthquakes, we must contend with appreciable probabilities that failure will occur in the near future. Otherwise, all the wealth of this world would prove insufficient to fill our needs: the most modest structure would be fortresses. We must also face uncertainty on a large scale, for it is our task to design engineering systems—about whose pertinent properties we know little—to resist earthquakes and tidal waves—about whose characteristics we know even less."

Nathan M. Newmark and Emilio Rosenblueth

Although many test parameters are investigated using the logistical and financial advantages of small-scale testing, it is not feasible to explore all possible combinations of governing parameters through experimentation. Chapter 4 reports on the structural level simulation conducted to complement the data obtained from the experimental program in Chapter 3. First, the numerical tool developed in Chapter 2 is validated at the component and system levels using the data from the experimental program. A parametric study is then conducted at the component level to investigate the effect of engineered cementitious composites (ECC) tensile strength and ductility on the structural level response metrics: stiffness, strength, ductility, and energy absorption capacity. It is observed that the structural level response metrics change considerably depending on the material properties. Information obtained from structural level simulation by using a validated tool is aimed at linking the performance of ECC between the scales: material and system. Additionally, structural applications of ECC and existing code regulations are reviewed to provide background information regarding the development of seismic design parameters for ECC structures. This last point has not been the focus of existing studies and is mentioned here briefly as recommended future work.

4.1. BACKGROUND

This section first reviews prior studies on the modeling of ECC at the structural (component, sub-assemblage) level that are related to the structural level simulation conducted here. The advantages of ECC for sustainable construction, recent applications of ECC on large projects,

and existing regulations on structural design using ECC are then reviewed. These topics are relevant to the development of seismic design parameters for ECC structures and are covered here very briefly and recommended for future research.

4.1.1. Modeling of ECC Structural Members

Nagai et al. (2002) performed finite element analysis of structural walls with high-performance fiber-reinforced cementitious composites (HPFRCC) to predict the shear-force rotation-angle response. Uniaxial stress-strain relationships were assumed for HPFRCC in tension and compression. It was shown that the finite element model was capable of predicting the envelope response from cyclic testing of shear walls.

Han et al. (2003) implemented the previously mentioned (Section 2.1.3) cyclic constitutive model developed for ductile fiber-reinforced cementitious composites (DFRCC) in a commercial finite element analysis software using a total strain-based rotating crack approach. The finite element model was used to predict the response of cantilever column elements tested by Fischer and Li (2003a). It was observed that finite element analysis could simulate the experimental response with reasonable accuracy, notwithstanding its deficiency in predicting the initial stiffness of the specimens. The work by Han et al. (2003) could be considered as one of the most rigorous approaches in literature to the modeling of DFRCC elements.

Suwada and Fukuyama (2006) investigated the shear behavior of simple HPFRCC members through testing and finite element analysis. In finite element analysis, uniaxial stress-strain relationships were employed for compressive and tensile material response. To model HPFRCC behavior, a trilinear model was used for tension, and the relationship by Fafitis and Shah (1985), which was developed for regular concrete, was employed for compression. The bond model by Morita and Kaku (1975) was used to represent the relative deformation between the steel reinforcement and the matrix. A smeared crack approach with rotating crack direction was adopted. Finite elements results well captured the response of the specimens up to peak loading. A parametric study that was performed using the analytical tool indicated that the tensile properties of the HPFRCC had a significant influence on member response at different magnitudes for different reinforcement configurations.

Ahmed et al. (2007b) developed a finite element model based on the smeared cracking approach to simulate the corrosion-induced cracking of ordinary and fiber reinforced concrete. Monotonic stress-strain envelopes, for ordinary concrete and fiber-reinforced concrete (FRC), were used, and unloading and reloading behaviors under load reversals were not modeled. The model was used to predict corrosion-induced damage in beams. Good correlations between the experimental results and the finite element model were observed.

Dick-Nielsen et al. (2007) developed a plasticity based damage mechanics model for ECC and showed that by combining a matrix and a fiber model, the formulation could provide accurate information about crack opening, spacing and orientation which could be used for the assessment of ECC structures in serviceability state.

Shin et al. (2007) used a lattice model to simulate the three point bending test of composite beams (concrete and DFRCC). The model was able to capture the experimental behavior, and the numerical studies showed increased peak loads and deformation capacities for composite beams when compared to concrete counterparts. Closed form equations to predict the shear strength (Shimizu et al., 2004) and the moment-curvature response (Soranakom and Mobasher, 2008) of rectangular beams were also developed.

4.1.2. Advantages of ECC

In addition to enhanced structural performance (Section 3.1.3), ECC has advantages that improve the sustainability of structural systems. Studies that demonstrate the additional advantages of ECC in terms of increased sustainability are briefly reviewed below.

4.1.2.a. Greenness

Through bending tests, Ahmed et al. (2007a) showed that up to 50 percent replacement of cement with fly ash resulted in no significant reduction in flexural strength. Moreover, an increase in deflection capacity was observed with increasing fly ash content up to 50 percent of replacement. More recently, Lepech et al. (2008) proposed an increased sustainability framework for ECC through combining preliminary analysis techniques, infrastructure application requirements, and micromechanical materials tailoring tools. Industrial waste materials such as green foundry sand, cement kiln dust and fly ash were assessed as potential substitutes for original ECC constituents. The results from this study were promising, and it was shown that increased infrastructure sustainability could be achieved through application of green ECC. Lepech et al. (2008) also demonstrated that through a micromechanics-based design theory it was possible to predict the load deformation response of ECC. And through properly tailoring fiber, matrix and interface properties it was feasible to design for the desired material properties.

4.1.2.b. Durability

It was shown through several studies that ECC exhibited very low water and chloride permeability due to strain hardening and multiple cracking behaviors with very small crack widths which significantly improved the corrosion resistance of the material over ordinary concrete (Ahmed and Mihashi, 2007). Damage induced by cracking concrete (such as corrosion of steel) could be mitigated by employing HPFRCC (Fukuyama et al., 2007). Reduced shrinkage cracking, 2.5 times less crack width compared to mixtures without fibers, was observed in ECC (Li, 2003a; Rouse and Billington, 2007). The fatigue life of ECC was shown to be several times higher than that of concrete (Zhang and Li, 2002; Suthiwarapirak et al., 2004). Elimination of spall process and small crack widths also reduced the maintenance cost of ECC applications. Freeze thaw, abrasion and wear resistance, early age strength, long term strain capacity (Li and Lepech, 2004) and weathering resistance (Li et al., 2004) of ECC were found to be superior to those characteristics of concrete. In addition, ECC was shown to retain its improved mechanical properties under highly alkaline environments when mechanically loaded (Sahmaran and Li, 2008).

4.1.2.c. Self-Healing, Self-Consolidation and Piezoresistivity

Yang (2009) demonstrated that ECC exhibits autogenous healing under wet-drying cycles. Several measures including the resonant frequency, re-loading behavior under pre-cracked conditions and stiffness recovery displayed considerable self-healing. When used, the self-healing feature of ECC could improve the long-term durability of civil infrastructure. Kong et al. (2003) showed that by employing hydrophilic polyvinyl alcohol (PVA) fibers a self-consolidating ECC mixture could be produced. In hardened state the material still exhibited tensile strain capacity up to five percent. Hou and Lynch (2005) showed that by utilizing the piezoresistive property (electrical resistance correlated with mechanical strain) of ECC, the specimens could self-measure the mechanical strain in field conditions.

4.1.2.d. ECC in other Forms

It was shown that ECC could also be produced in sprayable form (Kanda et al., 2002; Kim et al., 2004), that it is amenable to the extrusion process (Stang and Li, 1999) and could be produced in full-scale without any compromise in mechanical properties (Kanda et al., 2004; Lepech et al., 2008). Wang and Li (2006) showed that ECC could attain high early strength (within four hours after placement) as high as 21 MPa. These properties of ECC render the material suitable for a wide variety of retrofitting applications. Arisoy and Wu (2008) demonstrated that lightweight HPFRCC could be produced. This study also demonstrated the controllability of the material mechanical properties. By changing the volume fraction of fibers and fly ash content the ductility and the strength of the material could be modified in a relatively controlled manner. Similarly, results from Wang and Li (2006) showed that composite properties of ECC could be controlled by reducing the variability of key microstructure parameters.

It was observed that the tensile strain capacity of ECC could drop drastically (from three percent to half a percent) with increased straining rate (Yang and Li, 2005). Therefore to achieve the desired mechanical performance, ECC was required to be redesigned for seismic loading rates. Proper selection of fiber type, length, as well as the tailoring of material micromechanical properties was crucial for adequate performance under high strain rates.

4.1.3. Structural Applications of ECC

To provide high vibration damping and energy absorption during an earthquake, precast ECC coupling beams were used for connecting the core walls of three high-rise reinforced concrete (RC) residential buildings in Japan (Figure 4.1): 27-story Glorio Roppongi High Rise in central Tokyo, 41-story Nabeaure Tower in Yokohama, and 60-story Osaka Tower in Osaka. The Michigan Department of Transportation used ECC link-slab for replacing a conventional bridge deck expansion joint in southeastern Michigan [Figure 4.1(c)]. The tensile ductility, crack width control, freeze-thaw, weather exposure, wheel load abrasion, wear and fatigue resistance of ECC were exploited for enhanced bridge deck durability. By reducing the steel corrosion rate, the maintenance interval of the bridge deck was extended. Life-cycle analysis indicated that if ECC was used in all expansion joints on the bridge, approximately 40 percent reduction in terms of

primary energy usage and CO_2 emission (responsible for global warming), 50 percent less solid waste generation, and 38 percent less raw material consumption could be achieved. The total life-cycle cost (LCC) savings were evaluated to be approximately 16 percent over the 60 years service life, which was approximated as twice that of the conventional RC bridge (Keoleian et al., 2005).

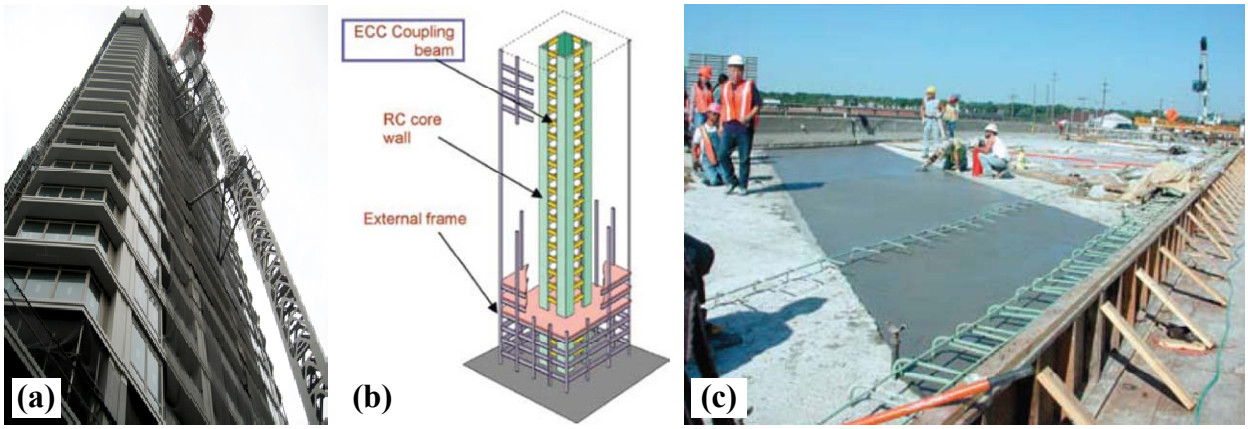

Figure 4.1. Structural applications of ECC, (a) Nabeaure Tower, Yokohama, Japan, (b) Glorio Roppongi High Rise, Tokyo, Japan, (c) Groove Street Bridge, Ypsilanti, Michigan, USA

ECC was also used for the surface repair of a damaged earth retaining wall in Gifu Japan in 2003. Very small crack widths have been observed since the applications, proving the durability of ECC (Li, 2008). Underground structures that need to comply with large deformations and/or structures that require leak prevention are other potential applications of ECC.

4.1.4. Code Regulations on Construction Using ECC

The Japan Society of Civil Engineers (JSCE) published the first and only recommendations for design with HPFRCC (JSCE, 2008). Since tensile characteristics of HPFRCC play a crucial role in structural response, JSCE limited the acceptable material to that with 0.5 percent minimum tensile strain capacity and 0.2 mm maximum average crack width. Recommendations comprised two types of HPFRCC, namely casting and spraying. Spraying was included to allow for the utilization of enhanced material properties in retrofitting applications. Steel reinforced HPFRCC and jacketing of RC members with HPFRCC was allowed; however, monolithic use of HPFRCC was prohibited. Recommendations were limited to composites with synthetic fibers with a fiber-volume fraction less than or equal to two percent. Test methods were included to determine the tensile yield strength, ultimate tensile strain capacity, average maximum crack widths and variations in crack widths. In terms of material properties, recommendations were provided for strength and ultimate strain in tension and compression, Young's modulus, Poisson's ratio, thermal characteristics, shrinkage, creep, fatigue and maximum crack widths. Structural design regulations for bending moment and axial force, shear forces, torsion, fatigue and rigid body stability were included. Serviceability, structural detailing and resistance to

environmental actions were also regulated. No limitation to the minimum ratio of confinement reinforcement was specified when the tensile yield strength of HPFRCC was larger than 1.5 MPa. Reduction in shear reinforcement reduces costs related to material usage and labor (due to less detailing work and prevention of congestion during concrete pouring). Therefore, clear guidance on the amount of confinement reinforcement remains to be addressed with further testing and analytical work.

JSCE regulations address several regulatory requirements with regards to design and construction with HPFRCC; however, there are still several research needs before the recommendations become fully fledged. First of all, the recommendations were based on limited experimental data, and further testing is required. Issues that require further research are: (i) design of critical regions with HPFRC (with respect to bond strength, anchorage lengths and specific guidance on shear reinforcement reduction); and (ii) standard seismic design parameters such as equivalent stiffness and damping (at different limit states) for displacement-based design; response modification, displacement amplification, and force reduction factors for force-based design (see Section 4.4 for more details).

4.2. VALIDATION OF THE ECC CONSTITUTIVE MODEL AT THE STRUCTURAL LEVEL

In this section the ECC constitutive model developed in Chapter 2 is validated at the structural level (component and system) using data from the experimental program presented in Chapter 3. The material level validation was provided in Section 2.3, and Section 4.2 completes the validation of the constitutive model at three levels: material, component and system.

As described in Section 2.4, the ECC constitutive model is implemented into ZEUS NL (Elnashai et al., 2010) to enable structural scale simulations. Below, the validation of the model at the component and system levels is provided using this numerical tool.

4.2.1. Component Level Validation

The cross-sectional dimensions and reinforcement detailing of the small-scale columns modeled here are shown in Figure 3.18. The columns are 381 mm (15 inches) high. Two different configurations with 0.87 and 1.29 percent longitudinal reinforcement are considered.

As reported in Section 3.2.2, four different ECC mixtures are tested as a part of the experimental program. Material-level data for the mechanical properties of these mixtures are not sensitive enough to allow for reliable structural modeling of each mixture separately. Therefore, based on the information provided in Section 3.2.2, a generic ECC mixture, for which the envelope curves are shown in Figure 4.2, is used to validate the ECC constitutive model. The properties of reinforcing bars are determined based on the stress-strain response of the material obtained from uniaxial testing as shown in Figure 3.15(a). The Ramberg-Osgood (1943) model is selected in ZEUS NL to simulate the behavior of steel as shown in Figure 4.3. The backbone curve for the Ramberg-Osgood model is given by

$$\varepsilon = \frac{\sigma}{E} + a_{RS}\left(\frac{\sigma}{b_{RS}}\right)^{n_{RS}} \tag{4.1}$$

where E is the initial tangent modulus, σ is the stress on the backbone curve, and a_{RS}, b_{RS} and n_{RS} are material constants that are usually determined by a best-fit to experimental data. The parameters of the Ramberg-Osgood model for steel is obtained from curve fitting to experimental data and given in Figure 4.3.

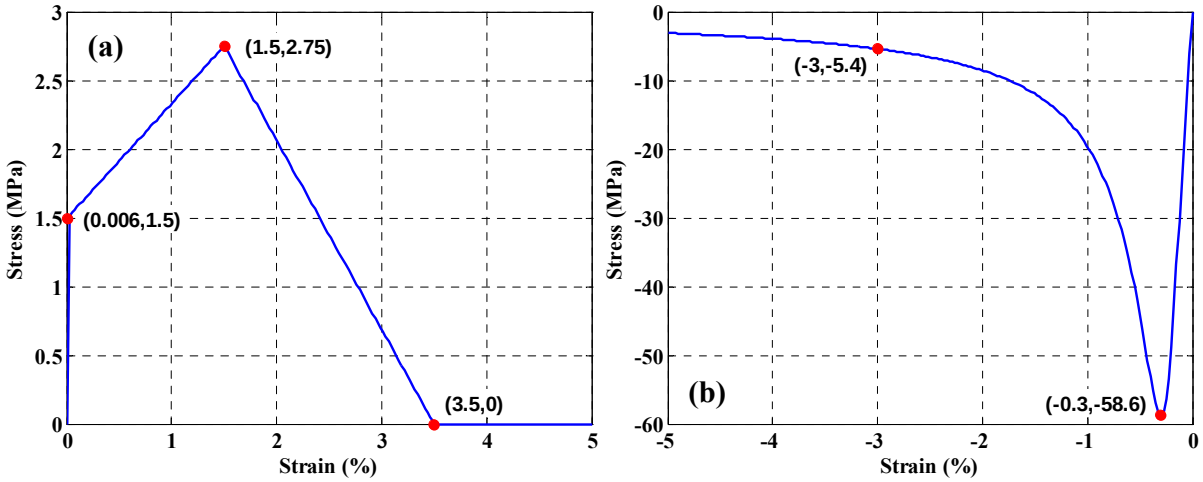

Figure 4.2. ECC envelope curves in (a) tension and (b) compression

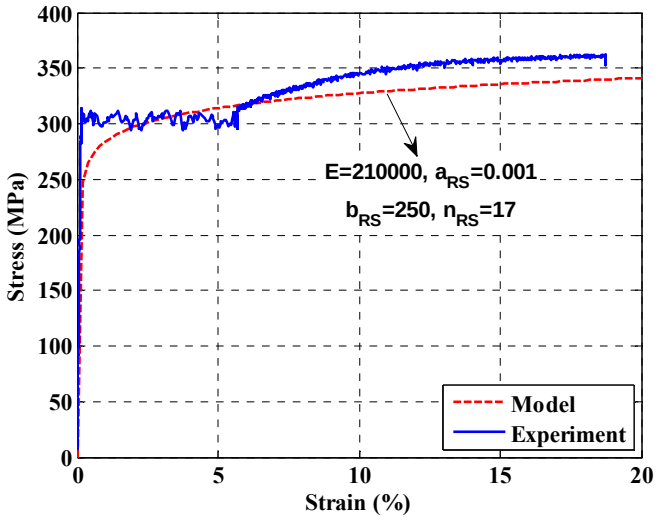

Figure 4.3. Steel models used in simulation of ECC structural members

The results from cyclic tests are compared against the ZEUS NL simulation in Figure 4.4(a, b). The plots on the left show the case with 0.87 percent longitudinal reinforcement while the ones on the right pertain to the case with 1.29 percent longitudinal reinforcement. In both cases an axial compressive load equal to 7.5 percent of the axial column capacity is applied to simulate the loading during experiments. It is observed that the ECC constitutive model captures with

reasonable accuracy the various features from the tests such as maximum strength, stiffness and strength degradation, and pinching. A shortcoming of the model in predicting the initial stiffness of the specimens is seen; however, this shortcoming is attributed reasons including the micro-cracks in the specimens that reduce the initial stiffness and assumption of perfect boundary conditions in finite element model.

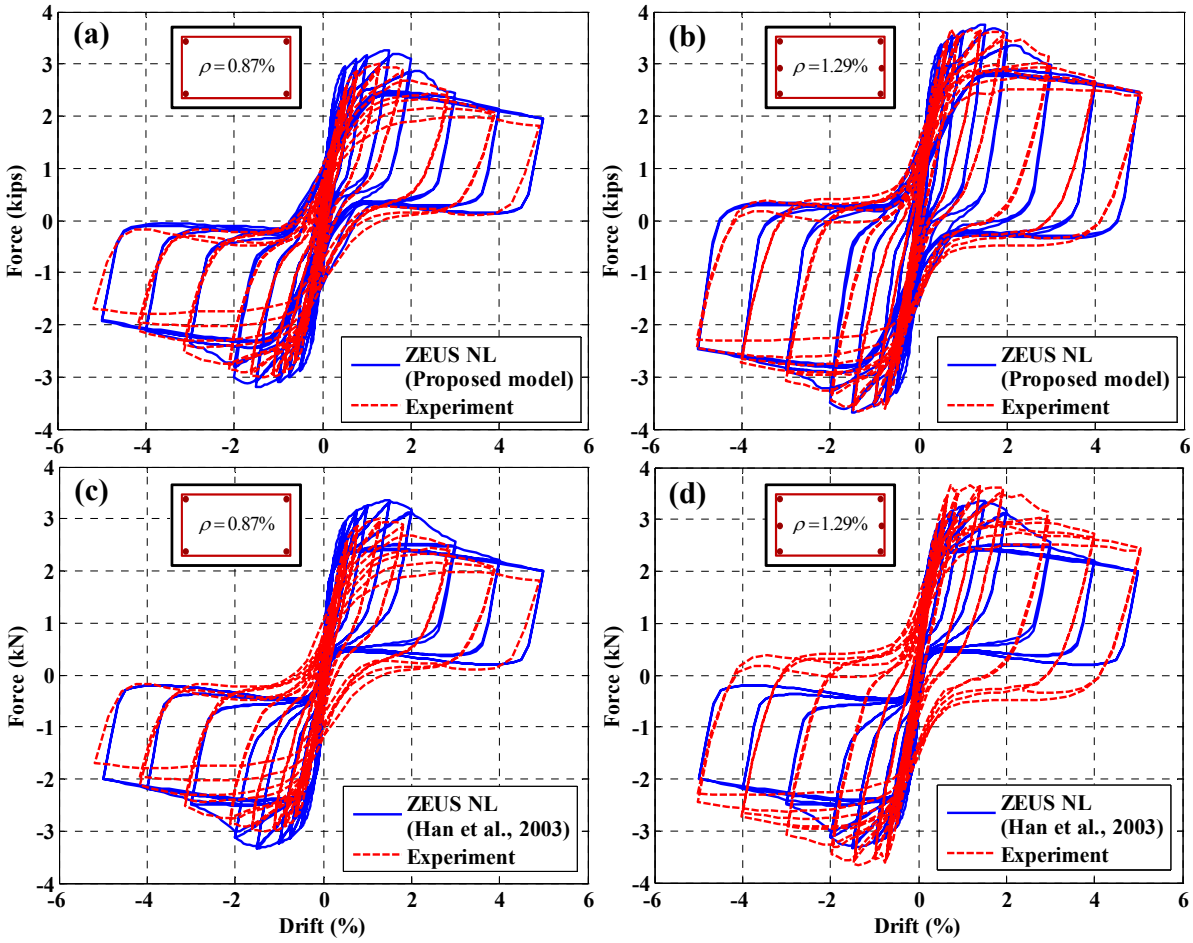

Figure 4.4. Comparison of experimental data with model simulation under cyclic loading, (a, b) proposed (c, d) original model by Han et al. (2003); (a, c) 0.87 percent (b, d) 1.29 percent longitudinal reinforcement

It is also important to assess the performance of the original model proposed by Han et al. (2003) using the same analysis tool and the same experimental data in order to see the improvements in accuracy achieved with the proposed model resulting from the features added to the original model. For this purpose, the original model is also implemented into the same analysis software, ZEUS NL, and the response of ECC columns is simulated. The results are compared in Figure 4.4(c, d). When compared to the results from the proposed model, the original model shows significant pinching resulting from the fact that the Han et al. (2003) constitutive relationship always passes through the origin. This feature has been improved in the proposed model by using a plastic strain model for ECC and transition curves from tension to

compression and vice versa as described in Sections 2.2.3 and 2.2.5. It is also observed that the proposed model more closely predicts the lateral strength of the columns for both configurations with different reinforcement ratios.

In order to illustrate the match between experimental results and numerical simulation for the proposed model, the envelope curve obtained from the cyclic tests and the secant stiffness (at peak drifts of each cycle) are plotted in Figure 4.5 and Figure 4.6 as a function of drift for the specimen with 0.87 and 1.29 percent longitudinal reinforcement, respectively. Note that the distinction between the proposed and original model in the legend of Figure 4.4 is dropped for figures from this point onwards, and all the comparisons relate to the proposed model. It is seen that the model is capable of predicting the peak force and strength and stiffness degradation with acceptable accuracy, notwithstanding the difference in initial stiffness.

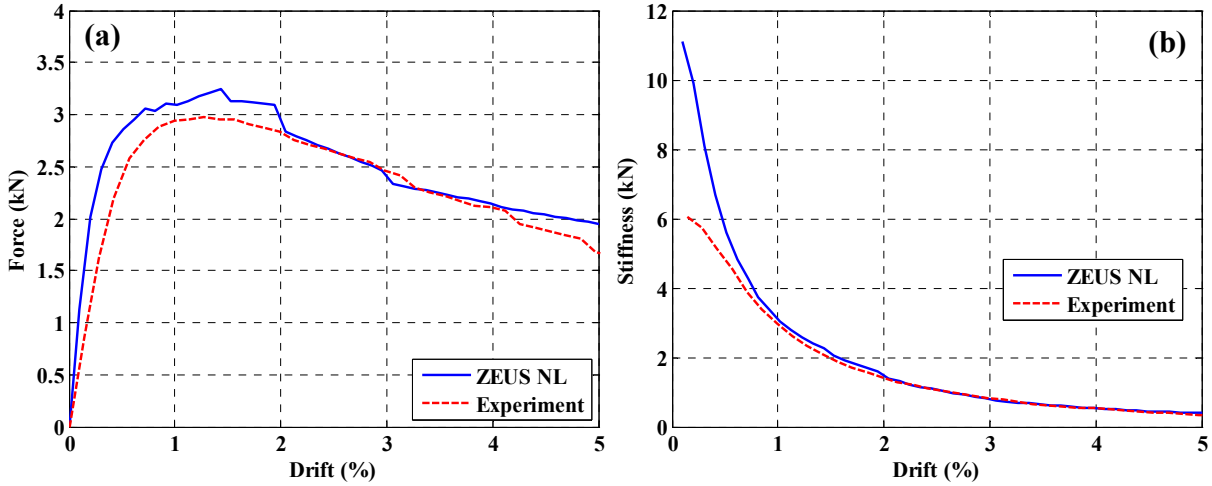

Figure 4.5. Comparison of (a) envelope curves (b) stiffness degradation for the case with 0.87 percent longitudinal reinforcement

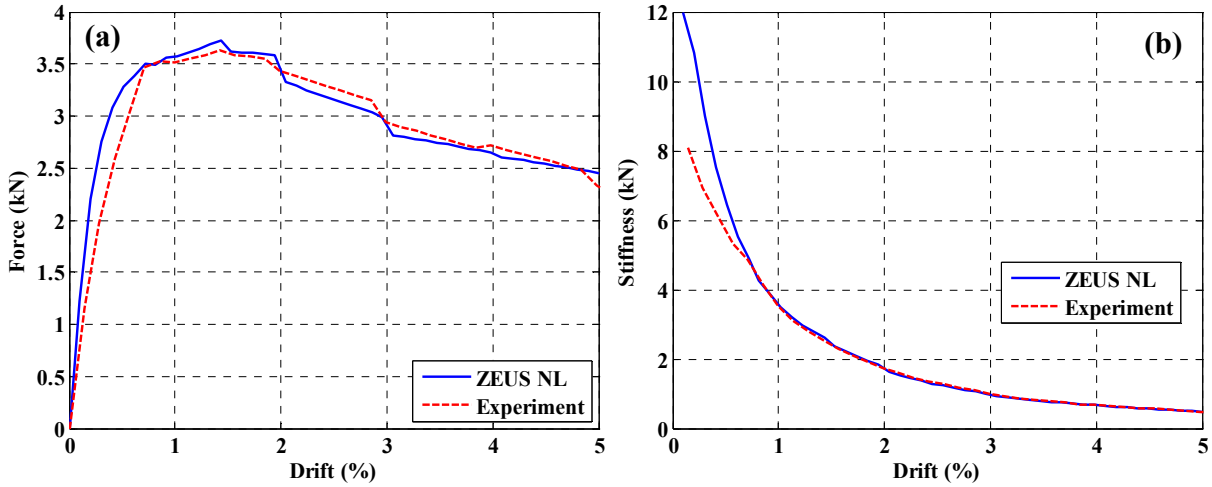

Figure 4.6. Comparison of (a) envelope curves and (b) stiffness degradation for the case with 1.29 percent longitudinal reinforcement

4.2.2. System Level Validation

System level validation of the ECC constitutive model is performed using the data from static time history (STH) tests and hybrid simulation. As described in more detail in Section 3.6.3, in STH, the deformations (translations and rotations), as well as the axial force applied to the columns are determined from inelastic dynamic analysis under a selected ground motion. In hybrid simulation, the frame is subjected to the same earthquake excitation; however, the experimental module (left-exterior first story column) is tested in the lab and the rest of the frame is simulated numerically in ZEUS NL. System behavior is investigated in both cases, since the entire structure is modeled.

As shown in Table 3.8, four different cases are considered for STH tests and hybrid simulation. For comparison purposes here, the results from hybrid simulation and STH tests are used, respectively, for case 2, and cases 3 and 4. Comparisons for case 1 are not provided since the structural frame is made from RC, and the ECC constitutive model is not utilized in modeling. The measured lateral force and moment in the experiment are compared against the ZEUS NL simulation in time domain and versus the relevant deformation in Figure 4.7 through Figure 4.12. Very good correlations are obtained between the experiment and numerical analysis. The difference between the experimental data and simulation results in terms of peak forces and peak moments is calculated to be always within 20 percent. A larger discrepancy is observed at the initial stages of loading. This discrepancy is due to deficiency of the numerical model in predicting the initial stiffness of the specimens, as mentioned earlier. The columns are subjected to the most realistic representation of a typical earthquake-induced loading that can be achieved in a static planar test. The ensuing response of the column is affected by several factors such as the variation in axial load [column is even subjected to tension in certain cases as seen in Figure 3.47(b)] and the fixity (rotation changes with time). Therefore, the response is very difficult to predict. Taking these into account, the ZEUS NL simulation is considered as an accurate prediction of actual behavior.

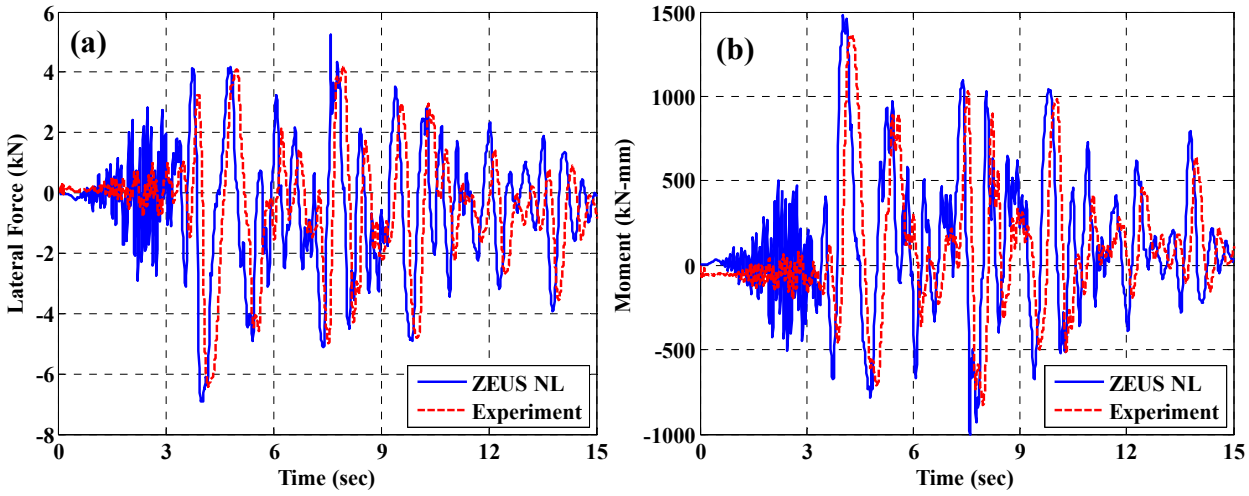

Figure 4.7. Simulation vs. experiment for case 2 (a) lateral force and (b) moment histories

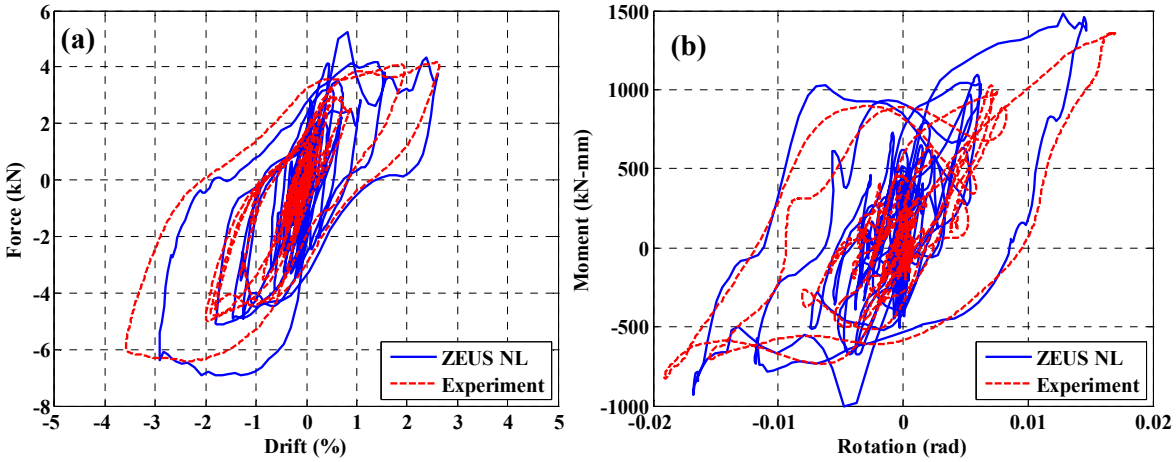

Figure 4.8. Simulation vs. experiment for case 2, (a) lateral force vs. drift, and (b) moment vs. rotation

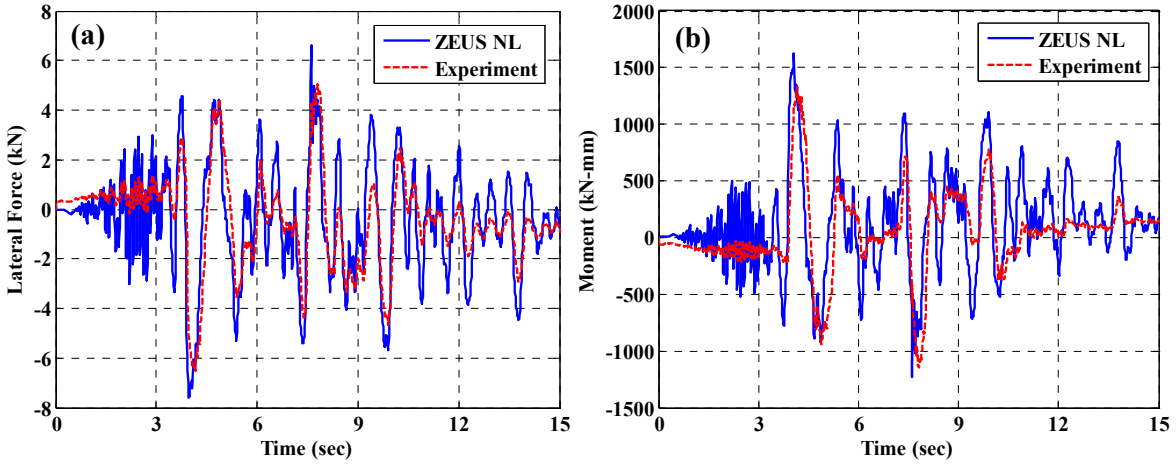

Figure 4.9. Simulation vs. experiment for case 3, (a) lateral force, and (b) moment histories

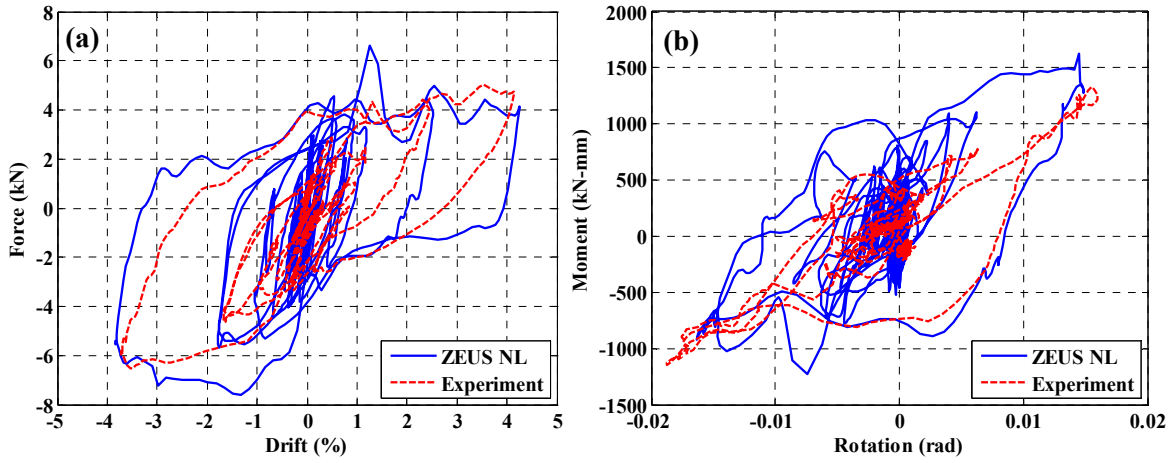

Figure 4.10. Simulation vs. experiment for case 3, (a) lateral force vs. drift, and (b) moment vs. rotation

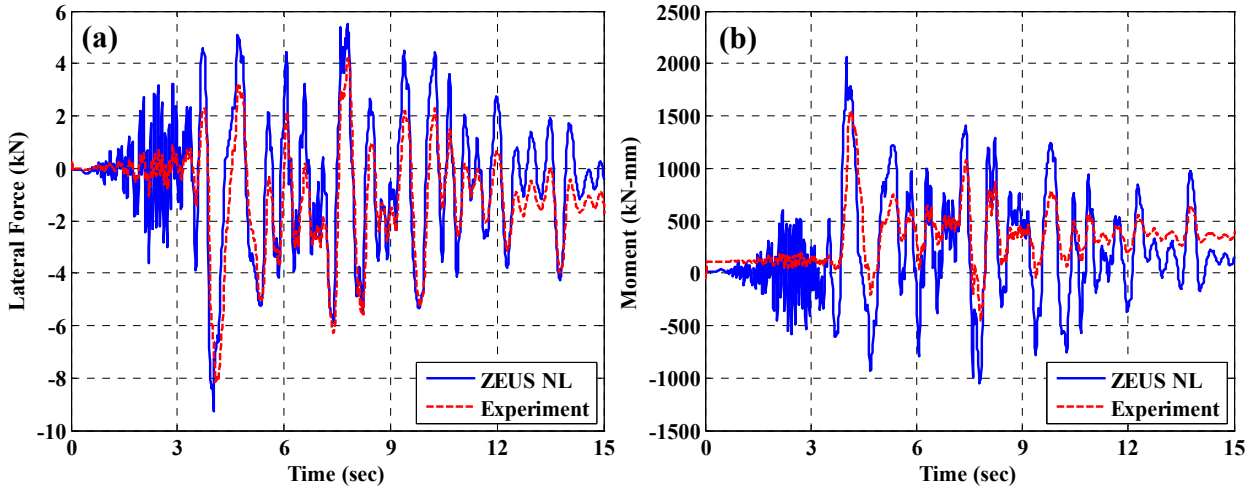

Figure 4.11. Simulation vs. experiment for case 4, (a) lateral force, and (b) moment histories

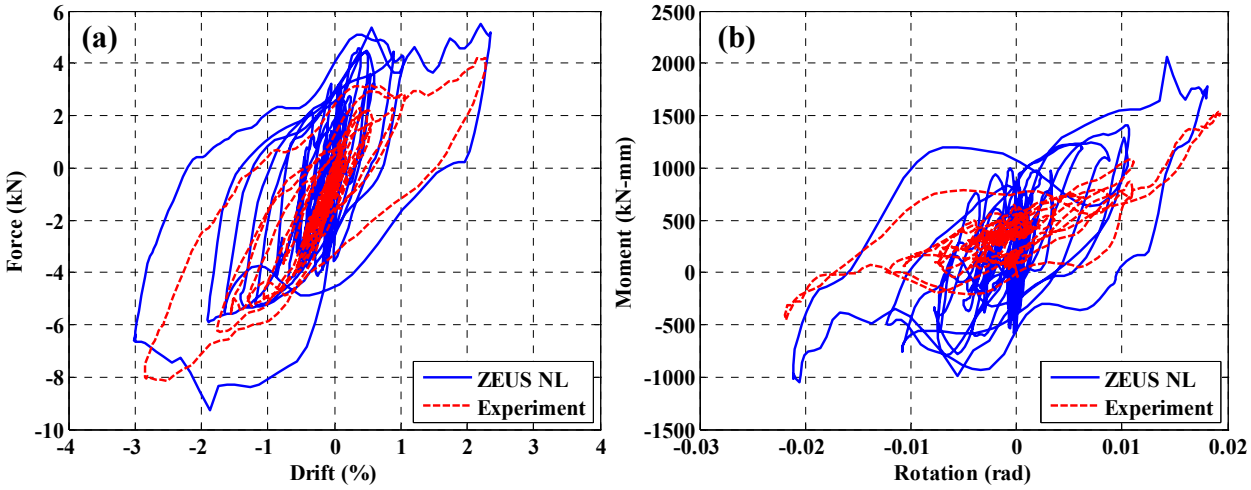

Figure 4.12. Simulation vs. experiment for case 4, (a) lateral force vs. drift, and (b) moment vs. rotation

4.3. PARAMETRIC ANALYSIS OF ECC COLUMNS

The most important features of ECC are its high strength and ductility capacities in tension. These features might greatly affect the response of structural members because the entire cross-section of the ECC member is capable of resisting applied tensile actions even in the cracked state. As shown in Figure 4.2(a), the material undergoes strain hardening after cracking and does not immediately lose its resistance as in the case of concrete. Testing of ECC at the stress-strain level demonstrated that the tensile properties of the material might vary to a significant extent depending on several factors, particularly, the type of fibers, mixture constituents, and shape of test specimens (Kesner and Billington, 2004; Lepech, 2006; Yang et al., 2007; amongst others). Therefore, it is worthwhile to investigate the effect of ECC tensile properties on the response of structural components through a parametric study.

The dimensions and reinforcement detailing of the ECC column investigated here are shown in Figure 4.13 alongside the loading protocol for the simulations. The aspect ratio is chosen to be relatively high so that the failure of the columns is governed by flexural deformations, which is consistent with modern seismic design practice. The loading protocol used for this parametric study is the same as the one used in the cyclic tests in the experimental program described in Chapter 3. Three variables are chosen for the parametric study: the level of axial load (2.5, 5 and 7.5 percent of the axial column strength), reinforcement ratio (0.75, 1.0 and 1.25 percent), and ECC properties in tension.

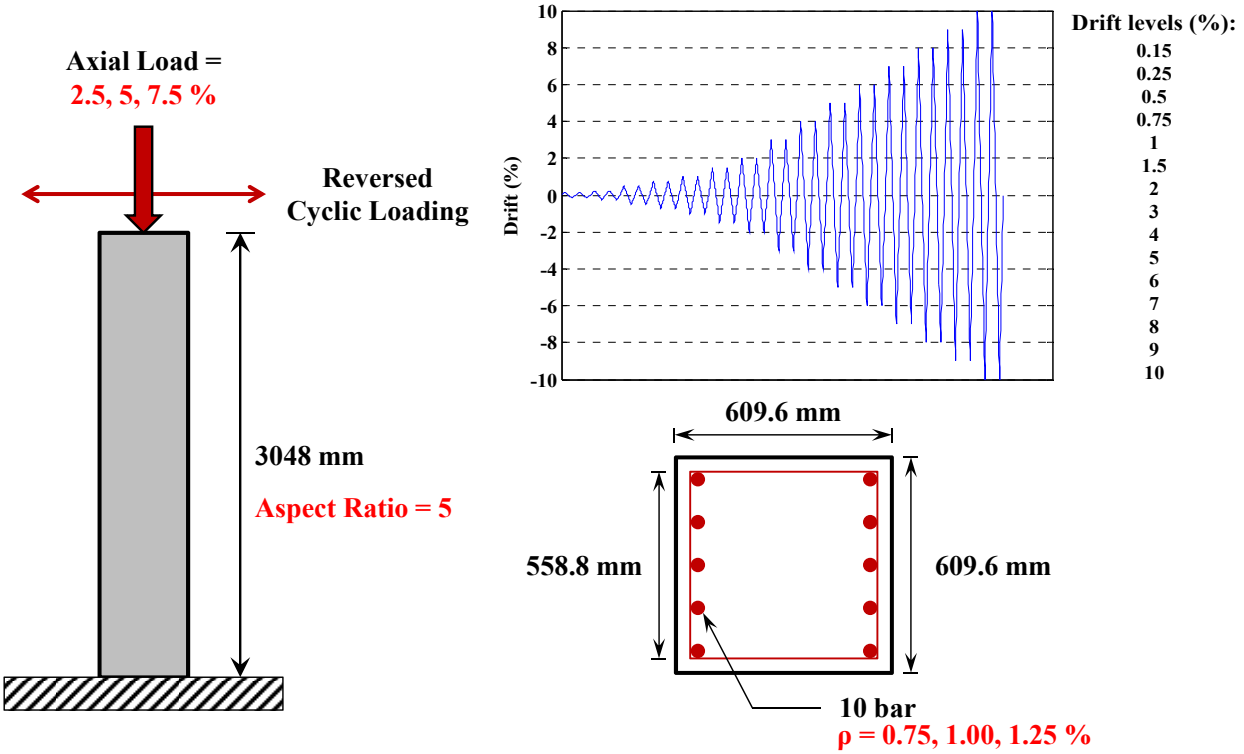

Figure 4.13. Details of the ECC specimen, and loading regime for the parametric study

Three different levels of axial loading represent columns from three frames with different height-to-width ratios. A higher level of axial load corresponds to a more slender structure where the column loads are higher due to increased overturning under lateral loads. The considered reinforcement ratios are deliberately chosen to be lower than that commonly observed in buildings so that the column response is dominated by the tensile contribution of ECC. The considered ECC mixtures with different tensile properties are plotted in Figure 4.14(a). To capitalize on the effect of ECC tensile properties, the stress-strain responses of different mixtures in compression are assumed to be the same, as shown in Figure 4.14(b). Nine different mixtures with different strength, σ, and ductility, μ, are considered (see Table 4.1 for material properties). The mixtures are labeled as low σ – low μ, low σ – intermediate μ, and so on. The ECC tensile properties are based on actual material response observed in several studies (Kesner and Billington, 2004; Lepech, 2006; Yang et al., 2007; amongst others).

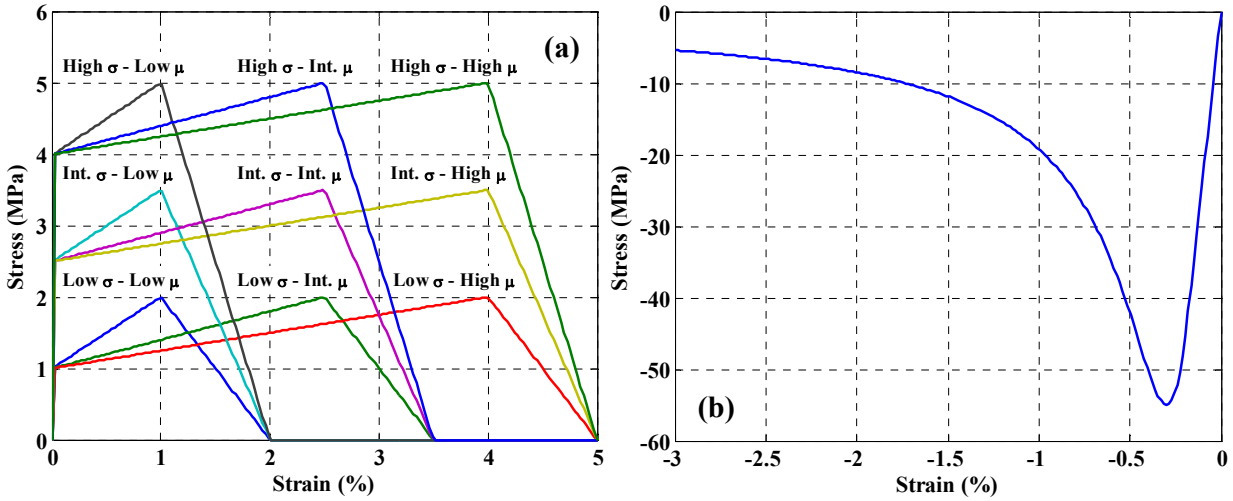

Figure 4.14. (a) Tensile properties of the considered ECC mixtures – σ and μ designate material strength and ductility respectively, and (b) stress-strain response in compression – assumed to be the same for all mixtures

Table 4.1. Properties of considered ECC mixtures (see Table 2.2 for parameter definitions)

	E	ε_{t0}	ε_{tp}	σ_{tp}	ε_{tu}	ε_{cp}	σ_{cp}	ε_{cu}	σ_{cr}
Low σ - Low μ	25000	4.00E-05	0.01	2	0.02	-0.003	-55	-0.1	-1.5
Low σ - Int. μ	25000	4.00E-05	0.025	2	0.035	-0.003	-55	-0.1	-1.5
Low σ - Hihg μ	25000	4.00E-05	0.04	2	0.05	-0.003	-55	-0.1	-1.5
Int. σ - Low μ	25000	0.0001	0.01	3.5	0.02	-0.003	-55	-0.1	-1.5
Int. σ - Int. μ	25000	0.0001	0.025	3.5	0.035	-0.003	-55	-0.1	-1.5
Int. σ - Hihg μ	25000	0.0001	0.04	3.5	0.05	-0.003	-55	-0.1	-1.5
High σ - Low μ	25000	0.00016	0.01	5	0.02	-0.003	-55	-0.1	-1.5
High σ - Int. μ	25000	0.00016	0.025	5	0.035	-0.003	-55	-0.1	-1.5
High σ - Hihg μ	25000	0.00016	0.04	5	0.05	-0.003	-55	-0.1	-1.5

Four response metrics at the member level are evaluated for each of the 81 combinations (three axial load levels x three reinforcement ratios x nine ECC mixtures): initial stiffness, peak lateral force resistance (or strength), ductility, and energy absorption capacity up to failure. The same definitions for yield, maximum, and ultimate (10 percent reduction) points, based on Park (1988), are used, see Section 3.8.2 and Figure 3.35(b). The envelope curves are obtained for each of the 81 cases, and the yield, maximum and the ultimate points are found. The initial stiffness of the specimens is defined as the ratio of the force corresponding to 20 percent of the peak lateral force resistance to the drift at this point. The peak lateral force resistance is defined as the lateral strength of the specimen. Member ductility is defined as the ratio of the drift at the ultimate point to that at yield. Finally, the energy absorption capacity up to failure is defined as the sum of areas within complete cycles up to the attainment of the ultimate drift.

The results from the parametric study are summarized in Figure 4.15. The bars are organized into groups of nine (nine different ECC mixtures) for each of the axial load level – reinforcement

ratio combination. In Figure 4.15, axial load and reinforcement ratio are denoted with F and ρ respectively. Low, intermediate and high F are 2.5, 5 and 7.5 percent of the column axial capacity, respectively. Similarly, low, intermediate and high ρ are equal to 0.75, 1.0 and 1.25 percent. Each group is subdivided into groups of three depending on the material strength, which is designated with L, I and H for low, intermediate, and high (on the horizontal axis) respectively. Finally, the three bars (in each subgroup of three) that are shown differently stand for a different material ductility (as indicated in the figure legend). The results are normalized by dividing each value by that of the column with low σ – low μ material in the low F – low ρ group. The results are interpreted below for each of the member level response metrics: stiffness, strength, ductility and energy absorption capacity.

It is seen that material ductility has almost no effect on the initial stiffness of the member. However, an increase in material strength causes an increase in stiffness that varies from 43 percent for the low F – low ρ group to seven percent for the high F – high ρ group. The change in material strength has a more pronounced effect on member stiffness, especially for members with a lower reinforcement ratio.

It is also observed that material ductility has a very limited effect on member strength. However, similar to the case of stiffness, member strength increases with increasing material strength. The increase in member strength with increasing material strength ranges from 53 percent in the case of low F – low ρ to 28 percent in the case of high F – high ρ. The change in material strength has a similar effect on member strength more or less independent of F and ρ.

Material ductility has a major impact on the member ductility. It is observed that the increase in member ductility can be as high 120 percent due to an increase in material ductility. Despite exceptions, the general trend is that member ductility is reduced with increasing material strength. This reduction is mainly due to a sharper decrease in the load carrying capacity once the peak load is reached, resulting in an ultimate point with a lower drift value. One subtle feature is that an intermediate level of F is beneficial for member ductility. This level of axial force helps a greater portion of the member remain in compression, which contributes to the load carrying capacity without major degradation. The levels of ρ considered here do not significantly affect member ductility.

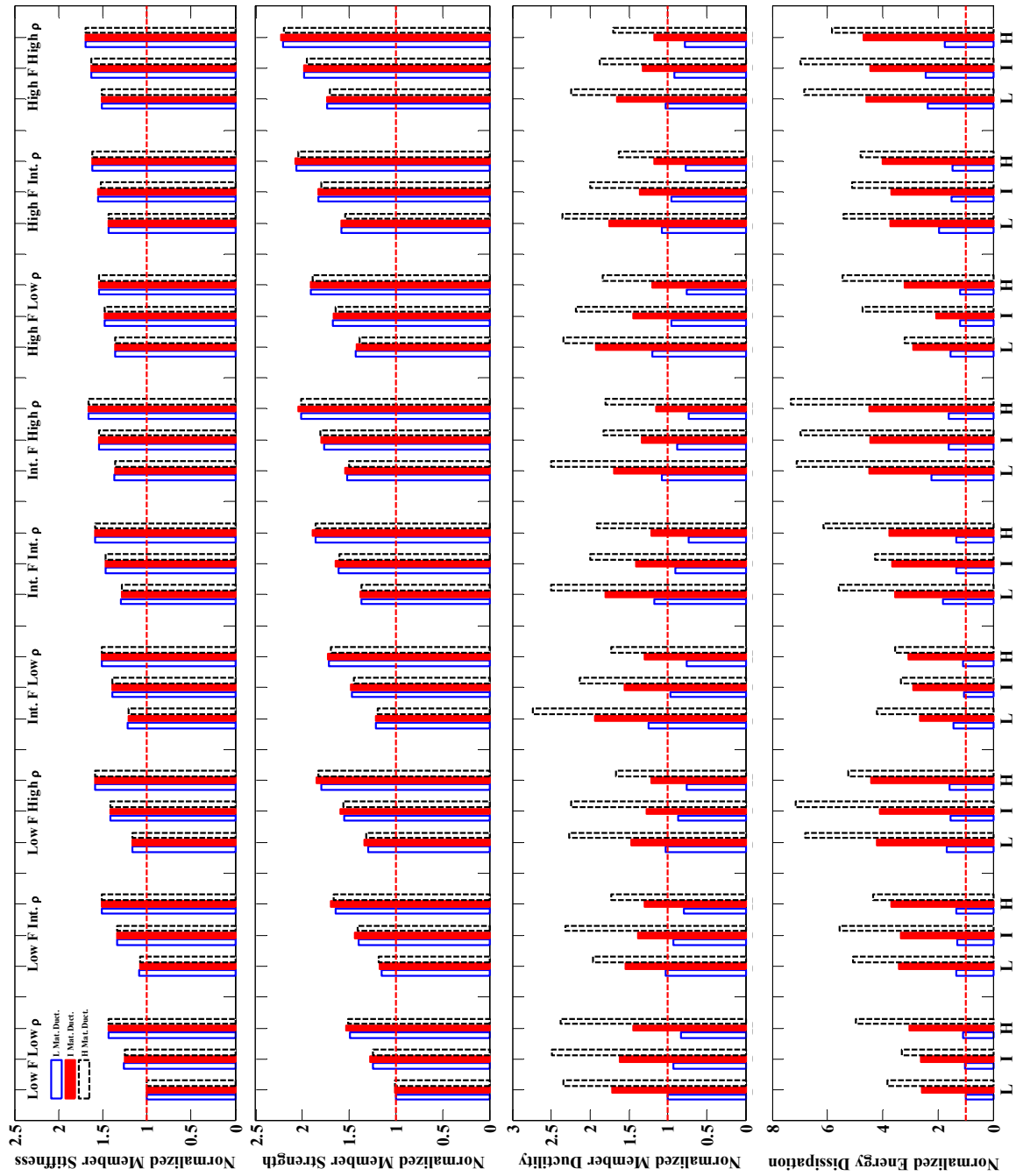

Figure 4.15. Comparison of response metrics: stiffness, strength, ductility and energy absorption

It is seen that the material ductility has the greatest impact on the energy absorption capacity of the member. Increasing in material ductility can cause an increase of as high as 435 percent in the energy absorption capacity of the member. The reason for this observation is easily understood if the cyclic responses of members (in the high F – high ρ group) with low and high ductility are compared (see Figure 4.16). The significant increase in energy absorption capacity results not only from the more stable hysteretic loops but also from an increase in the drift corresponding to the ultimate point. As mentioned earlier, the energy absorption capacity is calculated up to the drift level corresponding to the member failure (ultimate point). It is difficult to observe a general trend between the material strength and the energy absorption capacity of the member; however, it is seen that the latter increases with increasing ρ.

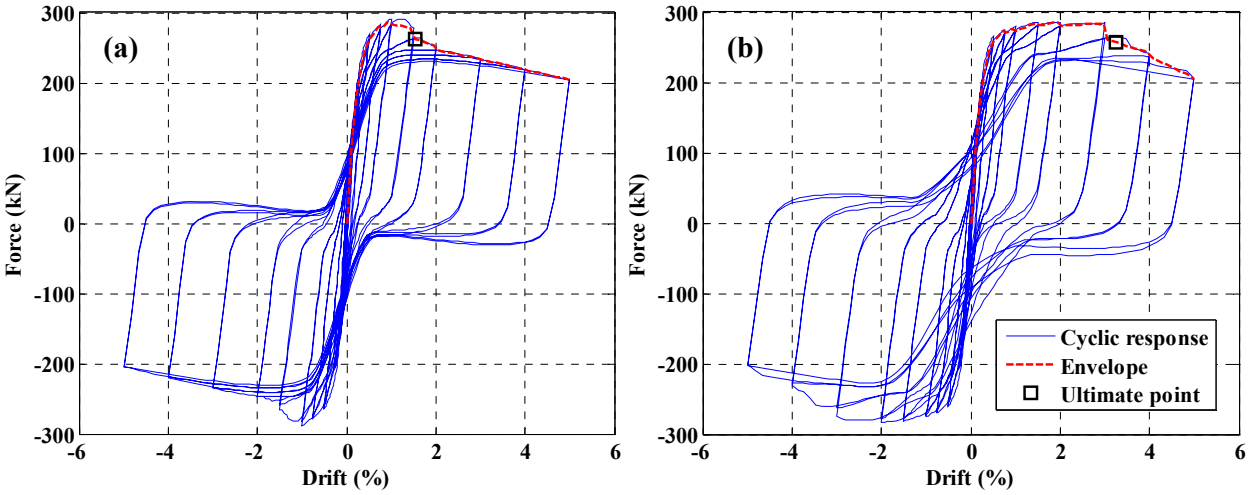

Figure 4.16. Comparison of the responses of members in the high F – high ρ group (a) low σ – low μ, and (b) low σ – high μ

It is not possible to investigate all possible combinations of the parameters contributing to the member response; however, the parametric study conducted here provides a good understanding of the impact of material- and section-level parameters on the response of columns with a focus on ECC tensile properties.

4.4. RECOMMENDED RESEARCH ON DEVELOPMENT OF SEISMIC DESIGN GUIDELINES FOR ECC STRUCTURES

ECC has various advantages over conventional concrete in terms of improved mechanical performance (see Chapters 2 and 3), seismic sustainability and LCC (see Chapters 4 and 5). As reviewed in detail in Section 4.1.4, JSCE published the first and only recommendations for design with ECC and other cementitious materials classified under HPFRCC (JSCE, 2008). Various aspects of structural design are covered; however, very limited guidance is provided regarding the seismic design of structures. The use of ECC and other HPFRCC is increasing rapidly, and due to improved damage tolerance and energy absorption capacities of the material, most of these applications are aimed at improving the seismic performance of structures.

Therefore, there is a need for derivation of the most commonly used seismic parameters for ECC structures so that ECC is more confidently used, and the applications become more prevalent. Table 4.2 lists the most commonly used parameters for the seismic design of buildings both for force- and displacement-based approaches. The derivation of these parameters is a recommended future work that is deemed critical by this study.

Table 4.2. Most commonly used parameters for seismic design of buildings

Design Parameter	Design Method
Force reduction factor Displacement amplification factor Curvature ductility Displacement ductility Overstrength factor Plastic hinge length	Force-Based Design
Displacement reduction factor Equivalent stiffness Equivalent damping Floor acceleration Residual crack width Permanent displacement	Deformation-Based Design

4.5. CONCLUSIONS

Structural level simulation is conducted in Chapter 4 using the numerical tool developed in Chapter 2, first to validate the proposed constitutive model for ECC and then to complement the existing data from the experimental program presented in Chapter 3.

Experimental data from cyclic, STH tests and hybrid simulation conducted on ECC columns (the latter two more realistically represent the loading and boundary conditions that would be produced by an earthquake) are utilized in the validation of the model at the component and system levels. The response of ECC columns in the experimental study is simulated, and it is observed that the model captures the behavior of the material at the structural level equally well as it does at the material level (see Section 2.3). It is seen that the numerical tool gives close predictions of the experimental behavior under realistic loading and boundary conditions.

The sensitivity of the structural level response metrics, stiffness, strength, ductility and energy absorption capacity to ECC tensile strength and ductility is investigated through parametric analysis of ECC columns. It is observed that the material properties have a major effect on member strength, ductility and energy absorption capacity while member stiffness is relatively insensitive. Member strength, ductility and energy absorption capacity increase more than 50, 100 and 400 percent with increasing material strength, ductility, and ductility respectively. The material properties considered in the parametric study are not hypothetical but based on the stress-strain level testing of the material, and although the numbers are specific to

the member configuration considered here, the parametric study provides a good understanding of what can be achieved in terms of performance enhancement at the structural level by changing the tensile properties of the material, in this case ECC.

The numerical tool developed in Chapter 2, being extensively validated at the material, component and system levels, is proposed as an accurate tool for structural-level simulation under monotonic, cyclic and earthquake loading. The material model and the structural level analysis tool are available in an open-source environment for use by the structural earthquake engineering community (http://code.google.com/p/zeus-nl/).

Finally, the need for derivation of seismic design parameters for ECC structures is highlighted. The relevant literature is reviewed in Section 4.1, and derivation of seismic design parameters is recommended as future work to increase the use of ECC and thereby to improve the safety, economy and sustainability of seismic design for buildings.

5

LIFE-CYCLE COST OPTIMIZATION

"Inventing is the mixing of brains and materials. The more brains you use, the less materials you need."

Charles F. Kettering

In Chapter 5, life-cycle cost (LCC) optimization of structures is discussed with the goal of addressing the economy and sustainability objectives of the seismic design framework described in Chapter 1. Performance-based earthquake engineering (PBEE) methodology is followed considering multiple levels of earthquake hazard (also a requirement of LCC analysis) and multiple levels of performance objectives. The background information provides a detailed description and review of studies on seismic hazard assessment, selection and scaling of ground motions, PBEE, and optimization in structural design. Studies on testing multi-material structural components [concrete and engineered cementitious composites (ECC)] are also reviewed since they are related to the LCC optimization problem. Following the background section is a derivation of seismic hazard for a selected site in San Francisco, CA, and the selection and scaling of proper earthquake time histories for inelastic dynamic analysis. A framework for LCC optimization of reinforced concrete (RC) structures is proposed, and the methodology is applied to two-story two-bay structural frames. The use of ECC for the optimal seismic design of structures is discussed in the application example.

5.1. BACKGROUND

Section 5.1 starts with a description of the terminology followed in this chapter. Different approaches to characterizing seismic hazards are first described. The procedure to determine the uniform hazard spectrum/spectra (UHS) for representing different levels of hazard intensity is then explained, and previous studies on selection and scaling of earthquake ground motions are reviewed. Second, the evolution of the performance-based seismic design (PBSD) concept is provided and key documents in the process of including PBSD approaches in design codes are reviewed. The needs for research to fully utilize these concepts are outlined. A detailed review of previous studies on structural optimization is then provided. These studies are reviewed

chronologically and in the order from least to most relevant to the present study. Finally, a review of literature on testing multi-material (concrete and ECC) structural members is given.

5.1.1. Terminology

Objective (merit) function: A function that measures the performance of a design. For every possible design, the objective function takes a different value. Examples include the maximum interstory drift and initial cost.

Design (decision) variables: A vector that specifies design. Each element in the vector describes a different structural property that is relevant to the optimization problem. The design variables take different values throughout the optimization process. Examples include section dimensions and reinforcement ratios.

Performance levels (objectives or metrics): Predefined levels that describe the performance of the structure after an earthquake. Usually the following terminology is used to define the damage (limit) state (or performance) of the structure: immediate occupancy (IO), life safety (LS) and collapse prevention (CP). Occurrence of each damage state is determined based on the exceedance of a threshold value in terms of structural capacity.

Hazard levels: Predefined levels used to describe the earthquake intensity that the structure might be subjected to. Hazard levels are usually described by earthquake return periods (or annual frequency of exceedance) and represented by acceleration response spectrum. It is required to consider multiple levels of hazard to calculate the LCC of a structure. Each hazard level is usually mapped to a single or multiple performance levels.

Space of design (decision) variables or search space: The boundaries of the search space are defined by the range of design variables. The dimension of the search space is equal to the number of design variables in the problem. The search space could be continuous for continuous design variables or discrete for discrete design variables, or certain dimensions could be continuous and the rest could be discrete.

Solution (objective function) space: Usually the solution space is unbounded or semi-bounded. The dimension of the solution space is equal to the number of objective functions in the optimization problem. The optimal solution(s) is defined in the solution space. The set of optimal solutions in the solution space is referred to as a Pareto-front or Pareto-optimal set, as described below.

Pareto-optimality: To define Pareto-optimality, consider the function $f : \Re^k \rightarrow \Re^l$ which assigns each point, $\boldsymbol{x}$ in the space of decision variables to a point, $\boldsymbol{y} = f(\boldsymbol{x})$ in the solution space. Here f represents the objective functions, k is the number of decision variables, and l is the number of objective functions to assess the performance of each $\boldsymbol{x}$ (or equal to the dimension of f). The Pareto-optimal set of solutions is constructed by comparing the points in the solution space based on the following definition: a point $\boldsymbol{y}$ in the solution space strictly dominates another point $\bar{\boldsymbol{y}}$ if each element of $\boldsymbol{y}$ is less than or equal to the corresponding parameter of $\bar{\boldsymbol{y}}$ (that is, $y_{\boldsymbol{i}} \leq \bar{y}_i$) and at least one element, i^* is strictly less (that is, $y_{i^*} < \bar{y}_{i^*}$), assuming that this is a minimization problem. Thus, the Pareto-front is the subset of points in the set of $\boldsymbol{Y} = f(\boldsymbol{X})$, that

are not strictly dominated by another point in $\boldsymbol{Y}$. Pareto-optimality is illustrated in Figure 5.1: the plot is in the solution space, and the figure axes are two objective functions, f_1 and f_2. Assuming that the objective is minimization of both f_1 and f_2 the Pareto-front lies at the boundary that minimizes both objectives as shown in the figure.

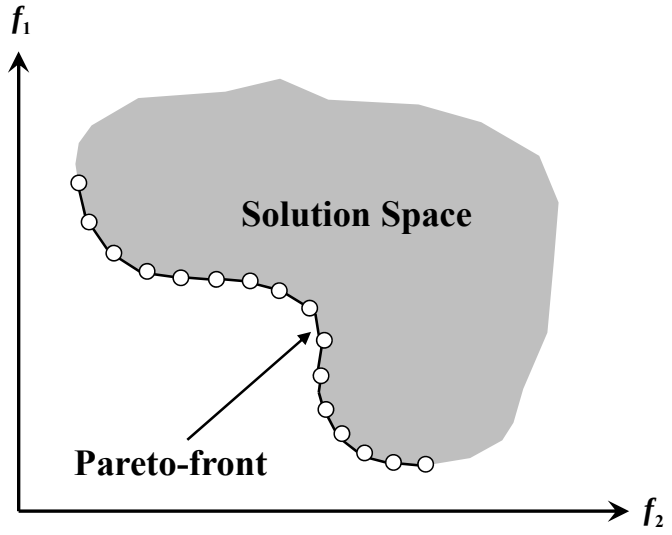

Figure 5.1. Illustration of Pareto-optimality

5.1.2. Seismic Hazard Assessment and Development of Uniform Hazard Spectra

Two approaches, deterministic and probabilistic seismic hazard assessment (DSHA and PSHA), are mostly used for seismic hazard assessment at a given site. The main difference between the two approaches is that PSHA incorporates the element of time in hazard assessment. The steps leading to a DSHA can be summarized as follows (Kramer, 1996): (1) characterize all potential earthquake sources that might affect the site and determine the maximum event that each source could produce; (2) select an appropriate relationship to determine the ground motion parameters at the site for each source; (3) find the maximum ground motion parameter at the site and identify the corresponding source; and (4) develop/select response spectrum or ground motions to represent the earthquake excitation.

For PSHA the first two steps are the same as those in DSHA, while steps three and four become: (3) for each earthquake source determine the frequency of earthquake occurrence based on existing information; and (4) to quantify the ground motion parameters, combine all sources taking into account their relative contribution and calculate the probability of exceedance of spectral ordinates or ground motion parameters for a selected time interval. PSHA is attributed to Cornell (1968), and since then a considerable amount of research has been devoted to this subject (e.g. McGuire, 1995; Abrahamson, 2000; Steidl, 2000). There is a strong opposition to PSHA by some researchers because of the way uncertainty is treated and earthquake frequencies for long return periods are calculated (Castaños and Lomnitz, 2002; Krinitzsky, 2002; Paul, 2002). A more reasonable approach is expressed as using both methods to complement each other (McGuire, 2001; Bommer, 2002, 2003). It is beyond the scope of this study to assess and

validate the two approaches for seismic hazard analysis; however, PSHA has well made its way in seismic design codes: UBC (ICBO, 1997) and FEMA 450 (FEMA, 2003b) represent a design response spectrum based on probabilistic zonation maps. Therefore, in this study UHS is used to characterize the seismic hazard for a selected site (see Section 5.2.1).

Several parameters were defined in literature to characterize the intensity of earthquake ground motions. Ground motion intensity may be described using one or more of the three characteristics: amplitude, frequency content and duration. The most commonly used parameters to describe (1) amplitude, (2) frequency content, and (3) duration are: (1) PGA, PGV, and PGD, (2) predominant period, power spectrum intensity, and Housner spectrum intensity, and (3) duration, and Arias Intensity, respectively. It should be noted that power spectrum and Arias intensities are related to all three characteristics while Housner spectrum intensity is related to both amplitude and frequency.

Response spectral representation of seismic hazard is accepted by most current seismic design codes (ICBO, 1997; CEN, 2004). Acceleration, velocity and displacement response spectra are developed by calculating the peak response parameters (maximum acceleration, velocity and displacement) for a single-degree-of-freedom (SDOF) system at a number of specified structural frequencies. Acceleration, velocity and displacement response spectra are considered as appropriate representations of ground motion characteristics for structures with high, intermediate and low fundamental frequencies of vibration, respectively (Elnashai and Di Sarno, 2008). UHS is a particular response spectrum in that it is developed by obtaining the spectral ordinates through individual PSHA. As a result of this approach, the spectrum has equal probabilities of exceedance at all frequencies of vibration (Kramer, 1996). In this study, UHS (for acceleration) are used to characterize the seismic hazard and to select earthquake ground motions (see Section 5.2). The fundamental period of vibration of the building structures considered here is within the range from 0.3 sec to 0.5 sec; therefore, the acceleration response spectrum is deemed a viable choice for hazard representation.

As described in Section 5.2.1, the UHS used here are based on developments by the United States Geological Survey (USGS) on national seismic hazard mapping (USGS, 2008). PSHA, as briefly outlined above, was used by USGS in the development of 2008 hazard maps. Four different classes of earthquake source models were included: (1) smooth-gridded seismicity, (2) uniform background source zones, (3) geodetically derived source zones, and (4) faults. The first two sources were determined from earthquake catalogs to characterize the hazard from earthquakes within a magnitude range from 5 to 6.5. The third source was used to derive the hazard from magnitude 6.5 and that of the largest potential earthquake. The faults mostly represented the earthquakes that had magnitudes greater than 6.5. A comprehensive and uniform (in terms of magnitude and distance measures) earthquake catalog was assembled. Hazards from specific sources were represented with truncated-exponential (McGuire and Arabasz, 1990) or Guttenberg-Richter (1944) magnitude frequency distributions. Ground motion attenuation relationships (step two in the above description of seismic hazard assessment) are used to determine the ground motion at a site as a function of source characteristics and propagation

path. The attenuation relationships are obtained based on regression analysis of strong ground motion catalogs.

In 2008 hazard mapping, three attenuation relationships were utilized for crustal earthquakes in the Western United States (US): Boore and Atkinson (2008), Campbell and Bozorgnia (2008), and Chiou and Youngs (2008). These attenuation relationships were developed as a part of the NGA project (PEER, 2005). The existing PEER database of ground-motion recordings was expanded, updated and afterwards used as the earthquake catalog (ground motions used in this study are also selected from the PEER database, see Section 5.2.3) for attenuation relationships. The models included wider ranges of magnitudes, distances, site conditions, and response spectral periods of vibration. Advanced functional forms were utilized for predicting equations. Simulation of rock ground motions was performed. Site response and deep basin amplifications as well as directivity effects were also taken into account. An overview of the NGA project and comparison of the NGA attenuation relationships can be found in Power et al. (2008) and Abrahamson et al. (2008), respectively.

In 2008 hazard mapping, a logic tree approach was utilized to combine different elements of the seismic hazard model including the source models and attenuation relationships. In the logic tree approach, alternative models were assigned weighting factors that could be interpreted as the relative likelihood of that model being correct. Such a method allowed for incorporating the uncertainty associated with the selection of models. Finally, first hazard curves were calculated for a number of spectral acceleration values; they were then interpolated at selected annual rates of exceedance (or return periods) to obtain the desired UHS.

5.1.3. Selection and Spectrum Matching of Earthquake Ground Motion Time Histories

In this research, structural assessment is performed with finite element analysis tools and using inelastic time history analysis. In order to conduct the analyses, acceleration time histories are required. Researchers have used different techniques to select records from databases or generate artificial ground motions (e.g. Ghaboussi and Lin, 1998; Naeim et al., 2004). Here, the earthquake records are selected based on several criteria such as conformance with fault characteristics, mean magnitude and distance obtained from PSHA analysis, and soil conditions as explained in detail in Section 5.2.3.

Scaling and spectral matching are the two options to achieve correspondence between the selected ground motion records and the hazard levels. Scaling is simply multiplication of the record by a constant factor to equate a selected intensity measure of the record and hazard level, whereas, spectral matching involves modifying the frequency content of the ground motion to match a spectrum associated with the selected hazard level. Researchers use spectrum-compatible earthquake records to reduce the number of analyses required to quantify the mean or median of demand on a structure, especially when a large of number of analyses is required, as in the case for the optimization procedure used herein.

Here, in order to achieve a direct correspondence between ground motion time histories and hazard levels, the design ground motions are adjusted such that the response spectrum of the time

histories matches UHS that describe the hazard level. Researchers used two different approaches for spectral adjustment of ground motion time histories: frequency domain and time domain methods. Spectral matching is performed in the frequency domain by adjusting the Fourier amplitude spectrum of the record (e.g. Rizzo et al., 1975; Silva and Lee, 1987). The advantages of frequency domain methods are that the outcome records are based on real time histories, the target spectrum is matched closely, and the matching process is not computationally demanding. However, changing the Fourier spectrum distorts the velocity and displacement time histories and might result in unrealistic energy content and excessive displacement demands for the modified records (Naeim and Lew, 1995). Time domain spectral matching modifies the acceleration time history by adding wavelets (e.g. Abrahamson, 1992; Mukherjee and Gupta, 2002b, a; Suárez and Montejo, 2005). This approach introduces less energy content to the time histories and retains the time-varying amplitude characteristics of the records. However, this method is known to be more computationally costly.

In Section 5.2.4, the methods by Abrahamson (1992) and Mukherjee and Gupta (2002b) are compared, and the results from the former are utilized for analysis here. Mukherjee and Gupta (2002b) use the continuous wavelet transform to decompose the seed record into a number of time series with energy in non-overlapping frequency ranges. Each time series is then scaled such that when they are combined they produce the spectrum-compatible record. With this method the duration of the seed record was retained; however, the compatible accelerograms might have different amplitudes and frequency contents from the seed record. The method Abrahamson (1992) also used wavelets; however, instead of the continuous wavelet transform, the responses of elastic SDOF systems were utilized. This approach allowed for the spectrum matching to be made with smaller modifications to the seed records. More detailed comparison of the two approaches is available in Hancock et al. (2006). Improved versions of the method by Abrahamson (1992) have been developed by Hancock et al. (2006), and Al Atik and Abrahamson (2010).

5.1.4. Performance-Based Seismic Design

PBSD approaches have attracted considerable attention in the past decades motivated by the excessive damage observed in earthquakes especially the 1994 Northridge and the 1995 Hyogo-ken Nanbu (Kobe) earthquakes. In the case of the Northridge earthquake, although the number of casualties was relatively low (57 people lost their lives) as compared to other earthquakes, the amount of structural and nonstructural damage was excessive. The total loss was estimated to be approximately $40 billion (Eguchi et al., 1998). It was observed that the life safety objective could be achieved with existing design practices; however, the losses were unacceptably high. Thus, the engineering community began to question the effectiveness of seismic design codes. This inquiry led the researchers to PBSD, a well-known and relatively mature concept today.

As opposed to traditional seismic codes that aim to provide structures with adequate strength and ductility for life safety, and stiffness for serviceability limits, PBSD is a broader approach where the objective is to achieve stated performance objectives for structures subjected to stated seismic hazard levels. Using the multilevel, multicriteria approach offered by PBSD, the

structural design will be under direct and explicit control, and the expectations of stakeholders for more explicit codes that define design objectives will be fulfilled. The basic principles of the approach are further discussed below as a part of the review on the development of PBSD.

Although PBSD has only been extensively studied since the earthquake incidents mentioned above, the underlying concept dates back to the 1960's. The first appearance of performance-based design (PBD) in building codes was with the development of Structure for Building Regulations (Den nordiske komite for bygnings bestemmelser, 1978) by the Nordiska komitten for byggbestammelser (NKB), a committee that was established to develop building codes for the Northern European countries, as reported by Inokuma (2002). Later on the PBD was recognized by the International Organization for Standardization (ISO, 1980, 1984). Other nations followed the implementation of PBD in building codes: United Kingdom (Heseltine, 1991), New Zealand (BIA, 1995), Australia (ABCB, 1996) and Japan (JSCE, 2000). It is noteworthy that PBSD is also known as the limit states design in Europe. In the US, PBSD was introduced with Vision 2000 (SEAOC, 1995) as a response to the Northridge earthquake. The documents ATC-40 (ATC, 1996) and FEMA 273 and 274 (FEMA, 1997b, a) were developed to lay the foundations for inclusion of PBSD concepts in building codes (PBSD approaches in these documents are reviewed below). It is important to note that PBSD and displacement-based design (DBD) are occasionally used interchangeably, due to the fact that in PBSD the performance levels are mostly based on deformations. However, this kind of a usage is misleadingly restrictive since other structural response metrics such as inelastic energy absorption may also be used to define performance levels.

The objective of Vision 2000 (SEAOC, 1995) was to develop design recommendations for predictable seismic performance of buildings (considering multiple objectives) under different levels of earthquake hazard. To this end, a series of (1) earthquake design levels, (2) performance levels and (3) design performance objectives were defined. (1) Earthquake design levels were expressed in terms return periods as shown in Table 5.1. (2) Performance level was defined as the maximum desired extent of damage to a building for a given earthquake design level. The performance level was determined by the condition of both the structural and nonstructural components. Four performance levels were defined: fully operational, operational, life-safety, and near collapse. Damage states of structural components were mapped to performance levels. (3) Finally, a design performance objective was described as the desired performance level for the building for each earthquake design level. Design performance objectives were dependent on the building's occupancy, the importance of functions occurring within the building, economic considerations including costs related to building damage and repair and business interruption, and considerations of the potential importance of the building as a historic or cultural resource. Recommended design performance objectives for buildings were mapped to earthquake design levels as shown in Figure 5.2. The multilevel (earthquake design levels) and multi-criteria (basic to safety critical objective) nature of PBSD was determined as shown in Figure 5.2. Conventional codes do not evaluate the performance of buildings after the onset of damage; satisfying the life safety objective is the only goal. PBSD differs from the traditional seismic design codes because of its various performance objectives that allow the stakeholder to make decisions considering economy and safety. The recommended elastic and inelastic design

approaches in Vision 2000 (SEAOC, 1995) included: force and strength methods, energy-based approaches, DBD, and prescriptive design approaches.

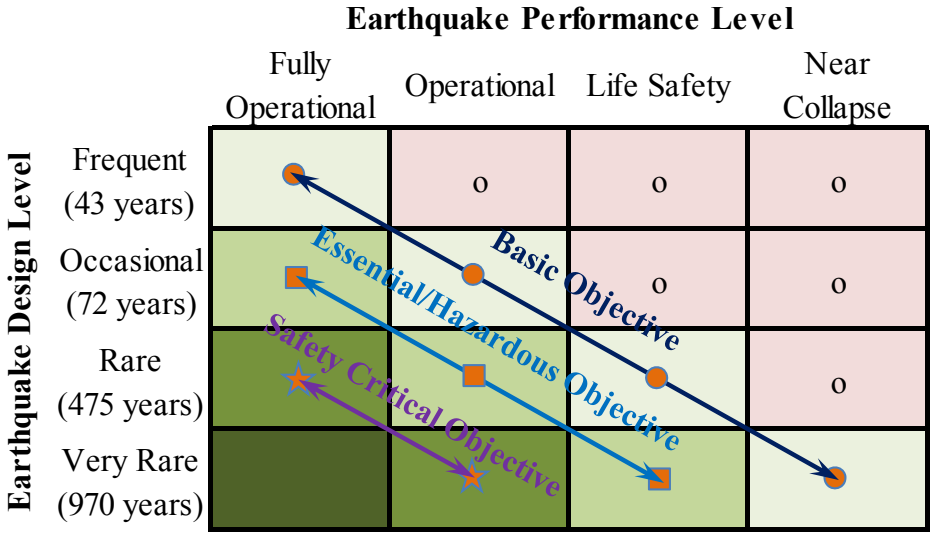

Figure 5.2. Recommended performance objectives for buildings in Vision 2000 (SEAOC, 1995), o denotes unacceptable performance.

Table 5.1. Earthquake design levels in Vision 2000 (SEAOC, 1995)

Earthquake Design Level	Return Period	Probability of Exceedance
Frequent	43 years	50% in 30 years
Occasional	72 years	50% in 50 years
Rare	475 years	10% in 50 years
Very Rare	970 years	10% in 100 years

ATC-40 (ATC, 1996) focused on RC buildings and emphasized the use of the capacity spectrum method (CSM). In CSM, buildings were represented as SDOF systems and the performance point was determined through an iterative procedure as the intersection of the capacity and over-damped demand spectra. It has been shown by several studies that the CSM exhibits certain shortcomings and could yield inaccurate and unconservative results under certain cases (e.g. Chopra and Goel, 2000; Gencturk and Elnashai, 2008).

In FEMA 273 (FEMA, 1997b) a similar framework to that of Vision 2000 (SEAOC, 1995) was presented. However, different design performance objectives and earthquake design levels were adopted (Figure 5.3). Threshold values for structural and nonstructural components at various performance levels were tabulated for various building types including steel, RC, masonry and wood. System performance levels were described in terms of local (individual element) performance levels. Linear and nonlinear, static and dynamic procedures were recommended in FEMA 273.

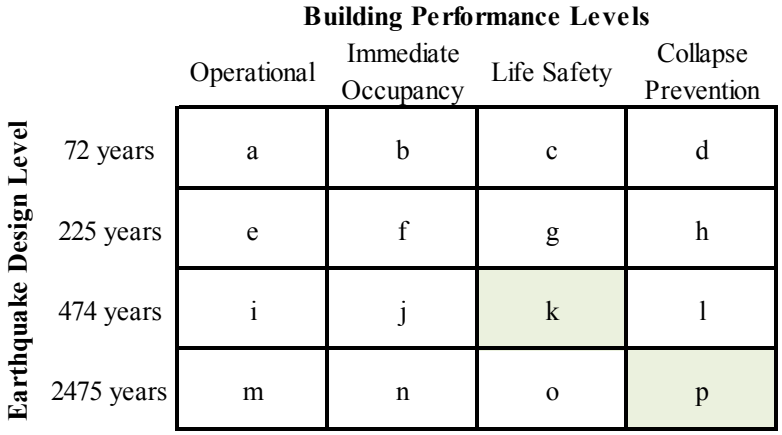

k + p = Basic Safety Objective
k + p + any of a, e, i, m; or b, f, j, or n = Enhanced Objectives
o = Enhanced Objective
k alone or p alone = Limited Objectives
c, g, d, h = Limited Objectives

Figure 5.3. Recommended rehabilitation objectives for buildings in FEMA 273 (FEMA, 1997b)

It is worth mentioning that the above reviewed documents (Vision 2000, ATC-40 and FEMA 273) were deterministic in nature. In other words, the aleatory (record to record variability) and the epistemic uncertainty (lack of sufficient knowledge in describing seismic events and structural performance) were not accounted for. In Wen et al. (2003), aleatory and epistemic uncertainties are respectively referred to as "randomness" and "uncertainty." FEMA 350 document (FEMA, 2000) developed by the SAC Joint Venture (to investigate the possible causes of widespread damage to steel structures in aftermath of the Northridge earthquake and to provide design standards and building code provisions for moment-resisting steel frame structures) was visionary in terms of incorporating randomness and uncertainty in a PBSD framework. The probabilistic framework was later published as a research article (Cornell et al., 2002) and utilized in an extensive number of studies (e.g. Liu et al., 2004).

The Pacific Earthquake Engineering Research (PEER) Center, one of the three earthquake engineering research centers in the US, determined PBEE as one of its fundamental research thrusts. PBEE differs from PBSD in that emphasis is placed on system-level performance assessment and probabilistic characterization. The PEER methodology is formed of four stages: hazard analysis, structural analysis, and damage analysis that leads to decision-making. Details regarding PBEE can be found in Porter (2003), Deierlein et al. (2003) and Moehle and Deierlein (2004), amongst others. The PEER approach is relevant to this study in the sense that the listed four stages are assembled here in an optimization framework that involves the use of ECC.

It is concluded from this review of the fundamental documents (Vision 2000, ATC-40 and FEMA 273) that the PBSD framework is the same for all three. In other words, it is agreed that seismic design should be based on multiple performance objectives for stated earthquake hazard levels; however, the definition for earthquake design levels, performance levels and performance

objectives show considerable variation. Differences between Vision 2000 and FEMA 273 in terms of earthquake design levels and performance objectives can easily be observed if Figure 5.2 and Figure 5.3 are compared. Furthermore, there is consensus neither on metrics to be selected as indicators of performance levels, nor on their relation to different damage states. However, interstory drift is mostly preferred as a performance level indicator since it is closely related to the development of P-Δ instability (a system level indicator) and to the amount of local deformation imposed on the vertical elements and beam-column connections (component level indicators). Interstory drift is also utilized in this study as one of the performance metrics.

Amongst research areas that are required to improve PBSD concepts as discussed by Ghobarah (2001) and Krawinkler (1999), the following are identified as critical to this study: (1) to determine the relationship between the structural response parameters, performance levels and damage states, and (2) to develop accurate and computationally efficient structural analysis tools. Items (1) and (2) are systematically addressed through experimentation and validated structural analysis tools as described in Chapters 3 and Chapter 2, respectively.

5.1.5. Optimization in Structural Design

In this section a review of previous studies on structural optimization is provided. Structured and unstructured optimization problems are described, and a number of studies on topology optimization are also briefly examined. Then, studies are reviewed that address gradient-based single-objective optimization problems, followed by those that deal with multi-objective problems and use heuristic approaches. Distinctions are made based on the adopted method of structural analysis (code based, linear/nonlinear, static/dynamic). Finally, studies are reviewed in detail that are most relevant to the work presented herein, i.e. those that handle multi-objective problems with due consideration of Pareto-optimality (see description in Section 5.1.1) within a probabilistic PBSD framework. It is important to note that in the following review the optimization approaches are stressed rather than the outcomes of individual studies due to the fact that the covered topics vary widely and are mostly not relevant to the present study. This extensive literature review provides the necessary background to choose/develop an efficient procedure to solve the problem considered herein.

5.1.5.a. Structured vs. Unstructured Optimization Problems

In an unstructured design problem, the number of joints in the structure, the joint support locations, and the number of members connected to each joint are unknown. In other words, topology and shape of the structure should be optimized in addition to the shape of the individual elements. In contrast, for structured design problems the total number of design variables remains fixed and known. The problem is usually reduced to the optimization of the properties (that are relevant to the solution) of individual elements. Figure 5.4 further illustrates the concept of structured and unstructured design problems (Raich and Ghaboussi, 2000). A structured optimization problem, where the design variables include the geometrical properties of individual elements and the amount of material usage, is considered in this study.

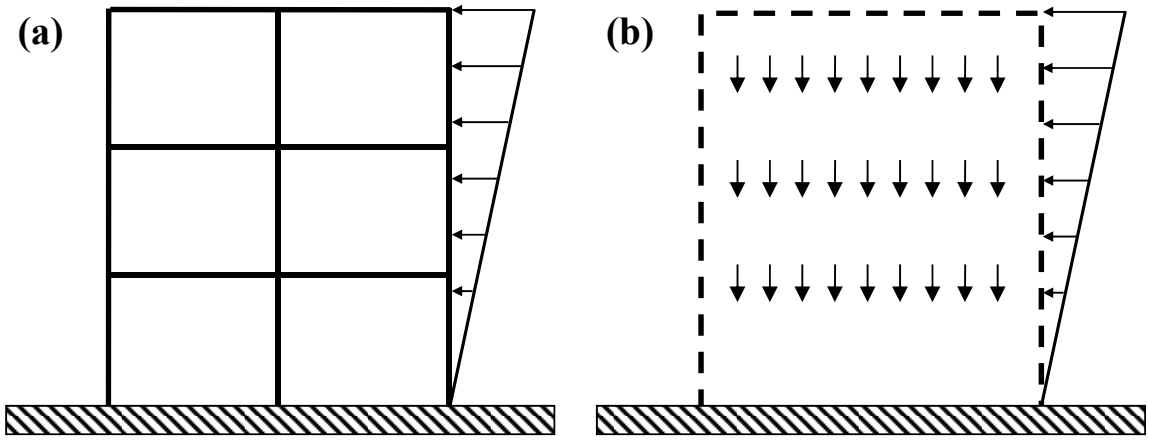

Figure 5.4. Illustration of (a) structured and (b) unstructured design problems (Raich and Ghaboussi, 2000)

5.1.5.b. Topology Optimization

Several studies in literature deal with the topology optimization of structures. Some examples include the following. Diaz and Bendsøe (1992) developed a formulation for shape optimization of elastic structures under multiple load cases. Ali and White (2001) used topology optimization to determine the location and amount of reinforcement as well as the position of compressive struts in discontinuity regions of RC structures. Liang and Steven (2002) used the PBD concept for topology optimization of linear elastic continuum structures, particularly plane stress structures and bending plates. Overall stiffness and efficiency of material usage were selected as the objectives. It is worth mentioning the study by Bendsøe et al. (1994) in which a methodology was developed to determine the optimal material properties of a continuum structure. Although it was restricted to linear elastic materials and small-deformations, the algorithm was innovative in terms of finding the optimal values for the elements of the constitutive tensor and determining the optimal configuration of the material throughout the structure consistent with the objective for globally optimal design. The results indicated that the optimized material was orthotropic with the directions of orthotropy following the directions of principal strains.

5.1.5.c. Single-Objective and Gradient-Based Optimization

Earlier attempts in structural optimization were more oriented towards use of conventional gradient-based optimization algorithms. For the most part, the (single-) objective function was selected as the minimum weight (for steel structures) or the minimum total cost. Various structural performance metrics were applied as constraints to the problem. Use of gradient-based algorithms necessitated the existence of continuous derivatives of both the objective function and the constraints. As a consequence, analytical formulations (by and large based on design codes) were adopted to evaluate performance metrics. Because these studies were based on single-objective, the concept of Pareto-optimality was not considered. The following is a review of some of the relevant studies.

Feng et al. (1977) were amongst the first researchers to incorporate dynamic loads (through modal analysis) in structural optimization. The structural weight was minimized using a state-space steepest descent method (a gradient-based algorithm) subjected to constraints on displacement, stress, structural frequency and member sizes. Bertero and Zagajeski (1979) proposed the use of linear and nonlinear programming techniques to obtain the optimum beam and column sizes as well as the volume of flexural reinforcement. Constraints were based on the kinematic theorem of simple plastic theory. Seismic input was represented with an inelastic design spectrum, and model analysis was used for analysis of multi-degree-of-freedom (MDOF) systems. Inelastic static and dynamic analyses were utilized to evaluate the performance of final designs.

Cheng and Truman (1985) developed an optimization framework for design of RC and steel structures using the optimality criteria (OC) approach. Elastic static and dynamic (modal) analyses were used for structural assessment. Discrete member properties were converted to continuous forms to conform to the requirements of the optimization algorithm. Several example problems were studied where the structural weight (or cost) was chosen as the objective function, and constraints on displacements were applied. Code-based design procedures were also evaluated in this study. Kanagasundaram and Karihaloo (1990) used two nonlinear programming methods to solve the minimum cost problem for RC structures, specifically, multi-span beams, and columns. The total cost included the costs of concrete, reinforcing steel and formwork, and the design variables were selected as the cross-sectional dimensions and the reinforcement ratio. Assessment was conducted using the Australian design code for concrete structures.

Cameron et al. (1992) compared the mathematical programming and OC methods (Berke, 1970) for tall slender frameworks. The objective function was selected as the minimization of weight, subjected to constraint on interstory drift. Moharrami and Grierson (1993) used the OC method to determine the width, depth and longitudinal reinforcement of member sections in RC structures. The objective was to minimize the cost of concrete, steel and formwork subject to constraints on strength and stiffness. Performance of structures under gravity and static lateral loads was considered and evaluated based on the existing codes for structural design. Adamu et al. (1994) investigated the optimization of RC beams using the OC method. Performance assessment was conducted using a code-based approach. Design variables were selected as the width and depth of the beams. Chung and Sun (1994) used sequential linear programming to minimize the total cost of RC beams subjected to constraints on displacements, stresses and section sizes. Inelastic finite element analysis was used to conduct the performance assessment. Zielinski et al. (1995) studied the design of rectangular RC short-tied columns using nonlinear programming. Minimum cost design was sought, subjected to constraints including ultimate strength and spacing of reinforcements. The depth and with of the cross-section as well as the reinforcement ratio were selected as design variables. Fadaee and Grierson (1996) investigated the effect of combined axial load, biaxial moments and biaxial shears on RC members based on a developed explicit formulation to evaluate capacity. The OC method was used, and the width and depth of sections and the reinforcement area were selected as design variables.

Pezeshk (1998) compared linear vs. nonlinear analysis for optimal design of steel frame structures. The OC approach was used, and the objective was selected as minimization of weight subject to constraints on displacement. It was shown that the nonlinear analysis provided more efficient design solutions. Memari and Madhkhan (1999) studied the weight minimization of 2-D braced and unbraced steel frames using the allowable stress design based on AISC provisions (AISC, 2005). The frames were subjected to gravity and seismic forces, determined using equivalent static force and response spectrum analysis. Limits on combined bending and axial stress, shear stress, buckling, slenderness and drift were applied. The feasible directions method (a gradient-based algorithm) was used for optimization. Chan (2001) investigated the optimal lateral stiffness design of tall buildings using the OC approach. The objective function was to minimize the cost subject to lateral drift response. The proposed method was applied to an 88-story building.

Chan and Zou (2004) utilized the method of virtual work to explicitly express the drift response of RC structures in terms of the design variables. The explicit formulation allowed for the use of the OC method. A two-phase optimization approach was adopted. In the first phase, member sizes were determined based on an elastic (response spectrum) analysis, and in the second phase the reinforcement ratio was found through static pushover analysis. Zou and Chan (2005a) used OC to determine the member sizes for RC frame structures. The objective function and constraint were selected as the minimum cost and lateral drift performance, respectively. Response spectrum and elastic time history analysis according to the Chinese seismic design code were used for structural performance assessment. Explicit formulation of drift responses was achieved by using the method of virtual work. Multiple earthquake loading conditions were considered. Chan and Wang (2006) investigated the optimization of RC sections to satisfy the serviceability stiffness criteria in terms of maximum lateral displacement and interstory drift with a minimum cost. The OC method was adopted. In a recent study, Zou (2008) applied the OC approach to the design of base-isolated concrete buildings. Similar to previous studies by the same author, the principle of virtual work was used to explicitly formulate the lateral drift response. The superstructure was assumed to behave elastically while the base-isolation system was allowed to go into the inelastic range. Response spectrum loading was used, and the interstory drift of the superstructure and the lateral displacement of the base-isolation system were chosen as the performance metrics.

5.1.5.d. Single-Objective and Heuristic Optimization

Although the gradient-based approaches are computationally efficient, the problems that can be solved are limited because the objective function, constraints and their sensitivities must be expressed explicitly. The latter condition imposes a limitation on an analysis procedure that may be selected for structural assessment. Furthermore, the design variables should be continuous over the search domain. In other words, discrete design variables such as the reinforcement ratio in RC structures cannot directly be accounted for in gradient-based optimization algorithms. As a consequence, as reviewed in Section 5.1.5.c, researchers used methods such as the principle of virtual work in order to analytically express the objective function as well as the constraints. The

review indicated that the gradient-based optimization algorithms most often selected were the OC approach and linear and nonlinear programming.

With the immense advance in computational power of recent years, researchers were increasingly directed to incorporate more accurate analysis tools such as static pushover analysis and dynamic time history analysis through finite element modeling in structural optimization. However, because these analysis techniques require algorithms that do not entail the continuity of functions or the existence of derivatives, researchers had to abandon the conventional gradient-based approaches. Heuristic approaches progressively became popular in structural optimization. A further advantage of heuristic algorithms is that they are very effective in terms of finding the global minimum of highly nonlinear and/or discontinuous problems where the gradient-based algorithms are usually trapped in a local minimum. In this section, a review of studies that solve single-objective problems in structural design using heuristic approaches is provided.

Jenkins (1992) was amongst the first researchers to employ genetic algorithms (Holland, 1975; Goldberg, 1989) in structural optimization. Genetic algorithms (GA) were selected due to the discrete nature of the design variables in the problem formulation. The objective was to reduce the cost of plane frame structures subject to constraints on stresses and displacements. Linear elastic analysis was conducted to evaluate structural performance. The study by Balling and Yao (1997) could be considered significantly ahead of its time. It was recognized that the optimization of RC frames was more challenging when compared to the optimization of steel frames due to the complexity associated with reinforcement design. Thus, a multilevel approach was proposed for minimum cost design of RC structures (including the costs of material, fabrication, and placement of concrete and reinforcement). The standard stiffness method was used to analyze 3-D frames and determine cross-sectional dimensions while the reinforcement topology was found from individual member analysis. As a result, the optimization of reinforcement detailing is conducted together with the optimization of cross-sectional dimensions. This approach allowed for the investigation of the effect of reinforcement distribution, bar diameters, number of bars, cutoff and bend points, size and spacing of stirrups and ties. Simulated annealing (Kirkpatrick et al., 1983; Černý, 1985) was used to solve the discrete design problem (where no gradients exist). The traditional approach, where the total reinforcement area was considered as a design variable (as opposed to the reinforcement topology) was also investigated using a gradient-based optimization algorithm. It was concluded that the optimum values of section dimensions were insensitive to the number, diameter, and topology of reinforcing bars. The major shortcoming of the study was the use of code-based approaches for individual member analysis.

Huang and Arora (1997) evaluated the computational efficiency of optimization approaches including the GA and simulated annealing (SA). Steel structures with standard sections were considered, and the objective function was to minimize the total cost subjected to constraints on stress, buckling and displacement. Camp et al. (1998) compared the traditional OC approach with GA for optimal design of 2-D steel structures. The objective function was selected as the minimum weight subject to constraints on serviceability and strength requirements based on the

AISC provisions (AISC, 2005). Finite element analysis was used for structural assessment. GA was found to be superior to conventional gradient-based approaches. Rajeev and Krishnamoorthy (1998) acknowledged the discontinuous nature of design variables (e.g. area of reinforcement) for RC structures due to practical constraints and used GA to solve the optimization problem (which was reduced to a combinatorial one). Cross-sectional dimensions and reinforcement detailing were selected as the design variables, and the proposed method was capable of providing solutions that were directly constructible. Kocer and Arora (1999) used both static and dynamic (linear and geometrically nonlinear time history) analysis within the optimal design framework of H-frame transmission poles. One accelerogram was used for design purposes. SA and GA were compared, and GA was found to yield more efficient design solutions. Pezeshk (2000) employed GA for the optimal design of steel framed structures. Both linear and geometrically nonlinear analysis were evaluated according to AISC provisions (AISC, 2005). Although both methods provided similar solutions, the geometrically nonlinear analysis was found to provide better results for certain cases. Ceranic (2001) applied the SA algorithm to the optimal design of RC retaining structures. Analysis was conducted based on the British Standards. It was found that the SA could be a valid approach for minimum cost design of RC retaining structures.

Lee and Ahn (2003) used GA to investigate the design of RC plane frames that were subject to combinations of gravity and lateral loads. The researchers recognized the discrete nature of the optimization problem for RC structures and constructed a database of sections for beams and columns. The database was then further reduced based on code requirements such as the reinforcement spacing and ratio of cross-sectional dimensions. Assessment of the structures was performed based on the ACI 318-08 (ACI, 2008) and UBC (ICBO, 1997) codes. In a similar study, Camp et al. (2003) investigated the minimization of material and construction costs for RC structures under serviceability and strength requirements. Foley and Schinler (2003) used evolutionary algorithms (EA)--which could be considered as improved GA--for weight optimal design of fully and partially restrained steel frames. Constraints in the serviceability and ultimate limit states were imposed. Fiber-based finite element modeling was adopted, and the connections were modeled separately to account for connection flexibility. To reduce the computational time, an incremental analysis algorithm employing constant-work constrained load increments without iterations was utilized. Govindaraj and Ramasamy (2005) investigated the design of RC continuous beams using GA. The total cost was selected as the objective function, and constraints on strength, serviceability, ductility, and durability were imposed. Only the cross-sectional dimensions (not the reinforcement ratio) were considered as design variables. Indian standards for RC design were used for assessment of beams.

Salajegheh and Heidari (2005) presented an optimization approach using SA and neural networks. Computational work associated with elastic time history analysis was reduced by decomposing the earthquake record into low and high frequency components and by using only the former in the analysis. Dynamic response of the structures was predicted using neural networks. Sahab et al. (2005b) investigated the applicability of GA and a multilevel hybrid method that included exhaustive search (Sahab et al., 2005a) to optimal design of RC flat slab buildings. The objective function was selected as the total cost of the structure including the cost

of concrete, formwork, reinforcement and foundation excavation. Analysis was conducted according to British Standards. Different options for GA were evaluated, and it was shown that GA could be used as an effective approach to solve the considered problem. Salajegheh et al. (2008) proposed using neural networks to predict the elastic dynamic response of structures thus to reduce the computational cost of structural analysis within the optimization framework. EA was used for minimization of structural weight. A similar optimization framework was depicted by Gholizadeh and Salajegheh (2009).

5.1.5.e. Multi-Objective and Heuristic Optimization

Up to this point studies on structural optimization with single-objective function have been reviewed. In most of this research, the merit function was selected to minimize the use of economic resources (e.g. material usage) and to determine the feasibility of design alternatives with constraints imposed on performance metrics such as displacements and stresses. The threshold values for performance metrics (that determine the feasibility of a design) were typically established based on code-suggested values. As a consequence of the formulation of the problem, single-objective optimization methods usually provide an optimal solution (which minimizes the merit function) that is feasible. However, the decision maker (usually the engineer or the stakeholders) does not have a broad view of the extent to which constraints are satisfied. Thus, the decision maker must either accept or reject optimal solution. On the other hand, in a multi-objective formulation of the design problem, more than one merit function (typically the ones that are most relevant to decision making process) is considered. The latter approach provides the decision maker with the flexibility to trade off between the equivalently optimum design solutions (Pareto optimal set) and to base the selection on rather transparent results. This incentive has led researchers to formulate optimization problems in a multi-objective format. To this end, the existing algorithms have been modified to accommodate multiple merit functions. A number of relevant studies are reviewed below.

Li et al. (1999) investigated the optimization of steel frames using a multilevel approach. The system was divided into subsystems, and optimization was performed by iterating between the subsystems and the system. Two objective functions were selected: maximization of total strain energy and minimization of total structural weight. Design variables were chosen as the member moment of inertias and cross-sectional dimensions. The finite element method was used to calculate the element forces and displacements. Constraints on frequency, strength, buckling and displacement were imposed, and the validity of designs was determined based on code provisions. Liu et al. (2006) studied the minimum weight design of steel moment-resisting frames. It was recognized that the material weight could not adequately represent the total construction expense of steel structures, so design complexity (number of different steel sections used in the construction) was considered together with the material weight as a merit function. GA was employed. The validity of designs was assessed, based on code provisions, through elastic finite element analysis. Pareto optimal sets were presented for the selected example cases. Further studies on multi-objective optimization are reviewed in Section 5.1.5.f.

5.1.5.f. Optimization Using the Performance-Based Seismic Design Approach

In this section, studies on structural optimization that consider the PBSD approach are reviewed. Similar to the outline followed in the preceding sections, first studies with single-objective function are reviewed followed by those that consider multiple merit functions. Finally, the literature on multi-objective optimization that incorporates different sources of uncertainty within the proposed frameworks is examined.

Single-objective

Balling et al. (1983) conducted one of the first studies on structural optimization that employed inelastic time history analysis. Although PBSD concepts were not well established at the time, Balling et al. considered two hazard levels for the seismic design of steel frames. The study focused on the design of a four-story three-bay building to illustrate the proposed methodology. Structural volume, inelastic energy dissipation and story drift were separately taken as objectives, and a feasible-directions optimization algorithm was used to determine the moment of inertia for columns and girders of the frame. Six earthquake ground motions were used for analysis. The records were first made uniform by scaling to the same spectral intensity, and were then scaled to the same PGA (0.15 g and 0.5 g) to represent the two hazard levels (moderate and severe shaking). Inelastic static analysis was used for gravity loads. Elastic and inelastic dynamic analyses were conducted for moderate and severe earthquakes, respectively. The building was represented with a lumped plasticity model having 20 DOFs. Constraints on forces and moments (to control the structural integrity under gravity loads), accelerations and drifts (to control nonstructural damage under moderate earthquake), and structure sway and energy dissipation (to control global stability and low cycle fatigue under severe earthquake) were imposed. One of the six records (that gives the maximum response) was used for the final optimization problem to reduce the computational time. Time history analysis was performed for the most intense 11 sec of the record with a time step of 0.01 sec. 4.3 h of CPU time required to make five iterations using inelastic dynamic analysis.

Ganzerli et al. (2000) studied the optimal PBSD of RC structures. Their purpose was the minimization of structural cost taking into account performance constraints (on plastic rotations of beams and columns) as well as behavioral constraints. Uncertainty associated with earthquake excitation and determination of the fundamental period of structure was taken into account. Static pushover analysis was used to determine the structural response. Zou and Chan (2005b) used the OC method for PBSD of RC buildings. Using the method of virtual work, the nonlinear inelastic drift responses generated by static pushover analysis were expressed in terms of design variables. CSM was employed to determine the structural response. A two phase methodology was proposed: based on their elastic responses, the sections were first sized to satisfy the serviceability requirements; second, the reinforcement ratios were used as design variables to achieve constraints on the inelastic interstory drift limits obtained by static pushover analysis.

Fragiadakis et al. (2006a) used EA for optimal PBSD of steel structures. Minimization of cost subject to constraints on interstory drift was targeted. Both inelastic static and inelastic dynamic procedures were employed. Discrete beam and column sections were selected as design

variables. 10 earthquake records were used to represent each hazard level, and mean structural response was taken as the performance measure. Uncertainty associated with structural modeling was also taken into account. Lagaros et al. (2006) evaluated modal, elastic and inelastic time history analysis, taking the European seismic design code as a basis, in an optimization framework. Steel structures were considered, and EA was used to solve the optimization problem. A fiber-based finite element modeling approach was adopted. Either 10 natural records or five artificial records were used to represent the hazard. Material weight was selected as the design objective. It was observed that lighter structures could be obtained when inelastic time history analysis (instead of elastic time history or modal analysis) and natural records were used instead of artificial records that were compatible with a certain design spectrum.

Fragiadakis and Papadrakakis (2008) studied the optimal design of RC structures. Both deterministic and reliability-based approaches were evaluated, and the latter was found to provide more economical solutions as well as more flexibility to the designer. The total cost of the structure was taken as the objective function, and compliance with European design codes was applied as a condition. EA was used to solve the optimization problem. Three hazard levels were considered. To reduce the computational time, fiber-based beam-column elements were used only at the member ends, and inelastic dynamic analysis was performed only if nonseismic checks performed through a linear elastic analysis were met. Sung and Su (2009) investigated PBSD of RC bridge piers using GA. Different performance objectives were determined based on the force-displacement relationship obtained from previous experimental work. Pushover analysis was used to evaluate the structural performance.

Multi-objective

Liu et al. (2003) investigated the optimal PBSD of steel moment frame structures. Merit functions were selected as the initial material and lifetime seismic damage costs. Reducing design complexity was also incorporated into the algorithm. Code provisions were followed to determine the validity of design alternatives. Static pushover analysis was used to derive an equivalent SDOF system that was utilized (together with the inelastic UHS) in computing the maximum interstory drift ratios. In a similar study by Liu et al. (2005), conflicting objectives were defined as the initial material cost (including the cost due to design complexity as a function of the number of different structural shapes) and the seismic performance. Two hazard levels were used, and the performance criterion was selected as the maximum interstory drift. Structural assessment was conducted using static pushover analysis based on seismic code provisions. GA was employed to solve the optimization problem. Liu (2005) formulated an optimal design framework for steel structures based on PBSD. The considered objectives were the material usage, initial construction expenses, degree of design complexity, seismic structural performance and lifetime seismic damage cost. Design variables were section types for members of the frames. The designs were evaluated for validity based on the existing code provisions. A lumped plasticity model was used for structural modeling. Both static pushover and inelastic dynamic (when structural response parameters were directly taken as objective functions) analysis were used. Fragiadakis et al. (2006b) used EA for optimal design of steel structures. Initial construction and life-cycle costs were considered as two merit functions. Constraints were

based on the provisions of European design codes. A fiber-based finite element model was used to conduct static pushover analysis to determine the inelastic response of structures. Deterministic structural damage states based on the maximum interstory drift was employed; however, probabilistic formulations were adopted for calculating the LCC.

Lagaros and Papadrakakis (2007) evaluated the European seismic design code vs. a PBSD approach for 3-D RC structures. The objective functions were selected as the initial construction cost and the maximum interstory drift. Cross-sectional dimensions and the longitudinal and transverse (for serviceability limit state only) reinforcement were the design variables. Three hazard levels were considered in the study, and the linear and nonlinear static procedures were used for design based on the European code and PBSD, respectively. EA was employed to solve the optimization problem. It was concluded that there was considerable difference between the results obtained from the European code and PBSD, and design solutions based on the former were more vulnerable to future earthquakes.

Ohsaki et al. (2007) explored the applicability of SA and taboo search (TS) algorithms for the optimal seismic design of steel frames with standard sections. The problem was formulated as a combinatorial one. Merit functions were selected to maximize the dissipated energy and to minimize the total volume of steel. A generalized plastic hinge model that considers the interaction between the bending moment and axial force in yield condition was used for structural modeling. Incremental dynamic analysis was used to compute the responses of the structure, and geometrical and material nonlinearities were considered in time history analysis. It was concluded that TS was more advantageous than SA in terms of the diversity of the Pareto solutions and the ability of the algorithm to search the solutions near the Pareto front.

Zou et al. (2007) used the method of virtual work to achieve an explicit formulation for the multi-objective optimization of RC frames. The OC method was then used to minimize the initial material cost and the expected damage loss in a Pareto optimal sense. The method was formulated in two stages: elastic response spectrum analysis was first performed where the cross-sectional dimensions were considered as the only design variables, then section sizes were kept constant, and the reinforcement ratio was taken as the design variable for the static pushover analysis through which inelastic drift responses were calculated.

Multi-objective considering uncertainty

Beck et al. (1999) developed a reliability-based optimization method that considers uncertainties in modeling and loading for PBSD of steel structures. A hybrid optimization algorithm that combines GA and the quasi-Newton method was implemented. Performance criteria were selected as the lifetime drift risk, code-based maximum interstory drift and beam and column stresses. The ground motion was characterized by a probabilistic response spectrum, and different hazard levels were considered. The methodology was applied to a three-story structure. Section sizes were selected as design variables, and both continuous and discrete representations were considered. Linear elastic dynamic finite element analysis was used for performance assessment of the structure. Liu et al. (2004) studied PBSD of steel moment-resisting frames using GA. Three merit functions were defined: initial material costs, lifetime seismic damage costs, and the number of different steel section types. Maximum interstory drift

was used for the performance assessment of the frames through static pushover analysis. Code provisions were taken into account in design. Different sources of uncertainty in estimating seismic demand and capacity were incorporated into the analysis by using SAC/FEMA guidelines (Cornell et al., 2002). The results were presented as Pareto-fronts for competing merit functions. Final designs obtained from the optimization algorithm were assessed using inelastic time history analysis. Rojas et al. (2007) used GA for optimal design of steel structures taking into account both structural and nonstructural components. FEMA 350 (FEMA, 2000) and HAZUS (FEMA, 2003a) procedures, for structural and nonstructural damage respectively, were adopted to evaluate damage and to account for various sources of uncertainty. Two hazard levels were represented with two sets of seven records, inelastic time history analysis was conducted, and the median of the maximum response quantities (interstory drift and floor accelerations) was used to evaluate the performance of designs. Interaction surfaces were used to represent the inelasticity in finite element modeling of beam-column elements. Alimoradi et al. (2007; Foley et al., 2007) studied the optimal design of steel frames with fully and partially restrained connections using GA. Uncertainty associated with structural capacity and demand was treated based on the formulation in FEMA 350 (FEMA, 2000). Seven ground motion records were used to represent each of the two considered hazard levels. A lumped plasticity model, with special connection models, was used for inelastic time history analysis. The methodology was applied to a portal and a three-story four-bay frame. Interstory drift and column axial compression force were selected as the performance metrics. For the portal frame, the objectives were selected as the median drift for IO, the median drift for CP, and the total weight of the structure; and for the multistory frame the objectives were the minimization of member volume and minimization of the difference between the confidence levels in meeting a performance objective obtained from the global interstory drift and the column axial compression force.

5.1.5.g. Conclusions from the Literature Review on Structural Optimization

The preceding sections have reviewed previous work on structural optimization in detail. It is observed that the earlier studies were focused on single-objective optimization using gradient-based algorithms. The merit function was almost exclusively selected as the initial cost (or the material usage). Several constraints (most often based on code provisions) were applied to determine the validity of designs. Depending on whether steel or RC structures were considered, design variables were the section sizes and reinforcement ratios. The underlying reason for the selection of gradient-based algorithms was their relative computational efficiency required due to limited resources in the past decades. Explicit formulations, which could be evaluated with little effort, were used for both the objective function and the constraints.

Later on researchers recognized that practical design problems entailed the discrete representation of design variables (e.g. section sizes, reinforcement areas). Furthermore, code-based formulations to assess structural performance did not always accurately represent the actual behavior, thus, more advanced tools (e.g. finite element modeling) were needed. As a consequence of these requirements, the objective functions as well as the constraints (or their derivatives) became discontinuous. Hence, researchers resorted to heuristic approaches that did

not require existence gradients or the continuity of merit functions or constraints. With the advance of computational power and the increase in the availability of structural analysis tools, researchers have utilized more sophisticated analysis techniques such as nonlinear static analysis and inelastic dynamic analysis.

A further step in structural optimization was the adoption of multiple merit functions. In single-objective approaches, the provided optimal design solutions were not transparent in terms of the extent of satisfaction of various constraints on performance metrics. Therefore, researchers used multiple merit functions (usually the most relevant objectives were selected) to provide the decision maker with a set of equivalent design solutions so that a selection could be made based on the specific requirements of the project. With the increase in the popularity of PBSD approaches towards the end of the 1990's, structural optimization tools were tailored to accommodate the new design concepts. The multi-objective nature of PBSD naturally suits formulations that considered multiple merit functions, and several research works were published to formulate optimization frameworks from a PBSD standpoint.

Even though optimization in structural design has been well studied, there is still need for further research because:

- Only a limited number of studies have utilized advanced computational tools. Structural performance assessment was usually performed using code-based formulations or elastic analysis. Simplified modeling techniques were adopted whenever inelastic analysis was conducted.
- Existing studies have overwhelmingly focused on the optimization of steel structures due to well-defined design variables (i.e. section types) and availability of structural modeling tools.
- Most of the research effort has been devoted to the development of optimization methods; the real engineering problem to be solved remains.
- To the best of this author's knowledge, none of the existing studies have addressed the multi-objective PBSD of RC structures while considering the LCC and taking into account randomness due to ground motion variability, and uncertainty in structural modeling. Nor have any studies used rigorous analysis procedures to evaluate structural capacity and earthquake demand.

5.1.6. Previous Studies on Testing of Multi-Material Structural Elements

Reviewed in this section are previous studies on the testing of multi-material structural elements where a conventional material such as concrete and a high-performance fiber-reinforced cementitious composite (HPFRCC) are used together. These applications are relevant to the optimization problem investigated in Section 5.5. It is noteworthy that the studies reviewed here did not consider optimization of material properties or their distribution but rather used HPFRCC materials at critical regions of structural members to improve performance.

Billington and Yoon (2004) tested precast segmental concrete bridge piers with ductil fiber-reinforced cementitious composites (DFRCC) at plastic hinge locations. It was observed that improved performance with substantial increase in strength and energy dissipation capacity could be achieved by utilizing DFRCC. In a large-scale experimental study conducted by Parra-Montesinos et al. (2005) beam-column connections cast with HPFRCC showed signs of minor damage under large load reversals. The specimens could sustain drifts and beam rotation capacities as high as five percent and 0.04 rad, respectively. Peak shear stress measurements indicated that the current ACI 318-08 (ACI, 2008) shear stress limits for joints with beams framing into the column from two opposite sides could be safely used for connections with no confinement (shear) reinforcement. Moreover, although the minimum anchorage length requirements of ACI 318-08 (ACI, 2008) were not fulfilled, no debonding or slippage in rebars were observed. Results from Parra-Montesinos and Wight (2000) also confirmed the findings on improved bond strength. Parra-Montesinos et al. (2006) tested structural walls with a shear-to-span length ratio of 3.7 and fiber-reinforced cementitious composites (FRCC) applied at the plastic hinge locations. Existence of FRCC at the critical zone, where damage localization was expected, significantly improved the structural performance. One of the tested members with two percent volume fraction of steel fibers suffered little damage up to failure, which occurred due to fracture of the main longitudinal reinforcement at three percent drift. Moreover, no confinement reinforcement, which would increase labor cost and also cause congestion during concrete casting, was used in this specimen at the wall boundaries.

Lee and Billington (2008) investigated the effects of changes in the tensile characteristics of ECC (applied to plastic hinge locations to improve the seismic response characteristics) on the behavior of unbonded, post-tensioned bridge piers through computer simulation. Finite element modeling of bridge piers was performed, and the model was validated using experimental results from Billington and Yoon (2004). It was shown that increasing the tensile strain capacity of ECC without increasing the peak strength was the most efficient way of increasing strength and ductility in the bridge piers. In a study by Shen et al. (2008), a functionally graded beam with linearly increasing volume of fibers from zero percent in compression to two percent in tension region was produced. Flexural testing of beams indicated that functionally graded beams had 50 percent higher strength than those with the same overall fiber volume fraction.

Although not including an optimization framework, the above-mentioned studies alongside others on testing of shear critical and flexural critical structural components (see Section 3.1.3 for a review of pertinent previous experimental work) illustrate the potential for effective use of ECC through selective intervention. Specifically, critical regions (e.g. beam-column connections, structural wall regions at the base of buildings, plastic hinges at beam and column ends) in structural systems can be effectively identified through analysis and optimization algorithms; seismic performance can greatly be enhanced; life-cycle and construction costs can be reduced by proper exploitation of benefits such as confinement reinforcement relaxation, reduction in anchorage lengths and section sizes, reduced maintenance and post-earthquake repair needs; and increased sustainability of infrastructure can be achieved.

It is concluded from previous research that significant improvements (in terms of seismic performance) can be achieved by employing ECC at critical locations (i.e. regions that require characteristics such as shear resistance, high energy absorption, and damage tolerance) of structures. Costs due to material usage and lifetime seismic damage can be reduced, and structural performance can be tuned to the imposed demand if structural systems are designed within a multi-objective optimization framework. Previous studies warrant further exploration of the novel idea of multi-objective optimization of multi-material systems.

5.2. DEFINITION OF THE SEISMIC HAZARD

The objective of Section 5.2 is the selection of proper ground motion records to be used in inelastic dynamic analysis of considered structural frames in the optimization problem (see Sections 5.3 and 5.5). To this end, a geographical location is selected, and the site-specific hazard is developed in a consistent manner (i.e. taking into account the characteristics of the governing seismic sources and soil conditions). Three levels of seismic hazard are defined with 75, 475 and 2475 years return periods (YRP). These hazard levels are represented with UHS, and seven earthquake ground motions are selected for each level (considering the magnitude, distance, soil conditions and conformance to UHS). The records are made compatible with the respective UHS using time domain techniques. Out of seven ground motions, one record is selected for each hazard level and then utilized in seismic design of structural frames. The rest are used for assessment of designs and to quantify the variability in earthquake demand.

5.2.1. Site Location, Soil Conditions and Site-Specific Hazard

In order to have a realistic description of the seismic hazard, it is required that a specific site be selected and the governing hazard consistently derived. To achieve this objective, the location with the coordinates 37° 47′ 21.58′′ N, 122° 24′ 04.77′′ W is selected. The site is situated at the intersection of 2nd and Market St in San Francisco, CA (see Figure 5.5). The soil conditions in the San Francisco Bay area are shown in Figure 5.6. According to the provided map, the site class is determined as D on the NEHRP scale (as indicated in Table 5.2) with a shear wave velocity in the range from 180 m/sec to 360 m/sec. The major faults close to the selected site are shown in Figure 5.7. The governing faults for the selected site are the San Andreas, San Gregorio and Hayward faults (see Section 5.2.2, on disaggregation of hazard). The source to site distance is between 11 km to 24 km depending on the fault.

Table 5.2. NEHRP soil classification based on shear wave velocity (FEMA, 2003b)

Site Class	Shear Wave Velocity Range
A	$V_s > 1500$ m/sec
B	760 m/sec $< V_s \leq 1500$ m/sec
C	360 m/sec $< V_s \leq 760$ m/sec
D	180 m/sec $\leq V_s \leq 360$ m/sec
E	$V_s < 180$ m/sec
F	Requires site-specific evaluation

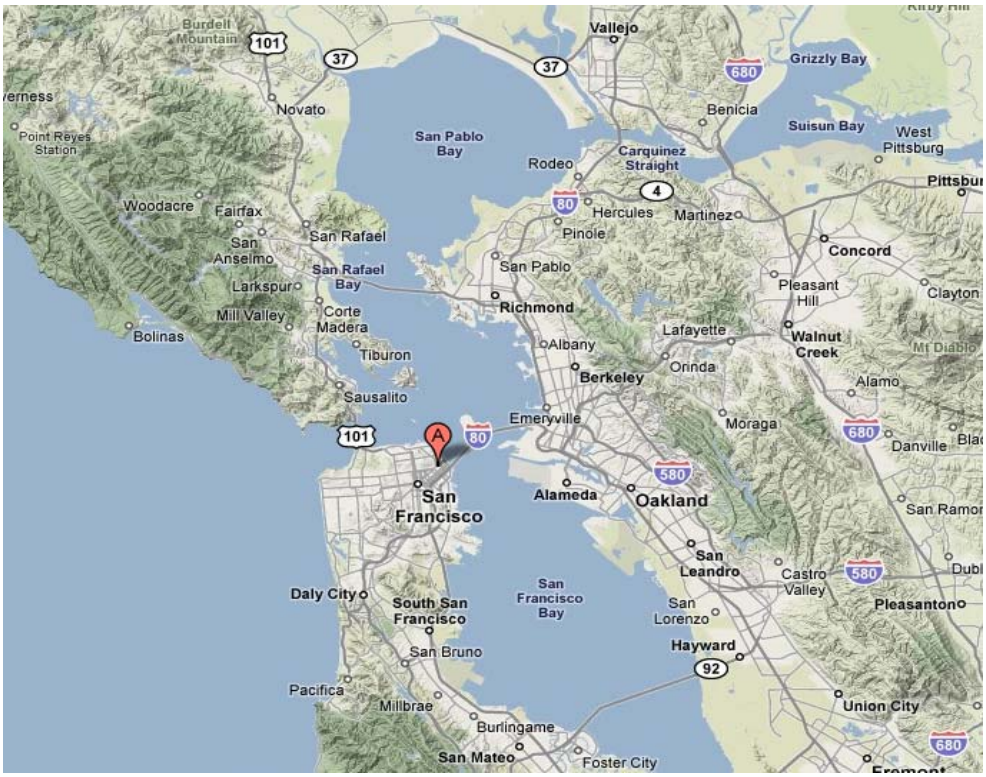

Figure 5.5. Location of the selected site (source: Google Maps, accessed on May 31, 2009, available from *http://maps.google.com/*)

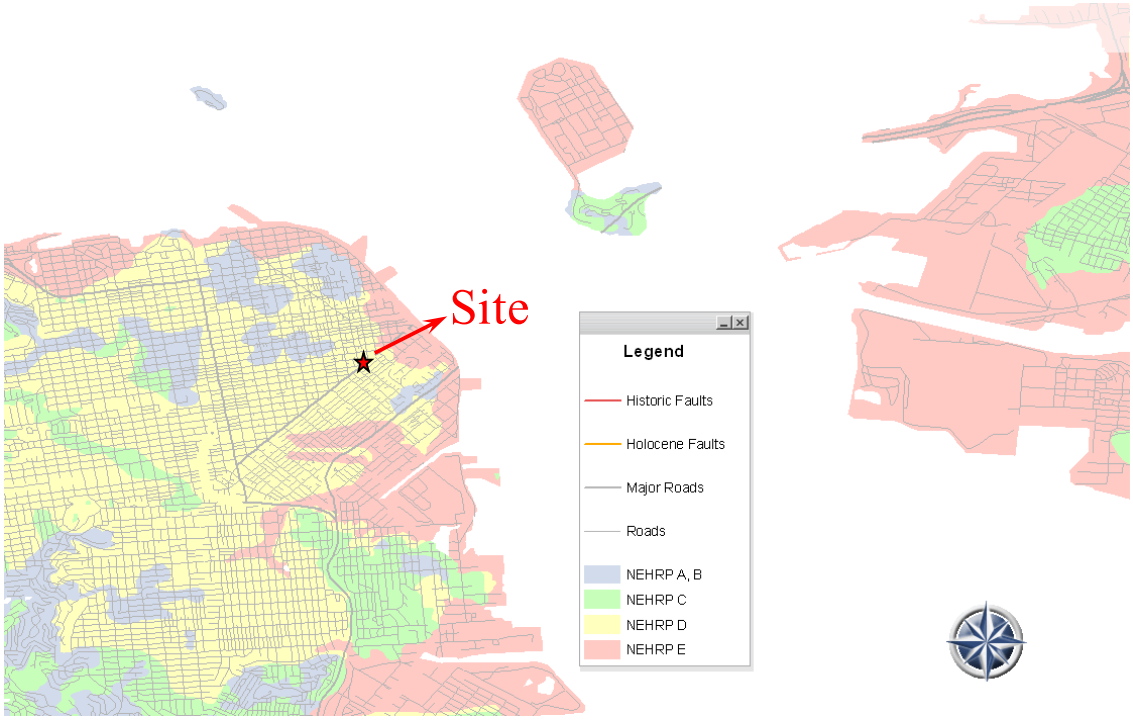

Figure 5.6. Soil type in the San Francisco Bay Area (USGS, 2009c), see Table 5.2 for soil classification

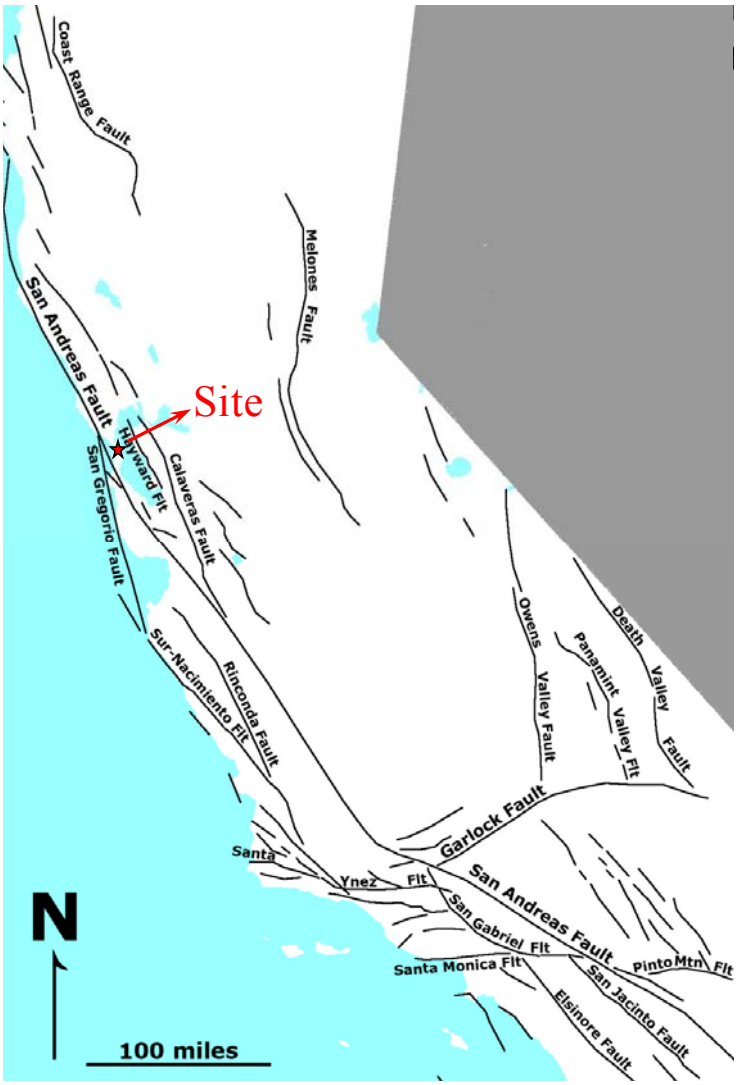

Figure 5.7. Major faults close to the selected site (USGS, 2009b)

The hazard curves are obtained using the online applet provided by USGS (2009a) as shown in Figure 5.8(a). With this information, UHS are then generated at five different return periods (i.e. 75, 225, 475, 975 and 2475 years) as shown in Figure 5.8(b); however, those shown with solid lines (i.e. 75, 475 and 2475 years) are selected and used here because they are considered to correspond to the three structural limit states: IO, LS and CP, respectively. The correspondence between hazard and structural performance levels is summarized in Table 5.3.

Table 5.3. Mapping between hazard and structural performance levels

Structural Limit State	Return Period	Probability of Hazard
Immediate Occupancy (IO)	75 years	50% in 50 years
Life Safety (LS)	475 years	10% in 50 years
Collapse Prevention (CP)	2475 years	2% in 50 years

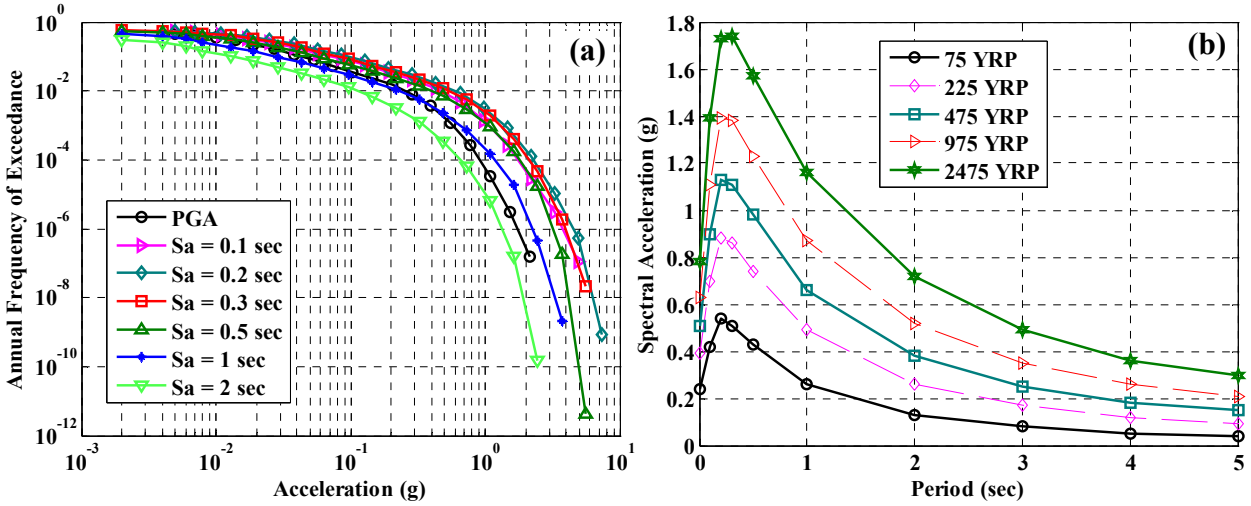

Figure 5.8. Site specific (a) hazard curves and (b) UHS at different return periods

5.2.2. Disaggregation of the Hazard

Disaggregation is performed at a particular location in order to determine the relative contribution of seismic sources to hazard. As a result of disaggregation calculations, the significant parameters (magnitude and distance) that characterize seismic hazard are determined. The same web-based applet used to obtain the UHS is utilized for this purpose (USGS, 2009a). It is important to note that local site conditions are included in the disaggregation calculations.

Disaggregation is performed at different structural periods ranging from 0 sec (corresponds to PGA) to 5 sec. The mean magnitude and distance values are determined from the charts, and the results are summarized in Table 5.4. As an example, the disaggregation results at a structural period of 0.3 sec (the most relevant period for the frames considered in this study, see Section 5.5) are shown in Figure 5.9(a). The results for other periods can be found in Appendix C, Section C.1. The relative contributions of different magnitudes and distance bins to the seismic hazard are represented with bars. From the disaggregation results provided in Figure 5.9(a) it is concluded that for a structural period of 0.3 sec at the selected location, San Andreas and Hayward faults (located at a distance of about 15 km) make the highest contribution to seismicity (from an event having a moment magnitude of approximately 7.5) at all hazard levels. It is important to note that different segments of the San Andreas and Hayward faults are considered as independent sources, and there exist other potential sources of seismicity at the selected location such as the San Gregorio fault.

For the two-story two-bay structural frames considered in this study (details of which are provided in Section 5.5) the critical period range is determined as 0.3 to 0.5 sec, depending on the stiffness of the beams and columns. However, taking into account the chance of having fundamental periods less than 0.3 sec during optimization and period elongation due to damage accumulation, a period range from 0 sec to 1 sec is considered (as highlighted in Table 5.4). The mean values for magnitudes and distances obtained from disaggregation for the latter period

range are summarized in Table 5.5. These values, together with the soil conditions, control the selection of the earthquake time histories to be used for seismic design and assessment purposes.

Table 5.4. Disaggregation results (S_a: spectral acceleration, R: distance, M_w: moment magnitude)

Period (sec)	Return Period								
	75 years			475 years			2475 years		
	S_a (g)	R (km)	M_w	S_a (g)	R (km)	M_w	S_a (g)	R (km)	M_w
0	0.24	20.30	6.90	0.51	15.10	7.14	0.78	13.50	7.25
0.1	0.42	19.70	6.83	0.90	15.10	7.04	1.39	13.50	7.12
0.2	0.54	21.12	6.87	1.13	15.80	7.08	1.73	14.20	7.19
0.3	0.51	22.40	6.92	1.11	16.00	7.16	1.74	14.20	7.29
0.5	0.43	23.50	7.00	0.98	16.20	7.27	1.57	14.10	7.42
1	0.26	26.80	7.12	0.66	17.40	7.44	1.16	14.50	7.62
2	0.13	32.60	7.21	0.38	19.50	7.59	0.72	15.80	7.76
3	0.08	31.30	7.25	0.25	17.90	7.65	0.49	15.30	7.81
4	0.05	29.30	7.25	0.18	16.90	7.66	0.36	14.80	7.82
5	0.04	29.40	7.25	0.15	16.50	7.65	0.30	14.20	7.80

Table 5.5. Governing magnitude and distance values for different return periods

Soil Class D (180 m/sec < Vs < 360 m/sec)				
Performance Goal	**Return Period**	**Magnitude (M_w)**	**Distance (km)**	**PGA (g)**
Immediate Occupancy	75 years	6.94	22.30	0.24
Life Safety	475 years	7.19	15.93	0.51
Collapse Prevention	2475 years	7.32	14.00	0.78

5.2.3. Selection of Earthquake Time Histories

Seven earthquake recordings are selected for each of the three return periods. The PEER Next Generation Attenuation Relationships (NGA) database (PEER, 2005) is utilized for this purpose for the following reasons: (1) distances and the shear wave velocities are available for most of the recording stations, (2) the database comprises several records that were generated by earthquakes with similar characteristics to the hazard at the considered site, and (3) the records are uniformly processed and reliable. The following criteria are used for selecting the records (in the order of priority):

a. Earthquakes having similar mechanisms to those pertinent to the faults affecting the site,

b. Magnitudes within ±1 of the governing magnitude for the considered return period,

c. Shear wave velocity of the recording station within the range from 180 m/sec to 360 m/sec (note: violated by a number of recordings),

d. The acceleration spectrum of the earthquake time history that matches as closely as possible the UHS associated with the considered return period.

Table 5.6. Selected records for three hazard levels with 75, 475 and 2475 YRP

#	NGA ID	Earthquake	Year	Magn. (M_w)	Station	PGA (g)	Vs (m/sec)	Distance (km)	PGA Scaling
75 Years Return Period									
1	458	Morgan Hill	1984	6.19	Gilroy Array #4	0.22	221.8	11.54	1.07
2	549	Chalfant Valley-02	1986	6.19	Bishop - LADWP South St	0.25	271.4	17.17	0.97
3	595	Whittier Narrows-01	1987	5.99	Bell Gardens - Jaboneria	0.22	308.6	17.79	1.10
4	739	Loma Prieta	1989	6.93	Anderson Dam (Downstream)	0.24	488.8	20.26	0.98
5	985	Northridge-01	1994	6.69	LA - Baldwin Hills	0.24	297.1	29.88	1.00
6	988	Northridge-01	1994	6.69	LA - Century City CC North	0.26	278	23.41	0.94
7	1009	Northridge-01	1994	6.69	LA - Wadsworth VA Hospital North	0.25	392.2	23.6	0.95
		MEAN	---	6.48	---	0.24	322.56	20.52	1.00
475 Years Return Period									
1	558	Chalfant Valley-02	1986	6.19	Zack Brothers Ranch	0.45	271.4	7.58	1.14
2	752	Loma Prieta	1989	6.93	Capitola	0.53	288.6	15.23	0.96
3	959	Northridge-01	1994	6.69	Canoga Park - Topanga Can	0.36	267.5	14.70	1.43
4	963	Northridge-01	1994	6.69	Castaic - Old Ridge Route	0.57	450.3	20.72	0.90
5	1508	Chi-Chi, Taiwan	1999	7.62	TCU072	0.49	468.1	7.03	1.04
6	1512	Chi-Chi, Taiwan	1999	7.62	TCU078	0.44	443.0	8.20	1.15
7	1513	Chi-Chi, Taiwan	1999	7.62	TCU079	0.74	364	10.97	0.69
		MEAN	---	7.05	---	0.51	364.70	12.06	1.05
2475 Years Return Period									
1	368	Coalinga-01	1983	6.36	Pleasant Valley P.P. - yard	0.59	257.4	8.41	1.32
2	727	Superstition Hills-02	1987	6.54	Superstition Mtn Camera	0.68	362.4	5.61	1.14
3	982	Northridge-01	1994	6.69	Jensen Filter Plant	0.57	373.1	5.43	1.37
4	1044	Northridge-01	1994	6.69	Newhall - Fire Sta	0.58	269.1	5.92	1.34
5	1085	Northridge-01	1994	6.69	Sylmar - Converter Sta East	0.83	370.5	5.19	0.94
6	1602	Duzce, Turkey	1999	7.14	Bolu	0.73	326	12.04	1.07
7	3474	Chi-Chi, Taiwan-06	1999	6.30	TCU079	0.62	364	10.05	1.25
		MEAN	---	6.63	---	0.66	331.79	7.52	1.20

Based on the above stated criteria, the records summarized in Table 5.6 are selected for hazards with 75, 475 and 2475 YRP. As shown in the table above, the conditions of magnitude, distance and site conditions (the three most important parameters that describe the characteristics of a ground motion) are closely met by the selected records. The mean values for each return period are also provided. Finally, the scaling values that would be used if the records were scaled to the PGA dictated by the UHS are shown. The criteria used in the selection of the records result in scaling factors that are very close to unity. Using scale factors that are close to unity is essential to retain the characteristics of the earthquake time histories. It is important to note that the records could be scaled so that the mean spectrum of records for each hazard level closely matches the corresponding UHS; however, this technique usually results in very high scaling factors (especially for UHS with high return periods since there exist only a limited number of recordings with similar frequency domain characteristics). When the selected earthquake time histories are used for assessment purposes, and for a realistic estimation of structural response, it is not desirable to alter the characteristics of the ground motions by using high scaling factors.

The shaded rows of Table 5.6 indicate the records selected to be used in the design of structural frames for different performance objectives through inelastic dynamic analysis

(Section 5.5). These records are modified to be compatible with the UHS (see Section 5.2.4). All seven records in each set are used to determine aleatory uncertainty in ground motion process. The focus of this chapter is optimal seismic design of new building (not assessment of existing buildings); therefore, the use of spectrum-compatible records (as also suggested by seismic design codes) is warranted. For assessment purposes, the use of unmodified (natural) records would be more appropriate. It might be argued that more records should have been used to obtain the average demand or the dispersion; however, several thousands of inelastic dynamic time history analysis have been conducted; therefore, one earthquake record at each hazard level has been used in order to reduce to computational demand. Besides, it is known that a much smaller set of spectrum-compatible records (compared to scaled records) is needed to determine the average demand (e.g. Hancock et al., 2006; Al Atik and Abrahamson, 2010).

The acceleration response spectra for the selected time histories listed in Table 5.6 are shown in Figure 5.9(b). It is observed that after scaling based on PGA, the mean spectrum of the selected ground motions for 75 YRP closely matches the UHS; however, for hazards with 475 and 2475 YRP, the UHS gives higher spectral acceleration values than the mean spectra. Nevertheless, for the period range of interest (i.e. 0-1 sec), the mean curves are almost always above UHS. It is therefore expected that the selected sets of records adequately represent the considered hazard levels. The acceleration, velocity and displacement spectra as well as the time histories for the individual records are provided in Appendix C, Section C.2.

5.2.4. Design Earthquake Ground Motions

The earthquake ground motions that are highlighted in Table 5.6 are selected for design of structural frames. To achieve direct correspondence between the ground motions used for dynamic analysis, hazard levels and structural response, the highlighted records are modified such that their response spectra are compatible with the UHS. As mentioned previously, the critical period range for the structural frames considered here is from 0.3 to 0.5 sec; however, period elongation occurs during the inelastic dynamic analysis due to damage accumulation. Therefore, the ground motions are fit to UHS for a period range of 0-1 sec. Two different tools are used for the latter purpose (1) WAVGEN (Mukherjee and Gupta, 2002b); and (2) RSPMatch (Abrahamson, 1993). The RSPMatch tool allows for the selection of a period range for which spectrum matching will be performed. However, this option is not available in WAVGEN; therefore, when WAVGEN is utilized the spectra of the original ground motions are retained for periods greater than 1 sec in order not to introduce unrealistic low frequency oscillations in the time histories. The spectra and the acceleration time histories for the design ground motions before and after spectrum matching are shown in Figure 5.10 and Figure 5.11, respectively. It is observed that the RSPMatch tool provides superior results both in terms of closely matching the target spectrum (Figure 5.10) and having a time-varying amplitude that is similar to that of the original record (Figure 5.11). Thus, in Section 5.5 the compatible records obtained from the RSPMatch tool are employed for structural design using optimization techniques. These records are shown in the last column of Figure 5.11.

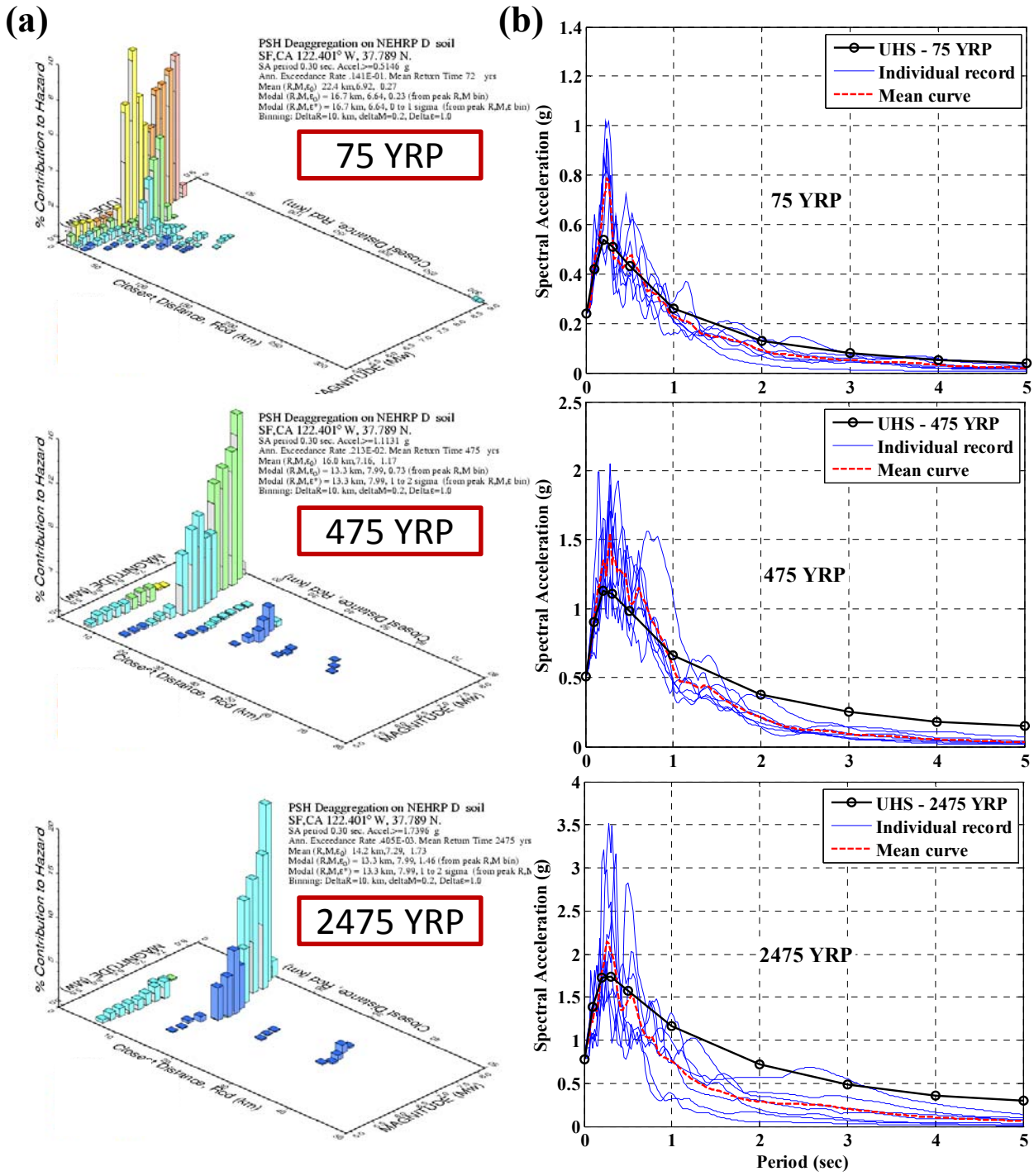

Figure 5.9. (a) Disaggregation results for 75, 475 and 2475 YRP at 0.3 sec (USGS, 2009a), (b) UHS and spectra for individual records at each return period

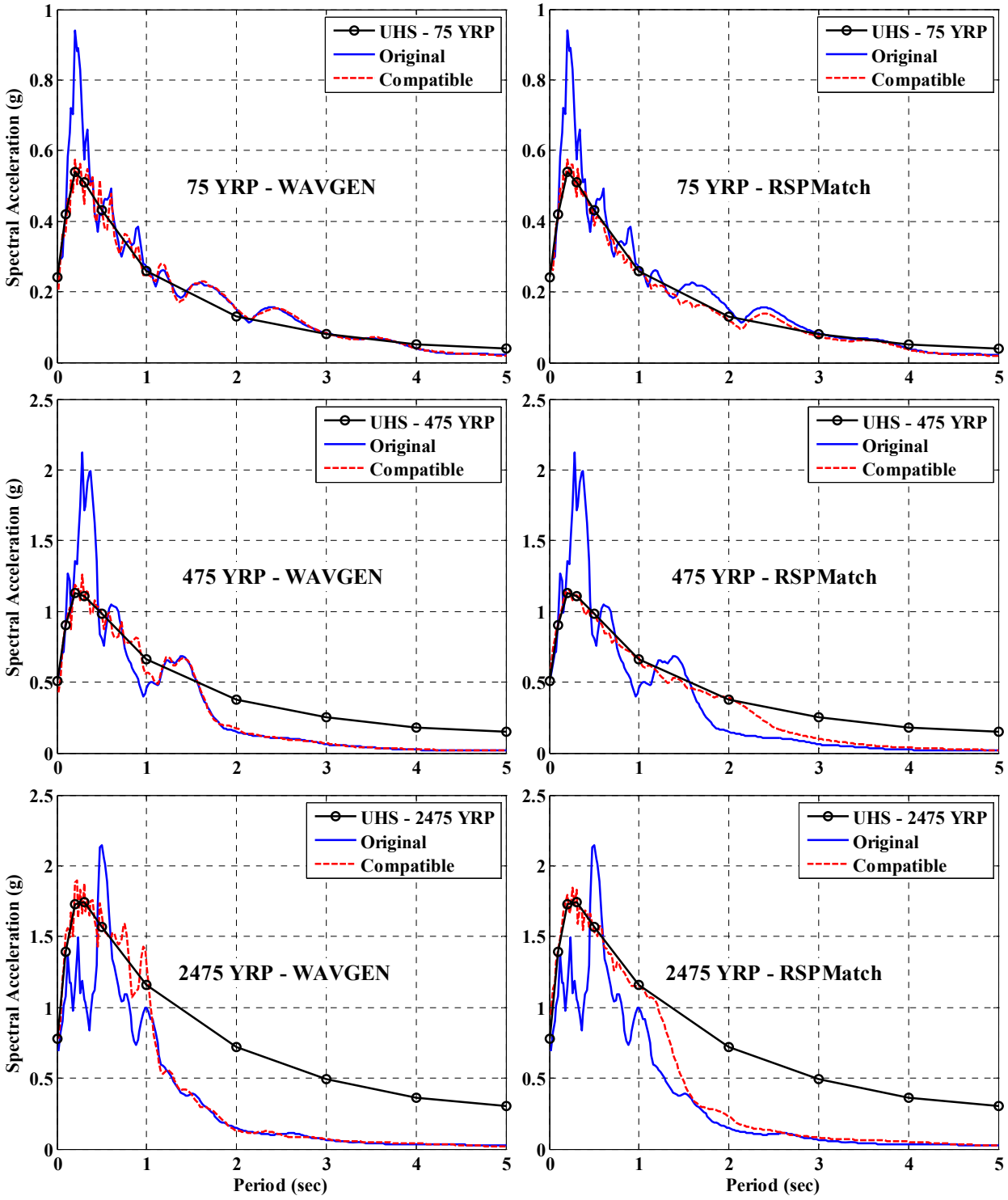

Figure 5.10. Spectra for design ground motions before and after spectrum matching using WAWGEN and RSPMatch

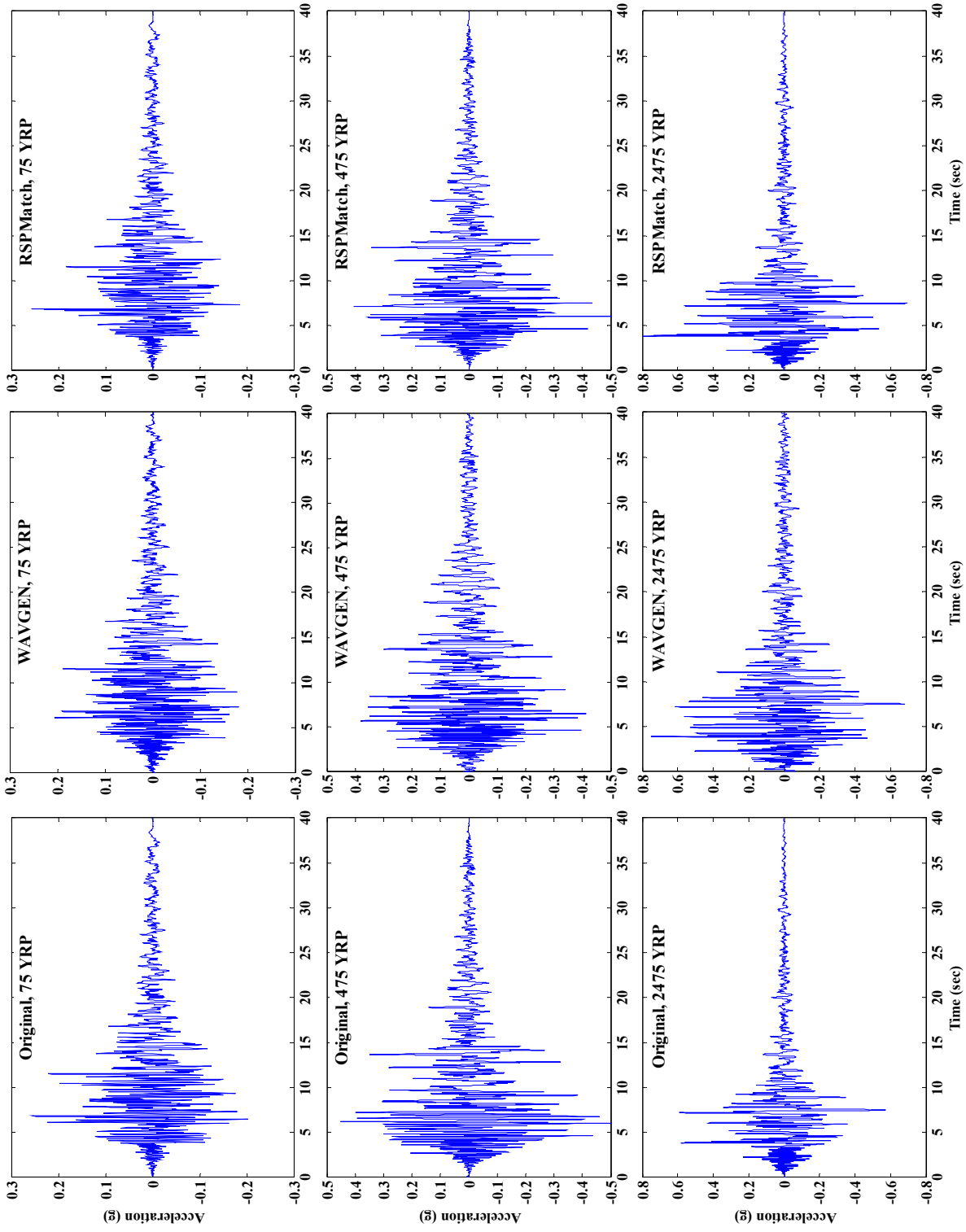

Figure 5.11. Original and spectrum-compatible ground motions for seismic design of structural frames

5.3. LIFE-CYCLE COST FORMULATION

This section is dedicated to derivation of the lifetime seismic damage cost of structures. The formulation is later on used in an optimization framework to investigate the lifetime seismic performance of RC, multi-material and ECC frames as discussed in Section 5.5; however, the derivations provided here are applicable to all structural types. The terminology used here is explained in Section 5.1.1.

The expected LCC of a structure is calculated as

$$E\left[C_{LC}\right] = C_0 + \int_0^L E\left[C_{SD}\right]\left(\frac{1}{1+\lambda}\right)^t dt = C_0 + \alpha L E\left[C_{SD}\right] \tag{5.1}$$

where C_0 is the initial construction cost, L is the service life of the structure and λ is the annual discount rate (here taken as 1 percent). Assuming that structural capacity does not degrade over time; the annual expected seismic damage cost, $E[C_{SD}]$, is governed by a Poisson process (implicit in hazard modeling), hence does not depend on time; and the structure is restored to its original condition after each hazard, the integral can be carried out as shown above. On the right hand side, α is the discount factor equal to $[1 - exp(-qL)]/qL$, where $q = ln(1 + \lambda)$. The initial cost estimation is discussed in the application example in Section 5.5, and $E[C_{SD}]$ is given by

$$E\left[C_{SD}\right] = \sum_{i=1}^{N} C_i P_i \tag{5.2}$$

where N is the total number of limit-states considered, P_i is the total probability that the structure will be in the ith damage state throughout its lifetime, and C_i is the corresponding cost as a fraction of the initial cost of the structure. P_i is given by

$$P_i = P\left(\Delta_D > \Delta_{C,i}\right) - P\left(\Delta_D > \Delta_{C,i+1}\right) \tag{5.3}$$

where Δ_D is the earthquake demand and $\Delta_{C,i}$ is the structural capacity, usually in terms of drift ratio, defining the ith damage state. The probability of demand being greater than capacity is evaluated as

$$P\left(\Delta_D > \Delta_{C,i}\right) = \int_0^{\infty} P\left(\Delta_D > \Delta_{C,i} \mid IM = im\right)\left|\frac{dv(IM)}{dIM}\right| dIM \tag{5.4}$$

where the first term inside the integral is the conditional probability of demand being greater than the capacity given the ground motion intensity, IM. This term is also known as the fragility function. The second term is the slope of the mean annual rate of exceedance of the ground motion intensity, in which $v(IM)$ defines the hazard curve and IM is PGA for this study. The conditional probability of demand being greater than the capacity (or fragility) is

$$P\left(\Delta_D > \Delta_{C,i} \mid IM = im\right) = \int_0^\infty P\left(\Delta_D > \delta \mid IM = im\right) f_{C,i}\left(\delta\right) d\delta \tag{5.5}$$

where δ is the variable of integration and $f_{C,i}$ is the probability density function for structural capacity for the i[th] damage state. This formulation assumes that demand and capacity are independent of each other. Structural capacity is assumed to follow a lognormal distribution with $\Delta_{C,i}$ and β_C that are, respectively, the mean and the standard deviation of the corresponding normal distribution. A preferred way of obtaining limit state threshold values is through pushover analysis. An example pushover curve is shown Figure 5.12(a) alongside the limit states. The lognormal probability density functions are illustrated in Figure 5.12(b), where threshold values 1, 2.5 and 7 percent interstory drift, respectively, are obtained from the pushover curve for the limit states IO, LS, and CP, respectively, and β_C is taken as 0.35. The uncertainty in capacity (here represented with β_C) accounts for factors such as modelling error and variation in material properties. A more detailed investigation of capacity uncertainty is available in Wen et al. (2004) and Kwon and Elnashai (2006).

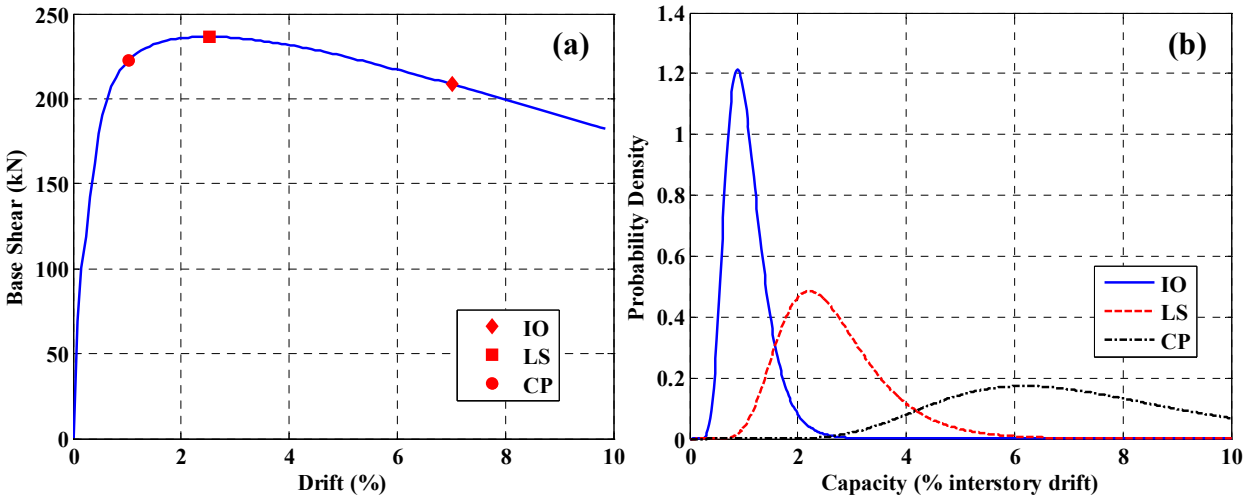

Figure 5.12. (a) A typical pushover curve and the limit state points that delineate the performance levels, (b) illustration of lognormal probability distributions for the three structural limit states

The earthquake demand is also assumed to follow a lognormal distribution, and the probability of demand exceeding a certain value, δ, is given by

$$P\left(\Delta_D > \delta \mid IM = im\right) = 1 - \Phi\left[\frac{\ln\left(\delta\right) - \lambda_{D|IM=im}}{\beta_D}\right] \tag{5.6}$$

where $\Phi[\cdot]$ is the standard normal cumulative distribution, $\lambda_{D|IM=im}$ is the natural logarithm of the mean of the earthquake demand as a function of the ground motion intensity, and β_D is the standard deviation of the corresponding normal distribution of the earthquake demand. Although

β_C and β_D are dependent on ground motion intensity, in most studies they are taken as constants due to lack of information. The evaluation of the dispersion in earthquake demand (here represented with β_D) is described in the application example in Section 5.5. The mean, μ_D, and the logarithmic standard deviation, β_D, of earthquake demand as continuous functions of the ground motion intensity could be described using (Aslani and Miranda, 2005)

$$\mu_D(IM) = c_1 \cdot IM^{c_2} \tag{5.7}$$

$$\mu_D(IM) = c_1 c_2^{IM} \cdot IM^{c_3} \tag{5.8}$$

$$\beta_D(IM) = c_4 + c_5 \cdot IM + c_6 \cdot IM^2 \tag{5.9}$$

where the constants c_1 through c_3 and c_4 through c_6 are determined by curve fitting to the data points that match the PGA of the ground motion records, with the mean and logarithmic standard deviation, respectively, of earthquake demand evaluated using inelastic dynamic analysis. Two different functional forms, Eqn. (5.7) and Eqn. (5.8), are given to estimate the mean of earthquake demand, μ_D. λ_D in Eqn. (5.6) is equal to $ln(\mu_D)$. Curve fitting to obtain, in continuous form, the mean and logarithmic standard deviation of the earthquake demand using Eqn. (5.8) and Eqn. (5.9) respectively, is shown in Figure 5.13.

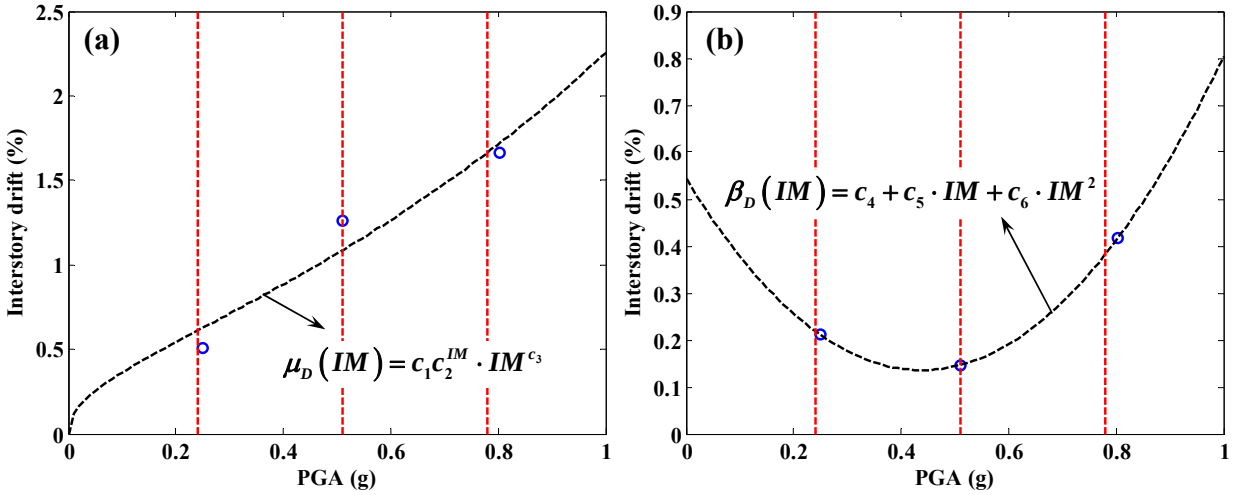

Figure 5.13. Curve fitting to obtain the (a) mean and (b) logarithmic standard deviation of earthquake demand in continuous form

The hazard curve can also be described in mathematical form

$$v(IM) = c_7 \cdot e^{c_8 \cdot IM} + c_9 \cdot e^{c_{10} \cdot IM} \tag{5.10}$$

where c_7 through c_{10} are constants to be determined from curve fitting to the hazard curve.

With the above-described formulation, each term in Eqn. (5.4) is represented as an analytical function of ground motion intensity, *IM*. Thus, using numerical integration, the desired

probabilities of Eqn. (5.3) can be easily calculated. As mentioned above, the cost of repair for the IO, LS, and CP limit states, C_i, in Eqn. (5.2) is usually taken as a fraction of the initial cost of the structure. Finally, the LCC is evaluated using Eqn. (5.1).

5.4. THE OPTIMIZATION ALGORITHM

A detailed review of most commonly used optimization algorithms is provided in the background section of Chapter 5. The objectives of the optimization problem considered here are highly nonlinear due to the inelastic dynamic analysis that is used to predict earthquake demand, and the derivatives with respect to the design variables are discontinuous. Furthermore, the design variables (i.e. section sizes and reinforcement ratios) are discrete. Therefore, the use of gradient-based optimization algorithms is not appropriate. As reviewed previously, the EA has been shown to be very efficient in solving combinatorial optimization problems. Here, the TS is selected and used to obtain the optimal solutions for the example application provided in Section 5.5.

5.4.1. Description of the Taboo Search Algorithm

The TS algorithm, first developed by Glover (1989, 1990), was adapted to multi-objective optimization problems by Baykasoglu et al. (1999b, a). An advantage of the TS algorithm is that a set of optimal solutions (Pareto-front or Pareto-set) can be obtained rather than a single optimal point in the objective function space. The methodology presented in Baykasoglu et al. (1999b, a) is used here with further modifications as described below.

The TS algorithm has also been applied to structural optimization problems. Bland (1998) applied the TS algorithm to the weight minimization of a space truss structure with various local minima and showed that the TS algorithm was very effective in finding the global minimum when both reliability and displacement constraints were applied. Manoharan and Shanmuganathan (1999) investigated the efficiency of TS, SA, GA and branch-and-bound in solving the cost minimization of steel truss structures. It was concluded that TS produced solutions better than or as good as both SA and GA, and it arrives at the optimal solution quicker than both of the other methods. As reviewed in Section 5.1.5.f, in a more recent study, Ohsaki et al. (2007) applied SA and TS algorithms for optimal seismic design of steel frames. It was concluded that TS was more advantageous than SA in terms of the diversity of its Pareto solutions and the ability of the algorithm to search the solutions near the Pareto front.

To describe the modified TS algorithm used here, the following definitions are first required. The taboo list includes points in the design space for which the objective functions are evaluated. Since inelastic dynamic time history analysis is computationally costly, this list is used to avoid multiple runs with the same combination of design variables. That is, no point in the taboo list is reevaluated. The Pareto list includes points that are not dominated by other points within the set for which the evaluation of objective functions is performed (i.e. the taboo list). The seed list includes the points around which optimal solutions are searched for. The latter are called as the neighboring points. These are basically the adjacent elements of the multidimensional array that

define the decision (or design) variables around the given seed point. The modified TS algorithm works as follows

a. Starting with the minimum cost combination, evaluate the objective function and add this point into taboo, seed and Pareto lists. Use this point as the initial seed point.

b. Find the neighboring points around the current seed. Here the number of neighboring points is chosen equal to the number of design variables and selected randomly amongst all the adjacent elements of the multidimensional array that defines the design variables.

c. Evaluate the objective function for all the neighboring points and add these into the taboo list.

d. Find the Pareto-front using the set of points for which the objective function is evaluated and update the Pareto list as the current Pareto-front.

e. Amongst the neighboring points for the current iteration, choose the one that is on the Pareto-front and minimizes the cost function as the next seed point. Add this point into the seed list. If there is no point that satisfies these conditions, randomly choose one of the points from the Pareto list amongst the ones not already in the seed list.

f. Check if the predetermined maximum number of objective function evaluations is exceeded; if yes, stop; if no, go to Step b.

5.4.2. Validation of the Taboo Search Algorithm

An important variable of the TS algorithm that must be established is the maximum number of objective function evaluations to obtain the set of optimal solutions. It is not feasible to search the entire search space to obtain the optimal solutions because here the earthquake demand is evaluated through inelastic dynamic analysis, which is accurate but computationally costly. Therefore, a maximum limit has to be set to the number of objective function evaluations (or the number design combinations that will be investigated) within the TS algorithm.

To perform this investigation the relatively simple frame shown in Figure 5.14 is utilized. Design variables considered for the optimization problem are the section dimensions and reinforcement ratios for the columns and beams. All the columns and both beams are assumed to have the same properties (a total of 6 design variables). The reinforcing bar diameter for the columns is fixed as 27 mm, and the number of reinforcing bars is varied between 4 and 24, with 2 bar increments to change the reinforcement ratio between 0.4-2.5 percent. For the beams, the reinforcement ratio is varied between 0.5-2 percent with 0.2 percent increments. Section dimensions vary with 50 mm increments between 406 mm and 762 mm for columns, and between 203 mm and 406 mm for beams. A total of 7704 possible combinations of the design variables are obtained as a result of selection on the minimum and maximum values and the increments. The initial cost is based only on the bare material costs. The unit prices for concrete and steel are assumed as \$130/m^3 and \$660/metric tons, respectively.

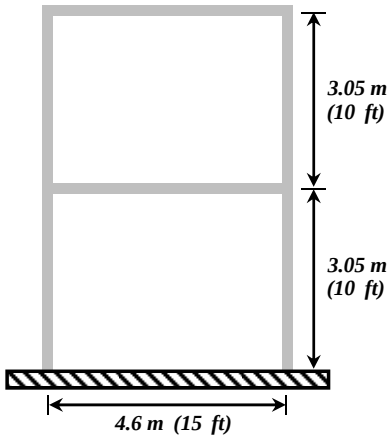

Figure 5.14. Selected frame to evaluate the performance of TS algorithm

For the relatively simple structure in the validation study, it is possible to perform inelastic dynamic analysis of all possible combinations of design variables. Investigation of all possible combinations is referred to as the exhaustive search (ES). The Pareto-front obtained from ES is considered as the exact solution for the problem since all possible combinations in the search space are evaluated. Therefore, the results from ES can be used to validate the TS algorithm. Initial cost vs. drift ratio, under the spectrum-compatible 475 YRP earthquake shown in Figure 5.11, is plotted for all possible combinations in Figure 5.15(a). The plot is in objective function space, and each design alternative is represented with a dot. The shown Pareto-front is the exact solution. It is compared to the TS algorithm solution, which is obtained with 770 objective function evaluations (10 percent of the total number of combinations) in Figure 5.15(b). It is observed that the TS algorithm is capable of finding, almost exactly, the Pareto-front from ES by searching 10 percent of the total number of combinations. Therefore, for the application example in Section 5.5, 10 percent of the total number of combinations is set as the maximum number of objective function evaluations to obtain the optimal solutions.

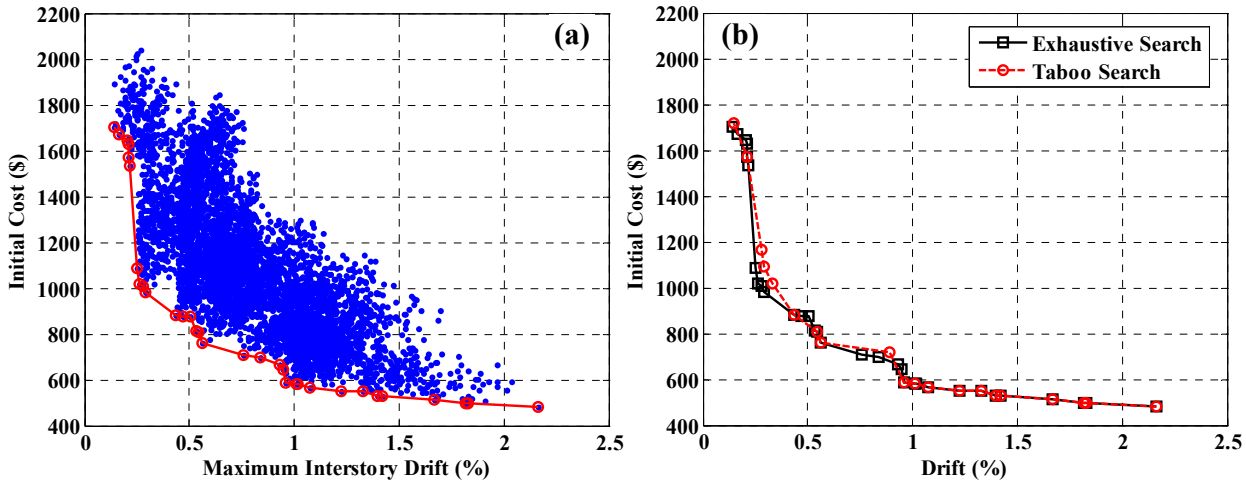

Figure 5.15. (a) Results from ES in the objective function space, (b) comparison of Pareto-fronts from ES and TS

5.5. APPLICATION OF THE LCC FORMULATION

Here the LCC formulation described in preceding sections is employed to investigate the use of ECC to improve the life-time performance of structural frames. Three different frames are considered: RC, multi-material and ECC. In the following, the reasoning behind the selection of the structural configuration, initial cost estimation, the evaluation of structural capacity and earthquake demand (as well as the associated uncertainty) are discussed. The structural frames are compared in terms of initial cost, LCC, and structural performance, also the objectives of the optimization problem.

5.5.1. Selected Structural Configuration and Cost Estimation

Two-story two-bay structural frames are selected. Three different frames are evaluated. The multi-material frame (referred to as MX) is illustrated in Figure 5.16. The critical locations, i.e. beam-column connections and the column bases, are made of ECC, while the rest of the frame is concrete. One tenth of the members' length on each side is assumed to be a critical region. RC only and ECC only frames are also considered, and the results from the three frames are compared. Seven design variables are defined for the optimization problem as given in Table 5.7, alongside the minimum and maximum values and increments. The combination of these design variables results in 30,000 cases that constitute the search space for each frame type.

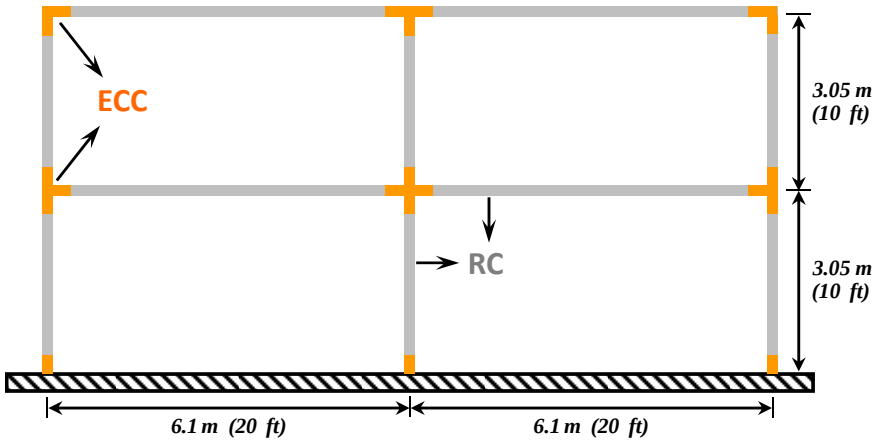

Figure 5.16. The considered structural frame for LCC optimization

Table 5.7. Design variables and ranges for the considered structural frames

	Minimum	Maximum	Increment
Column Reinforcement Ratio (%)	1.0	3.0	0.5
Beam Reinforcement Ratio (%)	1.0	3.0	0.5
Width of Exterior Columns (mm)	304.8	508	50.8
Width of Interior Columns (mm)	355.6	558.8	50.8
Width of Columns (mm)	304.8	457.2	50.8
Depth of Beams (mm)	406.4	558.8	50.8
Depth of Beams (mm)	304.8	406.4	50.8

Since this is an optimization problem requiring a large number of analyses, there is a compromise between the accuracy of structural response assessment and the complexity of the structure (or the number of decision variables). With an increase in the number of decision variables, the search space grows exponentially, impairing the feasibility of running the large number of analyses required to obtain the optimal solutions. The objective here is to evaluate and compare the structural performance of different frames (two of which feature ECC); therefore, accurately quantifying the structural response is essential. Thus, fiber-based finite element analysis is used (see Chapter 2 for more information on the numerical tool) to obtain the structural capacity and earthquake demand through nonlinear static (pushover) and inelastic dynamic time history analyses, respectively. In other words, accuracy is preferred over design complexity. Nevertheless, the two-story two-bay structural system depicted in Figure 5.16 represents an ordinary residential building and caters to the purpose of evaluating the performance of the different frames mentioned above. Furthermore, full beam-to-column (T) connections are included, and assessment of column overdesign requirements is featured.

As shown in Figure 5.16, 3.05 m (10 ft) and 6.1 m (20 ft) are selected as the story height and the bay width, respectively, which are typical values for ordinary buildings. The frame represents a middle frame that resists lateral loads in the 3-D configuration. In calculating the tributary area for the beams it is assumed that the bay width in the out-of-plane direction is the same, i.e. 6.1 m. As shown, 2-D modeling is performed for the building, and the lateral load resisting system in the out-of-plane direction is not considered. The dead and live loads for the floors are determined as 3.83 kN/m^2 (80 lb/ft^2) and 1.92 kN/m^2 (40 lb/ft^2), respectively, based on ASCE 7-05 (2006). The second floor is considered as a regular story, and full dead and live loads are applied. Gravity loads are calculated based on the distributed loads on beam tributary areas and applied as concentrated forces on the columns. The total seismic weight of the building is calculated based on the dead load plus the full live load. No vertical ground motion is considered in the finite element analysis of the frames; therefore lumped masses are located at the beam column connections.

It will be seen that the in-place cost (including both material and labor) of transverse reinforcement constitutes a significant portion of the cost of the structural frames considered here. Therefore, in order to determine the amount of reinforcement required for detailing the structural elements (beams and columns) and to check the code compliance of designs, the design spectral response acceleration parameters are first obtained from the International Building Code (2006), and lateral loads are calculated using the equivalent lateral force procedure of ASCE 7-05 (2006). In obtaining the design response acceleration parameters, the site and soil conditions described Section 5.2.1 are used. Gravity and lateral forces are then applied on a typical frame with intermediate values assigned to decision variables, considering the required load combinations based on ACI 318-08 (2008). Non-linear (considering P-Δ effects) elastic finite element analysis is performed to obtain the forces (axial, shear and bending moment) on the individual elements. It is noteworthy that although the element design forces obtained from analysis might differ depending on the relative stiffness of members that change with changing decision variables, the slight variations will not have a significant effect on the shear reinforcement design.

Once the forces on the beams and columns are determined, for each of the 30,000 designs mentioned above and for each of the structural frame types (i.e. RC, MX and ECC), the required shear reinforcement is determined based on ACI 318-08 (2008) if it is a RC element and JSCE (2008) if it is an ECC element.

The RC frames are assumed to be special moment resisting frames, and the shear design of beams and columns is carried out according to Chapter 11 and Sections 21.5 and 21.6 of ACI 318-08 (2008). The nominal shear strength, V_n, of a section is calculated as

$$V_n = V_c + V_s \tag{5.11}$$

where V_c and V_s are the nominal shear strengths provided by concrete and shear reinforcement, respectively. It is recommended in ACI 318-08 (2008) that for special moment resisting frames, if the axial compressive force on the member is less than 5 percent of the gross capacity of the section, V_c shall be taken as zero. Low levels of axial force is expected to occur during the dynamic response of the structure; therefore, in calculation of V_n, the contribution of the concrete is neglected. The nominal shear strength provided by the shear reinforcement is calculated as

$$V_s = \frac{A_v f_{yt} d}{s} \tag{5.12}$$

where s is the spacing of stirrups, A_v is the area of shear reinforcement within s, f_{yt} is the yield strength of shear reinforcement, and d is the depth of the section. V_n thus V_s is obtained from elastic finite element analysis as mentioned above. A_v and f_{yt} are fixed as 150 mm^2 and 310 MPa, respectively, and s is calculated according to Eqn. (5.12). In addition to the spacing requirements of Sections 21.5 and 21.6 in ACI 318-08 (2008), the equation that defines the minimum total cross-sectional area of transverse reinforcement, $A_{sh.min}$ is also applied

$$A_{sh,\min} = \max\left[0.3\frac{sb_c f_c^{'}}{f_{yt}}\left(\frac{A_g}{A_{ch}} - 1\right), 0.09\frac{sb_c f_c^{'}}{f_{yt}}\right] \tag{5.13}$$

where b_c is the core dimension perpendicular to the tie legs that constitute $A_{sh.min}$, f_c' is the compressive strength of concrete, A_g is the gross area of concrete section, A_{ch} is the cross-sectional area of the member measured to the outside edges of transverse reinforcement, and the remaining variables are defined previously.

For members of the ECC frames, the shear design of beams and columns is carried out according to recommendations by the Japan Society of Civil Engineers (2008) in which the design shear capacity, V_{yd} is obtained as

$$V_{yd} = V_{cd} + V_{sd} + V_{fd} + V_{ped} \tag{5.14}$$

where V_{cd} and V_{ped} are the design shear capacities provided by the mortar and prestressing steel (if any) and are taken equal to zero here. V_{sd} is the contribution of shear reinforcement steel and is obtained according to Eqn. (5.12) with a slight modification on d, which is taken equal to

$d/1.15$ and divided by a member factor equal to 1.1 (to convert the nominal capacity to design capacity). The shear strength provided by the reinforcing fiber, V_{fd} is given by

$$V_{fd} = \frac{f_{vd} b_w z}{\gamma_b \tan \beta_u} \tag{5.15}$$

where f_{vd} is the design tensile yield strength of ECC (here taken as 2.5 MPa), b_w is the width of the member, $z = d/1.15$, γ_b is the member factor equal to 1.3, and β_u is the angle of the diagonal crack surface to the member axis and is taken equal to $\pi/4$. It is important to note that Eqn. (5.11) and Eqn. (5.12) are used to calculate the nominal shear capacities, while Eqn. (5.14) and Eqn. (5.15) give the design shear capacities. The shear capacity of ECC does not degrade under load reversal, and the contribution from the reinforcing fiber that is obtained from Eqn. (5.15) is significantly larger than that provided by the shear reinforcement. As an example for a section 310 mm wide and with the material and rebar properties given above, the shear strength provided by the reinforcing fibers is equivalent to that provided by shear reinforcement with 70 mm spacing which is well below the spacing requirements of ACI 318-08 (2008) for the concrete sections considered here. Therefore, the required shear reinforcement according to Eqn. (5.14) is significantly lower for ECC sections.

JSCE (2008), prescribes no particular specifications for minimum number of stirrups when the design tensile yield strength of ECC, f_{vd}, is larger than 1.5 MPa. In other cases it is recommended that stirrup spacing be less than 3/4 of the effective depth of the member and less than 400 mm. When V_{sd} is greater than zero, the stirrup spacing shall be less than 1/2 of the effective depth and less than 300 mm. Here, f_{vd} is taken as 2.5 MPa; to be conservative; however, the minimum stirrup spacing requirement is applied in both cases whether V_{sd} is calculated to be greater than zero or not. For the MX frame where the structural elements constitute ECC at the element ends and concrete in the rest, requirements of each code are applied to the respective region.

The LCC of a building includes (not comprehensive)

- Initial cost
  - Cost of planning and design,
  - Cost of preparing the project site,
  - Material costs,
  - Fabrication cost,
  - Transportation cost of materials,
  - Receiving, handling and storage costs,
  - Erection cost,
  - Cost of operation of tools and machinery;
- Maintenance cost;

- Operating cost such as heating and electricity;
- Inspection cost to prevent a potentially major damage;
- Repair cost;
- Damage cost resulting from man-made or natural hazards;
  - Damage and repair cost of structural components,
  - Damage and repair cost of nonstructural components,
  - Cost due to loss of contents,
  - Relocation cost,
  - Direct/indirect economic loss,
  - Human injury cost,
  - Human fatality cost;
- Dismantling or demolishing cost.

Eqn. (5.1) and the LCC formulation here consider only the initial cost and damage cost due to a probable earthquake. Among the list of items under damage cost above, for simplicity only the damage and repair cost of structural components is considered. In accordance with the definition seismic hazard in Section 5.2, three structural damage states are used: IO, LS and CP. The repair cost for each damage state, C_i in Eqn. (5.2), is assumed to be 30, 70 and 100 percent, respectively, of the initial cost of the structure based on the correspondence of these damage states with the information provided by Fragiadakis et al. (2006b). For the hypothetical structural frames considered here, in the calculation of initial cost all the items given in the list above are taken into account except for the cost of planning, design and project site preparation. The cost of nonstructural components such as partitions and carpets is not included since they may vary significantly depending on the occupancy and use of building.

For the frames considered here, the initial cost is divided into material and labor costs which are calculated according to 2011 Building Construction Cost Data (RS Means, 2011). The material costs are shown in Table 5.8. A #3 and a #10 rebar (English) are used to calculate the cost of transverse and longitudinal reinforcement respectively. Bars for transverse reinforcement are assumed to be bent at the shop. The extra cost for bending is included in the prices shown in Table 5.8. The cost of steel is calculated based on a quantity of approximately 55 metric tons. The cost of ECC is taken as 2.5 times the cost of concrete, based on the detailed estimation in Section 3.2.2.

Labor costs are given in Table 5.9. RS Means (2011) does not differentiate between the cost of placing longitudinal and transverse reinforcement; however, it is known that placing and tying transverse reinforcement requires more time. Therefore, to differentiate the two it is assumed that placing transverse reinforcement takes 1.5 times longer than placing longitudinal reinforcement. The labor costs shown in Table 5.9 are adjusted accordingly. ECC mixtures do not include large particles. Additionally, as mentioned above, transverse reinforcement can be reduced for ECC

members due to higher shear strength provided by the fibers. Therefore, congestion is not observed in placing ECC, and very little compaction is required. These factors result in lower placing cost for ECC than for concrete. Here the cost of placing ECC is assumed to be 80 percent of the cost of placing concrete.

Table 5.8. Material costs

Item	Unit	Cost ($/unit)
Steel (longitudinal), A615 grade 40	metric ton	1018.5
Steel (transverse), A615 grade 40	metric ton	1253.8
Concrete, ready mix (35 MPa)	m^3	145.2
ECC, ready mix (60 MPa)	m^3	363.0
Cast-in-place concrete forming	m^2	29.6

Table 5.9. Labor costs

Item	Unit	Cost ($/unit)
Placing steel (longitudinal) in beams	metric ton	806.9
Placing steel (transverse) in beams	metric ton	2050.3
Placing steel (longitudinal) in columns	metric ton	948.0
Placing steel (transverse) in columns	metric ton	2182.6
Placing concrete	m^3	64.2
Placing ECC	m^3	51.4
Placing concrete forming	m^2	110.3

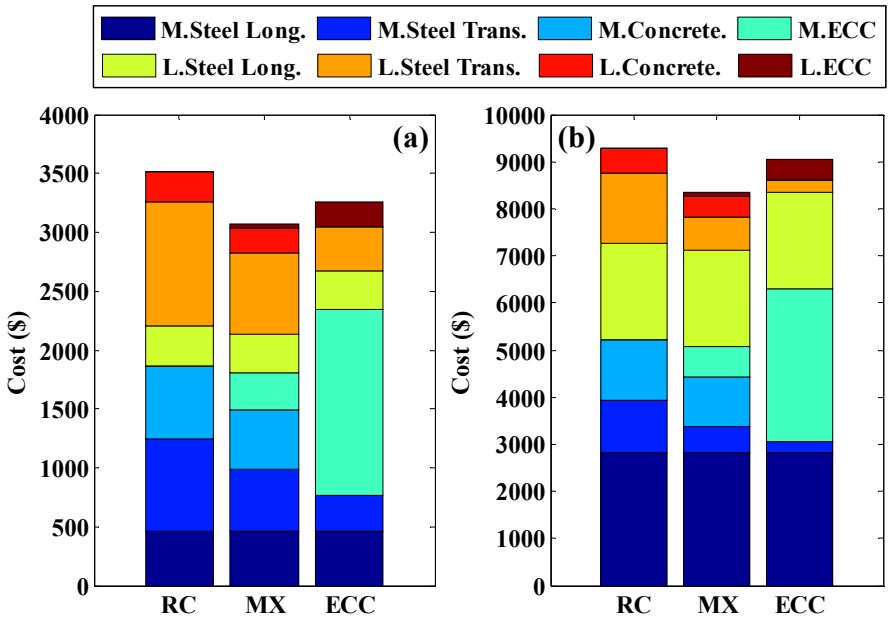

Figure 5.17. Breakdown of initial cost for the (a) lowest and (b) highest cost design alternative (M: material, L: labor)

The cost breakdown for the lowest and highest cost alternatives amongst the 30,000 design combinations is shown in Figure 5.17. It is seen that the increased cost of MX and ECC frames is due to the use of more expensive material, but the higher ECC cost is compensated for by a reduction in the material and labor cost of transverse reinforcement. It is observed that for the same combination of decision variables (listed in Table 5.7), the initial costs of the three frames are very close, with MX and RC frames having the lowest and highest cost, respectively. It is important to note that the cost of concrete forming is included in the calculation of initial cost; however, it is omitted in Figure 5.17 as it is the same for all frame types with the same cross-sectional dimensions.

5.5.2. Structural Capacity and Earthquake Demand

As mentioned earlier, structural performance is defined in three levels, IO, LS and CP, and these performance levels are mapped onto the three hazard levels with 75, 475 and 2475 YRP, respectively. The attainment of each performance level is described as reaching or exceeding a threshold value that defines the respective performance level (or structural limit state). It is noteworthy that the mapping between performance and hazard levels does not indicate that the respective hazard level is considered only in evaluating the probability of attaining a given performance level. As described in the Section 5.3, the fragility curve is first derived and then integrated over the entire range of the intensity measure to obtain the probability of reaching or exceeding each structural limit (or damage) state.

Structural capacity and earthquake demand are coupled. In other words, the capacity of a structure is not independent from the earthquake demand imposed on the structure. Capacity varies during strong ground shaking, and this variation in turn also influences the seismic forces acting on the structure. The most elegant way of evaluating the failure probabilities is through the joint probability density function of capacity and demand, which can be derived by Monte Carlo Simulation (MCS). However, there are various sources of uncertainty in evaluating failure probabilities including the inherent variability of ground motions and randomness in material properties. Accounting for all variability through MCS requires a large number of structural analyses. Performing MCS thus becomes infeasible when computationally demanding methods such as inelastic dynamic time history analysis is preferred. Therefore, it is assumed here that structural capacity is independent from earthquake demand.

Here, the limit state threshold values that define structural capacity are established using two different approaches. In the first approach, the threshold values are assumed to be the same for all frame types (RC, MX and ECC) and invariant to changes in decision variables. The threshold values for IO, LS and CP limit states are taken as 1, 2 and 4 percent of interstory drift following the recommendations by FEMA 273 (FEMA, 1997b). These are referred to here as generic limit states. In the second approach, to differentiate the responses of different frame types and to quantify the limit state threshold values more accurately, a finite element model is built for each optimal solution (those that are on the Pareto-front, see Section 5.5.3) and the limit state values are obtained from pushover analysis. The qualitative description of structural performance levels in FEMA 273 (FEMA, 1997b) provide a better correlation with the local response measures, i.e.

strains in steel, concrete and ECC. As an example, the CP performance level is defined as the occurrence of "extensive cracking and hinge formation in ductile elements, extensive spalling in columns and beams, and some reinforcement buckling." These descriptions may all be related to strains. The attainment of IO and LS limit states is defined as reaching or exceeding 0.5 and 5 percent strain, respectively, in longitudinal reinforcement in any of the columns or beams. These points are selected because they correspond to the onset of yielding and strain hardening in steel. The CP limit state is attained with 10 percent strain in longitudinal reinforcement or 1 percent compressive strain in the concrete (or ECC) core, whichever is reached first. Under load reversals these strain values might result in rupture or buckling of longitudinal reinforcement and/or crushing of core concrete (or ECC) leading to total loss of load carrying capacity and possibly resulting in progressive failure. In Figure 5.18 these limit states are shown on stress-strain curves of steel and concrete, which are also used as bases to define the constitutive models in the finite element modeling of concrete and steel materials.

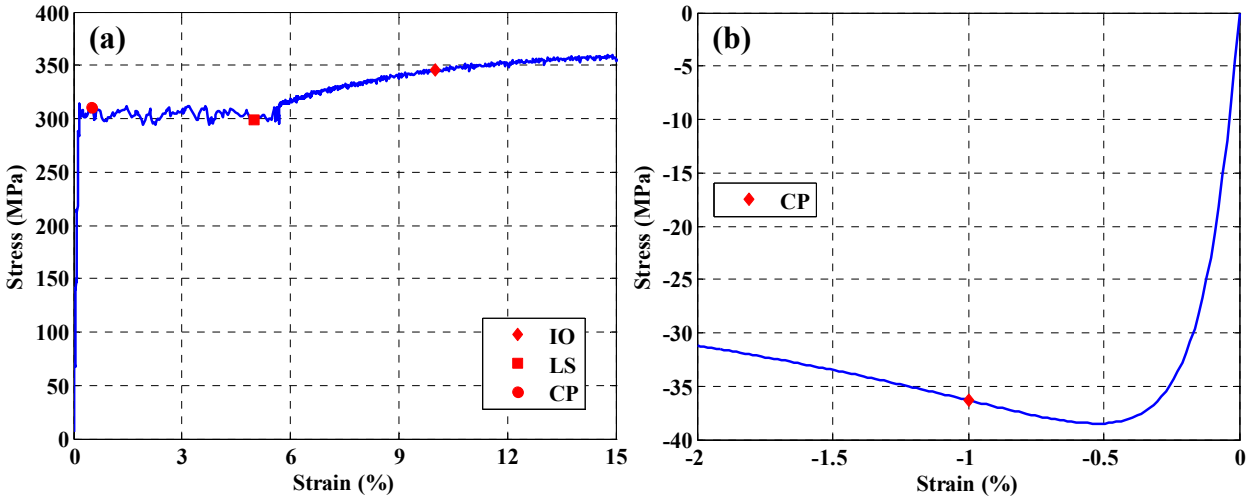

Figure 5.18. Limit state threshold value(s) defined on the stress-strain curve for (a) reinforcing steel, and (b) concrete

As mentioned earlier, finite element modeling is performed using ZEUS NL (Elnashai et al., 2010). For modeling concrete behavior, the nonlinear constant confinement constitutive relationship developed by Martinez-Rueda and Elnashai (1997) is used. The backbone curve in compression for the confined region is shown in Figure 5.18(b). The tensile and compressive strengths are selected as 2.7 MPa and 35 MPa, respectively, while a crushing strain of 0.35 percent is used. ECC is modeled using the constitutive relationship developed in Chapter 2 (model parameters are given in Table 5.10), and the Ramberg-Osgood model described in Section 4.2.1 is used to represent the response of reinforcing steel (the same model parameters are used as the ones shown in Figure 4.3). The limit state threshold values in terms of strains are mapped onto interstory drift through pushover analysis. This mapping is performed because the earthquake demand (as explained below) is defined in terms of interstory drift, and defining both structural capacity and earthquake demand in terms of same response quantity allows for the evaluation of failure probability using Eqn. (5.5).

Table 5.10. Parameters of the ECC constitutive model used for structural optimization

Parameter	E	ε_{t0}	σ_{t0}	ε_{tp}	σ_{tp}	ε_{tu}	ε_{cp}	σ_{cp}	ε_{cu}	σ_{cr}
Value	25000 (MPa)	6.9×10^{-5}	1.725 (MPa)	0.02	3.25 (MPa)	0.045	-0.003	-58.6 (MPa)	-0.1	-8.5 (MPa)

An example set of pushover curves for the three frames is shown in Figure 5.19 alongside the limit state threshold values of interstory drift, which are evaluated according to definitions made above. It is seen that there is a significant increase in the lateral load resistance of frames if ECC is used; however, the increase in the deformational capacity of the frames, i.e. the limit state threshold values, depends on the design variables, more specifically, the relative strength of beams and columns. The plot on the left exemplifies a case where the beams are significantly stronger than the columns (WCSB), while for the case on the right, the columns are stronger than beams (SCWB). It is seen that the structural capacity (according to the definitions above) of the SCWB frame is significantly higher than that of the WCSB frame. This difference is a consequence of concentration of the deformational demand at the column ends for the WCSB case. It is also observed that the capacity of MX frame is higher than RC and ECC frames which have similar capacities which results from the difference in locations of the plastic hinges for the three frames. For the RC and ECC frames the plastic hinges are confined to member ends while for the MX frame both the ECC portion of the members located at the ends (see Figure 5.16) and the adjacent RC elements yield. In other words, a certain portion of the deformational demand is transferred to the weaker adjacent elements, and attaining the threshold strain values is delayed. Similar or even slightly lower structural capacity for the ECC frame compared to the RC frame is again due to WCSB. Use of higher strength material ECC in beams increases the deformational demand in columns.

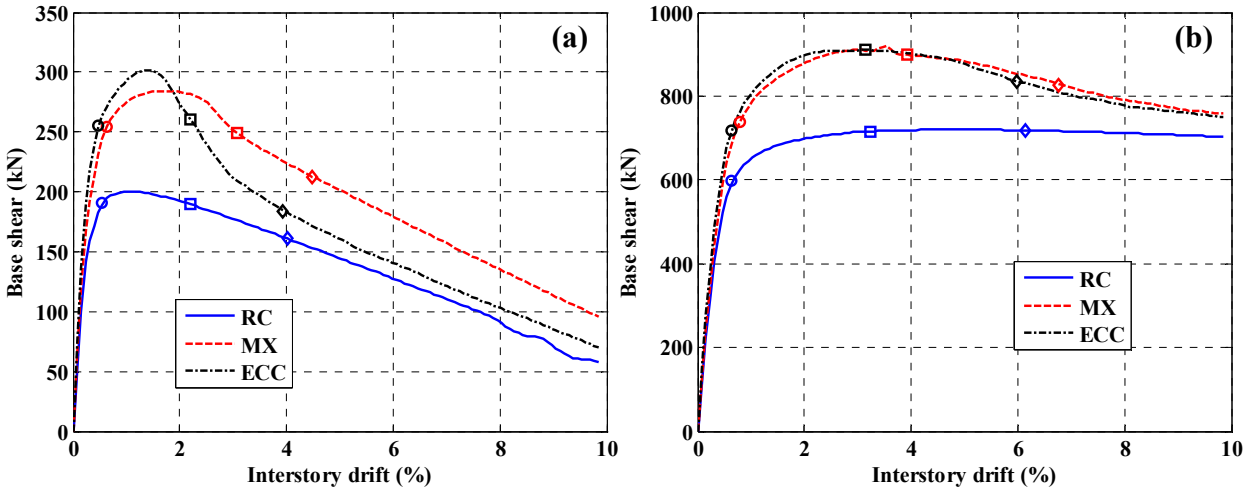

Figure 5.19. Example pushover curves (a) WCSB (b) SCWB cases

An important conclusion from these observations is that structural capacity is strongly affected by the decision variables. This fact warrants evaluation of capacity on a case-by-case basis for different designs in the search space. Here, the limit states are evaluated taking into account the properties of the frames for each design and are referred to as behavior-based limit

states (compare to generic limits states above). These behavior-based limit states are considered to be a more accurate representation of structural capacity. In Section 5.5.3, when LCC is evaluated, both generic and behavior-based limit states are used and the results compared.

The generic, i.e. 1, 2 and 4 percent interstory drift, and behavior-based limit states define the mean capacity of the structural frames, $\Delta_{C,i}$, at each limit state: IO, LS and CP. As mentioned in Section 5.3, the structural capacity is assumed to follow a lognormal distribution and to fully describe a lognormal distribution; it is also required to define the uncertainty (or dispersion) term, β_C. The uncertainty in capacity (due to sources such as modelling error, lack of knowledge and variation in material properties) was investigated in several studies, and the ranges are well established. In this study the uncertainty in capacity is assumed to be equal to 0.35, taking previous research as a reference (Wen et al., 2004; Kwon and Elnashai, 2006). This concludes the capacity evaluation of structural frames.

As described in Section 5.3, ground motion intensity, IM, is defined here in terms of PGA. The hazard curves for PGA and S_a at different structural periods are shown in Figure 5.8(a), and the derivation of site-specific ground motions compatible with different hazard levels is performed in Section 5.2. The PGA hazard curve is shown in Figure 5.20(a) along with curve fitting results using the functional form in Eqn. (5.10). For each design combination evaluated during the optimization process, the mean of earthquake demand at each hazard level (75, 475 and 2475 YRP), $\mu_{D|IM=im}$, is obtained by performing an inelastic dynamic time history analysis using the spectrum-compatible ground motions that are highlighted in Table 5.6 and shown in the rightmost column of Figure 5.11. As an example, Figure 5.20(b) shows the curve fitting to maximum interstory drift – PGA data points using a slightly different functional form than that given in Eqn. (5.7) [note that IM is raised to a power 2]. As mentioned earlier, these curve fitting operations are performed to represent each term in Eqn. (5.4) as an analytical function of the ground motion intensity and to facilitate the evaluation of the integral to obtain limit state probabilities.

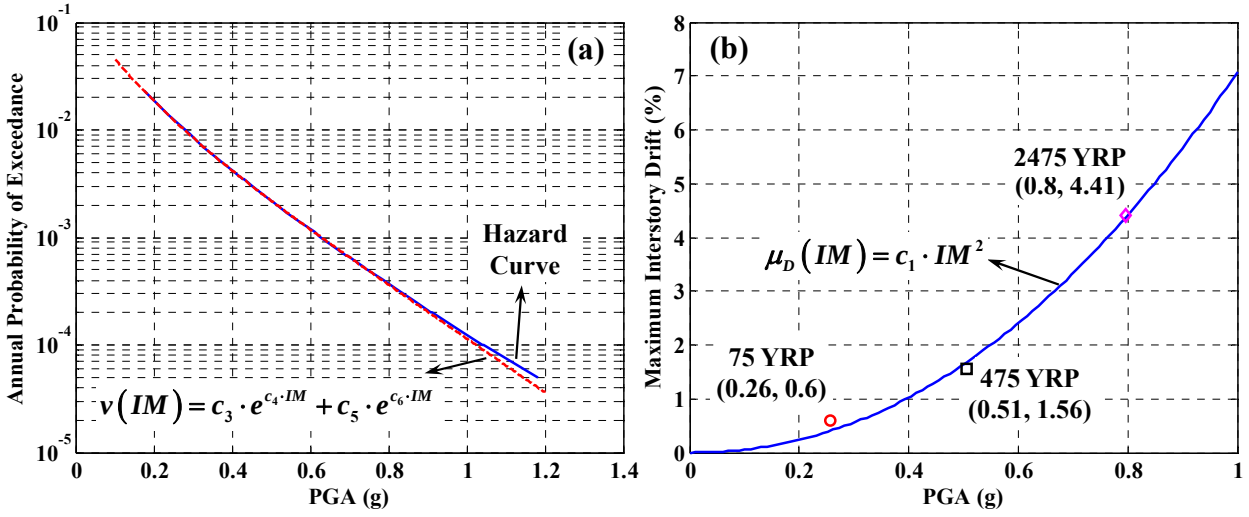

Figure 5.20. Curve fitting to (a) hazard curve (b) mean earthquake demand

Similar to the case of structural capacity, it is necessary to evaluate the dispersion in earthquake demand, β_D, to fully describe the lognormal distribution. In order to establish the β_D values for each hazard level used in the LCC model, 50 cases are selected randomly from the 30,000 combinations. The ground motions at each hazard level shown in Table 5.6 are scaled based on PGA to the corresponding values obtained from disaggregation (see Table 5.5). As shown in Table 5.6, the rigorous ground motion selection procedure results in scale factors that are close to unity which preserve the frequency domain characteristics of the records. Each of these 50 cases is subjected to scaled ground motions using inelastic dynamic time history analysis. A lognormal distribution is fitted to the earthquake demand at each return period and for each frame type to obtain the β_D values. They are then averaged for the 50 cases. The results are shown in Table 5.11. It is seen that the dispersion in earthquake demand increases for increasing hazard level. Here, 0.35, 0.4 and 0.5 are used as to describe the dispersion in earthquake demand at 75, 475 and 2475 YRP, respectively, and the dispersion is assumed to be invariant with respect to frame type.

Table 5.11. Dispersion in earthquake demand, β_D, at different hazard levels and for different frame types

	75 YRP	475 YRP	2475 YRP
RC Frame	0.33	0.41	0.53
MM Frame	0.42	0.41	0.48
ECC Frame	0.35	0.44	0.53

5.5.3. Optimization Results and Comparisons

Optimization results for each frame type and for each hazard level are shown in Figure 5.21. The results shown are in the solution space, i.e. the axes are two objectives of the problem: initial cost and structural performance (in terms of interstory drift). It is noteworthy that the structural capacity is not taken into account in this representation; in other words, the maximum interstory drift gives only the earthquake demand. Each dot in the figures represents a combination of design variables. A total of 3,000 dots exist in each plot (which is equal to the maximum number of objective function evaluations or 10 percent of the total number of combinations). The Pareto-fronts are also shown with solid lines. Note that after a certain level of interstory drift the initial cost starts to increase again (shown with a dotted line). The points on this portion of the line are not optimal solutions, and it is only shown to indicate the boundary of the search space. It is seen that the TS algorithm is very effective in confining the search to the portion of the search space close to the Pareto-front.

The Pareto-fronts are plotted separately in Figure 5.22. These results are very useful for decision makers. It allows the decision maker, whether the owner or the engineer, to choose among the set of optimal solutions depending on the requirements of the project. As an example, if the requirement of the project is that the maximum interstory drift under the 2475 year return period is less than four percent, one can easily find the least cost solution. Later, if the requirement of the project changes and it becomes necessary to limit the maximum interstory

drift to three percent, no additional analysis will be required to find the optimal solution. The Pareto-fronts for different frame types are compared in the right column of Figure 5.22. It is seen that the RC frame yields the highest initial cost solution for the same earthquake demand. The MX and ECC frames yield very similar results.

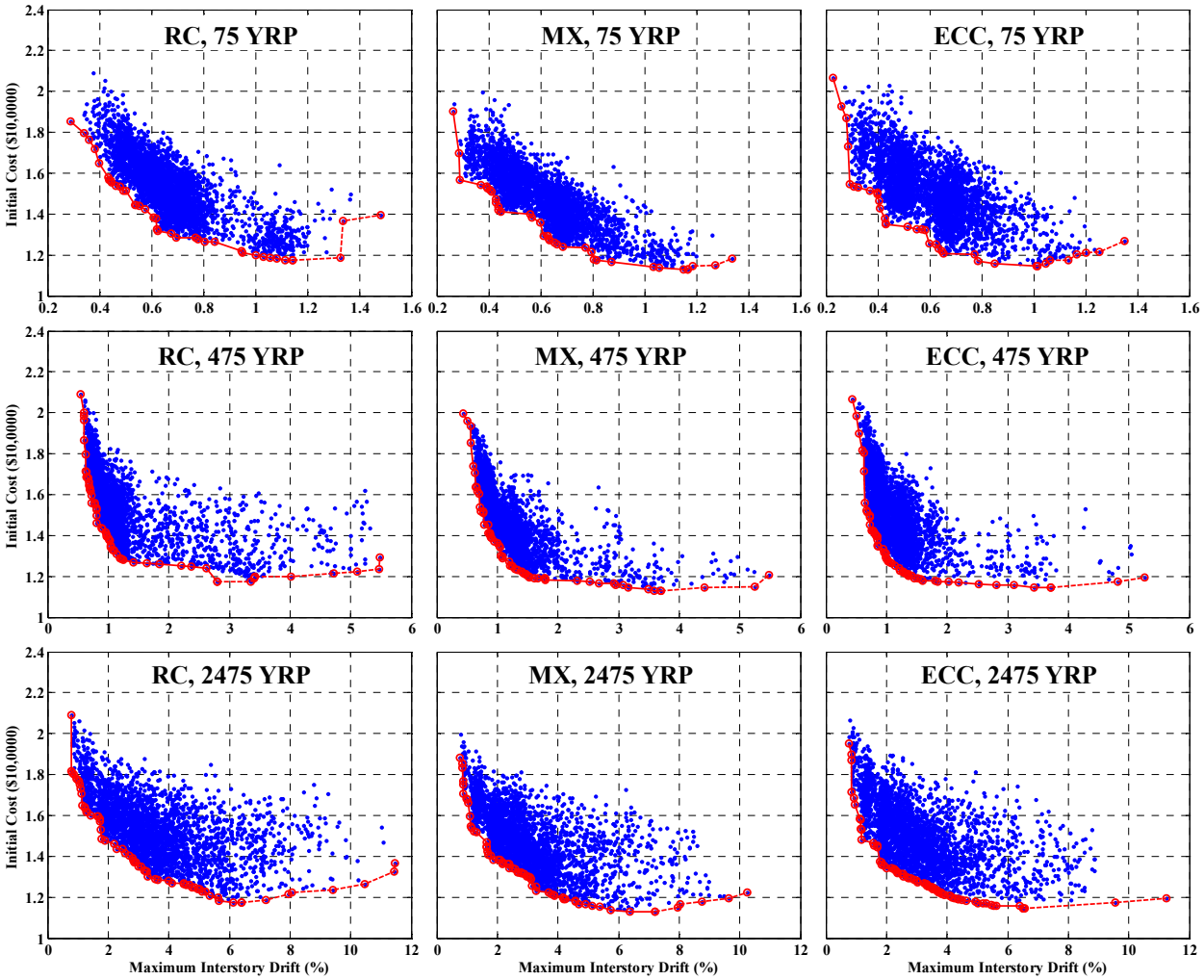

Figure 5.21. Optimization results for each frame type (RC, MX and ECC) and hazard level (75, 475 and 2475 YRP) in the solution space (initial cost vs. maximum interstory drift)

The seismic damage (or repair cost) of each frame is calculated using the LCC formulation described in Section 5.3 and the parameters specific to the application given in the preceding sections. The results (as a percentage of the initial cost) are shown in Figure 5.23. It is seen that if generic limit states are used (i.e. 1, 2 and 4 percent interstory drift for IO, LS and CP limit states, respectively) the RC frame yields the highest damage cost, while the MX and ECC frames give similar values [Figure 5.23(a)]. On the other hand, if behavior-based limit states are used, the difference between the three cases increases, and while again the RC frame yields the highest repair cost, the MX frame gives the lowest repair cost due to its increased structural capacity. The LCC (initial plus repair cost) is plotted against the maximum interstory drift obtained under

the 2475 YRP earthquake (hazard level is chosen arbitrarily) in Figure 5.24. The conclusions follow the same reasoning as explained for repair cost in Figure 5.23. It is seen in both figures that the LCC approaches the initial cost for solutions with high initial cost.

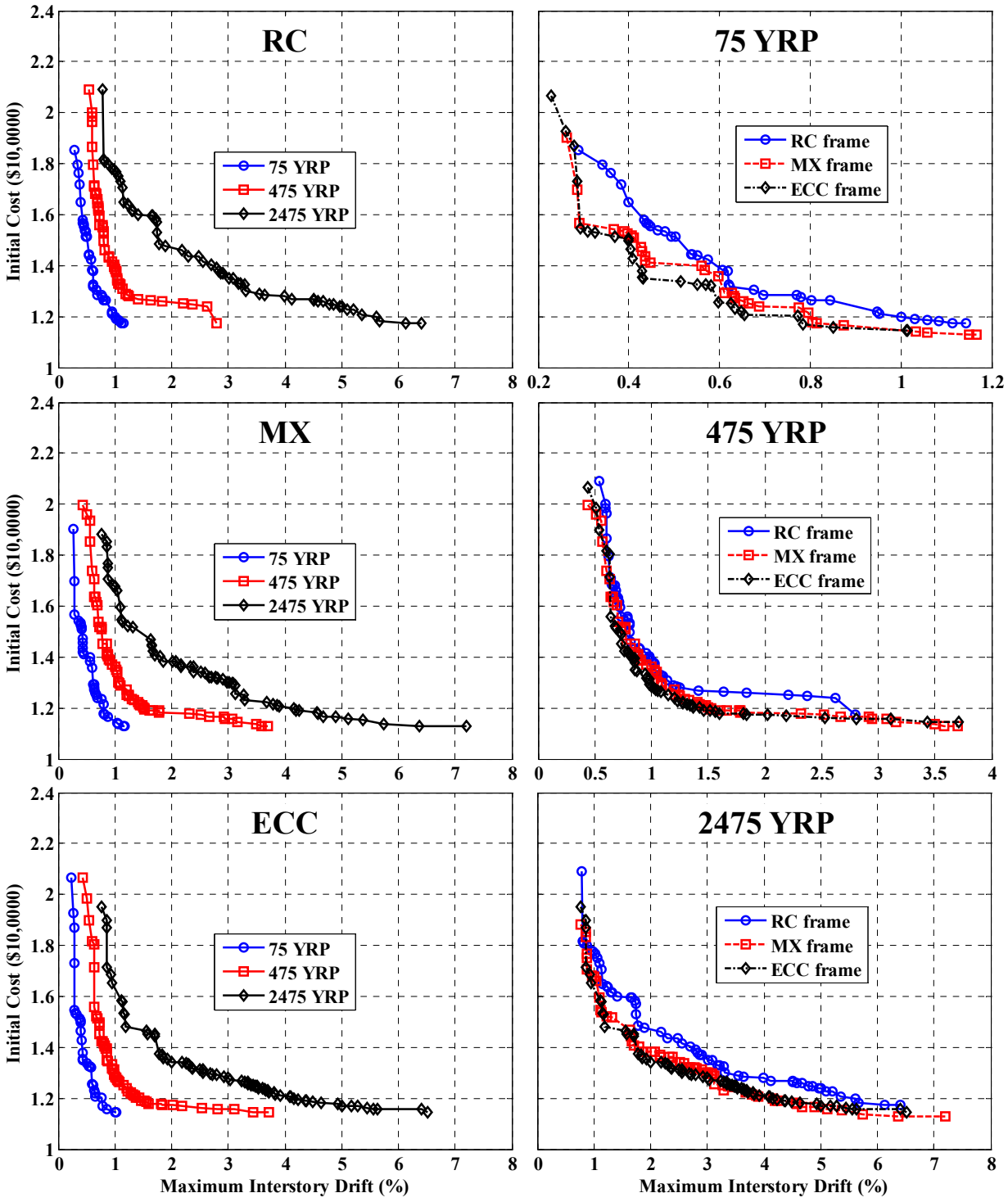

Figure 5.22. Pareto-fronts for different frame types (left column) and at different hazard levels (right column)

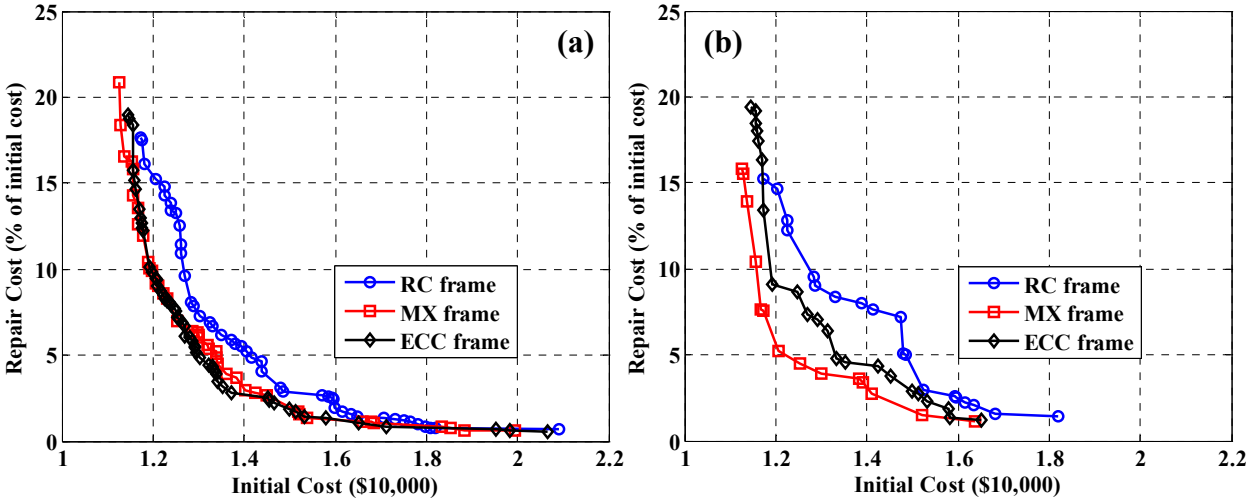

Figure 5.23. Repair (seismic damage) cost vs. initial cost using (a) generic (b) behavior-based limit states

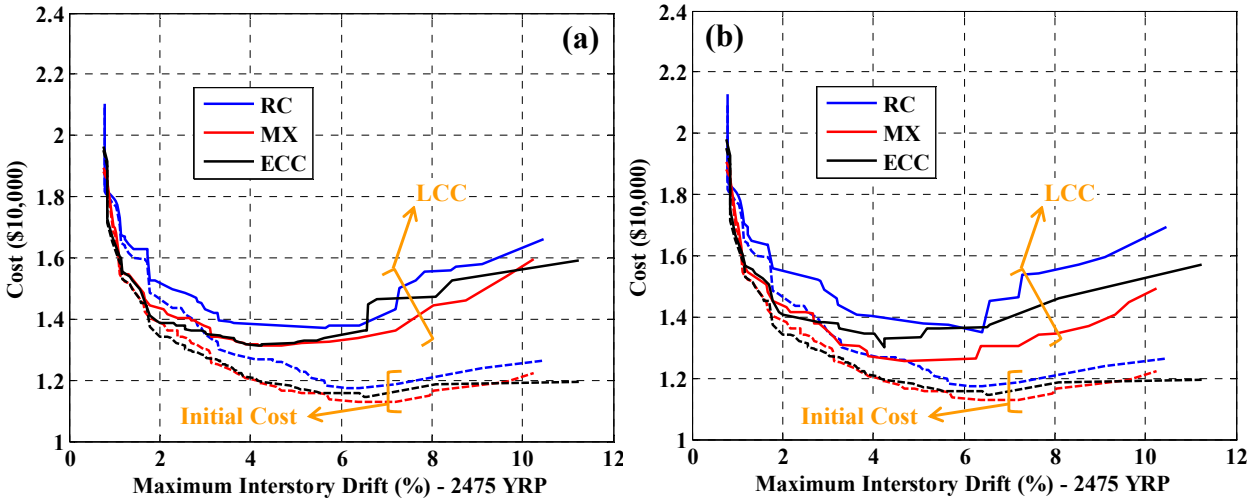

Figure 5.24. Initial and life-cycle cost vs. maximum interstory drift under the 2475 YRP earthquake, (a) generic (b) behavior-based limit states

5.6. CONCLUSIONS

The seismic design optimization that considers the LCC of buildings completes the seismic design framework described in Chapter 1. The shortcomings of studies in literature are identified through an extensive review, and a formulation is provided for LCC estimation that addresses the use of very rigorous procedures for each step from definition of seismic sources to generation of strong ground motions and structural response assessment. Contributions to the existing literature on the LCC assessment procedure result from

- Use of advanced analysis, which provides the most rigorous assessment of structural capacity and earthquake demand;

- Evaluation of the structural capacity (which has direct impact on the LCC) by taking into account not only the global behavior of the structure but also the local response, such as reinforcement yielding and concrete crushing;
- Use of system-specific limit states (rather than fixed value or generic limit states) to define structural capacity;
- Consideration of all major sources of uncertainty, from seismogenic source characteristics to material properties and structural modeling in calculating the limit state exceedance probabilities.

Seismic design optimization with consideration of the LCC is applied to three different structural systems to investigate potential ways to address the societal-level objectives of economy and sustainability that are described in Chapter 1. RC and ECC frames are considered in addition to a multi-material (MX frame) where ECC is applied selectively at the beam-column connections and column bases. The initial cost of these structural frames is calculated by taking into account all possible expenses that could make a difference in the cost estimation. Up-to-date prices are used for each item, and it is seen that as a result of savings in material and labor cost for shear reinforcement, MX and ECC frames have lower initial costs than the RC frame. In other words, the higher initial cost of ECC is compensated for by the savings in material and labor for shear reinforcement. Although the initial cost estimation is as simple as it could be, the findings are interesting because to the best of this author's knowledge, such an investigation has not been carried out before for the seismic design of buildings.

The optimization results indicate that if generic (fixed value) limit states are used the RC frame yields the highest repair and life-cycle cost while MX and ECC frames yield similar values. If behavior-based limit states are used, lower repair and life-cycle costs are obtained for the MX frame followed by the ECC and RC frames. This result is due to the higher structural capacity of the MX frame.

The most significant drawback of the LCC optimization methodology presented here is associated with the advanced analysis procedure for structural assessment. Structural capacity and earthquake demand are obtained from pushover and inelastic dynamic time history analysis which are computationally demanding and require considerable time when used to evaluate objective functions in an optimization problem. For a more complex structural system where more decision variables would be required, the computational time could increase to impractical levels. Furthermore, the cost estimation performed here is specific to buildings that are designed for high seismicity regions. For other structural types or for gravity load design where shear reinforcement is not a major source of cost, the use of ECC might not reduce the initial cost of the considered structural system.

6

CLOSURE

"Recent damaging earthquakes and hurricanes provided powerful reminders of how vulnerable we all are to the forces of nature. Even in an advanced industrial nation, our built environment is still quite susceptible to natural disasters. Consequently, one of the principal current challenges in structural engineering concerns the development of innovative design concepts to better protect structures, along with their occupants and contents, from the damaging effects of destructive environmental forces including those due to wind, waves and earthquakes."

Tsu T. Soong and Gary F. Dargush

Despite decades of observations and research, earthquakes remain the second deadliest natural hazard (following floods), posing great risk to human life and the social and economic welfare of societies. The focus of the research efforts presented here is the improvement of seismic design of buildings in terms of the societal level objectives of safety, economy and sustainability. A seismic design framework using consistent tools and rigorous formulations has been proposed for the comprehensive assessment of buildings subjected to earthquakes. A detailed conclusions section is provided at the end of each chapter. In the following, the main findings are summarized as bullet points, and recommendations for future research are provided.

6.1. CONCLUSIONS

Chapter 2 – Numerical Modeling of ECC

- A uniaxial constitutive model is developed for engineered cementitious composites (ECC). The model is compared against experimental data at the stress strain level, and it is observed that it captures the most distinct characteristics of the material response such as irrecoverable strains, pinching due to crack opening and closing, peak-to-peak stiffness within a cycle, and stiffness and strength degradation with reasonable accuracy.

- The only major drawback of the constitutive model is that it does not take into account degradation due partial looping. No experimental data are available to characterize the degradation due to partial loops, and improvements to the model are contingent upon further testing of material at the stress-strain level.
- The model is implemented into ZEUS NL, a fiber-based and finite element analysis package for structural-level simulations. The fiber-based analysis technique is selected for providing accurate estimations of the global response of complete structural systems with manageable computational demand.

Chapter 3 – Experimental Program

- An experimental program at the small-scale (with a scale factor of 1/8) is presented. Based on a detailed review of existing literature, the following are identified to be critical for success of small-scale testing: careful preparation of materials to match prototype behavior, consistency across specimens and high precision testing equipment capable of imposing desired loading and boundary conditions.
- Through the experimental program the performance of ECC is characterized at the component and system levels and compared against reinforced concrete (RC) behavior. Component behavior is investigated under monotonic and cyclic loading, while to investigate system behavior, sub-structured pseudo-dynamic testing (or hybrid simulation) is used.
- Making use of the logistical and financial advantages of small-scale testing, a range of parameters is investigated. It is demonstrated that the tests are repeatable and that different loading scenarios correlate well with each other.
- Important conclusions are made regarding material selection by comparing the performance of concrete and ECC mixtures with different costs and sustainability indices. It is observed that ECC specimens have a significantly higher initial stiffness compared to concrete specimens, ranging from 20 to 120 percent depending on the properties of the ECC mixture. The stiffness degradation of the two materials is similar, however.
- There is a significant amount of increase in lateral strength with ECC (over concrete) ranging from 43 to 68 percent.
- ECC member ductility is significantly higher than that of concrete when the life safety limit state is considered. Similar values are obtained for the collapse prevention limit state.
- ECC outperforms concrete with respect to energy absorption capacity. The increase in energy absorption is approximately 150 and 50 percent for life safety and collapse prevention limit states, respectively.
- Hybrid simulation of concrete and ECC frames under a ground motion representative of an earthquake that is associated with the collapse prevention socio-economic limit state

indicates that the cyclic tests under fixed-pinned and fixed-fixed boundary conditions are the lower and upper bounds, respectively, for the response of columns in terms of initial stiffness, strength, and energy absorption capacity. On the other hand, it is seen that stiffness and strength degradation under cyclic loading are significantly higher and do not correlate well with results obtained from hybrid simulation.

- The inter-correlation of the small-scale tests provides strong evidence in support of the use of ECC for seismic design applications.
- In general the findings support the main societal level objectives of this study. Specifically, the increased effectiveness in design with the use of ECC resulting from better utilization of longitudinal reinforcement, reduction in material usage and workmanship costs (due to higher shear resistance and confinement), and reduced deformational demand on structural members and higher damage tolerance that prevents structural damage are in line with the societal level objectives of safety, economy and sustainability in seismic design of buildings.

Chapter 4 – Structural Level Simulation

- Structural level simulation is conducted to validate the proposed constitutive model for ECC and to complement the existing data from the experimental program.
- Experimental data from cyclic, static time history (STH) tests and hybrid simulation conducted on ECC columns are utilized in the validation of the model at the component and system levels. The response of ECC columns in the experimental study is simulated using the numerical tool, and it is observed that the model captures the behavior of the material at the structural level equally well as it does at the material level. It is also seen that the numerical tool closely predicts the experimental behavior under realistic loading and boundary conditions, as shown in tests during hybrid simulation.
- The sensitivity of the structural level response metrics, stiffness, strength, ductility and energy absorption capacity, to ECC tensile strength and ductility is investigated through parametric analysis of ECC columns. It is observed that the material properties have a major effect on the member strength, ductility and energy absorption capacity while the member stiffness is relatively insensitive. The member strength, ductility and energy absorption capacity increase more than 50, 100 and 400 percent, with increasing material strength, ductility, and ductility respectively. The parametric study provides a good understanding of what can be achieved in terms of performance enhancement at the structural level by changing the tensile properties of the material, in this case ECC.
- The numerical tool, being extensively validated at the material, component and system levels, is proposed as an accurate tool for structural-level simulation under monotonic, cyclic and earthquake loading. The material model and the structural level analysis tool are available in an open-source environment for the use by the structural earthquake engineering community (http://code.google.com/p/zeus-nl/).

Chapter 5 – Life-Cycle Cost Optimization

- The shortcomings of studies in literature are identified through an extensive review. A life-cycle cost (LCC) formulation is provided that addresses these shortcomings using very rigorous procedures for each step from definition of seismic sources to generation of strong ground motions and structural response assessment. More specifically:
  - Advanced analysis tools are used to perform the most rigorous assessment of structural capacity and earthquake demand;
  - In evaluating the structural capacity not only the global behavior of the structure but also the local response, such as reinforcement yielding and concrete crushing, are taken into account;
  - System-specific limit states (rather than fixed value or generic limit states) are used to define the structural capacity;
  - All major sources of uncertainty, from seismogenic source characteristics to material properties and structural modeling are taken into account in calculating the limit state exceedance probabilities.
- Seismic design optimization with consideration of the LCC is applied to three different structural systems to investigate potential ways to address the societal-level objectives of economy and sustainability.
- RC and ECC frames are considered in addition to a multi-material (MX frame) where ECC is applied selectively at the beam-column connections and column bases. It is seen that as a result of savings in material and labor costs for shear reinforcement, MX and ECC frames have lower initial costs than the RC frame.
- The optimization results indicate that if generic (fixed value) limit states are used, the RC frame yields the highest repair and life-cycle cost while MX and ECC frames yield similar values. If behavior-based limit states are used, lower repair and life-cycle costs are obtained for the MX frame type followed by ECC and RC frames. This result is due to higher structural capacity of the MX frame.

6.2. RECOMMENDATIONS FOR FUTURE RESEARCH

Future research needs are based on the finding of this study and identified as follows:

- Further testing of ECC mixtures, at the stress-strain level under different loading scenarios, which have with different constituents, such as those investigated in this study.
- Development of multi-dimensional damage constitutive models for ECC based on the tests conducted at the stress-strain level.
- Implementation of the above mentioned constitutive models for detailed analysis of ECC structural components and sub-assemblages whose failure is governed by

combined shear, torsion and flexure. An example is 2-D or 3-D continuum modeling with discrete representation of reinforcement where bond slip feature is included.

- Comprehensive full- or large-scale testing of ECC with the main objective of investigating system behavior. Similar to testing ECC at the material level, the performance of mixtures with different costs, sustainability indices and mechanical properties should be investigated.
- Investigation of the performance of ECC under loads with strain rates similar to those observed during actual earthquakes through testing both at the material and structural level.
- Extensive structural level simulation supplemented with large-scale testing to derive seismic design guidance for typical ECC structures in both force- and displacement-based formats. More details are given in Section 4.4.
- Development of reliable damage cost models that include costs associated with damage to structural/nonstructural components, loss of contents, relocation, direct/indirect losses, and human fatality and injury. The damage cost models should also be mapped onto distinctly defined structural limit states for direct evaluation of LCC based on failure probabilities.
- Development of cost models to represent the environmental impacts of construction processes in terms of monetary value, or incorporating environmental impacts as a separate objective into the optimization problem.
- Development of complete LCC assessment tools that take into account all potential hazards and costs associated with initial construction, maintenance, operation, inspection, repair, damage and decommissioning.
- Development of simplified structural assessment tools with acceptable accuracy coupled with the use of high-performance computing for LCC optimization of complex structural systems with a large number of decision variables.

REFERENCES

ABCB (1996). *Building Code of Australia,* Australian Building Codes Board, CCH Australia Limited, Sydney, Australia.

Abrahamson, N. (1992). "Non-Stationary Spectral Matching," Seismological Research Letters, 63(1), 30.

Abrahamson, N., Atkinson, G. M., Boore, D. M., Bozorgnia, Y., Campbell, K. W., Chiou, B. S. J., Idriss, I. M., Silva, W. and Youngs, R. R. (2008). "Comparisons of the NGA Ground-Motion Relations," Earthquake Spectra, 24(1), 45-66.

Abrahamson, N. A. (1993). "Non-Stationary Spectral Matching Program RSPMatch," User's Manual.

Abrahamson, N. A. (2000). "State of the Practice of Seismic Hazard Evaluation." *GeoEng 2000*, Melbourne, Australia, 19-24.

Abrams, D. P. (1976). *Measured Hysteresis Relationships for Small-Scale Beams,* Civil Engineering Studies, Structural Research Series 432, University of Illinois at Urbana-Champaign, Urbana, Illinois, USA.

ACI (1979). *Committee 444: Models of Concrete Structures - State of the Art,* ACI 444 R-79, American Concrete Institute, Concrete International.

ACI (2008). *Building Code Requirements for Structural Concrete (ACI 318-08) and Commentary*, American Concrete Institute, Farmington Hills, Michigan, USA.

Adamu, A., Karihaloo, B. L. and Rozvany, G. I. N. (1994). "Minimum Cost Design of Reinforced Concrete Beams Using Continuum-Type Optimality Criteria," Structural and Multidisciplinary Optimization, 7(1), 91-102.

Ahmed, S. F., Maalej, M. and Paramasivam, P. (2007a). "Flexural Responses of Hybrid Steel-Polyethylene Fiber Reinforced Cement Composites Containing High Volume Fly Ash," Construction and Building Materials, 21(5), 1088-1097.

Ahmed, S. F. and Mihashi, H. (2007). "A Review on Durability Properties of Strain Hardening Fibre Reinforced Cementitious Composites (SHFRCC)," Cement and Concrete Composites, 29(5), 365-376.

Ahmed, S. F. U., Maalej, M. and Mihashi, H. (2007b). "Cover Cracking of Reinforced Concrete Beams Due to Corrosion of Steel," ACI Materials Journal, 104(2), 153-161.

Ahmed, S. F. U., Maalej, M. and Paramasivam, P. (2007c). "Analytical Model for Tensile Strain Hardening and Multiple Cracking Behavior of Hybrid Fiber-Engineered Cementitious Composites," Journal of Materials in Civil Engineering, 19(7), 527-539.

Ahmed, S. F. U., Mihashi, H. and Suzuki, S. (2006). "Mechanical Properties of Hybrid PVA Fibre Reinforced Cementitious Composites under Bending." *1st International Structural Specialty Conference, CSCE*, Calgary, Alberta, Canada, 1-10.

AISC (2005). *Steel Construction Manual, Load and Resistance Factor Design*, AISC 325-05, American Institute of Steel Construction.

Al Atik, L. and Abrahamson, N. (2010). "An Improved Method for Nonstationary Spectral Matching," Earthquake Spectra, 26(3), 601-617.

Ali, M. A. and White, R. N. (2001). "Automatic Generation of Truss Model for Optimal Design of Reinforced Concrete Structures," ACI Structural Journal, 98(4).

Alimoradi, A., Pezeshk, S. and Foley, C. M. (2007). "Probabilistic Performance-Based Optimal Design of Steel Moment-Resisting Frames. II: Applications," Journal of Structural Engineering, 133(6), 767-776.

Arisoy, B. and Wu, H. C. (2008). "Material Characteristics of High Performance Lightweight Concrete Reinforced with PVA," Construction and Building Materials, 22(4), 635-645.

ASCE (2006). *Minimum Design Loads for Building and Other Structures, ASCE/SEI 7-05*, American Society of Civil Engineers.

Aslani, H. and Miranda, E. (2005). "Probability-Based Seismic Response Analysis," Engineering Structures, 27(8), 1151-1163.

ASTM (2009). *Standard Specification for Deformed and Plain Carbon-Steel Bars for Concrete Reinforcement*, ASTM A615 / A615M - 09b, Book of Standards Volume 01.04, American Society for Testing of Materials, West Conshohocken, Pennsylvania, USA.

ATC (1996). *Seismic Evaluation and Retrofit of Concrete Buildings,* Report ATC-40, Applied Technology Council (ATC).

Bahn, B. Y. and Hsu, C. T. T. (1998). "Stress-Strain Behavior of Concrete under Cyclic Loading," ACI Materials Journal, 95(2), 178-193.

Balling, R. J., Pister, K. S. and Ciampi, V. (1983). "Optimal Seismic-Resistant Design of a Planar Steel Frame," Earthquake Engineering & Structural Dynamics, 11(4), 541-556.

Balling, R. J. and Yao, X. (1997). "Optimization of Reinforced Concrete Frames," Journal of Structural Engineering, 123(2), 193-202.

Baykasoglu, A., Owen, S. and Gindy, N. (1999a). "Solution of Goal Programming Models Using a Basic Taboo Search Algorithm," Journal of the Operational Research Society, 50(9), 960-973.

Baykasoglu, A., Owen, S. and Gindy, N. (1999b). "A Taboo Search Based Approach to Find the Pareto Optimal Set in Multiple Objective Optimization," Engineering Optimization, 31(6), 731-748.

Bažant, Z. P. (2005). *Scaling of Structural Strength*, Elsevier, Burlington, Massachusetts, USA.

Bažant, Z. P. and Kazemi, M. T. (1991). "Size Effect on Diagonal Shear Failure of Beams without Stirrups," ACI Structural Journal, 88(3), 268-276.

Beck, J. L., Chan, E., Irfanoglu, A. and Papadimitriou, C. (1999). "Multi-Criteria Optimal Structural Design under Uncertainty," Earthquake Engineering & Structural Dynamics, 28(7), 741-761.

Bendsøe, M. P., Guedes, J. M., Haber, R. B., Pedersen, P. and Taylor, J. E. (1994). "An Analytical Model to Predict Optimal Material Properties in the Context of Optimal Structural Design," Journal of Applied Mechanics, 61, 930-937.

Berard, A. (1874). *Improvement in Artificial Stone*, U.S. Patent No. 157 903.

Berke, L. (1970). *An Efficient Approach to the Minimum Weight Design of Deflection Limited Structures,* AFFDL-TM-70-04-FDTR, Wright-Patterson Air Force Base, Air Force Flight Dynamics Laboratory, Ohio, USA.

Bertero, V. V. and Zagajeski, S. W. (1979). "Optimal Inelastic Design of Seismic-Resistant Reinforced Concrete Framed Structures." *Nonlinear Design of Concrete Structures, CSCE-ASCE-ACI-CEB International Symposium*, Ontario, Canada, 219—272.

BIA (1995). *New Zealand Building Code,* Building Industry Authority, Standards New Zealand, Wellington, New Zealand.

Billington, S. L. and Yoon, J. K. (2004). "Cyclic Response of Unbonded Posttensioned Precast Columns with Ductile Fiber-Reinforced Concrete," Journal of Bridge Engineering, ASCE, 9, 353.

Bland, J. (1998). "Structural Design Optimization with Reliability Constraints Using Tabu Search," Engineering Optimization, 30(1), 55-74.

Bommer, J. J. (2002). "Deterministic vs. Probabilistic Seismic Hazard Assessment: An Exaggerated and Obstructive Dichotomy," Journal of Earthquake Engineering, 6(Special Issue 1), 43-73.

Bommer, J. J. (2003). "Uncertainty about the Uncertainty in Seismic Hazard Analysis," Engineering Geology, 70(1-2), 165-168.

Boore, D. M. and Atkinson, G. M. (2008). "Ground-Motion Prediction Equations for the Average Horizontal Component of PGA, PGV, and 5%-Damped PSA at Spectral Periods between 0.01 s and 10.0 s," Earthquake Spectra, 24(1), 99-138.

Brandt, A. M. (2008). "Fibre reinforced cement-based (FRC) composites after over 40 years of development in building and civil engineering," Composite Structures, 86(1-3), 3-9.

Burggrabe, A.-H. (1972). *Mikrobeton für modellstatische Untersuchungen: Grundlagen für d. Anwendung bewehrter Betonmodelle kleinen Maßstabes zur experimentellen Untersuchung von Stahlbetontragwerken*, Inst. f. Modellstatik (in German).

Caccese, V. and Harris, H. G. (1990). "Earthquake Simulation Testing of Small-scale Reinforced Concrete Structures," ACI Structural Journal, 87(1), 72-80.

Cameron, G. E., Chan, C. M., Xu, L. E. I. and Grierson, D. E. (1992). "Alternative Methods for the Optimal Design of Slender Steel Frameworks," Computers & Structures, 44(4), 735-741.

Camp, C., Pezeshk, S. and Cao, G. (1998). "Optimized Design of Two-Dimensional Structures Using a Genetic Algorithm," Journal of Structural Engineering, 124(5), 551-559.

Camp, C. V., Pezeshk, S. and Hansson, H. (2003). "Flexural Design of Reinforced Concrete Frames Using a Genetic Algorithm," Journal of Structural Engineering, 129(1), 105-115.

Campbell, K. W. and Bozorgnia, Y. (2008). "NGA Ground Motion Model for the Geometric Mean Horizontal Component of PGA, PGV, PGD and 5% Damped Linear Elastic Response Spectra for Periods Ranging from 0.01 to 10 s," Earthquake Spectra, 24(1), 139-171.

Canbolat, B. A., Parra-Montesinos, G. J. and Wight, J. K. (2005). "Experimental Study on Seismic Behavior of High-Performance Fiber-Reinforced Cement Composite Coupling Beams," ACI Structural Journal, 102(1), 159-166.

Castaños, H. and Lomnitz, C. (2002). "PSHA: Is It Science?," Engineering Geology, 66(3-4), 315-317.

CEN (2004). *Eurocode 8: Design of Structures for Earthquake Resistance,* Comite Europeen de Normalisation.

Ceranic, B., Fryer, C. and Baines, R. W. (2001). "An Application of Simulated Annealing to the Optimum Design of Reinforced Concrete Retaining Structures," Computers & Structures, 79(17), 1569-1581.

Černý, V. (1985). "Thermodynamical Approach to the Traveling Salesman Problem: An Efficient Simulation Algorithm," Journal of Optimization Theory and Applications, 45(1), 41-51.

Chan, C. M. (2001). "Optimal Lateral Stiffness Design of Tall Buildings of Mixed Steel and Concrete Construction," The Structural Design of Tall Buildings, 10(3), 155-177.

Chan, C. M. and Wang, Q. (2006). "Nonlinear Stiffness Design Optimization of Tall Reinforced Concrete Buildings under Service Loads," Journal of Structural Engineering, 132, 978-990.

Chan, C. M. and Zou, X. K. (2004). "Elastic and Inelastic Drift Performance Optimization for Reinforced Concrete Buildings under Earthquake Loads," Earthquake Engineering and Structural Dynamics, 33(8), 929-950.

Chandrangsu, K. and Naaman, A. E. (2003). "Comparison of Tensile and Bending Response of Three High Performance Fiber Reinforced Cement Composites." *International Workshop High Performance Fiber Reinforced Cement Composites*, eds. Naaman, A. E. and Reinhardt, H. W., 259-274.

Chang, G. A. and Mander, J. B. (1994). *Seismic Energy Based Fatigue Damage Analysis of Bridge Columns: Part 1 - Evaluation of Seismic Capacity,* Technical Report NCEER-94-0006, National Center for Earthquake Engineering Research, State University of New York at Buffalo, Buffalo, New York, USA.

Cheng, F. Y. and Truman, K. Z. (1985). *Optimal Design of 3-D Reinforced Concrete and Steel Buildings Subjected to Static and Seismic Loads Including Code Provisions,* Final Report Series 85-20, prepared by University of Missouri-Rolla, National Science Foundation, US Department of Commerce, Washington, District of Columbia, USA.

Chiou, B. S. J. and Youngs, R. R. (2008). "An NGA Model for the Average Horizontal Component of Peak Ground Motion and Response Spectra," Earthquake Spectra, 24(1), 173-215.

Chopra, A. K. and Goel, R. K. (2000). "Evaluation of NSP to Estimate Seismic Deformation: SDF Systems," Journal of Structural Engineering, 126(4), 482-490.

Chuang, E. Y. and Ulm, F. J. (2002). "Two-Phase Composite Model for High Performance Cementitious Composites," Journal of Engineering Mechanics, 128, 1314-1323.

Chung, T. T. and Sun, T. C. (1994). "Weight Optimization for Flexural Reinforced Concrete Beams with Static Nonlinear Response," Structural and Multidisciplinary Optimization, 8(2), 174-180.

Collins, M. P. and Kuchma, D. (1999). "How Safe Are Our Large, Lightly Reinforced Concrete Beams, Slabs, and Footings?," ACI Structural Journal, 96(4), 482-490.

Combescure, D. and Pegon, P. (1997). "[alpha]-Operator splitting time integration technique for pseudodynamic testing error propagation analysis," Soil Dynamics and Earthquake Engineering, 16(7-8), 427-443.

Cornell, C. A. (1968). "Engineering Seismic Risk Analysis," Bulletin of the Seismological Society of America, 58(5), 1583-1606.

Cornell, C. A., Jalayer, F., Hamburger, R. O. and Foutch, D. A. (2002). "Probabilistic Basis for 2000 SAC Federal Emergency Management Agency Steel Moment Frame Guidelines," Journal of Structural Engineering, 128(4), 526-533.

Deierlein, G. G., Krawinkler, H. and Cornell, C. A. (2003). "A Framework for Performance-Based Earthquake Engineering." *Pacific Conference on Earthquake Engineering*, Christchurch, New Zealand.

Den nordiske komite for bygnings bestemmelser (1978). *Strokturering av Byggregler (Structure for Building Regulations),* NKB Report No. 34, National Office of Building Technology and Administration, Oslo, Norway.

Dermitzakis, S. N. and Mahin, S. A. (1985). *Development of Substructuring Techniques for On-Line Computer Controlled Seismic Performance Testing,* Report UUCB/EERC-85/04, Earthquake Engineering Research Center, University of California, Berkeley.

Diaz, A. R. and Bendsøe, M. P. (1992). "Shape Optimization of Structures for Multiple Loading Conditions Using a Homogenization Method," Structural and Multidisciplinary Optimization, 4(1), 17-22.

Dick-Nielsen, L., Stang, H. and Poulsen, P. N. (2006). "Simulation of Strain-Hardening in ECC Uniaxial Test Specimen by Use of a Damage Mechanics Formulation." *Computational Modeling of Concrete Structures*, eds. Meschke, G., Borst, R. D., Mang, H. and Bicanic, N., Mayrhofen, Austria, 319-328.

Dick-Nielsen, L., Stang, H., Poulsen, P. N. and Kabele, P. (2007). "A Plastic Damage Mechanics Model for ECC." *FraMCos-6: 6th International Conference on Fracture Mechanics of Concrete and Concrete Structures*, eds. Carpinteri, A., Gambarova, P., G., F. and G., P., Catania, Italy, 1449-1456.

Dogan, E. and Krstulovic-Opara, N. (2003). "Seismic Retrofit with Continuous Slurry-Infiltrated Mat Concrete Jackets," ACI Structural Journal, 100(6), 713-722.

Eguchi, R. T., Goltz, J. D., Taylor, C. E., Chang, S. E., Flores, P. J., Johnson, L. A., Seligson, H. A. and Blais, N. C. (1998). "Direct Economic Losses in the Northridge Earthquake: A Three-Year Post-Event Perspective," Earthquake Spectra, 14, 245-264.

Elnashai, A. S. and Di Sarno, L. (2008). *Fundamentals of Earthquake Engineering*, Wiley, Chichester, United Kingdom.

Elnashai, A. S., Elghazouli, A. Y. and Dowling, P. J. (1990). "Verification of Pseudo-Dynamic Testing of Steel Members," Journal of Constructional Steel Research, 16, 153-161.

Elnashai, A. S. and Mwafy, A. M. (2002). "Overstrength and Force Reduction Factors of Multistorey Reinforced-Concrete Buildings," Structural Design of Tall Buildings, 11, 329-352.

Elnashai, A. S., Papanikolaou, V. K. and Lee, D. (2010). *ZEUS NL - A System for Inelastic Analysis of Structures,* User's Manual, Mid-America Earthquake (MAE) Center, Department of Civil and Environmental Engineeering, University of Illinois at Urbana-Champaign, Urbana, Illinois, USA.

Fadaee, M. J. and Grierson, D. E. (1996). "Design Optimization of 3D Reinforced Concrete Structures," Structural and Multidisciplinary Optimization, 12(2), 127-134.

Fafitis, A. and Shah, S. P. (1985). "Lateral Reinforcement for High-Strength Concrete Columns," ACI Special Publication, No. SP-87, 213-232.

Fantilli, A. P., Mihashi, H. and Vallini, P. (2005). "Strain compatibility between HPFRCC and steel reinforcement," Materials and Structures, 38(278), 495-503.

FEMA (1997a). *NEHRP Commentary on the Guidelines for the Seismic Rehabilitation of Buildings, FEMA 274*, Federal Emergency Management Agency, Washington, District of Columbia, USA.

FEMA (1997b). *NEHRP Guidelines for the Seismic Rehabilitation of Buildings, FEMA 273*, Federal Emergency Management Agency, Washington, District of Columbia, USA.

FEMA (2000). *Recommended Seismic Design Criteria for New Steel Moment-Frame Buildings, FEMA 350*, Federal Emergency Management Agency, Washington, District of Columbia, USA.

FEMA (2003a). *Multi-Hazard Loss Estimation Methodology, Earthquake Model: HAZUS-MH MRI,* Technical and User's Manual, Federal Emergency Management Agency, Washington, District of Columbia, USA.

FEMA (2003b). *NEHRP Recommended Provisions for Seismic Regulations for New Buildings and Other Structures, FEMA 450, Part 1: Provisions*, Federal Emergency Management Agency, Washington, District of Columbia, USA.

FEMA (2007). *Interim Testing Protocols for Determining the Seismic Performance Characteristics of Structural and Nonstructural Components (FEMA 461)*, Federal Emergency Management Agency, Washington, District of Columbia, USA.

Feng, T. T., Arora, J. S. and Haug, E. J. (1977). "Optimal Structural Design under Dynamic Loads," International Journal for Numerical Methods in Engineering, 11(1), 39–52.

Fischer, G. and Li, V. C. (2002). "Effect of Matrix Ductility on Deformation Behavior of Steel-Reinforced ECC Flexural Members under Reversed Cyclic Loading Conditions," ACI Structural Journal, 99(6), 781-790.

Fischer, G. and Li, V. C. (2003a). "Deformation Behavior of Fiber-Reinforced Polymer Reinforced Engineered Cementitious Composite (ECC) Flexural Members under Reversed Cyclic Loading Conditions," ACI Structural Journal, 100(1), 25-35.

Fischer, G. and Li, V. C. (2003b). "Intrinsic Response Control of Moment-Resisting Frames Utilizing Advanced Composite Materials and Structural Elements," ACI Structural Journal, 100(2), 166-176.

Foley, C. M., Pezeshk, S. and Alimoradi, A. (2007). "Probabilistic Performance-Based Optimal Design of Steel Moment-Resisting Frames. I: Formulation," Journal of Structural Engineering, 133(6), 757-766.

Foley, C. M. and Schinler, D. (2003). "Automated Design of Steel Frames Using Advanced Analysis and Object-Oriented Evolutionary Computation," Journal of Structural Engineering, 129(5), 648-660.

Fragiadakis, M., Lagaros, N. D. and Papadrakakis, M. (2006a). "Performance-Based Earthquake Engineering Using Structural Optimisation Tools," International Journal of Reliability and Safety, 1(1-2), 59-76.

Fragiadakis, M., Lagaros, N. D. and Papadrakakis, M. (2006b). "Performance-Based Multiobjective Optimum Design of Steel Structures Considering Life-Cycle Cost," Structural and Multidisciplinary Optimization, 32(1), 1-11.

Fragiadakis, M. and Papadrakakis, M. (2008). "Performance-Based Optimum Seismic Design of Reinforced Concrete Structures," Earthquake Engineering & Structural Dynamics, 37(6), 825-844.

Fukuyama, H., Iso, M., Ogaw, A. and Suwada, H. (2007). "Mitigation of Damage Due to Crack of RC Elements Utilizing High Performance Fiber Reinforced Cementitious Composites." *High Performance Fiber Reinforced Cement Composites 5 (HPFRCC 5)*, eds. Reinhardt, H. W. and Naaman, A. E., 427-435.

Fukuyama, H., Matsuzaki, Y., Nakano, K. and Sato, Y. (1999). "Structural performance of beam elements with PVA-ECC." *High Performance Fiber Reinforced Cement Composites 3 (HPFRCC 3)*, eds. Reinhardt, H. W. and Naaman, A. E., 531-542.

Fukuyama, H., Matsuzaki, Y., Sato, Y., Iso, M. and Suwada, H. (2000). "Structural Performance of Engineered Cementitious Composite Elements." *Composite and Hybrid Structures, 6th ASCCS International Conference on Steel-Concrete Composite Structures*, 969-976.

Fukuyama, H. and Suwada, H. (2003). "Experimental Response of HPFRCC Dampers for Structural Control," Journal of Advanced Concrete Technology, 1, 317-326.

Fukuyama, H., Suwada, H. and Ilseung, Y. (2002). "HPFRCC Damper For Structural Control." *JCI International Workshop on Ductile Fiber Reinforced Cementitious Composites (DFRCC): Application and Evaluation*, Takayama, Japan, 21-22 October.

Ganzerli, S., Pantelides, C. P. and Reaveley, L. D. (2000). "Performance-Based Design Using Structural Optimization," Earthquake Engineering & Structural Dynamics, 29(11), 1677-1690.

Gencturk, B. and Elnashai, A. S. (2008). "Development and Application of an Advanced Capacity Spectrum Method," Engineering Structures, 30, 3345-3354.

Geng, Y. P. and Leung, C. K. Y. (1997). "Micromechanics-based FEM Simulation of Fiber-Reinforced Cementitious Composite Components," Computers & Structures, 64(5-6), 973-982.

Ghaboussi, J. and Lin, C.-C. J. (1998). "New Method of Generating Spectrum Compatible Accelerograms Using Neural Networks," Earthquake Engineering & Structural Dynamics, 27(4), 377-396.

Ghobarah, A. (2001). "Performance-Based Design in Earthquake Engineering: State of Development," Engineering Structures, 23(8), 878-884.

Gholizadeh, S. and Salajegheh, E. (2009). "Optimal Design of Structures Subjected to Time History Loading by Swarm Intelligence and an Advanced Metamodel," Computer Methods in Applied Mechanics and Engineering, 198(37-40), 2936-2949.

Gilbertsen, N. D. and Moehle, J. P. (1980). *Experimental Study of Small-Scale R/C Columns Subjected to Axial and Shear Force Reversals,* Civil Engineering Studies, Structural Research Series 481, University of Illinois at Urbana-Champaign, Urbana, Illinois, USA.

Glover, F. (1989). "Tabu Search - Part I," ORSA Journal on Computing, 1(3), 190-206.

Glover, F. (1990). "Tabu Search - Part II," ORSA Journal on Computing, 2(1), 4-32.

Goldberg, D. E. (1989). *Genetic Algorithms in Search Optimization and Machine Learning,* Reading, Addison-Wesley Longman.

Govindaraj, V. and Ramasamy, J. V. (2005). "Optimum Detailed Design of Reinforced Concrete Continuous Beams Using Genetic Algorithms," Computers & Structures, 84(1-2), 34-48.

Gutenberg, B. and Richter, C. F. (1944). "Frequency of Earthquakes in California," Bulletin of the Seismological Society of America, 34(4), 185-188.

Habel, K., Denarie, E. and Bruhwiler, E. (2007). "Experimental Investigation of Composite Ultra-High-Performance Fiber-Reinforced Concrete and Conventional Concrete Members," ACI Structural Journal, 104(1), 93-101.

Hakuno, M., Shidawara, M. and Hara, T. (1969). "Dynamic Destructive Test of a Cantilever Beam Controlled by an Analog-Computer," Transactions of the Japan Society of Civil Engineers, 171, 1-9 (in Japanese).

Hakuno, M., Yokoyama, K. and Sato, Y. (1972). "Real Time Dynamic Test on a Model Pile Foundation," Transactions of the Japan Society of Civil Engineers, 200, 85-90 (in Japanese).

Han, T. S., Feenstra, P. H. and Billington, S. L. (2003). "Simulation of Highly Ductile Fiber-Reinforced Cement-Based Composite Components Under Cyclic Loading," ACI Structural Journal, 100(6), 749-757.

Hancock, J., Watson-Lamprey, J., Abrahamson, N. A., Bommer, J. J., Markatis, A., McCoyh, E. and Mendis, R. (2006). "An Improved Method Of Matching Response Spectra of Recorded Earthquake Ground Motions Using Wavelets," Journal of Earthquake Engineering, 10(1 supp 1), 67 - 89.

Hannant, D. J. (1978). *Fibre Cements and Fibre Concretes*, Wiley.

Heseltine, M. (1991). *Building and Buildings: The Building Regulations 1991*, HMSO Publications, No. 2768, London, United Kingdom.

Holland, J. H. (1975). *Adaptation in Natural and Artificial Systems,* Reading, University of Michigan Press, Ann Arbor, Michigan, USA.

Holub, C. (2005). "Similitude Considerations for Small Scale Distributed Hybrid Simulation of Reinforced Concrete Structures," MS Thesis, Department of Civil and Environmental Engineering, University of Illinois at Urbana-Champaign, Urbana, Illinois, USA.

Holub, C. (2009). "Interaction of Variable Axial Load and Shear Effects in RC Bridges," PhD Thesis, Department of Civil and Environmental Engineering, University of Illinois at Urbana-Champaign, Urbana, Illinois, USA.

Hou, T. C. and Lynch, J. P. (2005). "Monitoring Strain in Engineered Cementitious Composites Using Wireless Sensors." *International Conference on Fracture (ICF XI)*, Turin, Italy, 20–25.

Huang, M. W. and Arora, J. S. (1997). "Optimal Design of Steel Structures Using Standard Sections," Structural and Multidisciplinary Optimization, 14(1), 24-35.

ICBO (1997). *Uniform Building Code,* International Conference of Building Officials (ICBO), Whittier, California, USA.

ICC (2006). *International Building Code,* International Code Council (ICC), Washington, District of Columbia, USA.

Inokuma, A. (2002). "Basic Study of Performance-Based Design in Civil Engineering," Journal of Professional Issues in Engineering Education and Practice, 128, 30.

ISO (1980). *Performance Standards in Buildings - Contents and Presentation,* International Organization for Standardization, ISO6420-1980 (E), Geneva, Switzerland.

ISO (1984). *Performance Standards in Buildings - Principles for Their Preparations and Factors to be Considered,* International Organization for Standardization, ISO6421-1984 (E).

Izzuddin, B. A. and Elnasahi, A. S. (1993a). "Adaptive Space Frame Analysis, Part II: A Distributed Plasticity Approach," Proceedings of the Institution of Civil Engineers, Structures and Buildings, 99, 317-326.

Izzuddin, B. A. and Elnasahi, A. S. (1993b). "Eulerian Formulation for Large-Displacement Analysis of Space Frames," Journal of Engineering Mechanics, 119(3), 549-569.

Jain, S. K. and Navin, R. (1995). "Seismic Overstrength in Reinforced Concrete Frames," Journal of Structural Engineering, 121(3), 580-585.

Jenkins, W. M. (1992). "Plane Frame Optimum Design Environment Based on Genetic Algorithm," Journal of Structural Engineering, 118(11), 3103-3112.

Jeong, S.-H. and Elnashai, A. S. (2005). "Analytical Assessment of an Irregular RC Frame for Full-Scale 3D Pseudo-Dynamic Testing, Part II: Condition Assessment and Test Deployment," Journal of Earthquake Engineering, 9(2), 265-284.

JSCE (2000). *Earthquake Resistant Design Codes in Japan,* Japan Society of Civil Engineers, Tokyo, Japan.

JSCE (2008). *Recommendations for Design and Construction of High Performance Fiber Reinforced Cement Composites with Multiple Fine Cracks (HPFRCC)*, Japan Society of Civil Engineers, Tokyo, Japan.

Kabele, P. (2002). "Equivalent Continuum Model of Multiple Cracking," Engineering Mechanics (Association for Engineering Mechanics, Czech Republic), 9(1/2), 75-90.

Kanagasundaram, S. and Karihaloo, B. L. (1990). "Minimum Cost Design of Reinforced Concrete Structures," Structural and Multidisciplinary Optimization, 2(3), 173-184.

Kanda, T., Hiraishi, M. and Sakata, N. (2004). "Tensile Properties of ECC in Full-Scale Production." *Fifth International Conference on Fracture Mechanics of Concrete and Structures*, ed Li, V. C., Vail, Colorado, USA, 1013-1020.

Kanda, T., Saito, T., Sakata, N. and Hiraishi, M. (2002). "Fundamental Properties of Direct Sprayed ECC." *JCI International Conference on Ductile Fiber Reinforced Cementitious Composites (DFRCC) - Application and Evaluation*, 133-142, Takayama, Japan.

Kanda, T., Watanabe, S. and Li, V. C. (1998). "Application of Pseudo Strain Hardening Cementitious Composites to Shear Resistant Structural Elements," AEDIFICATIO Publishers, Fracture Mechanics of Concrete Structures, 3, 1477-1490.

Kappos, A. J. (1999). "Evaluation of Behaviour Factors on the Basis of Ductility and Overstrength Studies," Engineering Structures, 21(9), 823-835.

Karsan, I. D. and Jirsa, J. O. (1969). "Behavior of Concrete under Compressive Loadings," Journal of the Structural Division, ASCE, 95(ST12), 2543-2563.

Kelly, A. (1972). "Reinforcement of Structural Materials by Long Strong Fibres," Metallurgical and Materials Transactions B, 3(9), 2313-2325.

Keoleian, G. A., Kendall, A., Dettling, J. E., Smith, V. M., Chandler, R. F., Lepech, M. D. and Li, V. C. (2005). "Life Cycle Modeling of Concrete Bridge Design: Comparison of Engineered Cementitious Composite Link Slabs and Conventional Steel Expansion Joints," Journal of Infrastructure Systems, 11(1), 51-60.

Kesner, K. and Billington, S. L. (2005). "Investigation of Infill Panels Made from Engineered Cementitious Composites for Seismic Strengthening and Retrofit," Journal of Structural Engineering, 131(11), 1712-1720.

Kesner, K. E. and Billington, S. L. (2004). *Tension, Compression and Cyclic Testing of Engineered Cementitious Composite Materials,* Technical Report MCEER-04-0002, Multidisciplinary Center for Earthquake Engineering Research.

Kim, N.-S., Lee, J.-H. and Chang, S.-P. (2009). "Equivalent Multi-phase Similitude Law for Pseudodynamic Test on Small Scale Reinforced Concrete Models," Engineering Structures, 31(4), 834-846.

Kim, S. J. and Elnashai, A. S. (2008). *Seismic Assessment of RC Structures Considering Vertical Ground Motion,* MAE Center Report No. 08-03, Mid-America Earthquake (MAE) Center, Department of Civil and Environmental Engineeering, University of Illinois at Urbana-Champaign, Urbana, Illinois, USA.

Kim, W., El Attar, A. and White, R. N. (1989). *Small-Scale Modeling Techniques for Reinforced Concrete Structures Subjected to Seismic Loads,* Technical report NCEER-88-0041, National Center for Earthquake Engineering Research, Buffalo, New York, USA.

Kim, Y. Y., Fischer, G., Lim, Y. M. and Li, V. C. (2004). "Mechanical Performance of Sprayed Engineered Cementitious Composite Using Wet-Mix Shotcreting Process for Repair Applications," ACI Materials Journal, 101(1), 42-49.

Kirkpatrick, S., D., G. J. C. and Vecchi, M. P. (1983). "Optimization by Simulated Annealing," Science, 20(4598), 671-680.

Kocer, F. Y. and Arora, J. S. (1999). "Optimal Design of H-Frame Transmission Poles for Earthquake Loading," Journal of Structural Engineering, 125(11), 1299-1308.

Kong, H.-J., Bike, S. G. and Li, V. C. (2003). "Constitutive Rheological Control to Develop a Self-Consolidating Engineered Cementitious Composite Reinforced with Hydrophilic Poly(Vinyl Alcohol) Fibers," Cement and Concrete Composites, 25(3), 333-341.

Kramer, S. L. (1996). *Geotechnical Earthquake Engineering*, Prentice Hall, Upper Saddle River, New Jersey, USA.

Krawinkler, H. (1999). "Challenges and progress in performance-based earthquake engineering." *International Seminar on Seismic Engineering for Tomorrow – In Honor of Professor Hiroshi Akiyama*, Tokyo, Japan.

Krinitzsky, E. L. (2002). "Epistematic and Aleatory Uncertainty: A New Shtick for Probabilistic Seismic Hazard Analysis," Engineering Geology, 66(1-2), 157-159.

Krstulovic-Opara, N. and Al-Shannag, M. J. (1999). "Slurry Infiltrated Mat Concrete (SIMCON)-Based Shear Retrofit of Reinforced Concrete Members," ACI Structural Journal, 96(1), 105-115.

Kurihashi, Y., Taguchi, F., Kishi, N. and Mikami, H. (2006). "Experimental Study on Static and Dynamic Response Behavior of PVA Short-Fiber Mixed RC Slab." *2nd International Congress*, Naples, Italy.

Kwon, O.-S. and Elnashai, A. (2006). "The Effect of Material and Ground Motion Uncertainty on the Seismic Vulnerability Curves of RC Structure," Engineering Structures, 28(2), 289-303.

Kwon, O.-S. and Elnashai, A. S. (2007). *Probabilistic Seismic Assessment of Structure Foundation and Soil Interacting Systems,* NSEL Report Series, Report No. NSEL-004, Newmark Structural Engineering Laboratory, Department of Civil and Environmental Engineering, University of Illinois at Urbana-Champaign, Urbana, Illinois, USA.

Kwon, O.-S., Nakata, N., Elnashai, A. and Spencer, B. (2005). "A Framework for Multi-Site Distributed Simulation and Application to Complex Structural Systems," Journal of Earthquake Engineering, 9(5), 741-753.

Lagaros, N. D., Fragiadakis, M., Papadrakakis, M. and Tsompanakis, Y. (2006). "Structural Optimization: A Tool for Evaluating Seismic Design Procedures," Engineering Structures, 28(12), 1623-1633.

Lagaros, N. D. and Papadrakakis, M. (2007). "Seismic Design of RC Structures: A Critical Assessment in the Framework of Multi-Objective Optimization," Earthquake Engineering & Structural Dynamics, 36(12), 1623-1639.

Lankard, D. R. (1985). "Slurry Infiltrated Fiber Concrete (SIFCON): Properties and Applications." *Symposium on Very High Strength Cement Based Materials*, 42, ed Young, J. F., Pittsburgh, USA, 277-286.

Lee, C. and Ahn, J. (2003). "Flexural Design of Reinforced Concrete Frames by Genetic Algorithm," Journal of Structural Engineering, 129(6), 762-774.

Lee, W. K. (2007). "Simulation and Performance-based Earthquake Engineering Assessment of Self-centering Post-tensioned Concrete Bridge Systems," PhD Thesis, Department of Civil and Environmental Engineering, Stanford University, Palo Alto, California, USA.

Lee, W. K. and Billington, S. L. (2008). "Simulation of Self-Centring Fibre-Reinforced Concrete Columns," Engineering and Computational Mechanics, 161(2), 77-84.

Lepech, M. D. (2006). "A Paradigm for Integrated Structures and Materials Design for Sustainable Transportation Infrastructure," PhD Thesis, Civil Engineering, University of Michigan, Ann Arbor, Michigan, USA.

Lepech, M. D., Li, V. C., Robertson, R. E. and Keoleian, G. A. (2008). "Design of Green Engineered Cementitious Composites for Improved Sustainability," ACI Materials Journal, 105(6), 567-575.

Li, G., Zhou, R.-G., Duan, L. and Chen, W.-F. (1999). "Multiobjective and Multilevel Optimization for Steel Frames," Engineering Structures, 21(6), 519-529.

Li, V. C. (1992a). "Performance Driven Design of Fiber Reinforced Cementitious Composites." *4th International Symposium on Fiber Reinforced Concrete*, ed Swamy, R. N., 12-30.

Li, V. C. (1992b). "Postcrack Scaling Relations for Fiber Reinforced Cementitious Composites," Journal of Materials in Civil Engineering, 4(1), 41-57.

Li, V. C. (2003a). "Durable Overlay Systems with Engineered Cementitious Composites (ECC)," International Journal for Restoration of Buildings and Monuments, 9, 215-234.

Li, V. C. (2003b). "On Engineered Cementitious Composites (ECC) - A Review of the Material and Its Applications," Journal of Advanced Concrete Technology, 1, 215-230.

Li, V. C. (2006). "Bendable Composites - Ductile Concrete for Structures," Structure Magazine, July, 45-48.

Li, V. C. (2008). "Engineered Cementitious Composites (ECC) - Material, Structural, and Durability Performance," in *Concrete Construction Engineering Handbook,* Chapter 24*,* ed Nawy, E., CRC Press.

Li, V. C., Horikoshi, T., Ogawa, A., Torigoe, S. and Saito, T. (2004). "Micromechanics-Based Durability Study of Polyvinyl Alcohol-Engineered Cementitious Composite," ACI Materials Journal, 101, 242-248.

Li, V. C. and Lepech, M. (2004). "Crack Resistant Concrete Material for Transportation Construction." *Transportation Research Board Meeting*, January 11-15, Washington, District of Columbia, USA, Paper 04-4680.

Li, V. C. and Leung, C. K. Y. (1992). "Steady-State and Multiple Cracking of Short Random Fiber Composites," Journal of Engineering Mechanics, 118(11), 2246-2264.

Li, V. C. and Stang, H. (2004). "Elevating FRC Material Ductility to Infrastructure Durability." *6th RILEM Symposium on Fibre-Reinforced Concretes (FRC) - BEFIB*, Varenna (LC), Italy, 20-22 September, 2004, 171-186.

Li, V. C. and Wang, S. (2002). "Flexural Behaviors of Glass Fiber-Reinforced Polymer (GFRP) Reinforced Engineered Cementitious Composite Beams," ACI Materials Journal, 99(1), 11-21.

Li, V. C., Wang, S. and Wu, C. (2001). "Tensile Strain-Hardening Behavior of Polyvinyl Alcohol Engineered Cementitious Composite (PVA-ECC)," ACI Materials Journal, 98(6), 483-492.

Li, V. C. and Wu, H. C. (1992). "Conditions for Pseudo Strain-Hardening in Fiber Reinforced Brittle Matrix Composites," Journal of Applied Mechanics Review, 45(8), 390-398.

Liang, Q. Q. and Steven, G. P. (2002). "A Performance-Based Optimization Method for Topology Design of Continuum Structures with Mean Compliance Constraints," Computer Methods in Applied Mechanics and Engineering, 191(13-14), 1471-1489.

Liu, M. (2005). "Seismic Design of Steel Moment-Resisting Frame Structures Using Multiobjective Optimization," Earthquake Spectra, 21(2), 389-414.

Liu, M., Burns, S. A. and Wen, Y. K. (2003). "Optimal Seismic Design of Steel Frame Buildings Based on Life Cycle Cost Considerations," Earthquake Engineering & Structural Dynamics, 32(9), 1313-1332.

Liu, M., Burns, S. A. and Wen, Y. K. (2005). "Multiobjective Optimization for Performance-Based Seismic Design of Steel Moment Frame Structures," Earthquake Engineering & Structural Dynamics, 34(3), 289-306.

Liu, M., Burns, S. A. and Wen, Y. K. (2006). "Genetic Algorithm Based Construction-Conscious Minimum Weight Design of Seismic Steel Moment-Resisting Frames," Journal of Structural Engineering, 132(1), 50-58.

Liu, M., Wen, Y. K. and Burns, S. A. (2004). "Life Cycle Cost Oriented Seismic Design Optimization of Steel Moment Frame Structures with Risk-Taking Preference," Engineering Structures, 26(10), 1407-1421.

Lu, Y., Vintzileou, E., Zhang, G.-F. and Tassios, T. P. (1999). "Reinforced Concrete Scaled Columns under Cyclic Actions," Soil Dynamics and Earthquake Engineering, 18(2), 151-167.

Maalej, M. and Leong, K. S. (2005). "Engineered Cementitious Composites for Effective FRP-Strengthening of RC Beams," Composites Science and Technology, 65(7-8), 1120-1128.

Mahin, S. A. and Shing, P. B. (1985). "Pseudodynamic Method for Seismic Testing," Journal of Structural Engineering, 111(7), 1482-1503.

Mander, J. B., Priestley, M. J. N. and Park, R. (1988). "Theoretical Stress-Strain Model for Confined Concrete," Journal of Structural Engineering, 114(8), 1804-1826.

Manoharan, S. and Shanmuganathan, S. (1999). "A Comparison of Search Mechanisms for Structural Optimization," Computers & Structures, 73(1-5), 363-372.

Martínez-Rueda, J. E. and Elnashai, A. S. (1997). "Confined Concrete Model under Cyclic Load," Materials and Structures, 30(3), 139-147.

Matsumoto, T. and Mihashi, H. (2002). "JCI-DFRCC Summary Report on DFRCC Terminologies and Application Concepts." *JCI International Workshop on Ductile Fiber Reinforced Cementitious (DFRCC) - Application and Evaluation*, 59-66.

McGuire, R. K. (1995). "Probabilistic Seismic Hazard Analysis and Design Earthquakes: Closing the Loop," Bulletin of the Seismological Society of America, 85(5), 1275-1284.

McGuire, R. K. (2001). "Deterministic vs. Probabilistic Earthquake Hazards and Risks," Soil Dynamics and Earthquake Engineering, 21(5), 377-384.

McGuire, R. K. and Arabasz, W. J. (1990). "An Introduction to Probabilistic Seismic Hazard Analysis," in *Geotechnical and environmental geophysics,* ed Ward, S. H., Society of Exploration Geophysicists, Tulsa, Oklahoma, USA, 1, 333-353.

Memari, A. M. and Madhkhan, M. (1999). "Optimal Design of Steel Frames Subject to Gravity and Seismic Codes' Prescribed Lateral Forces," Structural and Multidisciplinary Optimization, 18(1), 56-66.

Mihashi, H., Otsuka, K., Akita, H. and Kikuchi, T. (2007). "Bond Cracking and Tension Stiffening Properties of a Deformed Bar Embedded in HPFRCC." *Advances in Construction Materials 2007*, eds. Grosse, C. U. and Reinhardt, H.-W., Heidelberg, 173-180.

Moehle, J. and Deierlein, G. G. (2004). "A Framework Methodology for Performance-based Earthquake Engineering." *13th World Conference on Earthquake Engineering*, Vancouver, British Columbia, Canada, Paper No. 679.

Moharrami, H. and Grierson, D. E. (1993). "Computer-Automated Design of Reinforced Concrete Frameworks," Journal of Structural Engineering, 119(7), 2036-2058.

Molina, F. J., Verzeletti, G., Magonette, G., Buchet, P. H. and Geradin, M. (1999). "Bi-Directional Pseudodynamic Test of a Full-Size Three-Storey Building," Earthquake Engineering & Structural Dynamics, 28(12), 1541-1566.

Morita, S. and Kaku, T. (1975). "Study on Bond Properties between Reinforcement and Concrete under Cyclic Loading," Journal of Structural and Construction Engineering (Transactions of Architectural Institute of Japan), 229, 15-24 (in Japanese).

Mosqueda, G., Stojadinovic, B., Hanley, J., Sivaselvan, M. and Reinhorn, A. (2008). "Hybrid Seismic Response Simulation on a Geographically Distributed Bridge Model," Journal of Structural Engineering, 134(4), 535-543.

Mukherjee, S. and Gupta, V. K. (2002a). "Wavelet-Based Characterisation of Design Ground Motions," Earthquake Engineering & Structural Dynamics, 31(5), 1173-1190.

Mukherjee, S. and Gupta, V. K. (2002b). "Wavelet-Based Generation of Spectrum-Compatible Time-histories," Soil Dynamics and Earthquake Engineering, 22(9-12), 799-804.

Naaman, A. E. (1972). "A Statistical Theory of Strength for Fiber Reinforced Concrete," PhD Thesis, Civil Engineering, Massachusetts Institute of Technology, Boston, Massachusetts, USA.

Naaman, A. E. (2007). "Tensile strain-hardening FRC composites: Historical evolution since the 1960," in *Advances in Construction Materials 2007*, 181-202.

Naeim, F., Alimoradi, A. and Pezeshk, S. (2004). "Selection and Scaling of Ground Motion Time Histories for Structural Design Using Genetic Algorithms," Earthquake Spectra, 20(2), 413-426.

Naeim, F. and Lew, M. (1995). "On the Use of Design Spectrum Compatible Time Histories," Earthquake Spectra, 11(1), 111-127.

Nagai, S., Kanda, T., Maruta, M. and Miyashita, T. (2002). "Shear capacity of ductile wall with high performance fiber reinforced cement composite." *1st fib Congress*, Osaka, Japan, 767-774.

Nagai, S., Kaneko, T., Kanda, T. and Maruta, M. (2004). "Structural Capacity of Reinforced PVA-ECC Dampers." *6th RILEM Symposium on Fibre-Reinforced Concretes (FRC) - BEFIB*, Varenna (LC), Italy, 20-22 September, 2004, 1227-1336.

Nagata, S., Kawashima, K. and Watanabe, G. (2004). "Seismic Response of RC C-Bent Columns based on a Hybrid Loading Test." *First International Conference on Urban Earthquake Engineering*, Tokyo Institute of Technology, Tokyo, Japan, 409-416.

Nakashima, M. and Kato, H. (1987). *Experimental Error Growth Behavior and Error Growth Control in On-Line Computer Test Control Method,* BRI-Report No. 123, Building Research Institute, Ministry of Construction, Tsukaba, Japan.

Ohsaki, M., Kinoshita, T. and Pan, P. (2007). "Multiobjective Heuristic Approaches to Seismic Design of Steel Frames with Standard Sections," Earthquake Engineering & Structural Dynamics, 36(11), 1481-1495.

Palermo, D. and Vecchio, F. J. (2003). "Compression Field Modeling of Reinforced Concrete Subjected to Reversed Loading: Formulation," ACI Structural Journal, 100(5), 616-625.

Panahshahi, N., Reinhorn, A. M., Kunnath, S. K., Lu, L. W., Huang, T. and Yu, K. (1991). "Seismic Response of a 1:6 Reinforced Concrete Scale-model Structure with Flexible Floor Diaphragms," ACI Structural Journal, 88(3), 315-324.

Park, R. (1988). "Ductility Evaluation from Laboratory and Analytical Testing." *9th World Conference on Earthquake Engineering*, Vol. VIII, Tokyo-Kyoto, Japan, 605-616.

Parra-Montesinos, G. J., Canbolat, B. A. and Jeyaraman, G. (2006). "Relaxation of Confinement Reinforcement Requirements in Structural Walls Through Use of Fiber Reinforced Cement Composites." *8th National Conference on Earthquake Engineering*, San Francisco, California, USA.

Parra-Montesinos, G. J. and Chompreda, P. (2007). "Deformation Capacity and Shear Strength of Fiber-Reinforced Cement Composite Flexural Members Subjected to Displacement Reversals," Journal of Structural Engineering, 133(3), 421-431.

Parra-Montesinos, G. J., Peterfreund, S. W. and Chao, S. H. (2005). "Highly Damage-Tolerant Beam-Column Joints Through Use of High-Performance Fiber-Reinforced Cement Composites," ACI Structural Journal, 102(3), 487-495.

Parra-Montesinos, G. J. and Wight, J. K. (2000). "Seismic Response of Exterior RC Column-to-Steel Beam Connections," Journal of Structural Engineering, 126(10), 1113-1121.

Paul, W. J. (2002). "Discussion," Engineering Geology, 66(1-2), 161-161.

PEER (2005). *Pacific Earthquake Engineering Research (PEER) Center: NGA Database,* Available from: http://peer.berkeley.edu/nga/, Accessed on January 1, 2009.

Pezeshk, S. (1998). "Design of Framed Structures: an Integrated Non-Linear Analysis and Optimal Minimum Weight Design," International Journal for Numerical Methods in Engineering, 41(3), 459-471.

Pezeshk, S., Camp, C. V. and Chen, D. (2000). "Design of Nonlinear Framed Structures Using Genetic Optimization," Journal of Structural Engineering, 126(3), 382-388.

Pinto, A. V., Pegon, P., Magonette, G. and Tsionis, G. (2004). "Pseudo-Dynamic Testing of Bridges Using Non-Linear Substructuring," Earthquake Engineering & Structural Dynamics, 33(11), 1125-1146.

Porter, K. A. (2003). "An Overview of PEER's Performance-Based Earthquake Engineering Methodology." *Ninth International Conference on Applications of Statistics and Probability in Civil Engineering (ICASP9)*, San Francisco, California, USA.

Power, M., Chiou, B. S. J., Abrahamson, N., Bozorgnia, Y., Shantz, T. and Roblee, C. (2008). "An Overview of the NGA Project," Earthquake Spectra, 24(1), 3-21.

Qian, S. and Li, V. C. (2006). "Elevating Material Ductility to Structural Performance of Steel Anchoring to ECC." *International RILEM Workshop on High Performance Fiber Reinforced Cementitious Composites in Structural Applications*, 529-537.

Raich, A. M. and Ghaboussi, J. (2000). "Evolving Structural Design Solutions Using an Implicit Redundant Genetic Algorithm," Structural and Multidisciplinary Optimization, 20(3), 222-231.

Rajeev, S. and Krishnamoorthy, C. S. (1998). "Genetic Algorithm-Based Methodology for Design Optimization of Reinforced Concrete Frames," Computer-Aided Civil and Infrastructure Engineering, 13(1), 63-74.

Ramberg, W. and Osgood, W. R. (1943). *Description of Stress-Strain Curves by Three Parameters,* Technical Note No. 902, 1943-07, National Advisory Committee for Aeronautics, Washington, District of Columbia, USA.

Repapis, C., Zeris, C. and Vintzileou, E. (2006). "Evaluation of the Seismic Performance of Existing RC Buildings: II. A Case Study for Regular and Irregular Buildings," Journal of Earthquake Engineering, 10(3), 429-452.

Rizzo, P. C., Shaw, D. E. and Jarecki, S. J. (1975). "Development of Real/Synthetic Time Histories to Match Smooth Design Spectra," Nuclear Engineering and Design, 32(1), 148-155.

Rojas, H., A. , Pezeshk, S. and Foley, C. M. (2007). "Performance-Based Optimization Considering Both Structural and Nonstructural Components," Earthquake Spectra, 23(3), 685-709.

Romualdi, J. P. and Batson, G. B. (1963). "Mechanics of Crack Arrest in Concrete," Journal of Engineering Mechanics Division ASCE, 89(EM3), 147-168.

Romualdi, J. P. and Mandel, J. A. (1964). "Tensile Strength of Concrete Affected by Uniformly Distributed and Closely Spaced Short Lengths of Wire Reinforcement," ACI Journal Proceedings, 61, 657-70.

Rouse, J. M. and Billington, S. L. (2007). "Creep and Shrinkage of High-Performance Fiber-Reinforced Cementitious Composites," ACI Materials Journal, 104(2), 129-136.

RS Means (2011). *Building Construction Cost Data 2011 Book*, RS Means, Reed Construction Data Inc., Kingston, Massachusetts, USA.

Saenz, L. P. (1964). "Discussion of Equation for the Stress-Strain Curve of Concrete by Desayi and Krishnan," ACI Journal, 61(9), 1229-1235.

Sahab, M. G., Ashour, A. F. and Toropov, V. V. (2005a). "Cost Optimisation of Reinforced Concrete Flat Slab Buildings," Engineering Structures, 27(3), 313-322.

Sahab, M. G., Ashour, A. F. and Toropov, V. V. (2005b). "A Hybrid Genetic Algorithm for Reinforced Concrete Flat Slab Buildings," Computers & Structures, 83(8-9), 551-559.

Sahmaran, M. and Li, V. C. (2008). "Durability of Mechanically Loaded Engineered Cementitious Composites under Highly Alkaline Environments," Cement and Concrete Composites, 30(2), 72-81.

Sakai, J., Kawashima, K. and Asce, M. (2006). "Unloading and Reloading Stress–Strain Model for Confined Concrete," Journal of Structural Engineering, 132, 112-122.

Salajegheh, E., Gholizadeh, S. and Khatibinia, M. (2008). "Optimal Design of Structures for Earthquake Loads by a Hybrid RBF-BPSO Method," Earthquake Engineering and Engineering Vibration, 7(1), 13-24.

Salajegheh, E. and Heidari, A. (2005). "Optimum Design of Structures against Earthquake by Wavelet Neural Network and Filter Banks," Earthquake Engineering & Structural Dynamics, 34(1), 67-82.

Sato, Y., Fukuyama, H. and Suwada, H. (2001). "A Proposal of Tension-Compression Cyclic Loading Test Method for Ductile Cementitious Materials," Journal of Structural and Construction Engineering (Transactions of Architectural Institute of Japan), No. 539, 7-12 (in Japanese).

SEAOC (1995). *Vision 2000, Performance Based Seismic Engineering of Buildings, Vols. I and II*, Structural Engineers Association of California (SEAOC), Sacramento, California, USA.

Seible, F., Hegemier, G. and Igarashi, A. (1996). "Simulated Seismic Laboratory Load Testing of Full-Scale Buildings," Earthquake Spectra, 12(1), 57-86.

Shen, B., Hubler, M., Paulino, G. H. and Struble, L. J. (2008). "Functionally-Graded Fiber-Reinforced Cement Composite: Processing, Microstructure, and Properties," Cement and Concrete Composites, 30(8), 663-673.

Shimizu, K., Kanakubo, T., Kanda, T. and Nagai, S. (2004). "Shear Behavior of Steel Reinforced PVA-ECC Beams." *13th World Conference on Earthquake Engineering*, Vancouver, British Columbia, Canada, Paper No. 704.

Shin, S. K., Kim, J. J. H. and Lim, Y. M. (2007). "Investigation of the Strengthening Effect of DFRCC Applied to Plain Concrete Beams," Cement and Concrete Composites, 29(6), 465-473.

Silva, W. and Lee, K. (1987). *WES Rascal Code for Synthesizing Earthquake Ground Motions, State-of-the-Art for Assessing Earthquake Hazards in the United States,* Report 24, Miscellaneous Paper S-73-1, US Army Corps of Engineers, Vicksburg, Mississippi, USA.

Sima, J. F., Roca, P. and Molins, C. (2008). "Cyclic constitutive model for concrete," Engineering Structures, 30(3), 695-706.

Sinha, B. P., Gerstle, K. H. and Tulin, L. G. (1964). "Stress-Strain Relations for Concrete under Cyclic Loading," Journal of American Concrete Institute, 61(2), 195-211.

Soranakom, C. and Mobasher, B. (2008). "Correlation of Tensile and Flexural Responses of Strain Softening and Strain Hardening Cement Composites," Cement and Concrete Composites, 30(6), 465-477.

Spencer, B., Elnasahi, A. S., Nakata, N., Seliem, H., Yang, G., Futrelle, J., Glick, W., Marcusiu, D., Ricker, K., Finholt, T., Horn, D., Hubbard, P., Keahey, K., Liming, L., Zaluzec, N., Pearlman, L. and Stauffer, E. (2004). *The MOST Experiment: Earthquake Engineering on the Grid,* Technical Report NEESgrid-2004-41, Network for Earthquake Engineering Research (NEES).

Stang, H. and Li, V. C. (1999). "Extrusion of ECC-Material." *High Performance Fiber Reinforced Cement Composites 3 (HPFRCC 3)*, eds. Reinhardt, H. W. and Naaman, A. E., 203-212.

Stang, H. and Li, V. C. (2004). "Classification of Fibre Reinforced Cementitious Materials for Structural Applications." *6th RILEM Symposium on Fiber-Reinforced Concretes (FRC) - BEFIB 2004*, Varenna, Italy, 197-218.

Steidl, J. H. (2000). "Site Response in Southern California for Probabilistic Seismic Hazard Analysis," Bulletin of the Seismological Society of America, 90(6B), S149-169.

Stojadinovic, B., Mosqueda, G. and Mahin, S. A. (2006). "Event-Driven Control System for Geographically Distributed Hybrid Simulation," Journal of Structural Engineering, 132(1), 68-77.

Suárez, L. E. and Montejo, L. A. (2005). "Generation of Artificial Earthquakes via the Wavelet Transform," International Journal of Solids and Structures, 42(21-22), 5905-5919.

Sung, Y.-C. and Su, C.-K. (2009). "Fuzzy Genetic Optimization on Performance-Based Seismic Design of Reinforced Concrete Bridge Piers with Single-Column Type," Optimization and Engineering, 11(3), 471-496.

Suthiwarapirak, P., Matsumoto, T. and Kanda, T. (2004). "Multiple Cracking and Fiber Bridging Characteristics of Engineered Cementitious Composites under Fatigue Flexure," Journal of Materials in Civil Engineering, 16, 433-443.

Suwada, H. and Fukuyama, H. (2006). "Nonlinear Finite Element Analysis on Shear Failure of Structural Elements Using High Performance Fiber Reinforced Cement Composite," Journal of Advanced Concrete Technology, 4, 45-58.

Takanashi, K., Udagawa, K., Seki, M., Okada, T. and Tanaka, H. (1975). "Nonlinear Earthquake Response Analysis of Structures by a Computer-Actuator On-Line System," Bulletin of Earthquake Resistant Structure Research Center, No. 8, Institute of Industrial Science, University of Tokyo, Japan.

The Chicago Manual of Style (2010). The University of Chicago Press, Chicago, Illinois, USA.

Tsai, K. C., Lai, J. W., Chen, C. H., Hsiao, B. C., Weng, Y. Y. and Lin, M. L. (2004). "Pseudo Dynamic Tests of a Full Scale CFT/BRB Composite Frame." *Structures Congress*, Nashville, Tennessee, USA.

USGS (2008). *Documentation for the 2008 Update of the United States National Seismic Hazard Maps,* Open-File Report 2008-1128, United States Geological Survey, Reston, Virginia, USA.

USGS (2009a). *2008 Interactive Deaggregations (Beta),* U.S. Geological Survey, Available from: http://eqint.cr.usgs.gov/deaggint/2008/index.php, Accessed on May 31, 2009.

USGS (2009b). *Major Faults of California,* U.S. Geological Survey, Available from: http://education.usgs.gov/california/maps/faults_names3.htm, Accessed on May 13, 2009.

USGS (2009c). *Soil Type and Shaking Hazard in the San Francisco Bay Area,* U.S. Geological Survey, Available from: http://earthquake.usgs.gov/regional/nca/soiltype/, Accessed on February 1, 2011.

van Zijl, G. P. A. G. (2007). "Improved Mechanical Performance: Shear Behaviour of Strain-Hardening Cement-Based Composites (SHCC)," Cement and Concrete Research, 37(8), 1241-1247.

Wanatabe, E., Sugiura, K., Nagata, K., Yamaguchi, T. and Niwa, K. (1999). "Multi-Phase Interaction Testing System by Means of the Internet." *1st International Conference on Advances in Structural Engineering Mechanics*, Seoul, Korea, 43-54.

Wang, S. and Li, V. C. (2006). "High-Early-Strength Engineered Cementitious Composites," ACI Materials Journal, 103(2), 97-105.

Wang, S. and Li, V. C. (2007). "Engineered Cementitious Composites with High-Volume Fly Ash," ACI Materials Journal, 104(3), 233-241.

Wen, Y. K., Ellingwood, B. R. and Bracci, J. M. (2004). *Vulnerability Function Framework for Consequence-Based Engineering,* Project DS-4 Report, Mid-America Earthquake (MAE) Center, Urbana, Illinois, USA.

Wen, Y. K., Ellingwood, B. R., Veneziano, D. and Bracci, J. M. (2003). *Uncertainty Modeling in Earthquake Engineering*, Mid-America Earthquake (MAE) Center, Urbana, Illinois, USA.

Xia, Z. and Naaman, A. E. (2002). "Behavior and Modeling of Infill Fiber-Reinforced Concrete Damper Element for Steel-Concrete Shear Wall," ACI Structural Journal, 99(6), 727-739.

Yang, E. H. and Li, V. C. (2005). "Rate Dependence in Engineered Cementitious Composites." *International RILEM Workshop on High Performance Fiber Reinforced Cementitious Composites (HPFRCC) in Structural Applications*, Honolulu, Hawaii, USA, 83-92.

Yang, E. H., Yang, Y. and Li, V. C. (2007). "Use of High Volumes of Fly Ash to Improve ECC Mechanical Properties and Material Greenness," ACI Materials Journal, 104(6), 620-628.

Yang, J. and Fischer, G. (2006). "Simulation of the Tensile Stress-Strain Behavior of Strain Hardening Cementitious Composites," in *Measuring, Monitoring and Modeling Concrete Properties*, 25-31.

Yang, Y., Lepech, M., Yang, E. H. and Li, V. C. (2009). "Autogenous Healing of Engineered Cementitious Composites under Wet-Dry Cycles," Journal of Cement and Concrete Research, 39(5), 382-390.

Yankelevsky, D. Z. and Reinhardt, H. W. (1989). "Uniaxial Behavior of Concrete in Cyclic Tension," Journal of Structural Engineering, 115(1), 166-182.

Yun, H. D., Kim, S. W., Jeon, E., Park, W. S. and Lee, Y. T. (2008). "Effects of Fibre-Reinforced Cement Composites' Ductility on the Seismic Performance of Short Coupling Beams," Magazine of Concrete Research, 60(3), 223-233.

Yun, H. D., Yang, I. S., Kim, S. W., Jeon, E., Choi, C. S. and Fukuyama, H. (2007). "Mechanical Properties of High-Performance Hybrid-Fibre-Reinforced Cementitious Composites (HPHFRCCs)," Magazine of Concrete Research, 59(4), 257.

Zhang, J. and Li, V. C. (2002). "Monotonic and Fatigue Performance in Bending of Fiber-Reinforced Engineered Cementitious Composite in Overlay System," Cement and Concrete Composites, 32(3), 415-423.

Zielinski, Z. A., Long, W. and Troitsky, M. S. (1995). "Designing Reinforced Concrete Short-Tied Columns Using the Optimization Technique," ACI Materials Journal, 92(5), 619-626.

Zou, X. K. (2008). "Integrated Design Optimization of Base-Isolated Concrete Buildings under Spectrum Loading," Structural and Multidisciplinary Optimization, 36(5), 493-507.

Zou, X. K. and Chan, C. M. (2005a). "An Optimal Resizing Technique for Seismic Drift Design of Concrete Buildings Subjected to Response Spectrum and Time History Loadings," Computers and Structures, 83(19-20), 1689-1704.

Zou, X. K. and Chan, C. M. (2005b). "Optimal Seismic Performance-based Design of Reinforced Concrete Buildings Using Nonlinear Pushover Analysis," Engineering Structures, 27(8), 1289-1302.

Zou, X. K., Chan, C. M., Li, G. and Wang, Q. (2007). "Multiobjective Optimization for Performance-Based Design of Reinforced Concrete Frames," Journal of Structural Engineering, 133(10), 1462-1474.

APPENDIX A

TEST RESULTS

In Appendix A raw data from testing of RC and ECC columns, as a part of the experimental program (Chapter 3), is provided. The details of the tests given in Table 3.5 are repeated in Table A.1 along with the test identification numbers which relate to the figures shown below.

Table A.1. Description of the test in the experimental program

TEST ID	Long. Reinf. Ratio (%)	Trans. Reinf. Ratio (%)	Mix Design	Type of Test	Axial Load (%)	Number of Specimens
1	0.87	0.36	Concrete	Monotonic	7.5	1
2-3	1.29	0.36	Concrete	Monotonic	7.5	2
4	0.87	0.12	ECC-HFA	Monotonic	7.5	1
5	1.29	0	ECC-HFA	Monotonic	7.5	1
6	0.87	0.36	Concrete	Cyclic	7.5	1
7-9	1.29	0.36	Concrete	Cyclic	7.5	3
10	0.87	0.12	ECC-HFA	Cyclic	7.5	1
11	1.29	0	ECC-HFA	Cyclic	7.5	1
12	1.29	0.12	ECC-HFA	Cyclic	7.5	1
13	1.29	0.18	ECC-HFA	Cyclic	7.5	1
14	1.29	0.12	ECC-M45	Cyclic	7.5	1
15	1.29	0.12	ECC-PPF	Cyclic	7.5	1
16	1.29	0.12	ECC-SF	Cyclic	7.5	1
17	1.29	0.12	ECC-HFA	Cyclic-Fixed	7.5	1
18	1.29	0.12	ECC-M45	Cyclic-Fixed	7.5	1
19	1.29	0.12	ECC-PPF	Cyclic-Fixed	7.5	1
20	1.29	0.12	ECC-SF	Cyclic-Fixed	7.5	1
21	1.29	N/A	ECC-HFA	STH	5	1
22	1.29	N/A	ECC-HFA	STH	10	1
23	0.87	0.36	Concrete	Hybrid	7.5	1
24	0.87	0.12	ECC-HFA	Hybrid	7.5	1
25	1.29	N/A	ECC-HFA	Hybrid	5	1
26	1.29	N/A	ECC-HFA	Hybrid	10	1

TEST ID	Long. Reinf. Ratio (%)	Trans. Reinf. Ratio (%)	Mix Design	Type of Test	Axial Load (%)
1	0.87	0.36	Concrete	Monotonic	7.5

Notes: none.

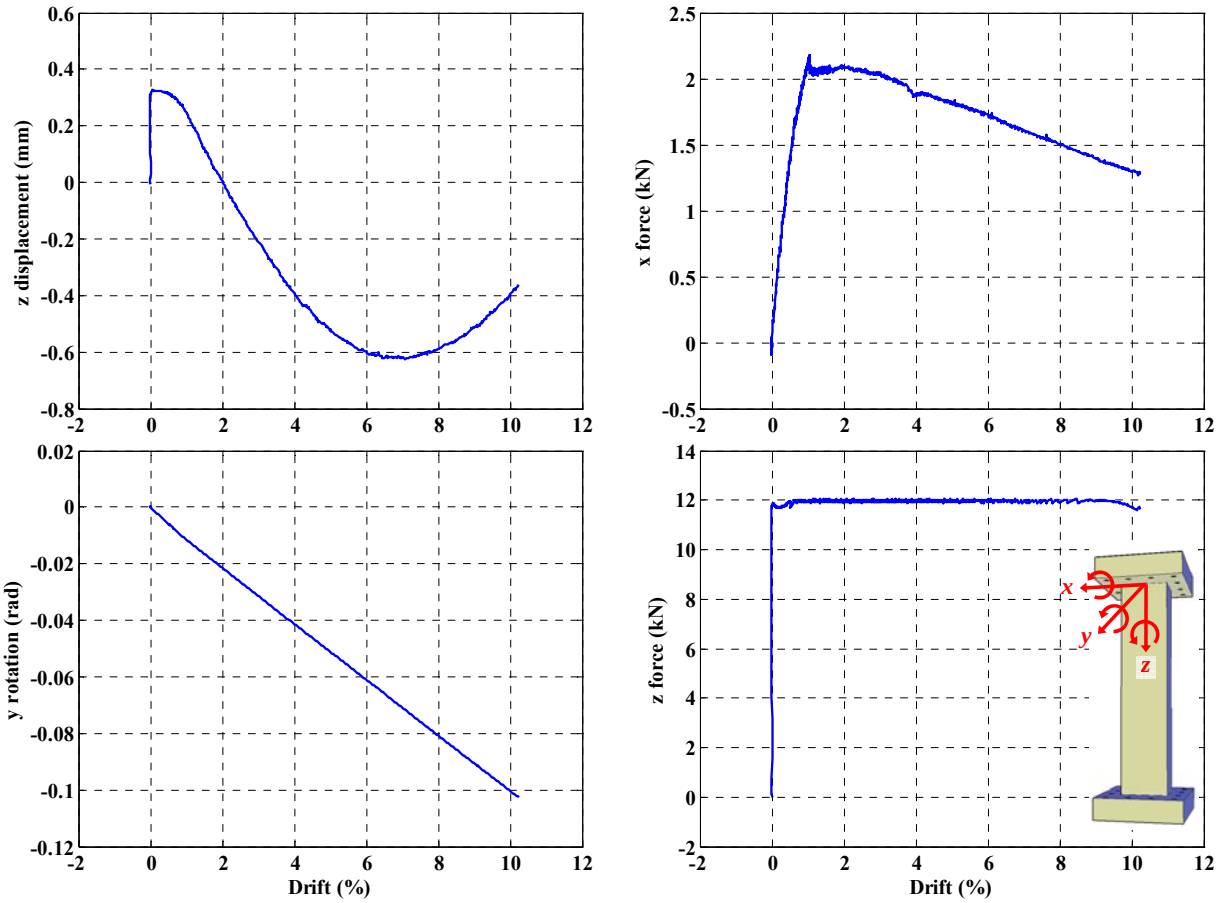

Figure A.1. Raw data from test #1

TEST ID	Long. Reinf. Ratio (%)	Trans. Reinf. Ratio (%)	Mix Design	Type of Test	Axial Load (%)
2	1.29	0.36	Concrete	Monotonic	7.5

Notes: none.

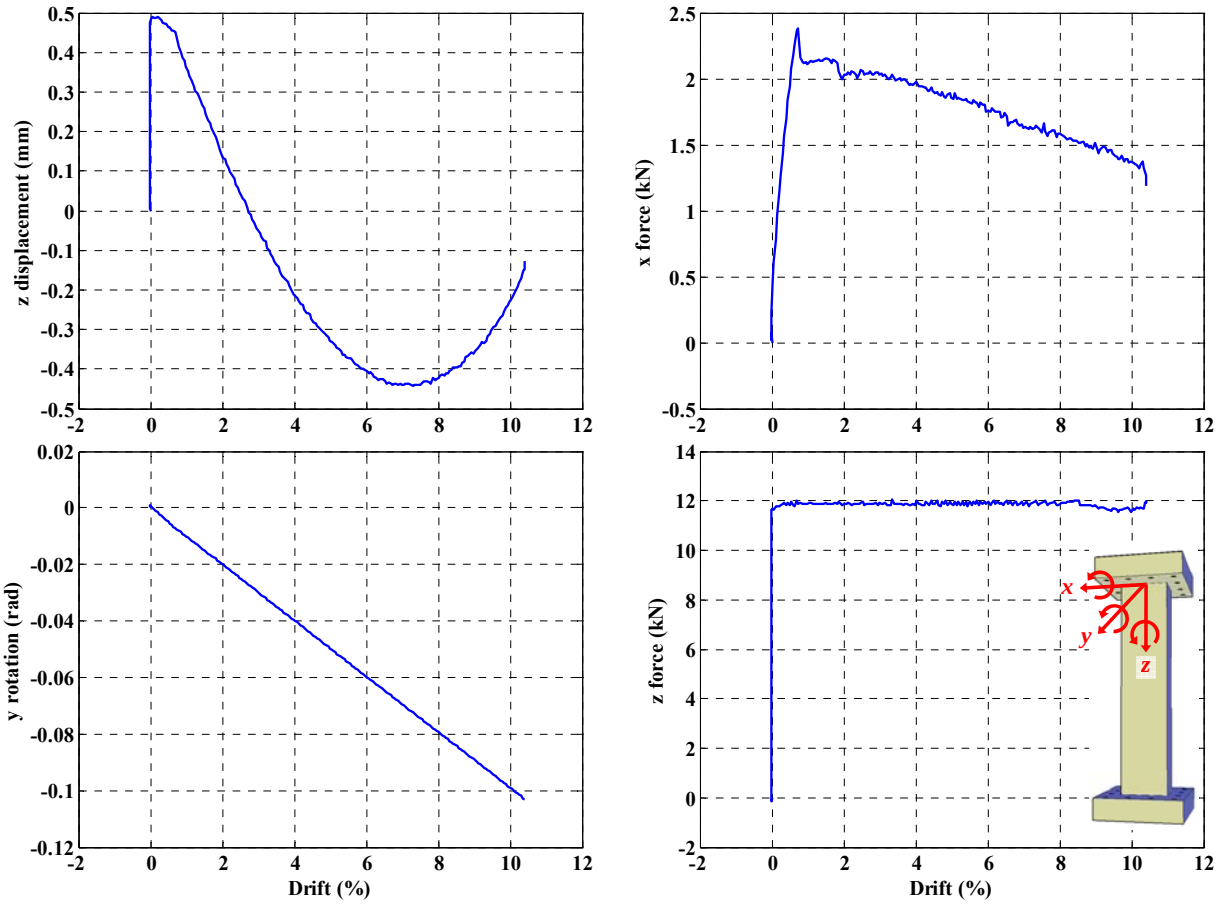

Figure A.2. Raw data from test #2

TEST ID	Long. Reinf. Ratio (%)	Trans. Reinf. Ratio (%)	Mix Design	Type of Test	Axial Load (%)
3	1.29	0.36	Concrete	Monotonic	7.5

Notes: same properties with test ID 1.

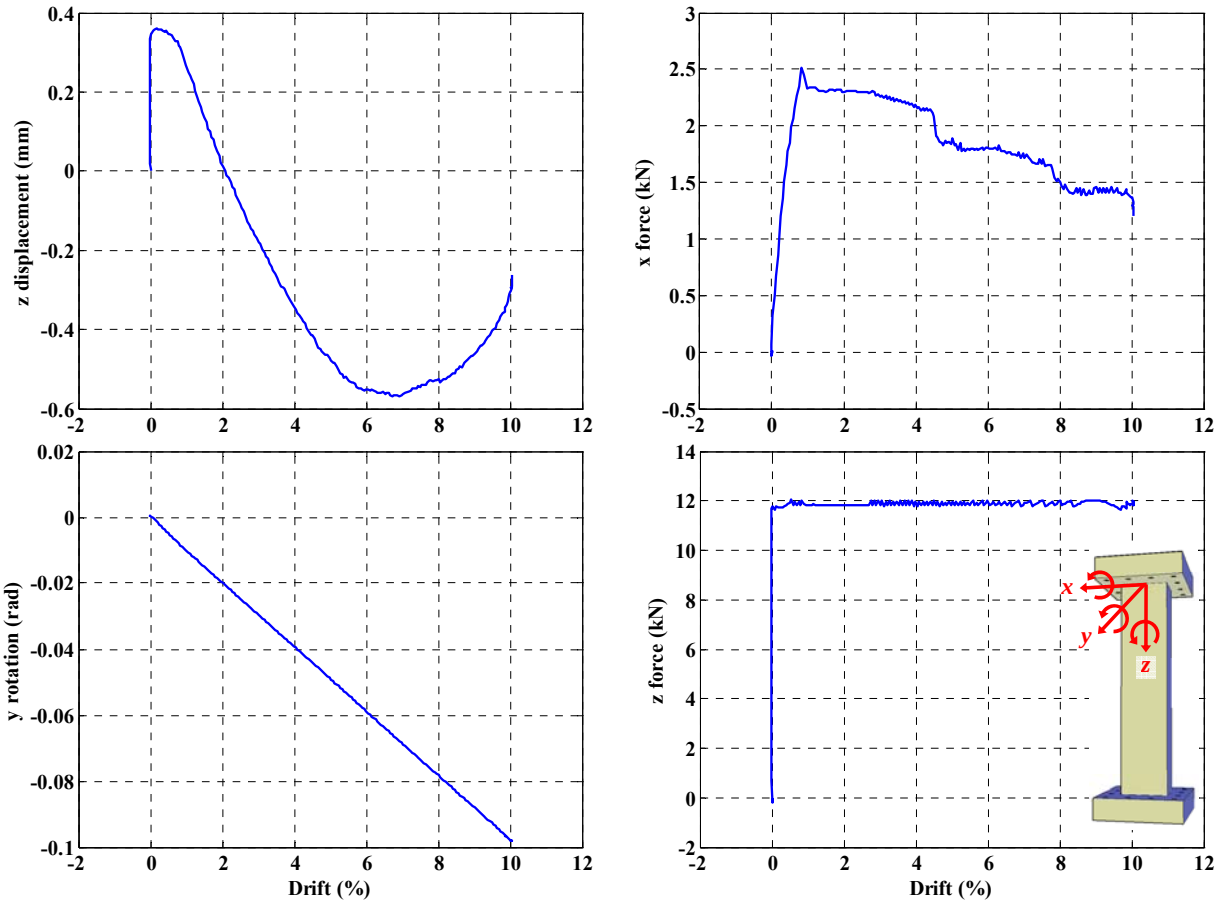

Figure A.3. Raw data from test #3

TEST ID	Long. Reinf. Ratio (%)	Trans. Reinf. Ratio (%)	Mix Design	Type of Test	Axial Load (%)
4	0.87	0.12	ECC-HFA	Monotonic	7.5

Notes: none.

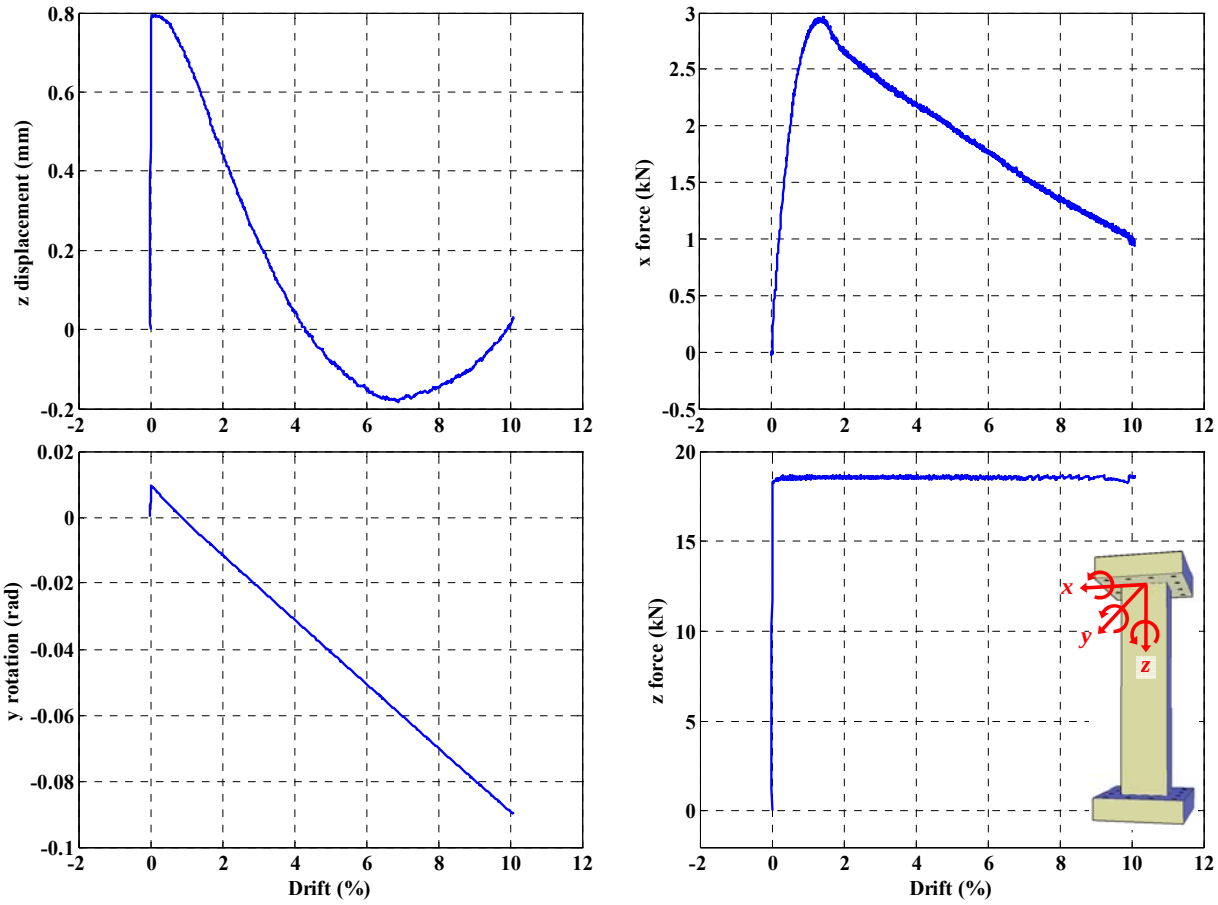

Figure A.4. Raw data from test #4

TEST ID	Long. Reinf. Ratio (%)	Trans. Reinf. Ratio (%)	Mix Design	Type of Test	Axial Load (%)
5	1.29	0	ECC-HFA	Monotonic	7.5

Notes: none.

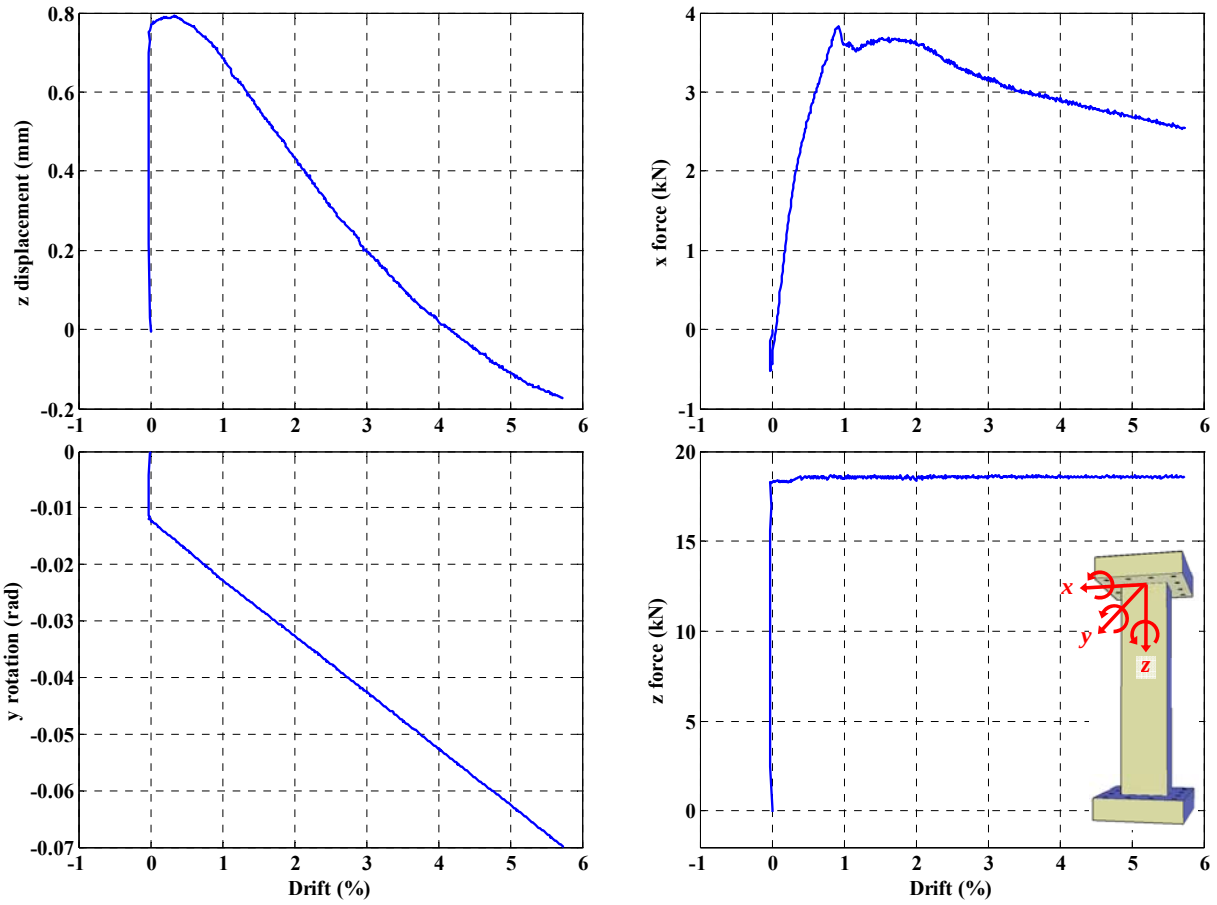

Figure A.5. Raw data from test #5

TEST ID	Long. Reinf. Ratio (%)	Trans. Reinf. Ratio (%)	Mix Design	Type of Test	Axial Load (%)
6	0.87	0.36	Concrete	Cyclic	7.5

Notes: none.

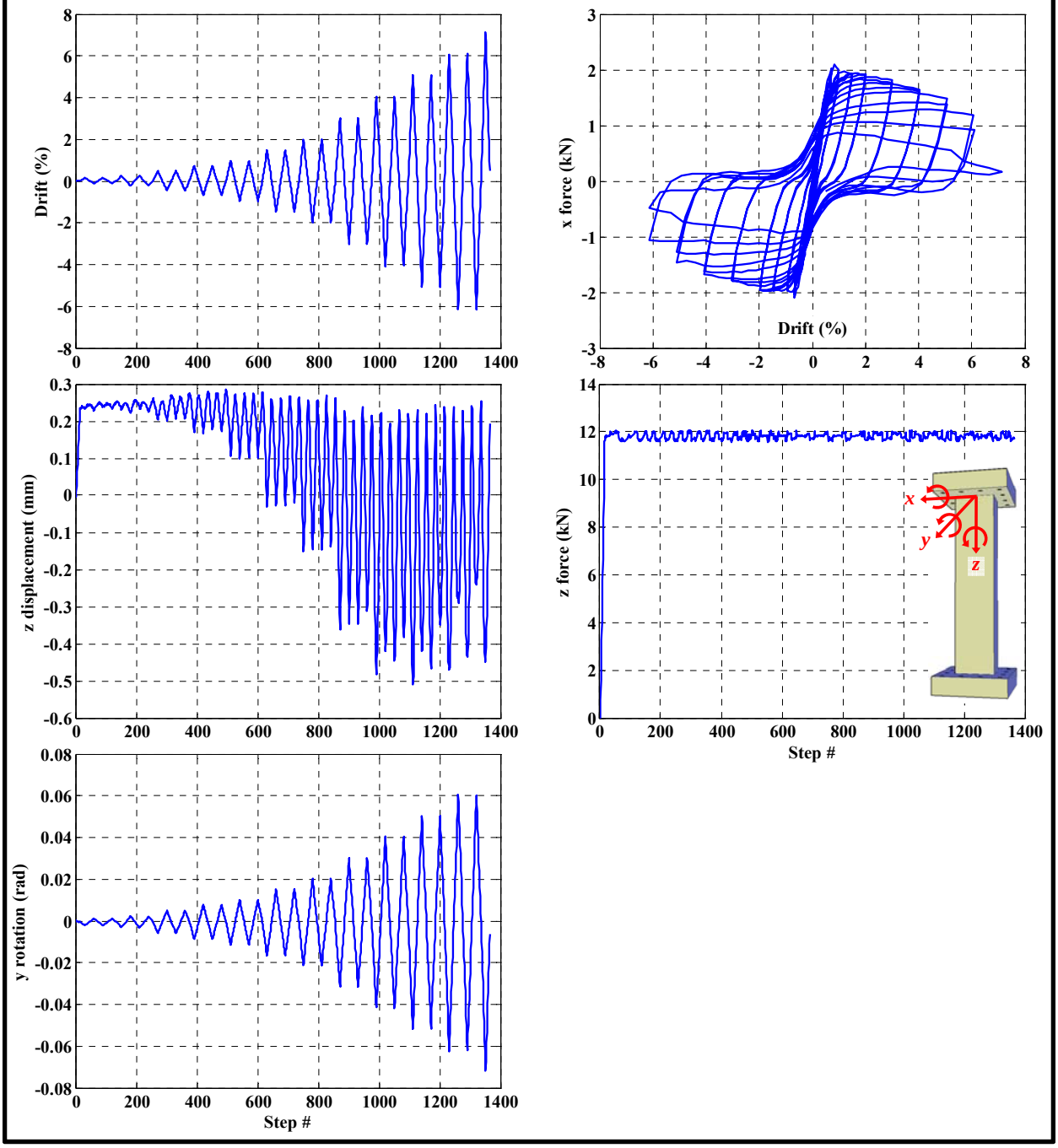

Figure A.6. Raw data from test #6

TEST ID	Long. Reinf. Ratio (%)	Trans. Reinf. Ratio (%)	Mix Design	Type of Test	Axial Load (%)
7	1.29	0.36	Concrete	Cyclic	7.5

Notes: none.

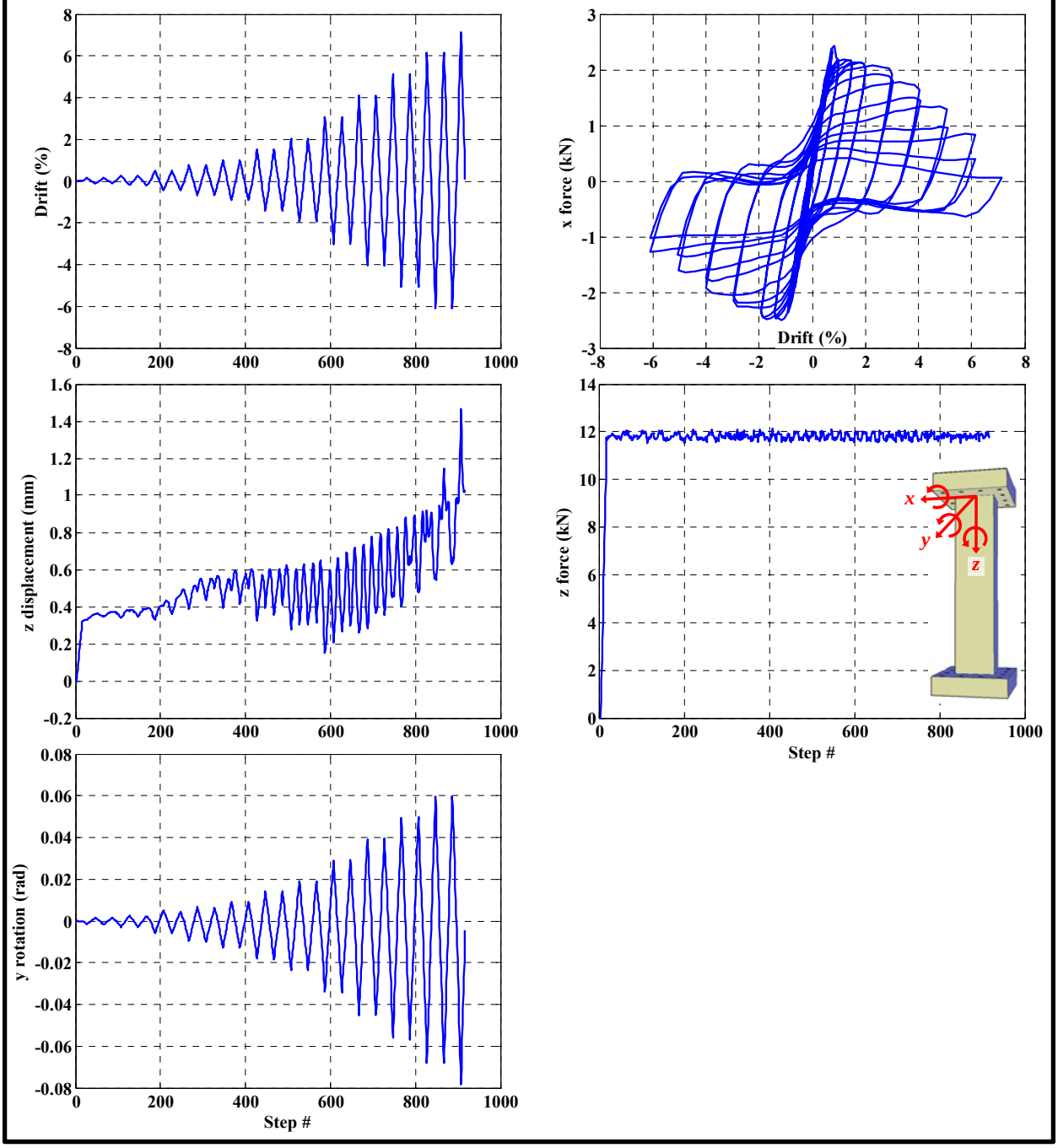

Figure A.7. Raw data from test #7

TEST ID	Long. Reinf. Ratio (%)	Trans. Reinf. Ratio (%)	Mix Design	Type of Test	Axial Load (%)
8	1.29	0.36	Concrete	Cyclic	7.5

Notes: same properties with test ID 7.

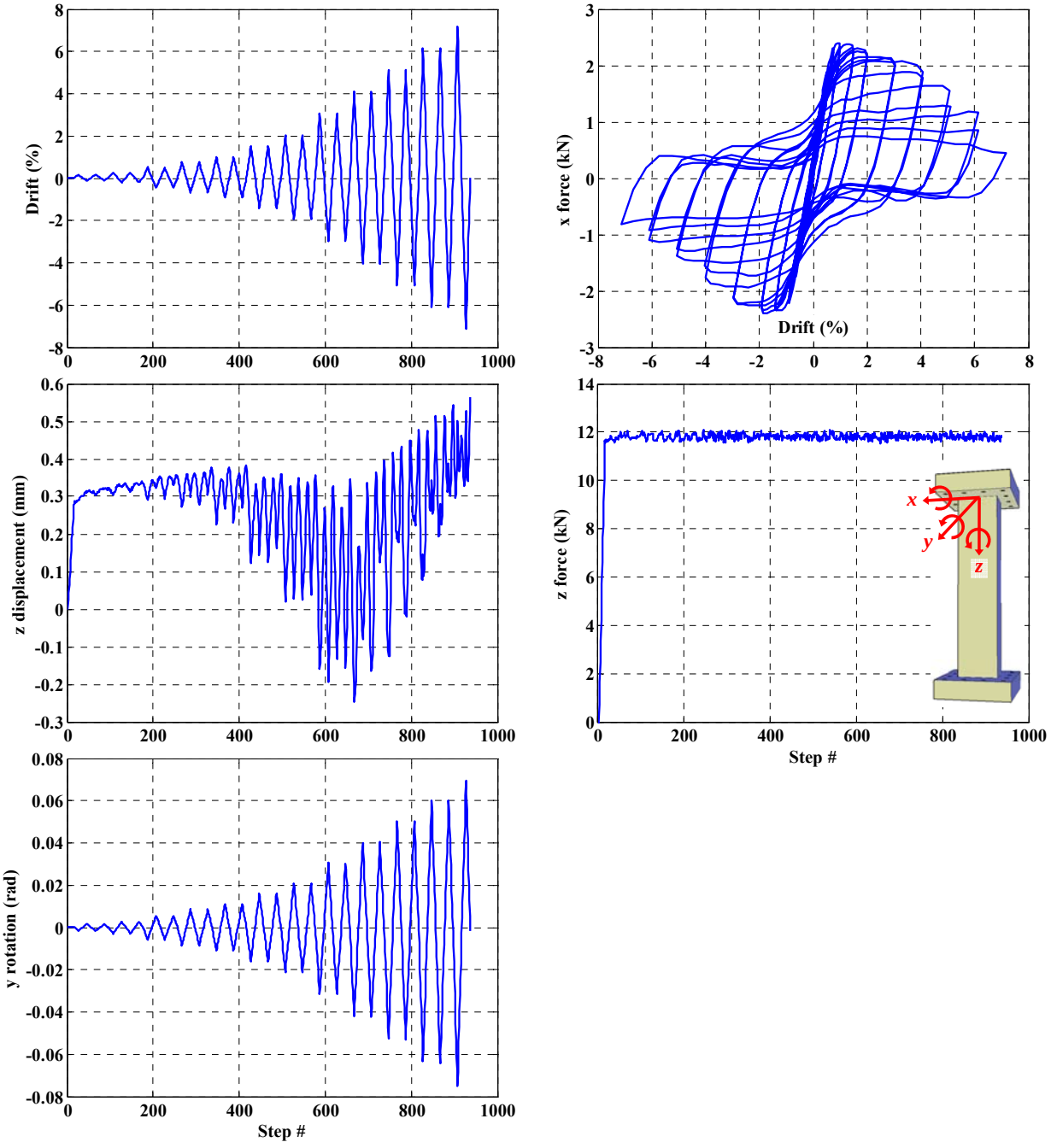

Figure A.8. Raw data from test #8

TEST ID	Long. Reinf. Ratio (%)	Trans. Reinf. Ratio (%)	Mix Design	Type of Test	Axial Load (%)
9	1.29	0.36	Concrete	Cyclic	7.5

Notes: same properties with test ID 7 and 8.

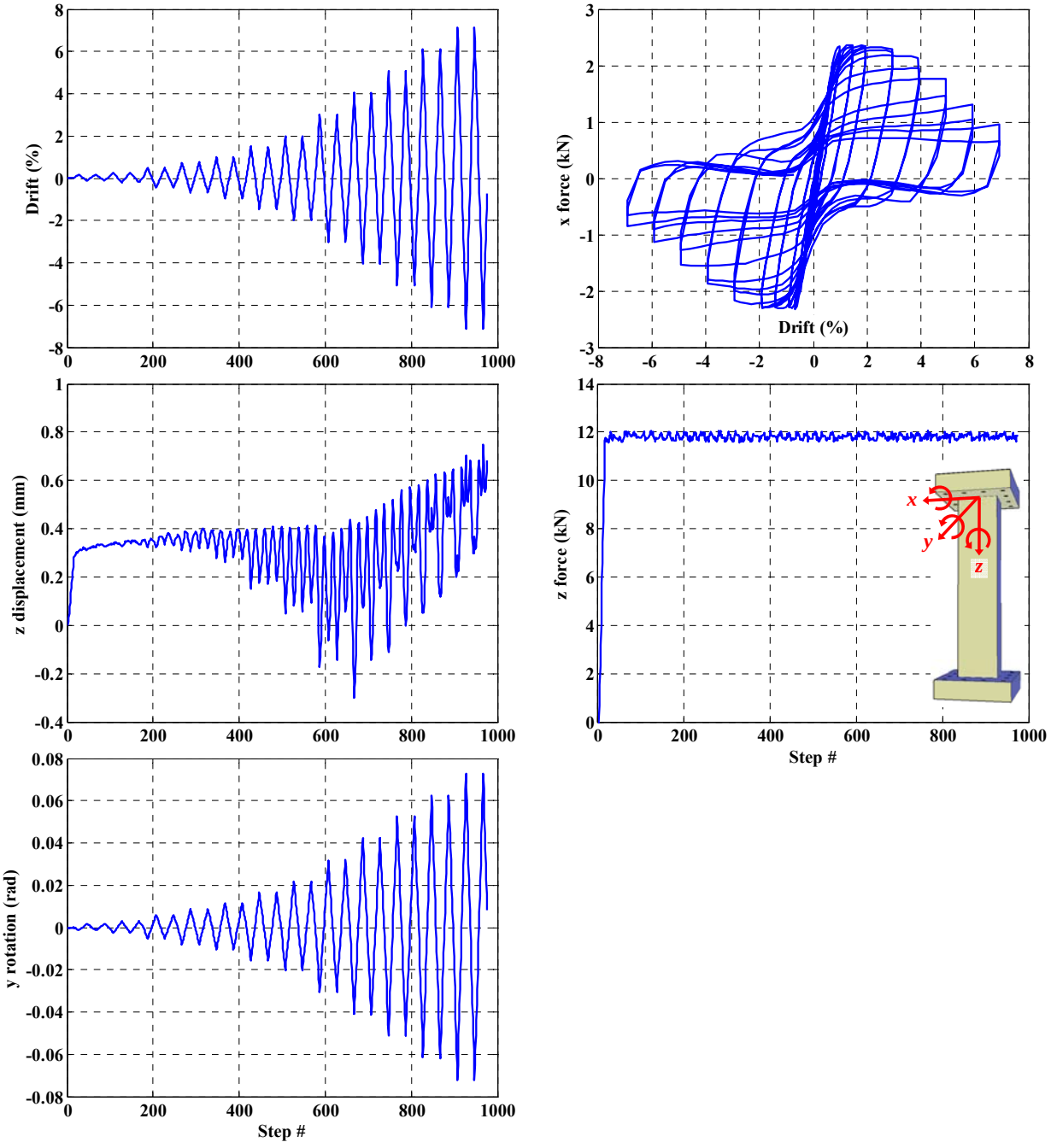

Figure A.9. Raw data from test #9

TEST ID	Long. Reinf. Ratio (%)	Trans. Reinf. Ratio (%)	Mix Design	Type of Test	Axial Load (%)
10	0.87	0.12	ECC-HFA	Cyclic	7.5

Notes: none.

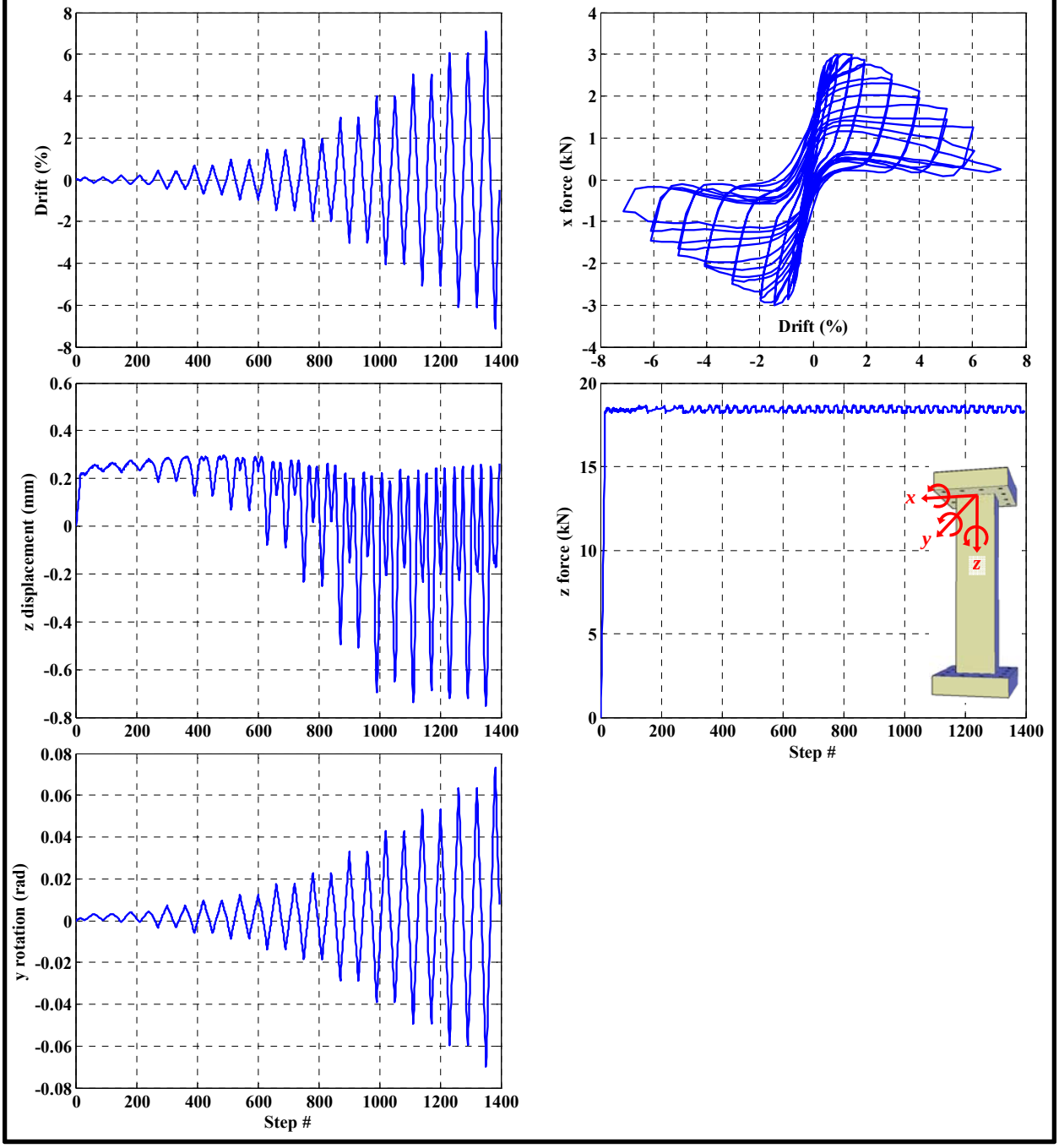

Figure A.10. Raw data from test #10

TEST ID	Long. Reinf. Ratio (%)	Trans. Reinf. Ratio (%)	Mix Design	Type of Test	Axial Load (%)
11	1.29	0	ECC-HFA	Cyclic	7.5

Notes: none.

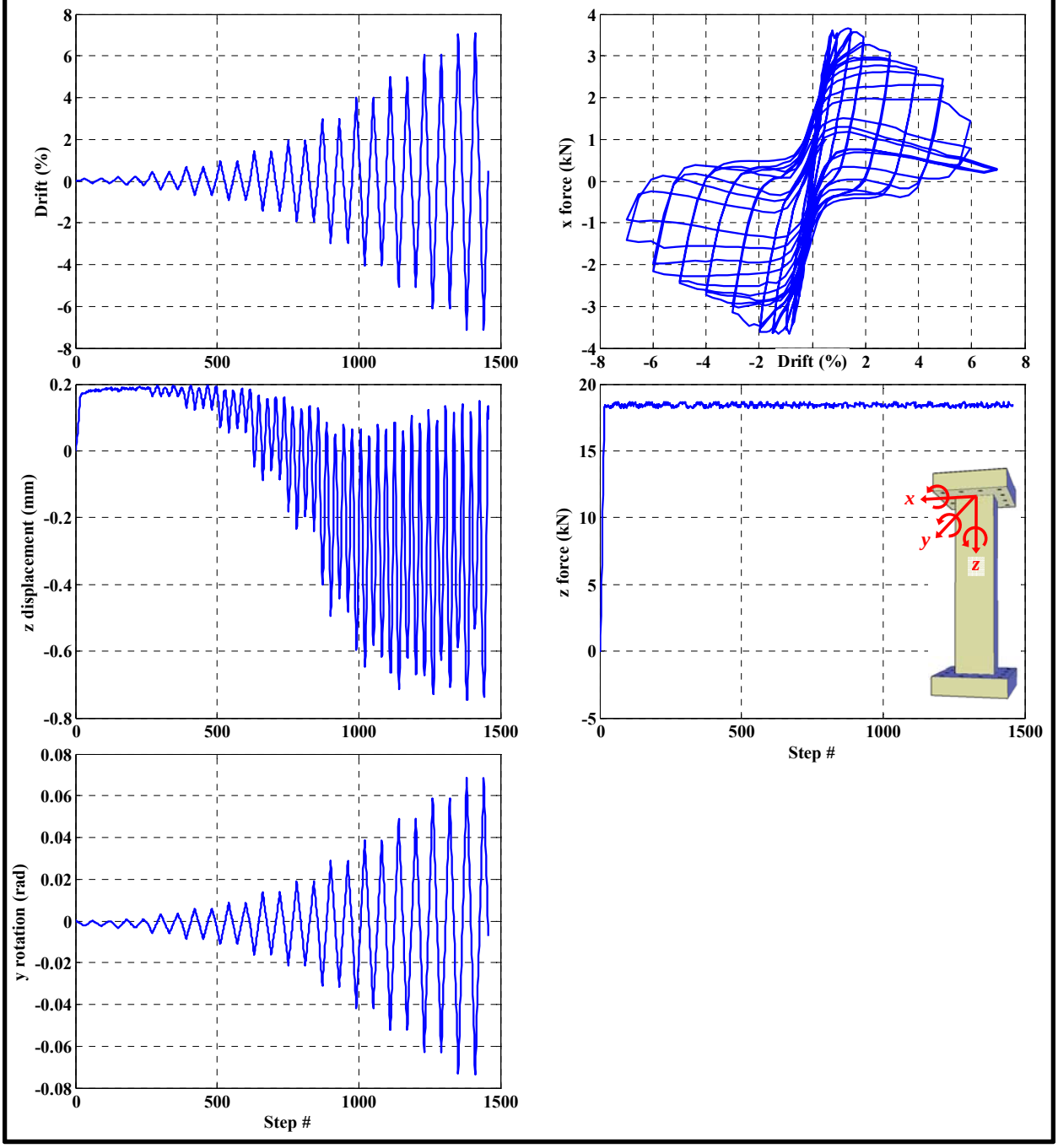

Figure A.11. Raw data from test #11

TEST ID	Long. Reinf. Ratio (%)	Trans. Reinf. Ratio (%)	Mix Design	Type of Test	Axial Load (%)
12	1.29	0.12	ECC-HFA	Cyclic	7.5

Notes: unknown error in z displacement reading at step #1090, see figures.

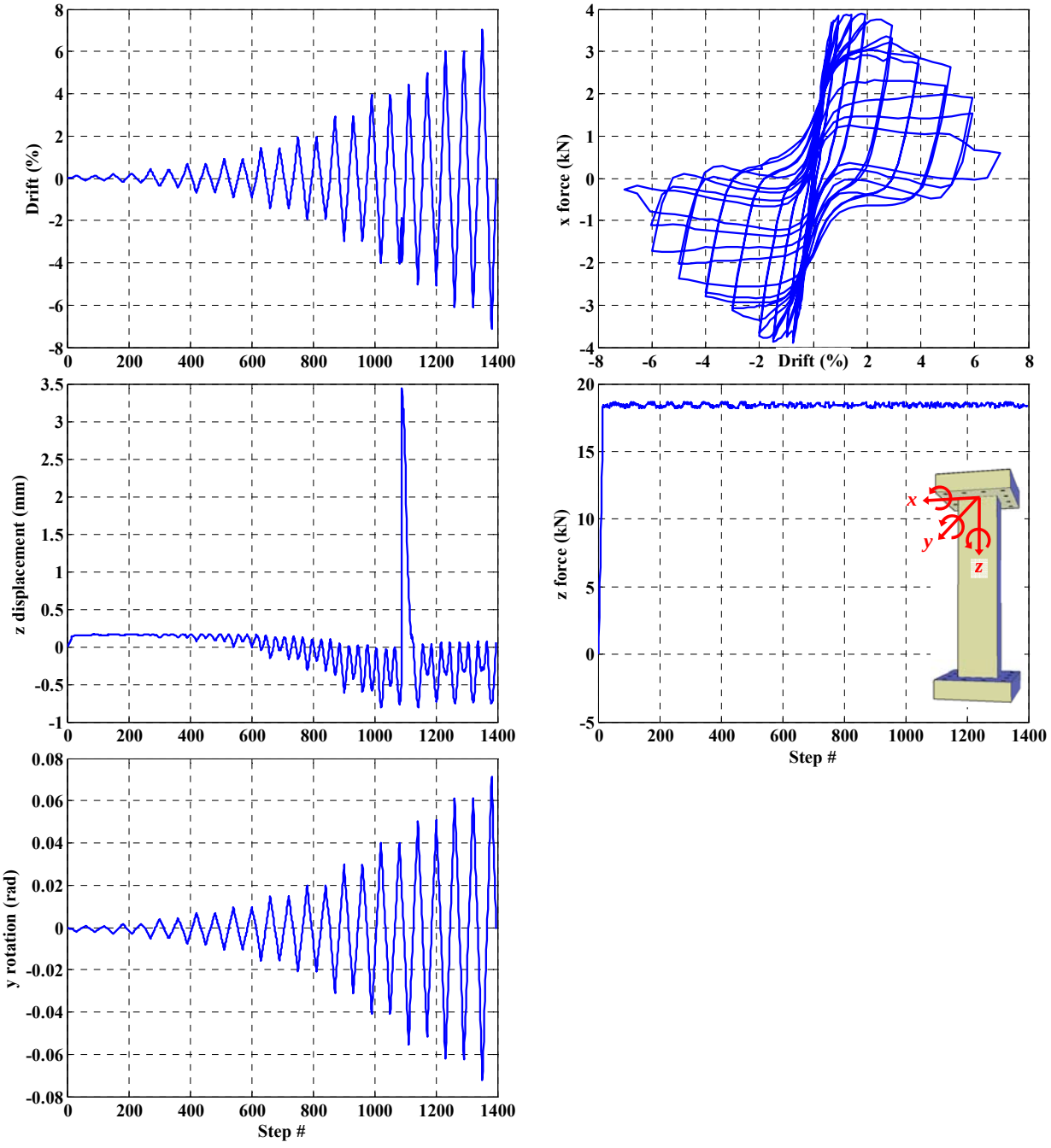

Figure A.12. Raw data from test #12

TEST ID	Long. Reinf. Ratio (%)	Trans. Reinf. Ratio (%)	Mix Design	Type of Test	Axial Load (%)
13	1.29	0.18	ECC-HFA	Cyclic	7.5

Notes: none.

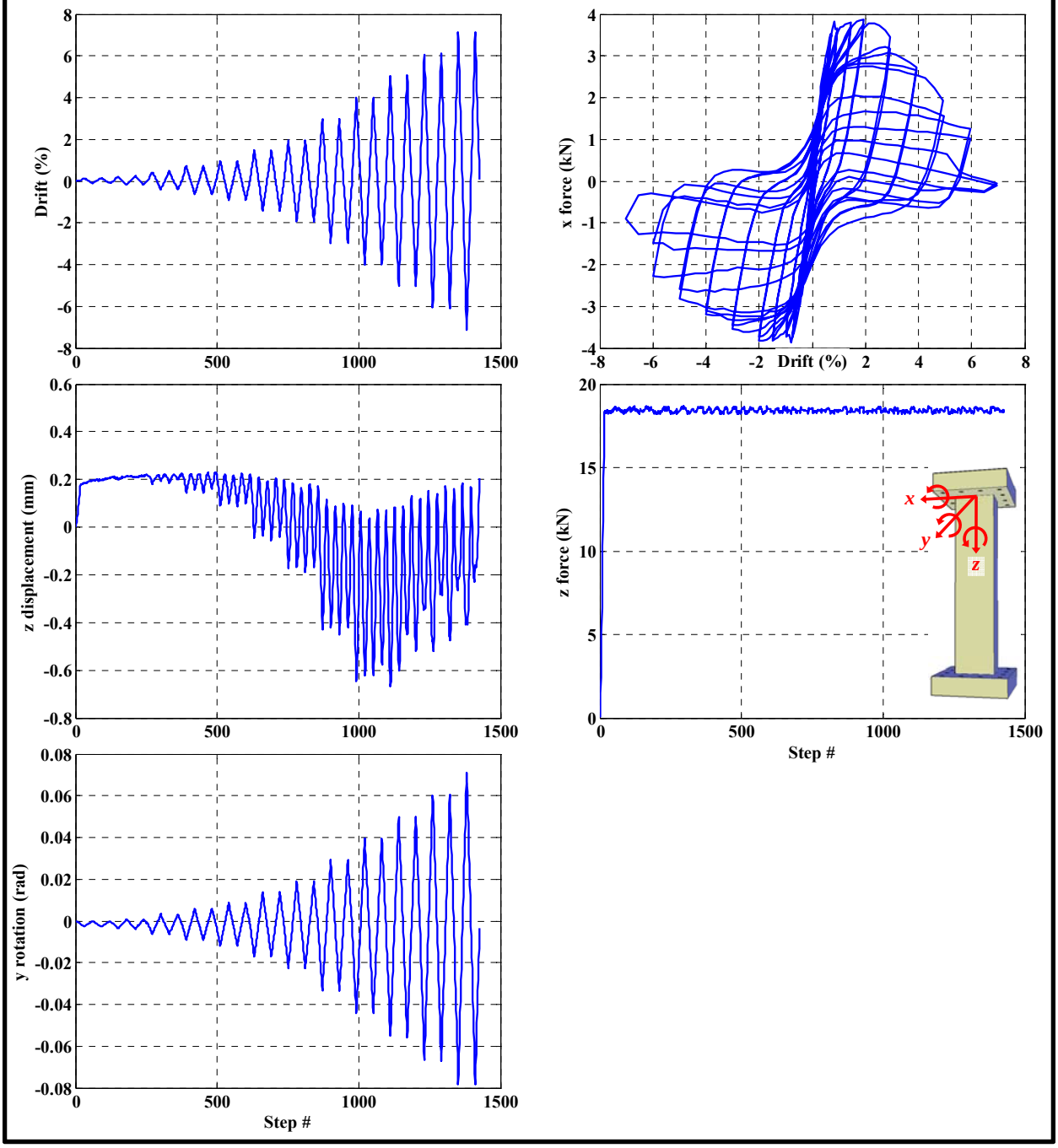

Figure A.13. Raw data from test #13

TEST ID	Long. Reinf. Ratio (%)	Trans. Reinf. Ratio (%)	Mix Design	Type of Test	Axial Load (%)
14	1.29	0.12	ECC-M45	Cyclic	7.5

Notes: none.

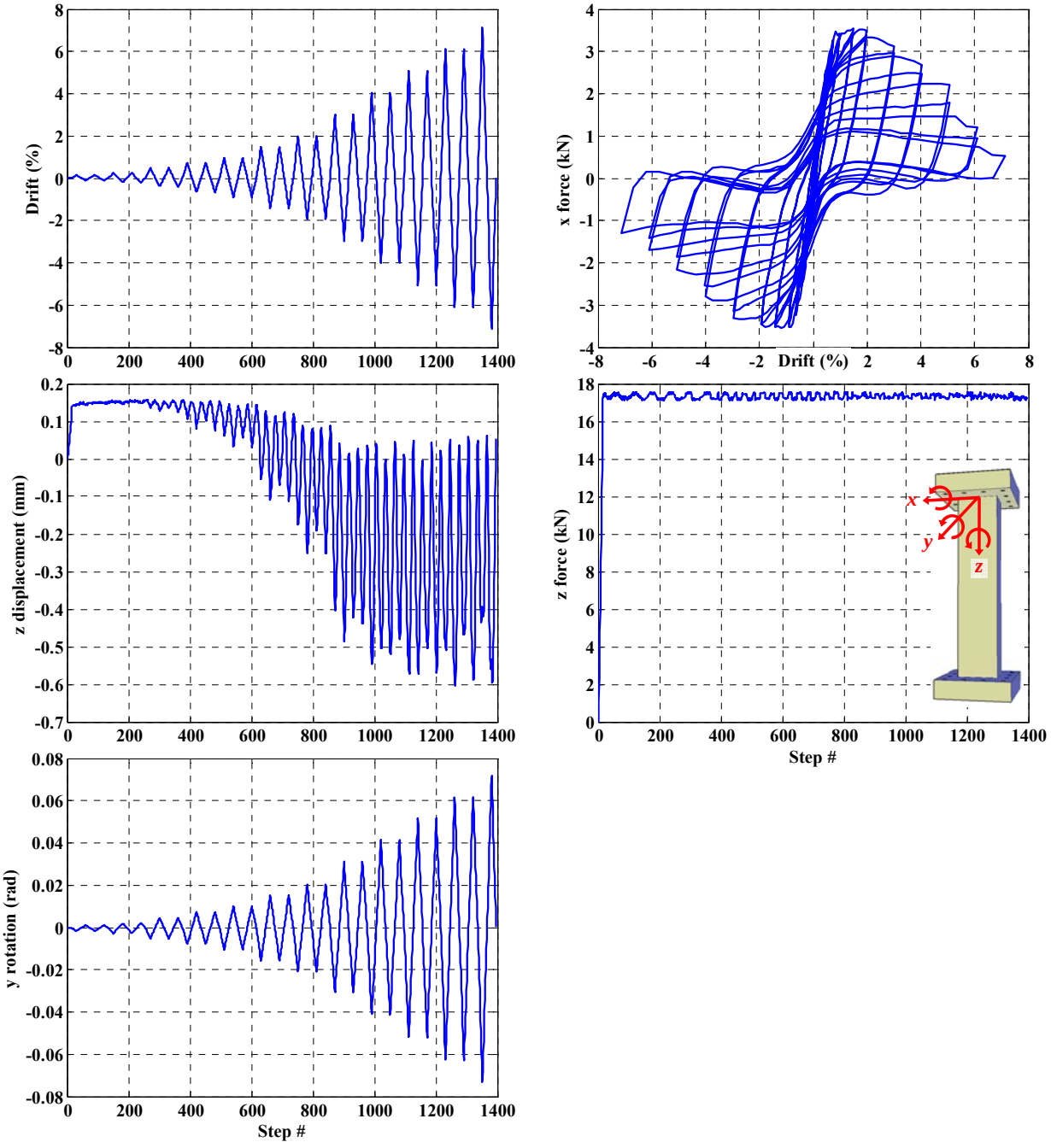

Figure A.14. Raw data from test #14

TEST ID	Long. Reinf. Ratio (%)	Trans. Reinf. Ratio (%)	Mix Design	Type of Test	Axial Load (%)
15	1.29	0.12	ECC-PPF	Cyclic	7.5

Notes: none.

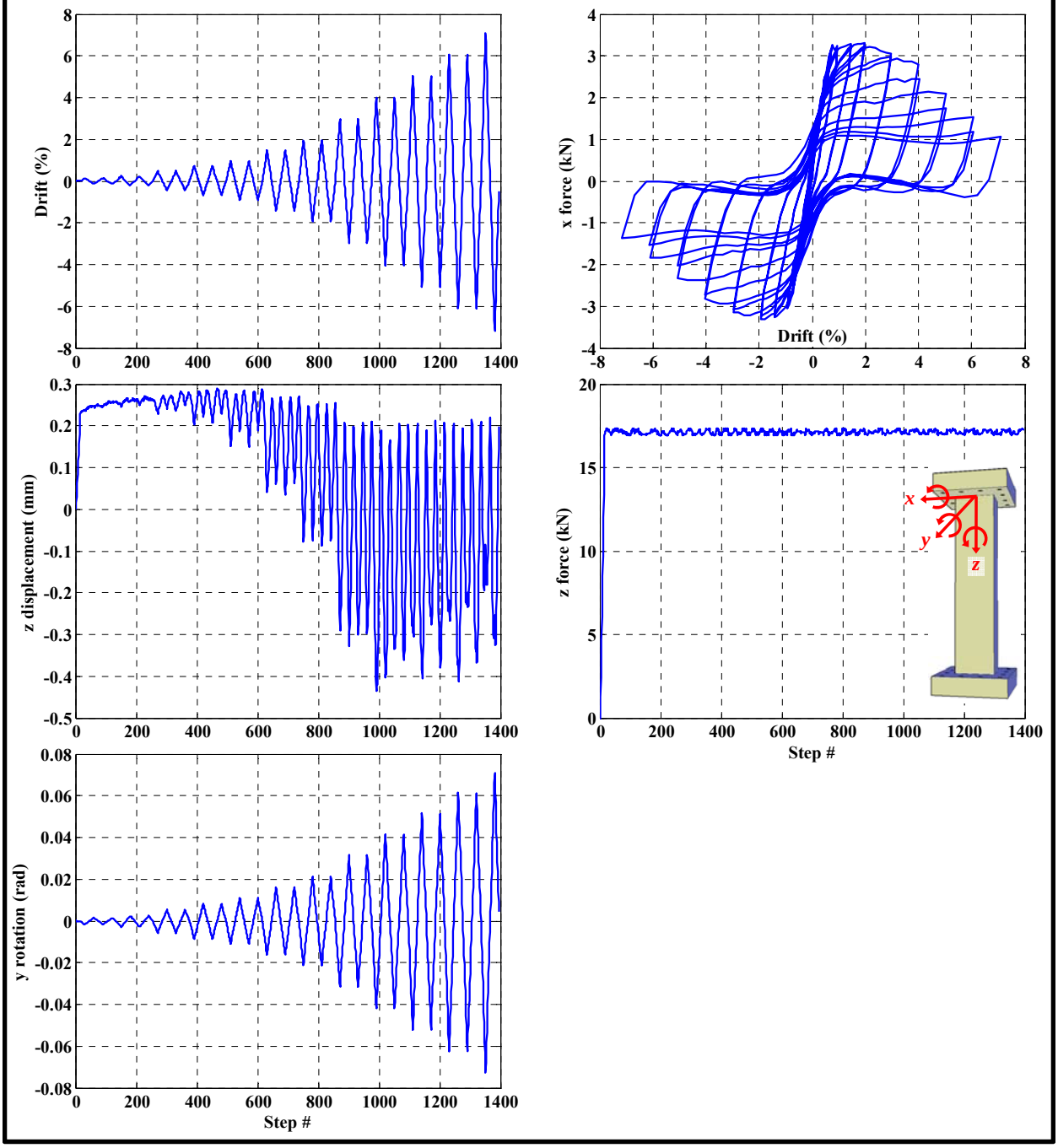

Figure A.15. Raw data from test #15

TEST ID	Long. Reinf. Ratio (%)	Trans. Reinf. Ratio (%)	Mix Design	Type of Test	Axial Load (%)
16	1.29	0.12	ECC-SF	Cyclic	7.5

Notes: none.

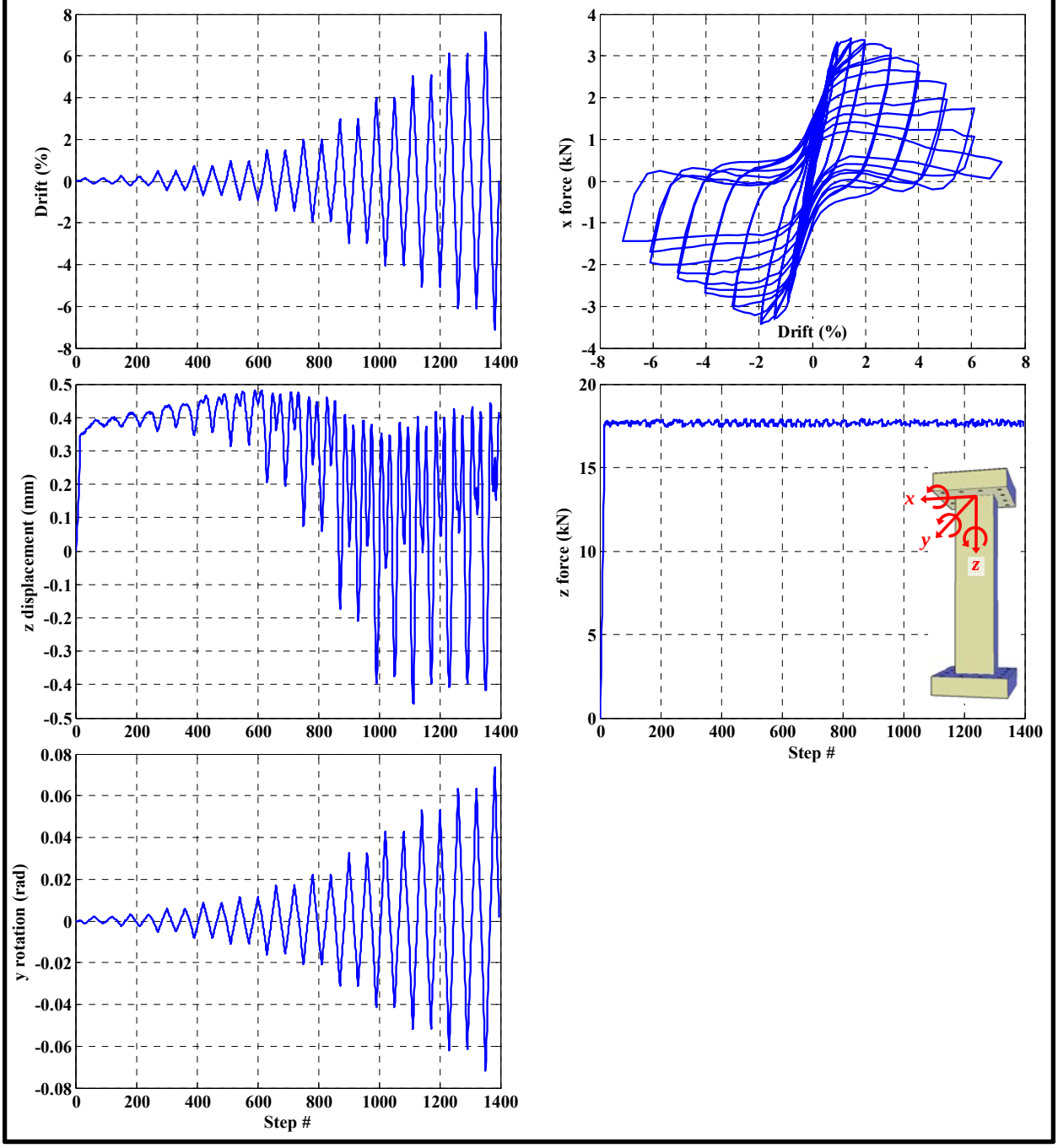

Figure A.16. Raw data from test #16

TEST ID	Long. Reinf. Ratio (%)	Trans. Reinf. Ratio (%)	Mix Design	Type of Test	Axial Load (%)
17	1.29	0.12	ECC-HFA	Cyclic-Fixed	7.5

Notes: perfectly fixed condition couldn't be achieved due to exceeding pLBCB capacity in z-direction at negative drifts. This is also the reason for nonzero y-rotation and asymmetric force-drift response.

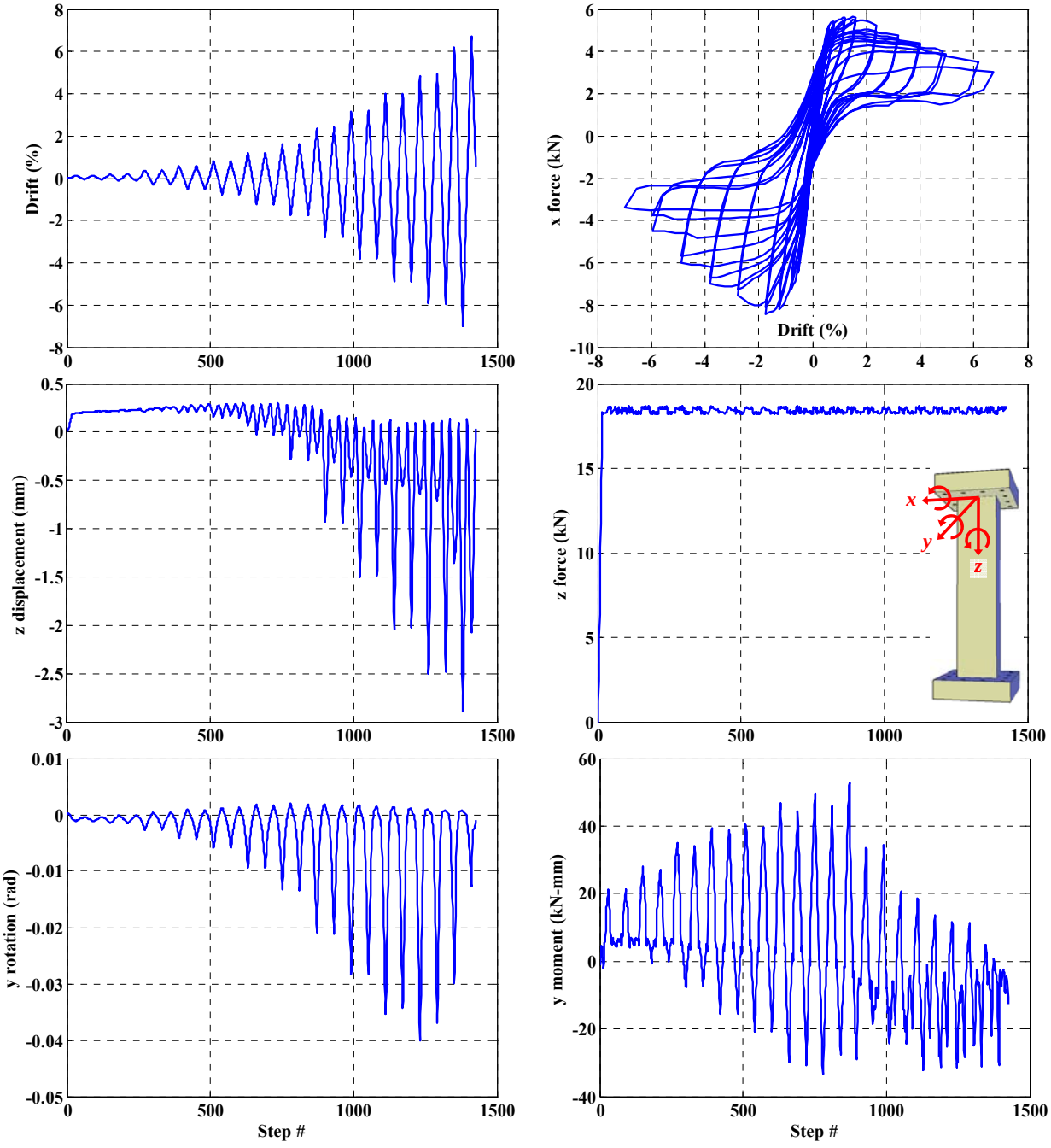

Figure A.17. Raw data from test #17

TEST ID	Long. Reinf. Ratio (%)	Trans. Reinf. Ratio (%)	Mix Design	Type of Test	Axial Load (%)
18	1.29	0.12	ECC-M45	Cyclic-Fixed	7.5

Notes: perfectly fixed condition couldn't be achieved due to exceeding pLBCB capacity in z-direction at negative drifts. This is also the reason for nonzero y-rotation and asymmetric force-drift response.

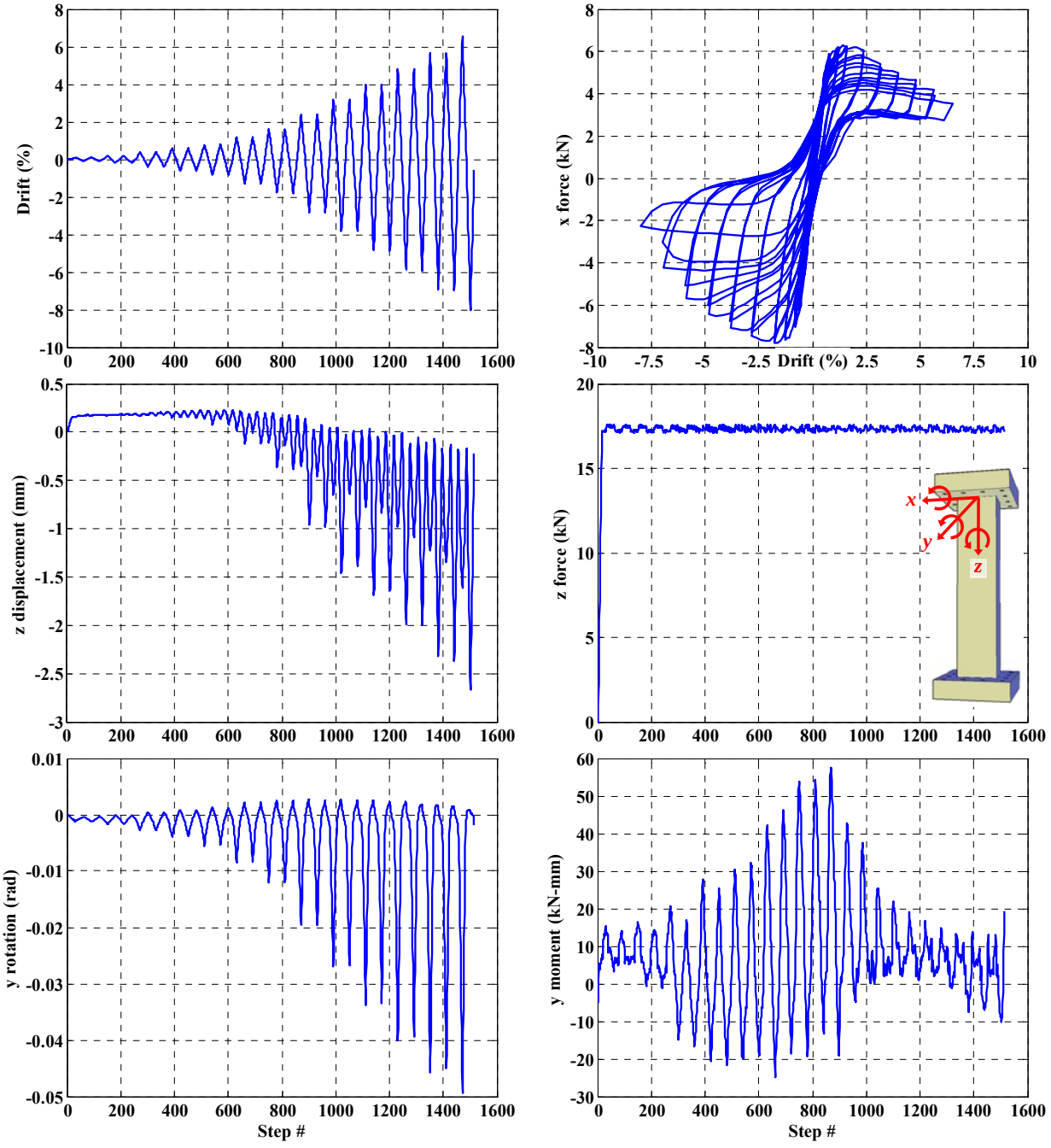

Figure A.18. Raw data from test #18

TEST ID	Long. Reinf. Ratio (%)	Trans. Reinf. Ratio (%)	Mix Design	Type of Test	Axial Load (%)
19	1.29	0.12	ECC-PPF	Cyclic-Fixed	7.5

Notes: perfectly fixed condition couldn't be achieved due to exceeding pLBCB capacity in z-direction at negative drifts. This is also the reason for nonzero y-rotation and asymmetric force-drift response.

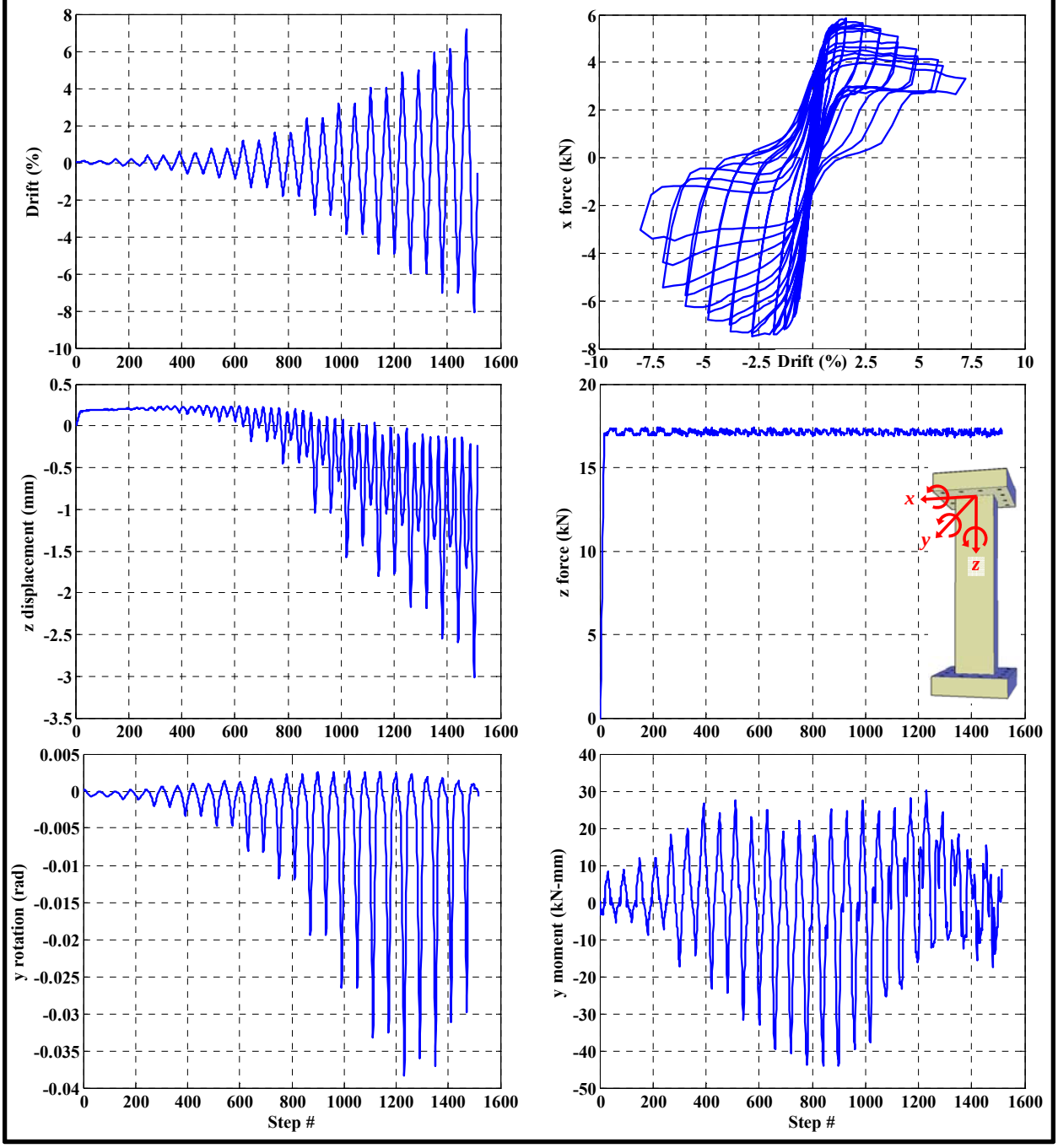

Figure A.19. Raw data from test #19

TEST ID	Long. Reinf. Ratio (%)	Trans. Reinf. Ratio (%)	Mix Design	Type of Test	Axial Load (%)
20	1.29	0.12	ECC-SF	Cyclic-Fixed	7.5

Notes: perfectly fixed condition couldn't be achieved due to exceeding pLBCB capacity in z-direction at negative drifts. This is also the reason for nonzero y-rotation and asymmetric force-drift response.

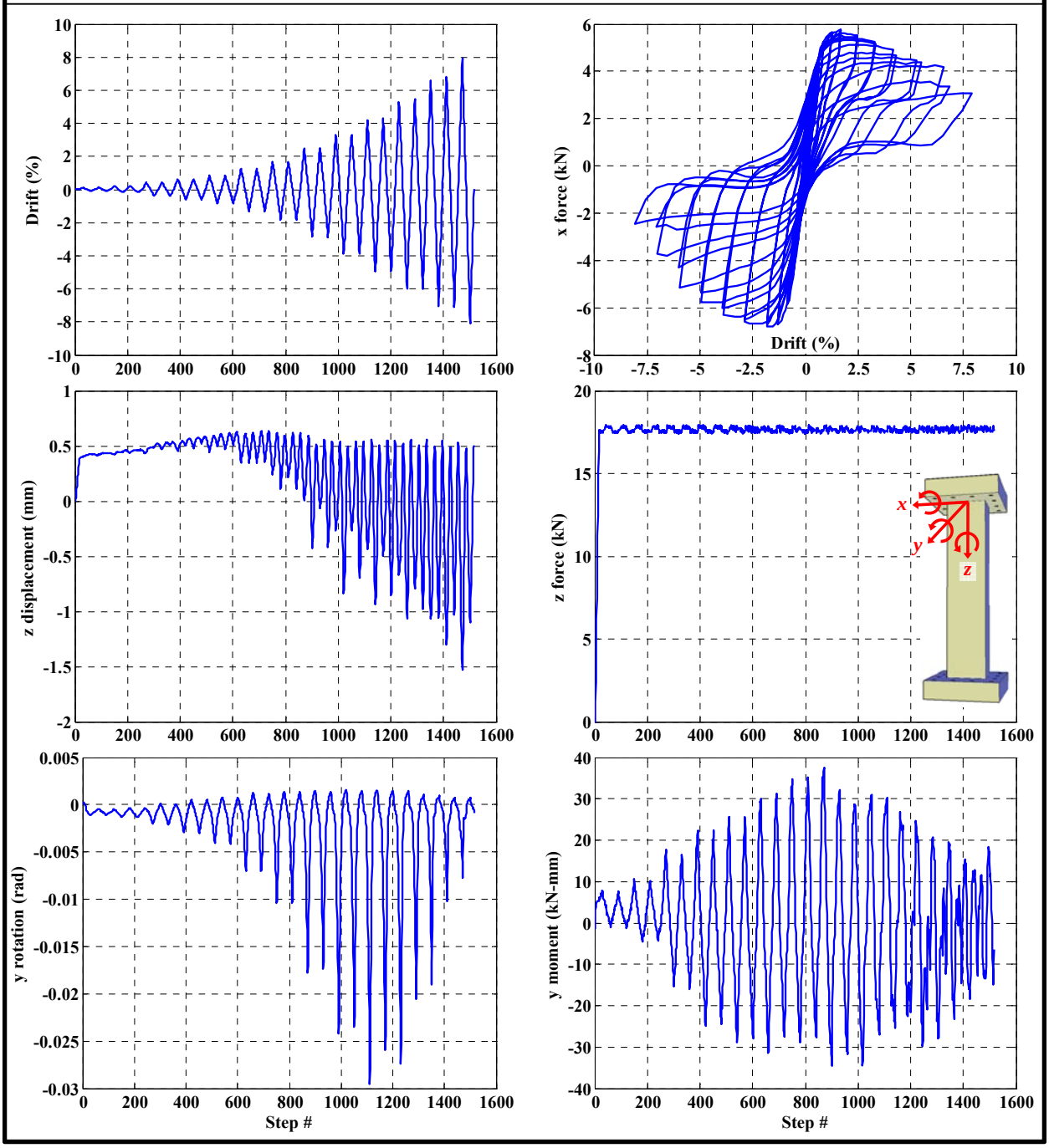

Figure A.20. Raw data from test #20

TEST ID	Long. Reinf. Ratio (%)	Trans. Reinf. Ratio (%)	Mix Design	Type of Test	Axial Load (%)
21	1.29	N/A	ECC-HFA	STH	5

Notes: none.

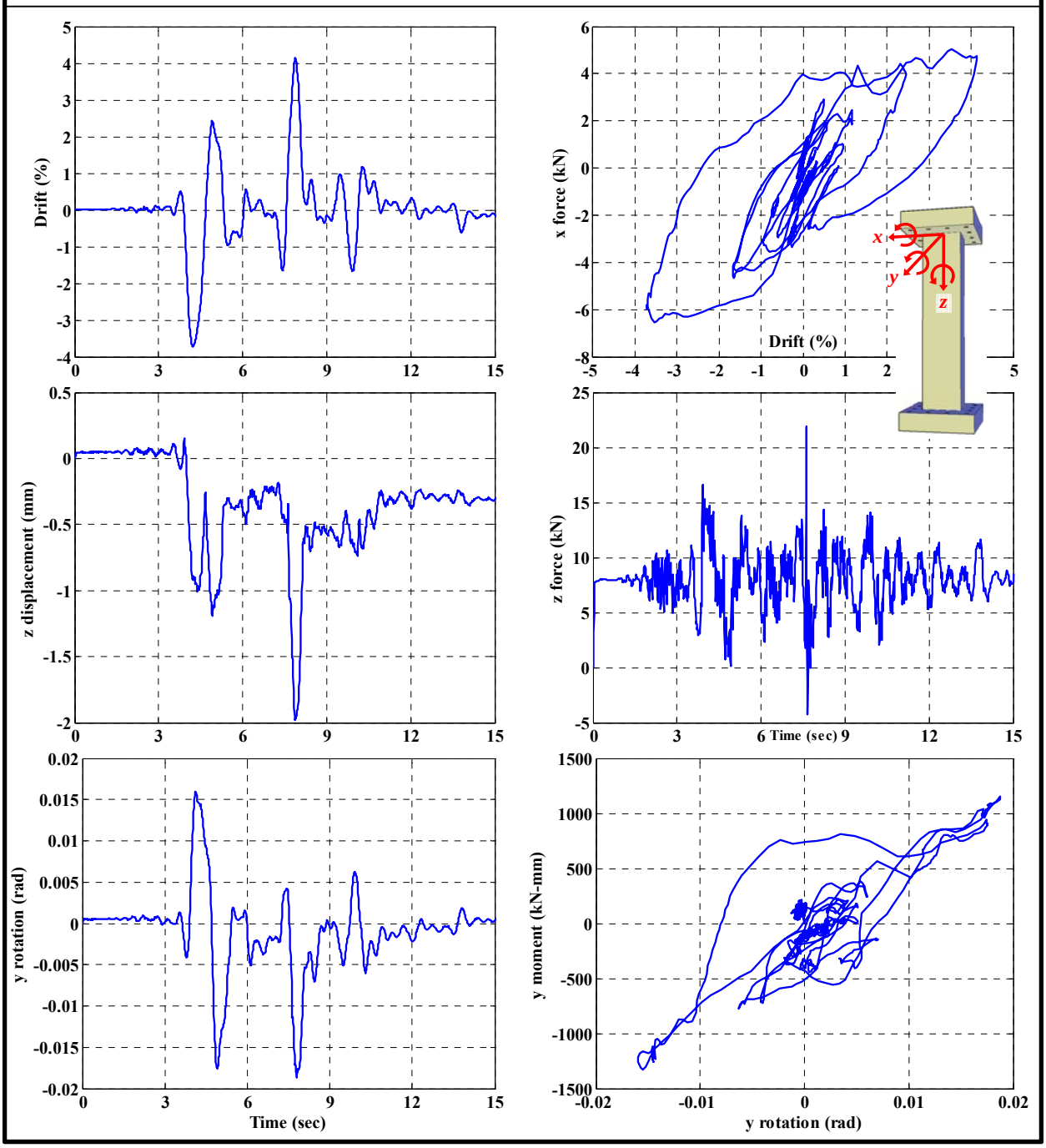

Figure A.21. Raw data from test #21

TEST ID	Long. Reinf. Ratio (%)	Trans. Reinf. Ratio (%)	Mix Design	Type of Test	Axial Load (%)
22	1.29	N/A	ECC-HFA	STH	10

Notes: none.

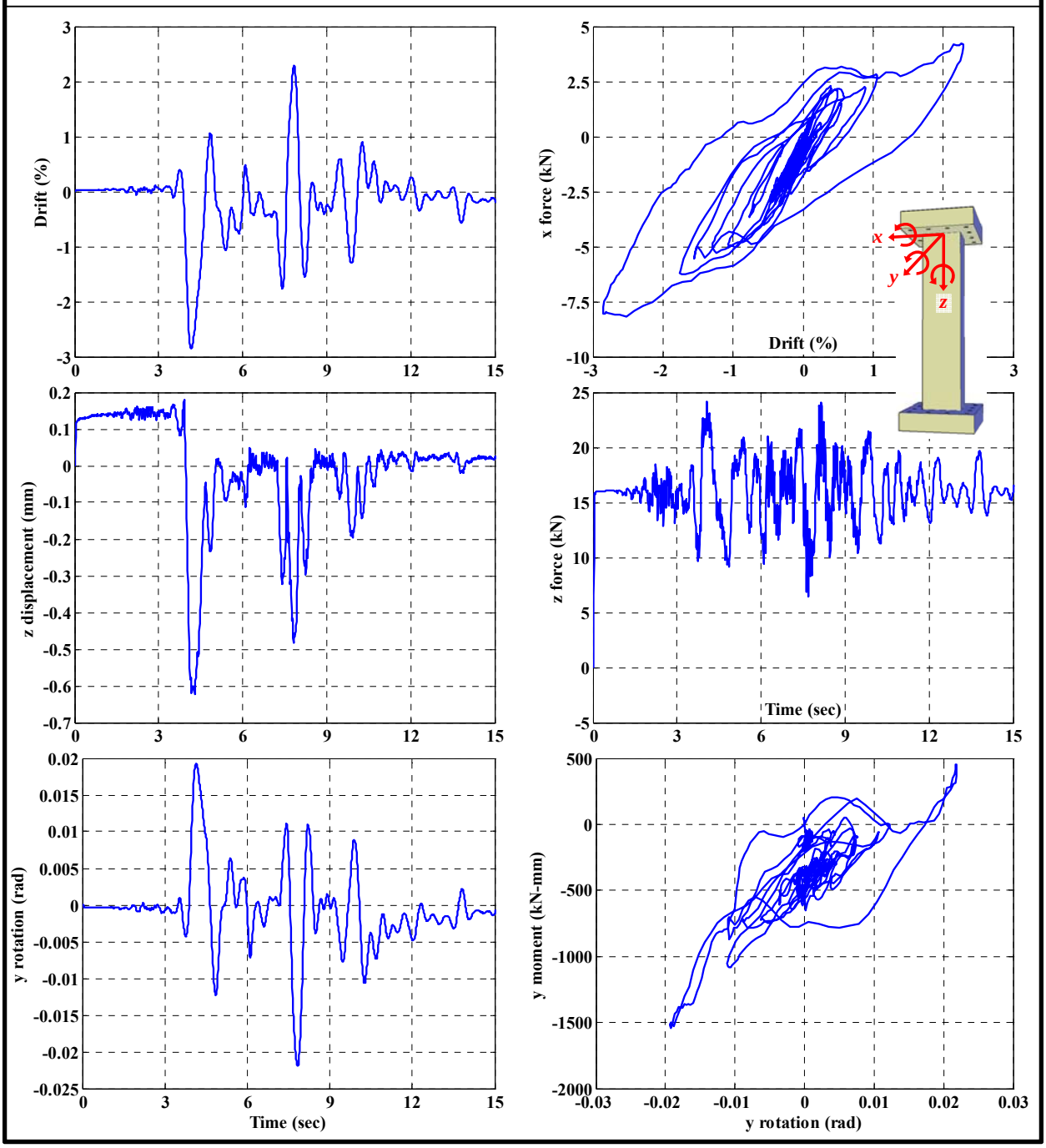

Figure A.22. Raw data from test #22

TEST ID	Long. Reinf. Ratio (%)	Trans. Reinf. Ratio (%)	Mix Design	Type of Test	Axial Load (%)
23	0.87	0.36	Concrete	Hybrid	7.5

Notes: none.

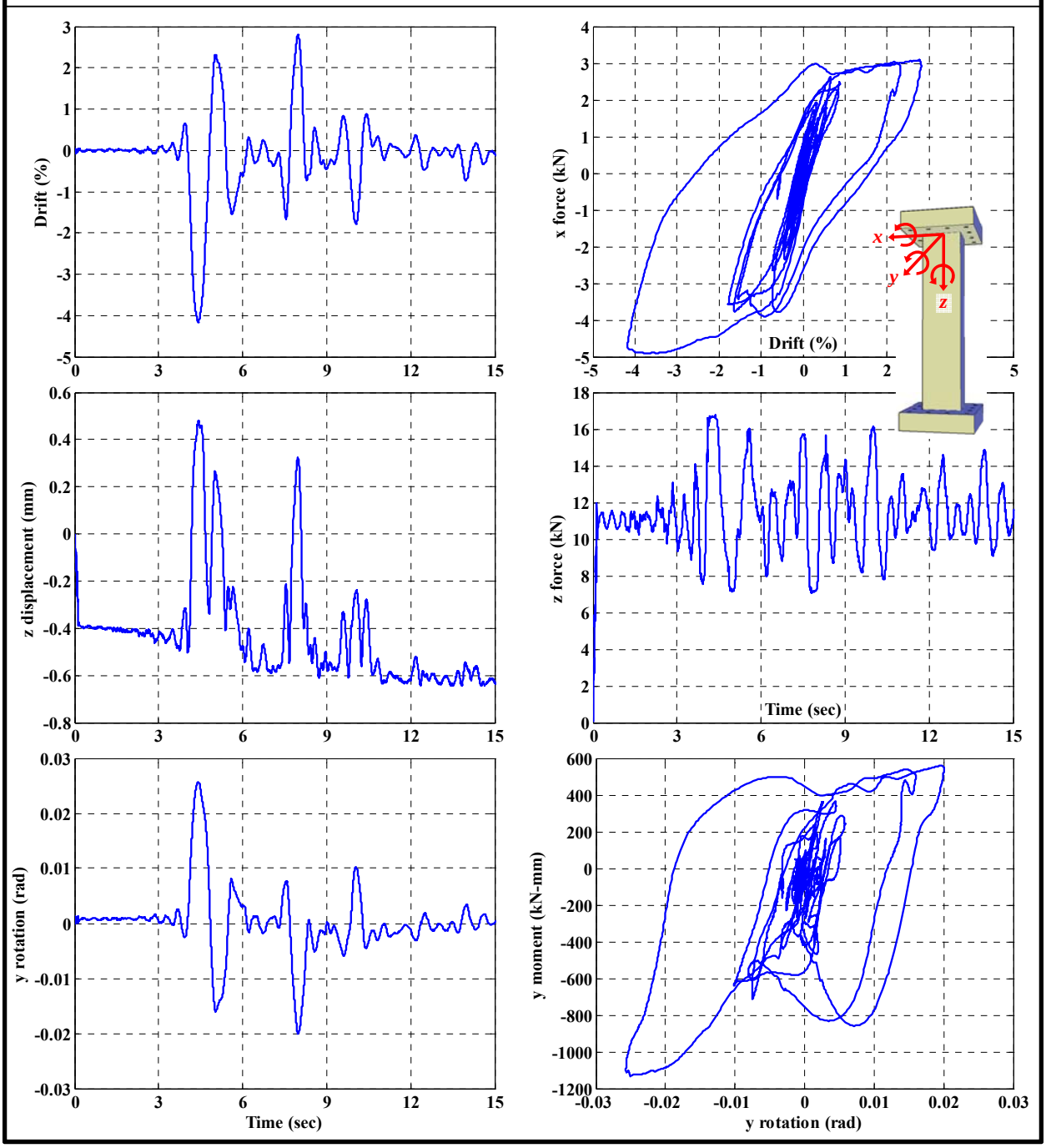

Figure A.23. Raw data from test #23

TEST ID	Long. Reinf. Ratio (%)	Trans. Reinf. Ratio (%)	Mix Design	Type of Test	Axial Load (%)
24	0.87	0.12	ECC-HFA	Hybrid	7.5

Notes: none.

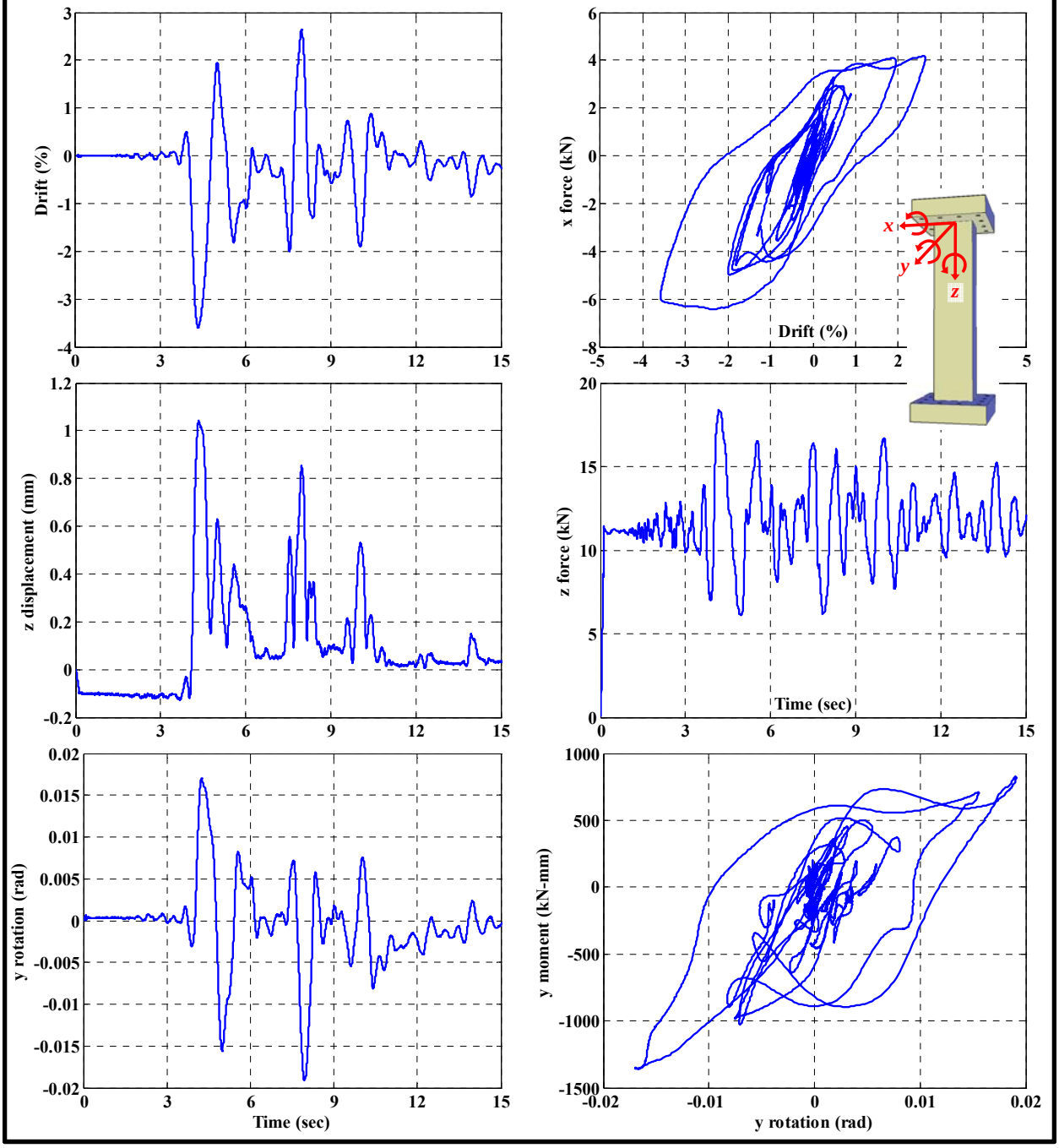

Figure A.24. Raw data from test #24

TEST ID	Long. Reinf. Ratio (%)	Trans. Reinf. Ratio (%)	Mix Design	Type of Test	Axial Load (%)
25	1.29	N/A	ECC-HFA	Hybrid	5

Notes: none.

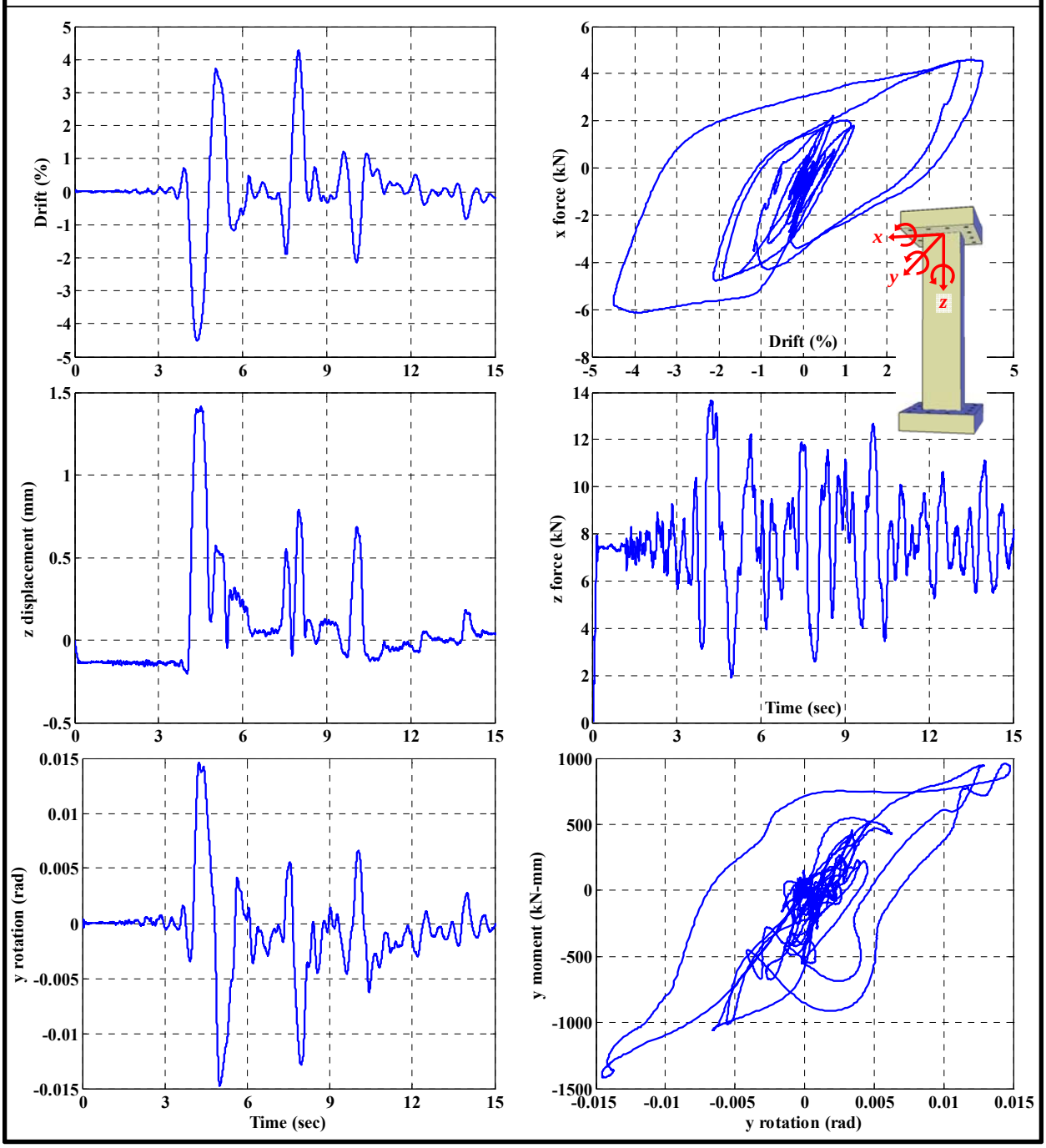

Figure A.25. Raw data from test #25

TEST ID	Long. Reinf. Ratio (%)	Trans. Reinf. Ratio (%)	Mix Design	Type of Test	Axial Load (%)
26	1.29	N/A	ECC-HFA	Hybrid	10

Notes: none.

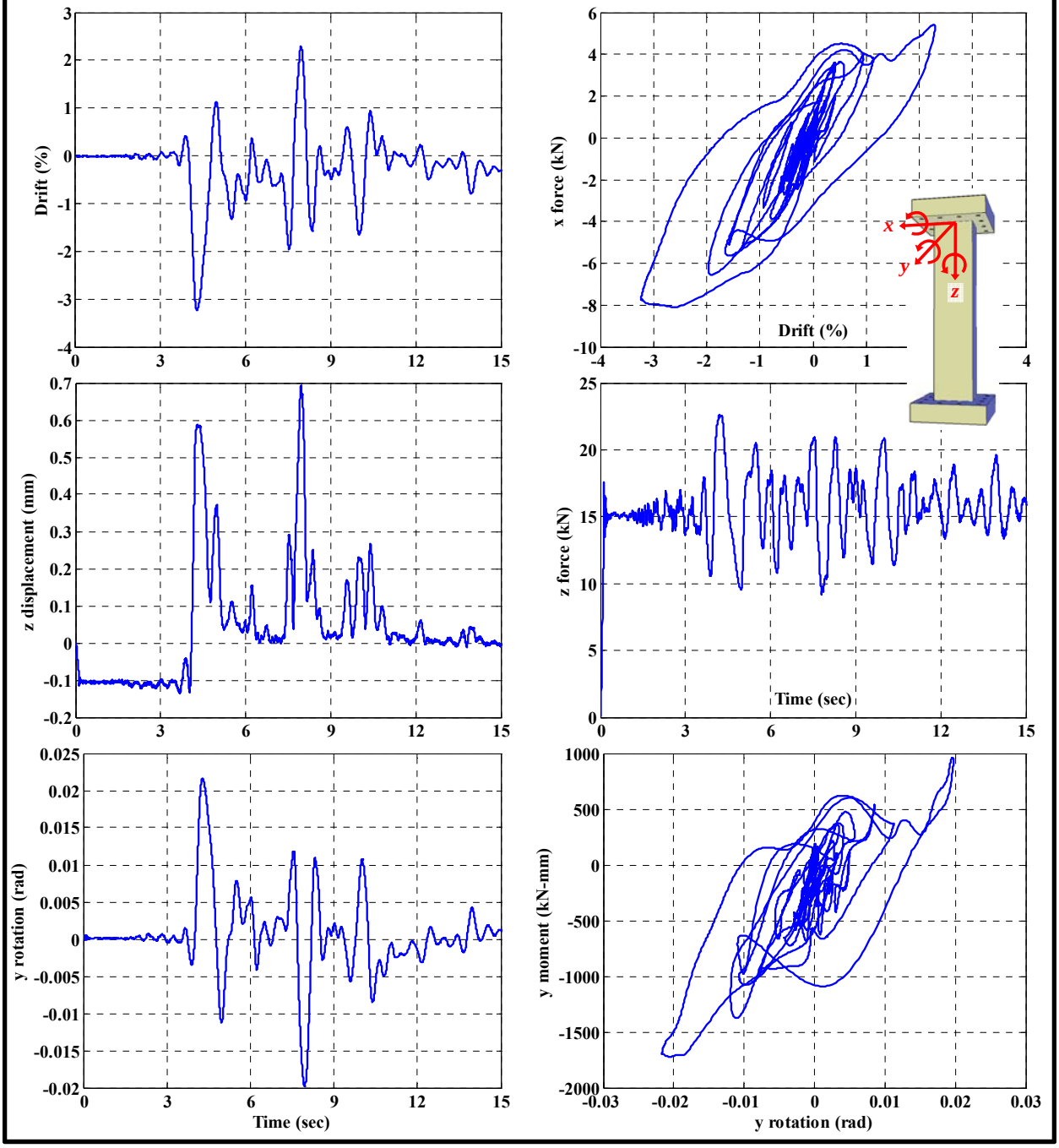

Figure A.26. Raw data from test #26

APPENDIX B

FORMWORK DESIGN DRAWINGS

In Appendix B, the design drawings for PVC formwork is provided. The formwork is composed of seven different parts which are numbered in Figure B.1. The formwork is symmetric with respect to both x and y axes.

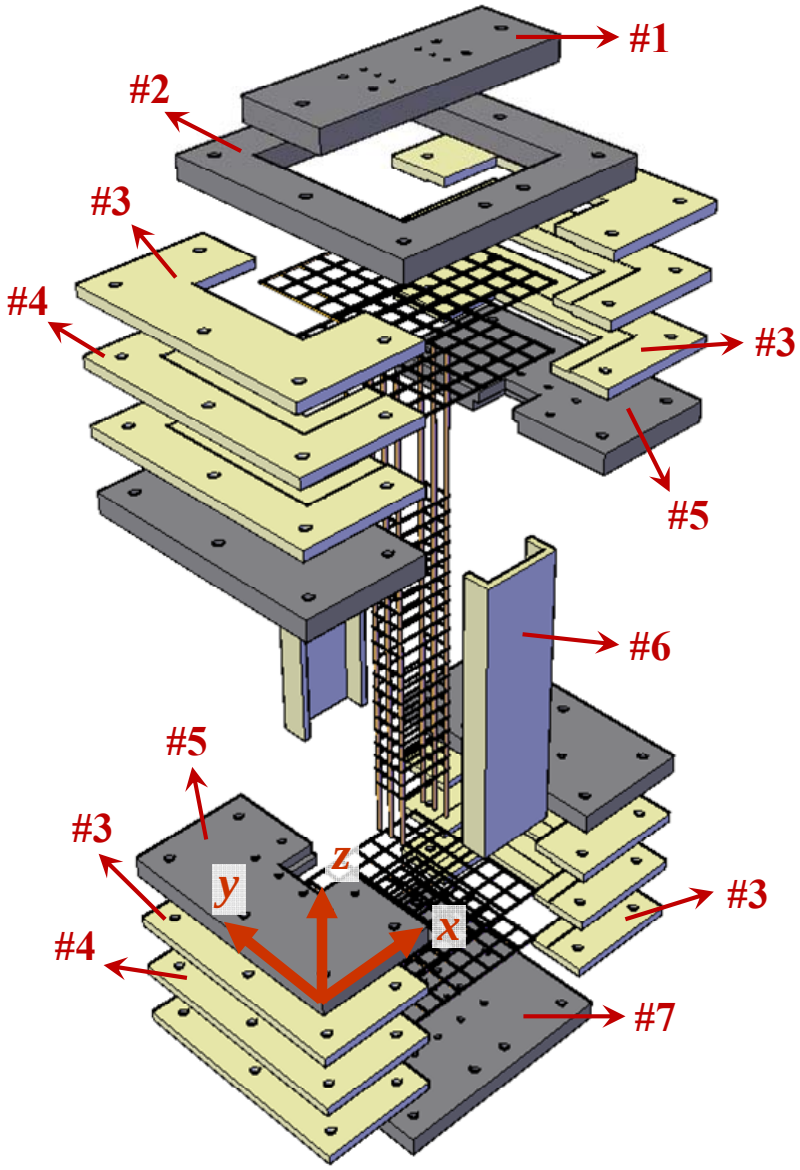

Figure B.1. Numbering of formwork parts

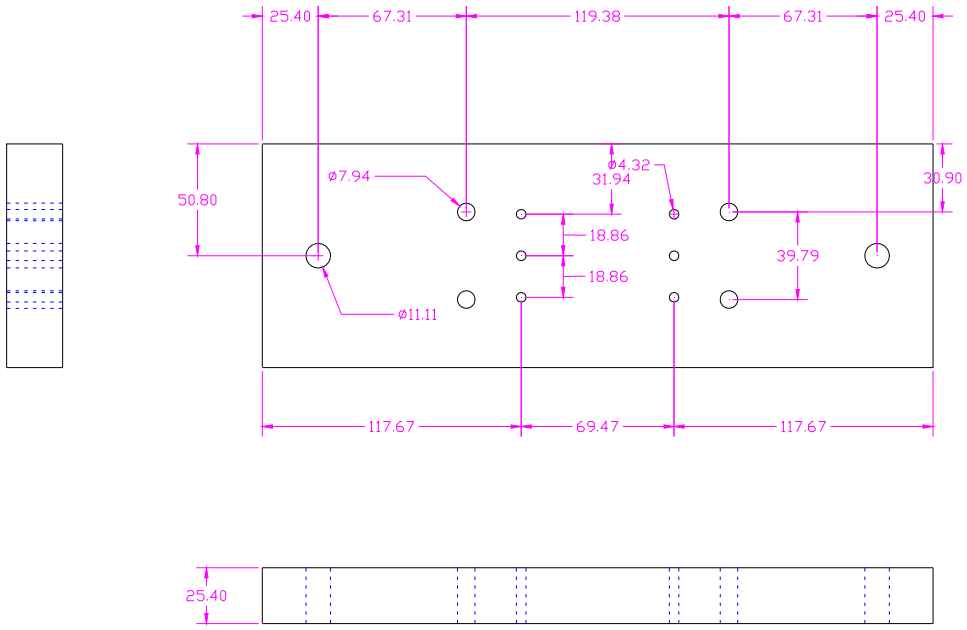

Figure B.2. Design drawing for part #1, a total of one piece (all values are in mm)

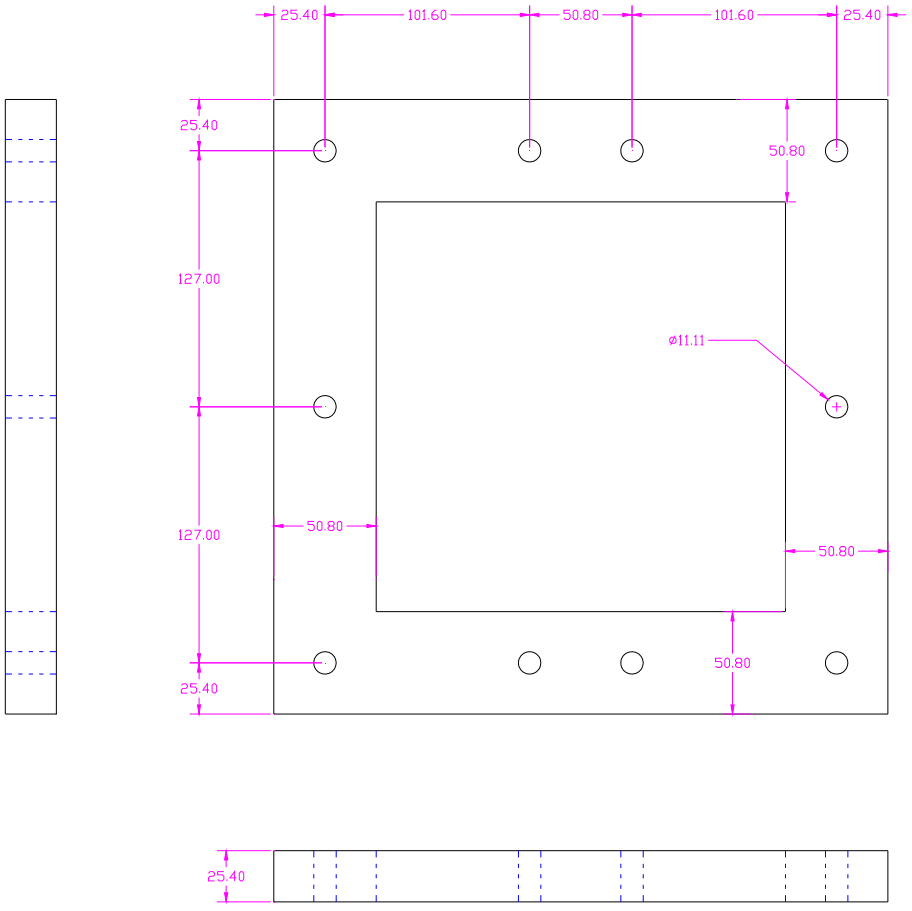

Figure B.3. Design drawing for part #2, a total of one piece (all values are in mm)

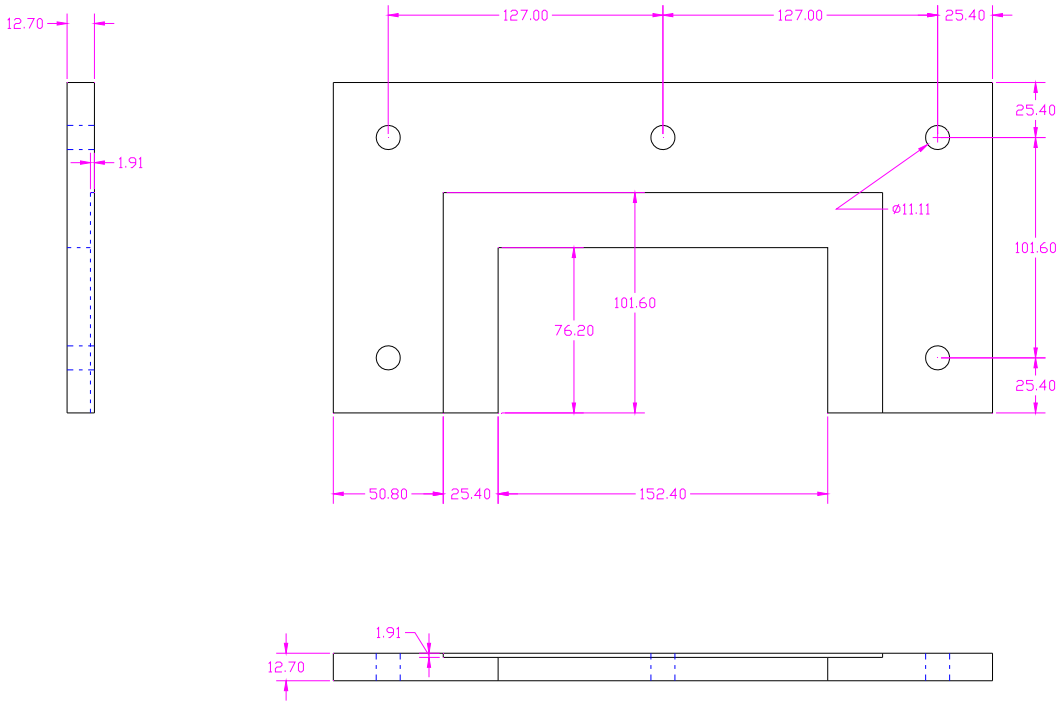

Figure B.4. Design drawing for part #3, a total of eight pieces (all values are in mm)

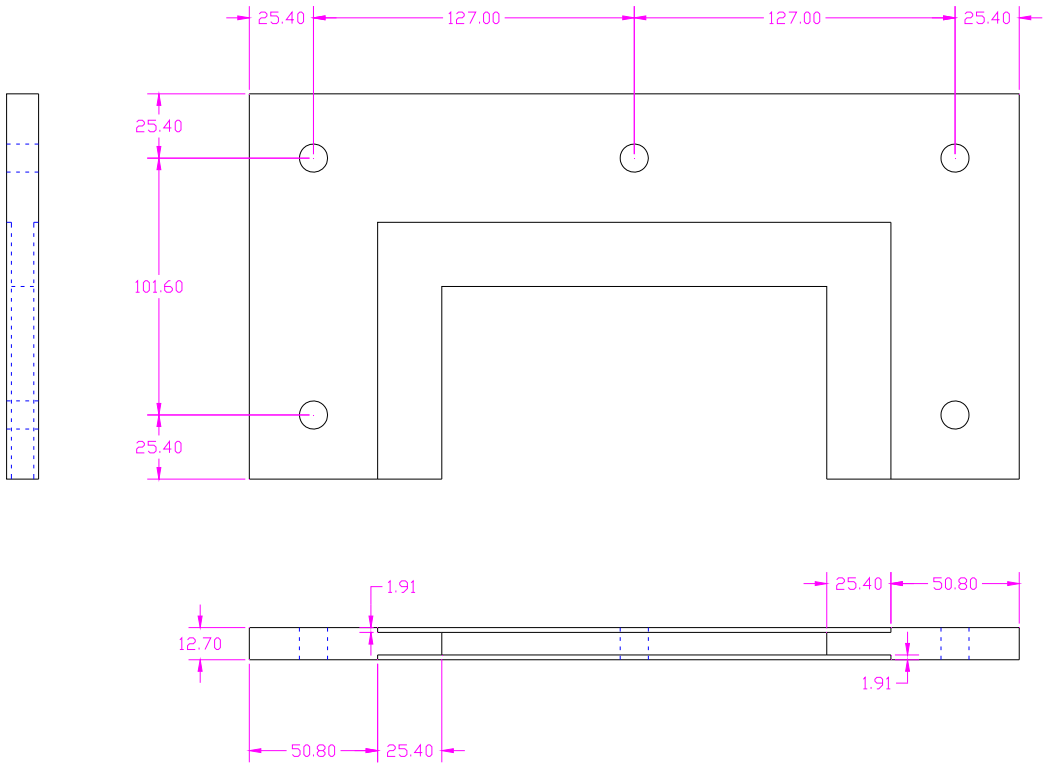

Figure B.5. Design drawing for part #4, a total of four pieces (all values are in mm)

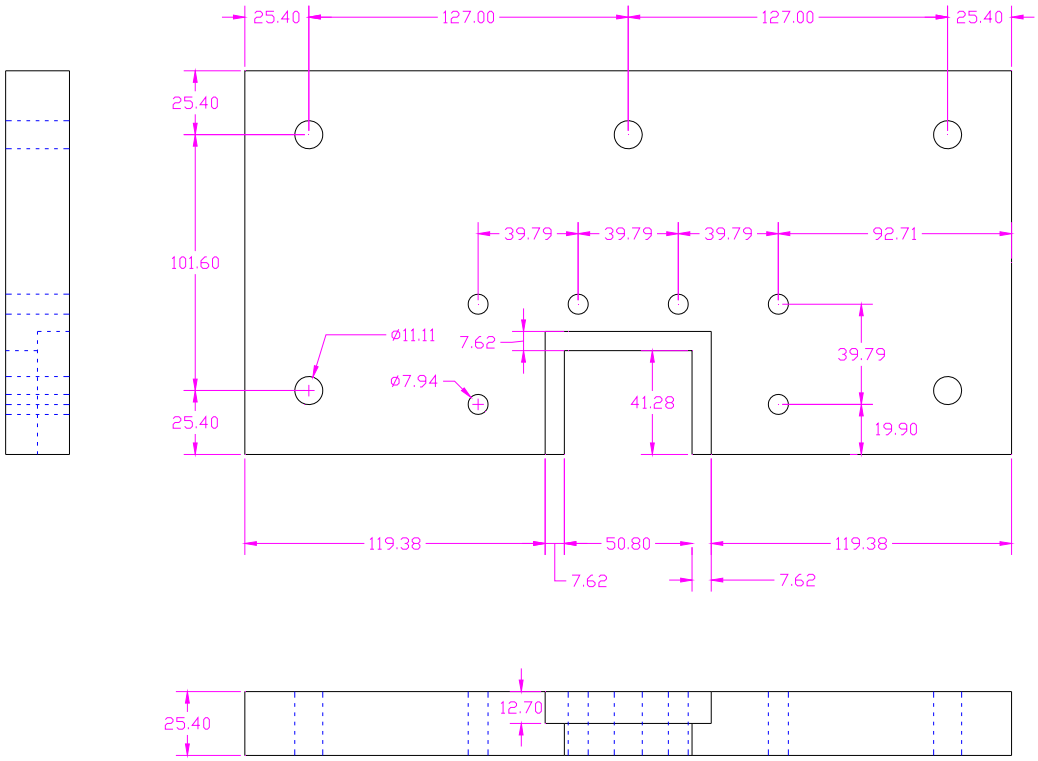

Figure B.6. Design drawing for part #5, a total of four pieces (all values are in mm)

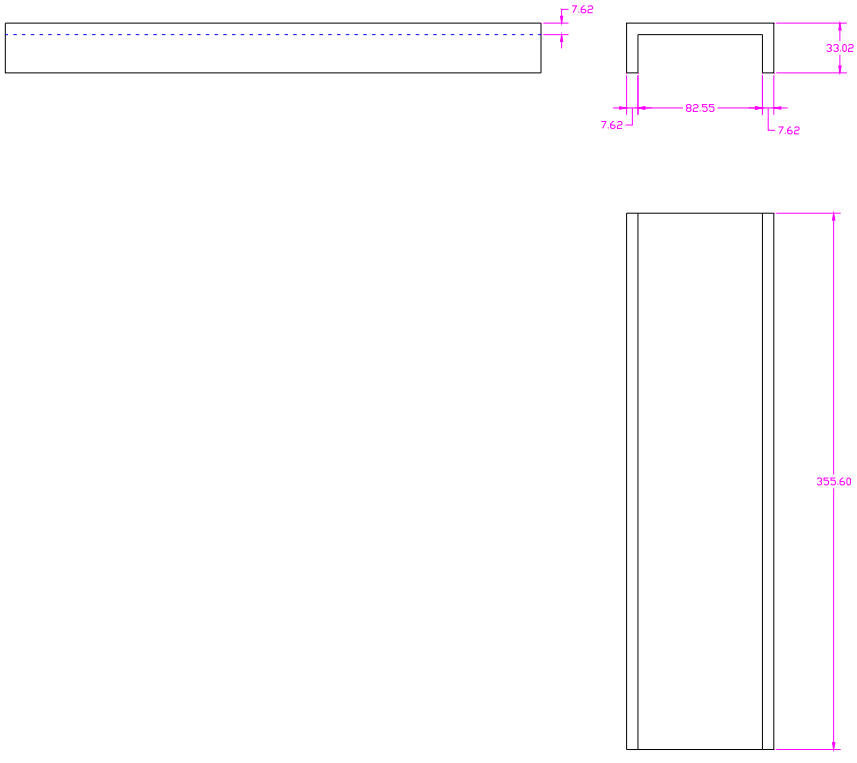

Figure B.7. Design drawing for part #6, a total of two pieces (all values are in mm)

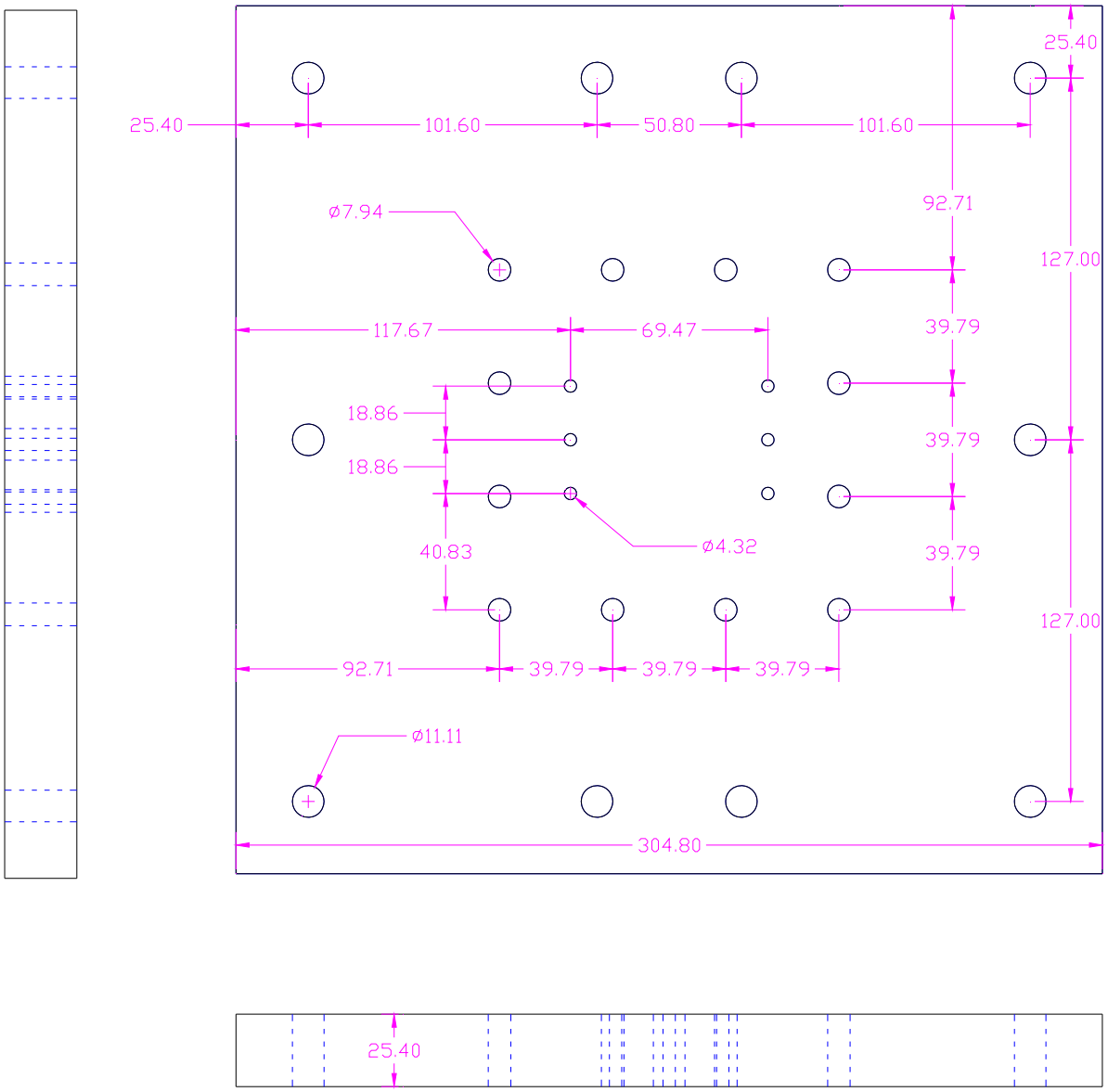

Figure B.8. Design drawing for part #7, a total of one piece (all values are in mm)

APPENDIX C

DISAGGREGATION RESULTS AND GROUND MOTIONS

C.1. DISAGGREGATION RESULTS

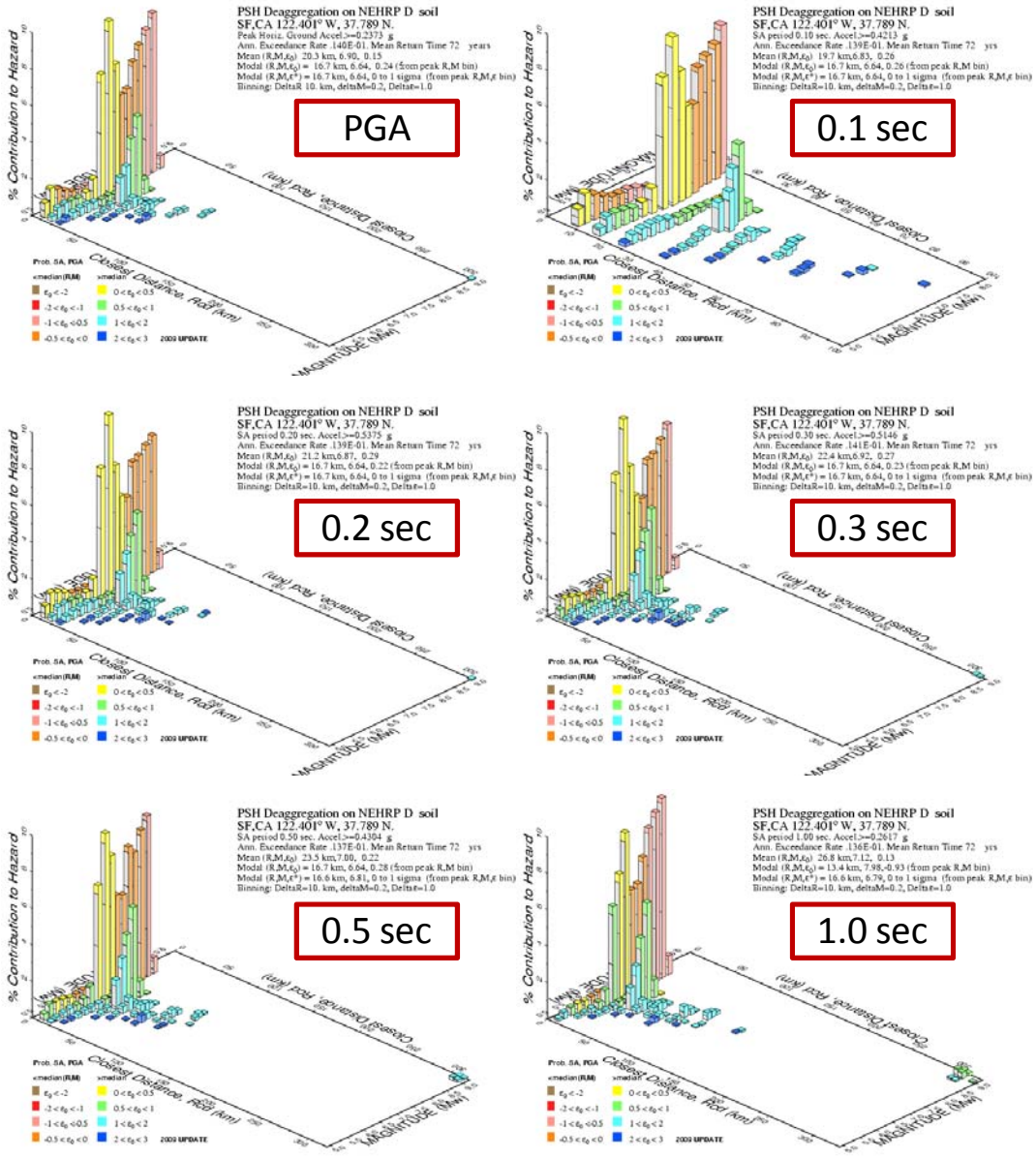

Figure C.1. Disaggregation results for the hazard with 75 YRP (USGS, 2009a)

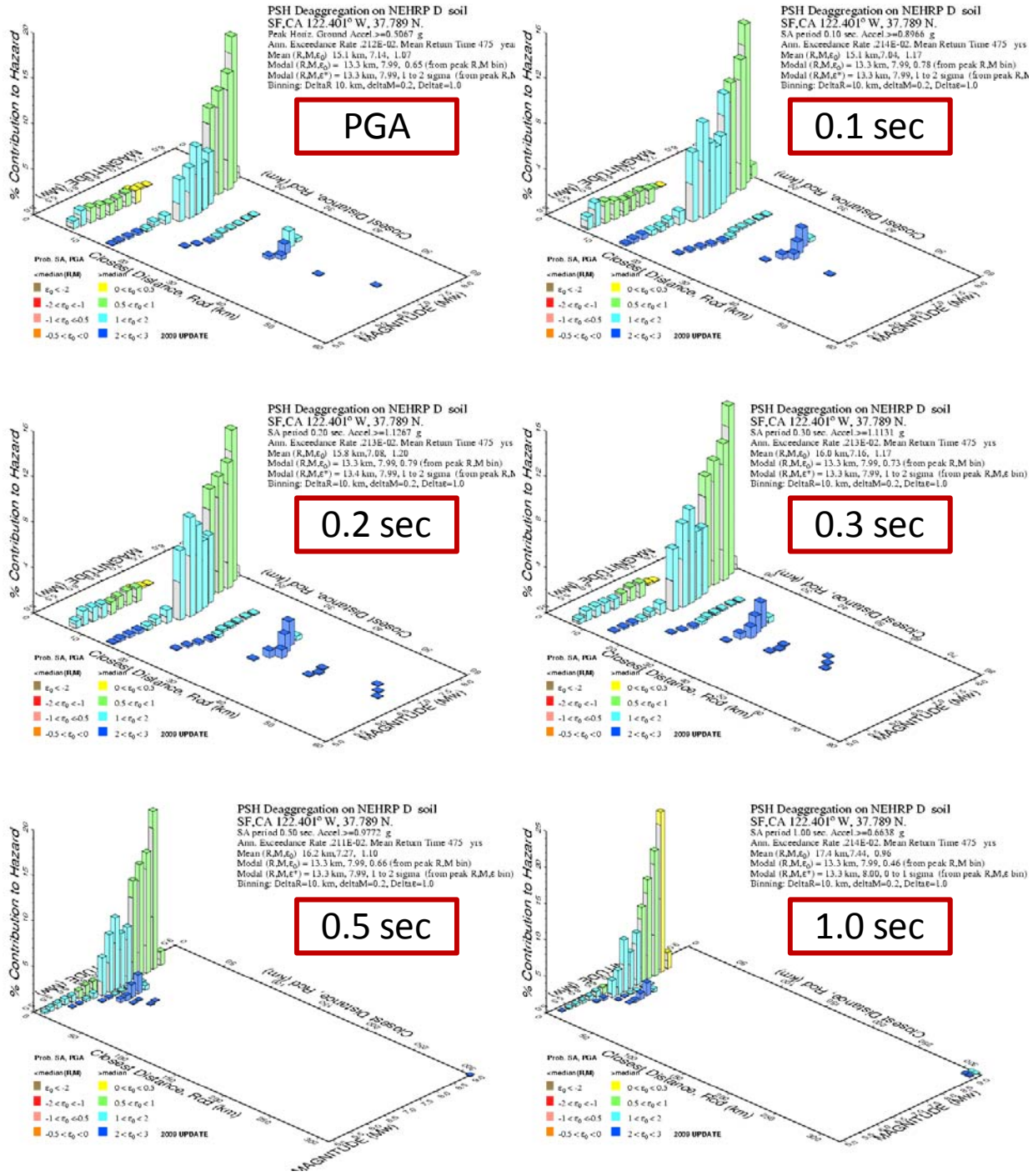

Figure C.2. Disaggregation results for the hazard with 475 YRP (USGS, 2009a)

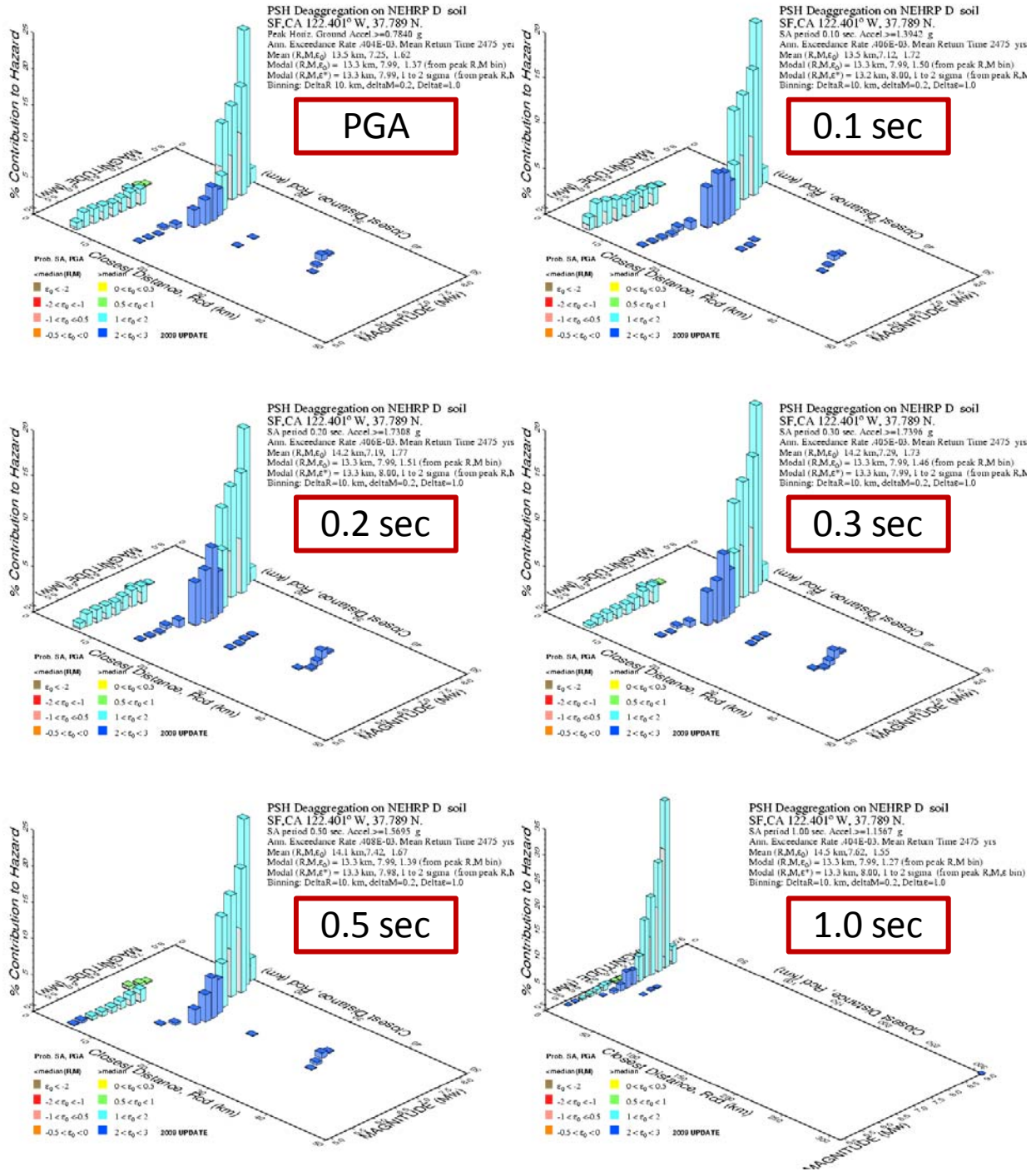

Figure C.3. Disaggregation results for the hazard with 2475 YRP (USGS, 2009a)

C.2. SPECTRA AND ACCELERATION TIME HISTORY OF GROUND MOTIONS

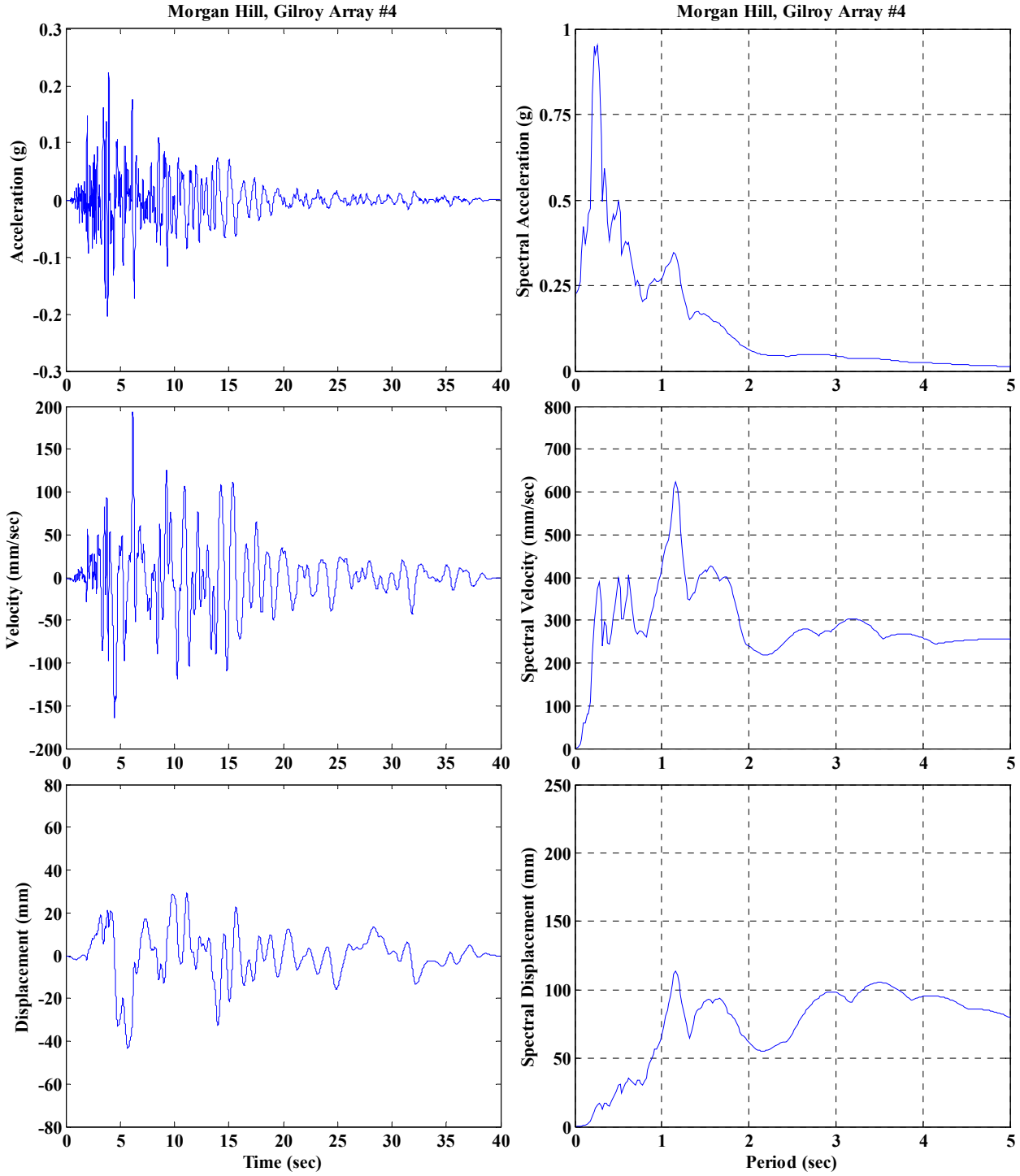

Figure C.4. 75 YRP, Morgan Hill, Gilroy Array #4

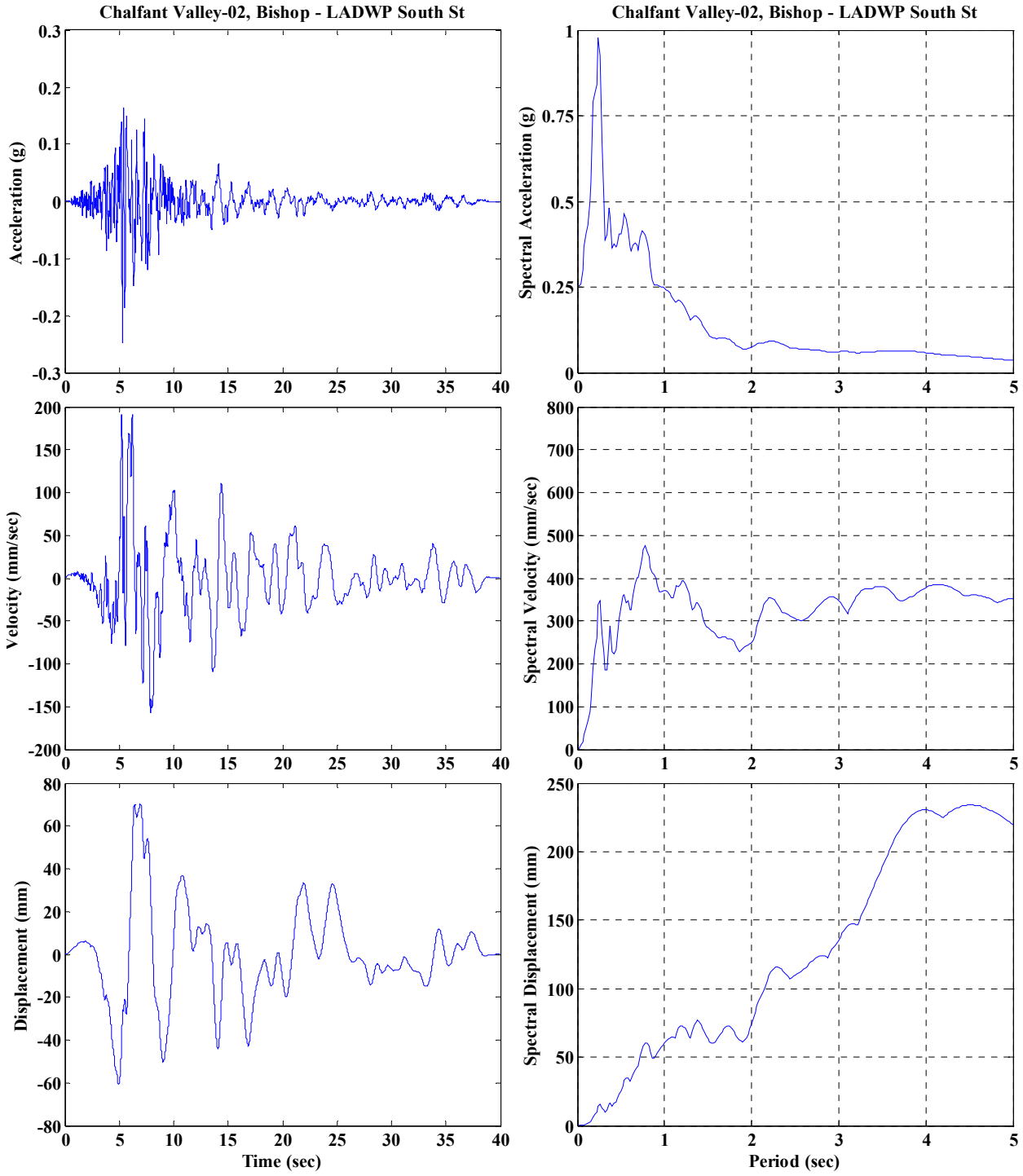

Figure C.5. 75 YRP, Chalfant Valley-02, Station: Bishop – LADWP South

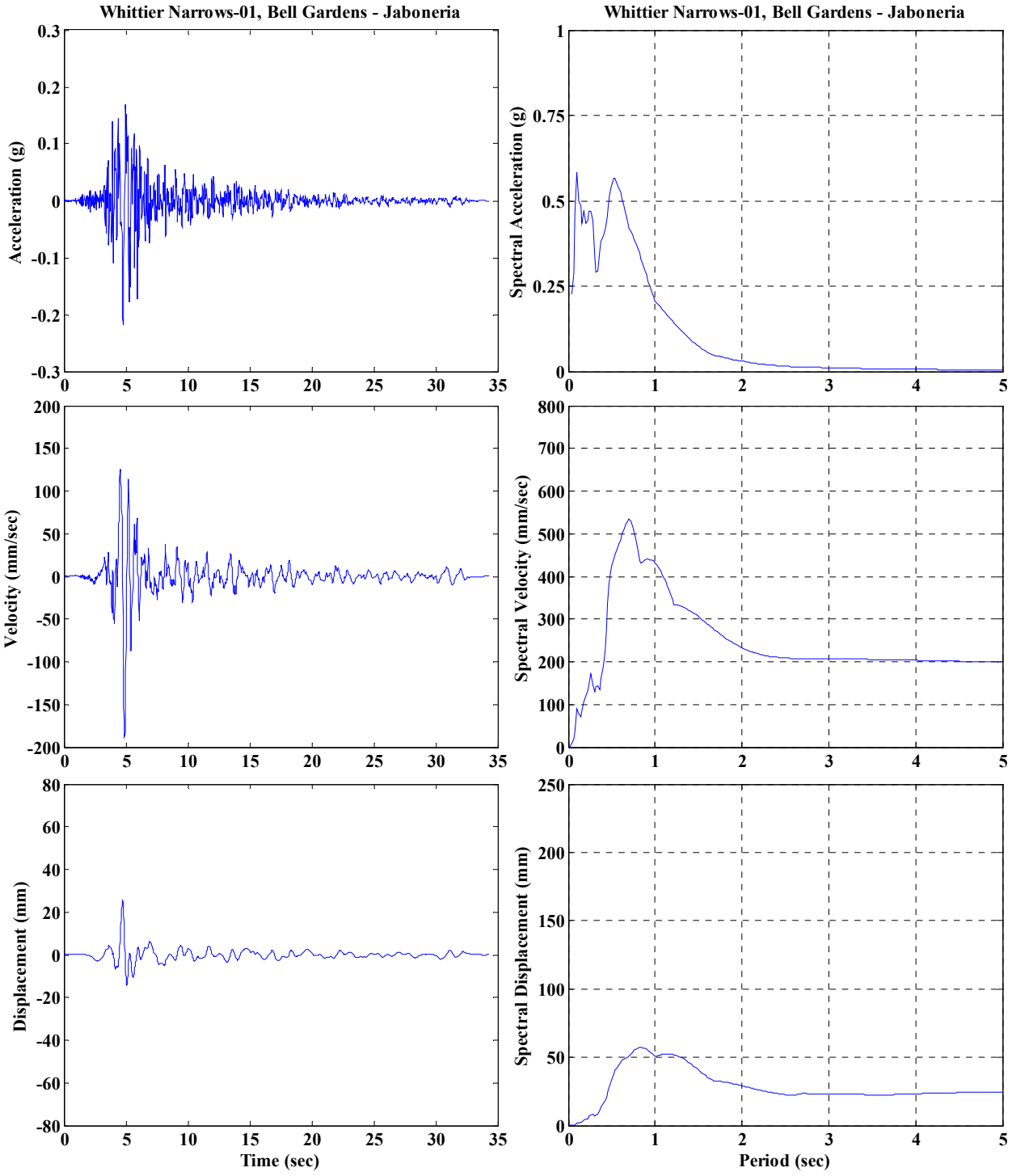

Figure C.6. 75 YRP, Whittier Narrows-01, Bell Gardens - Jaboneria

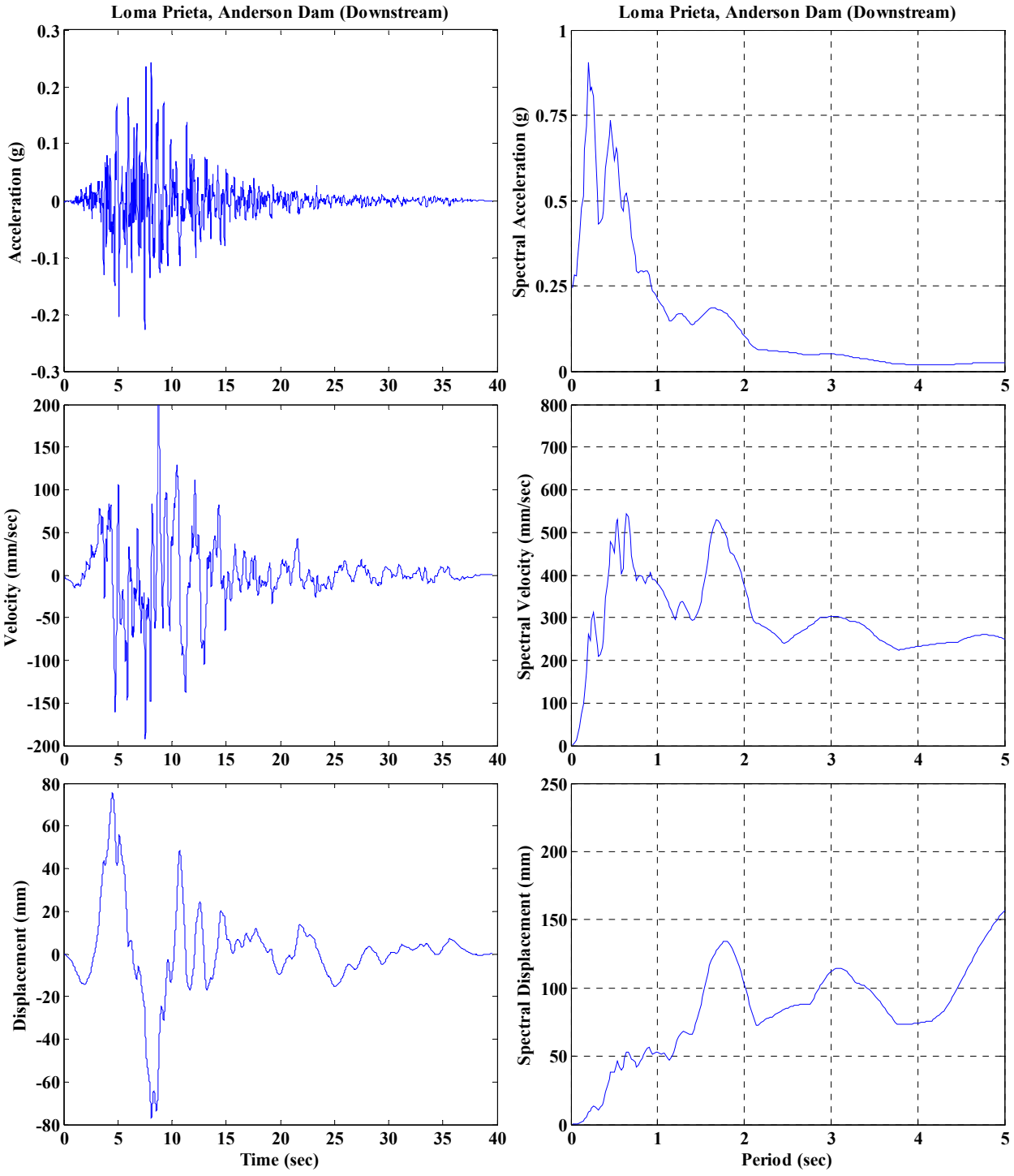

Figure C.7. 75 YRP, Loma Prieta, Anderson Dam (Downstream)

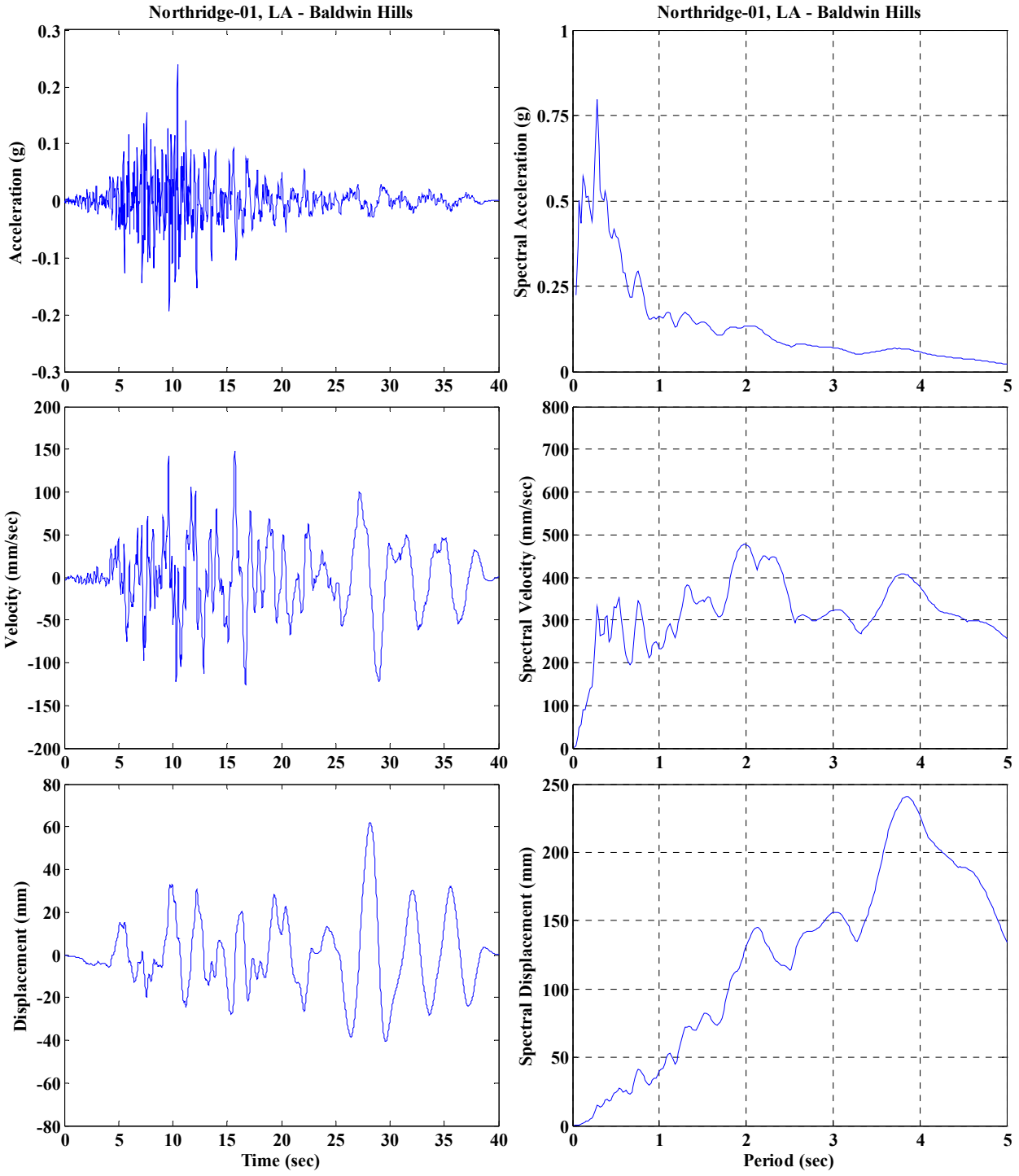

Figure C.8. 75 YRP, Northridge-01, LA - Baldwin Hills

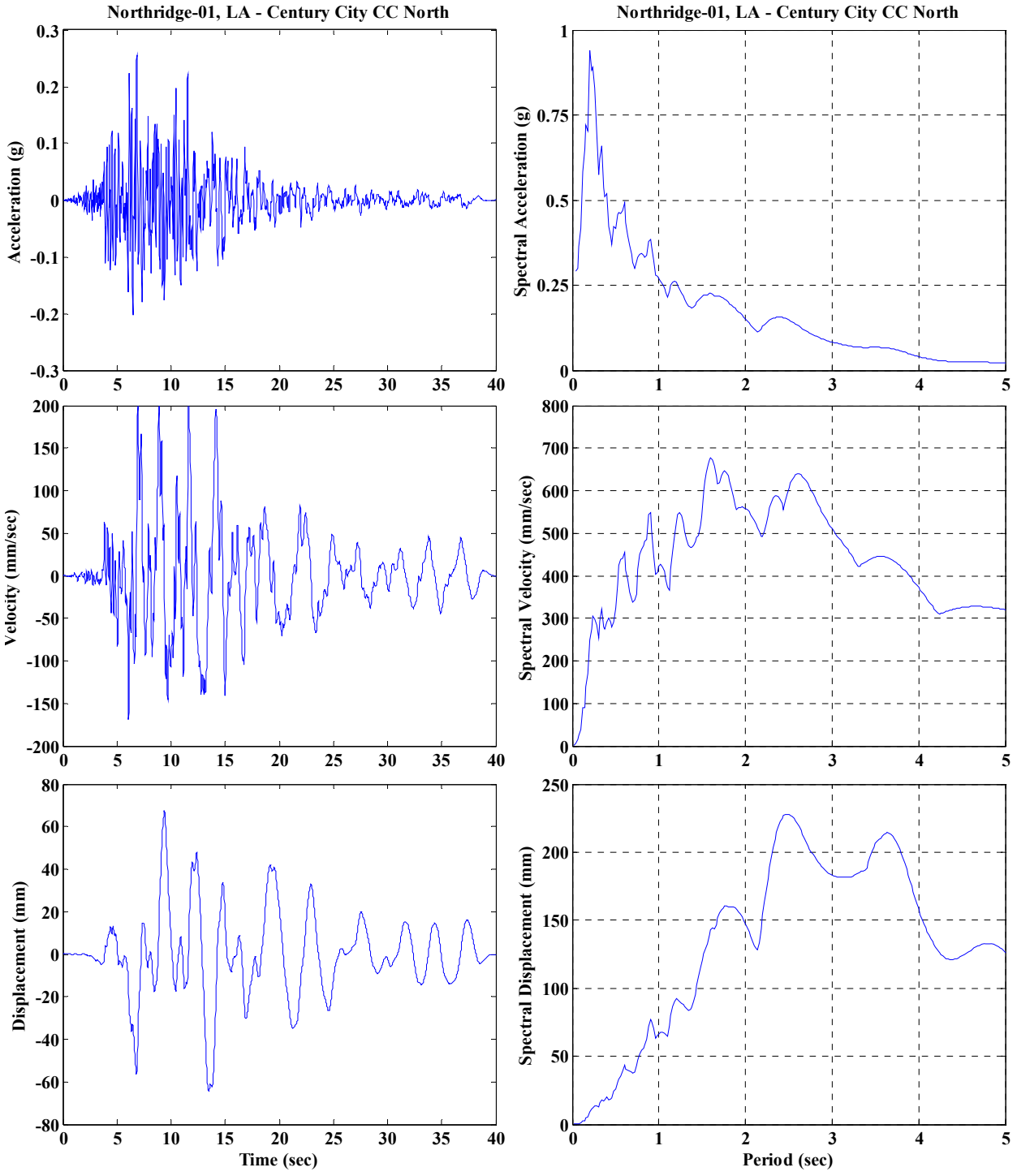

Figure C.9. 75 YRP, Northridge-01, LA - Century City CC North

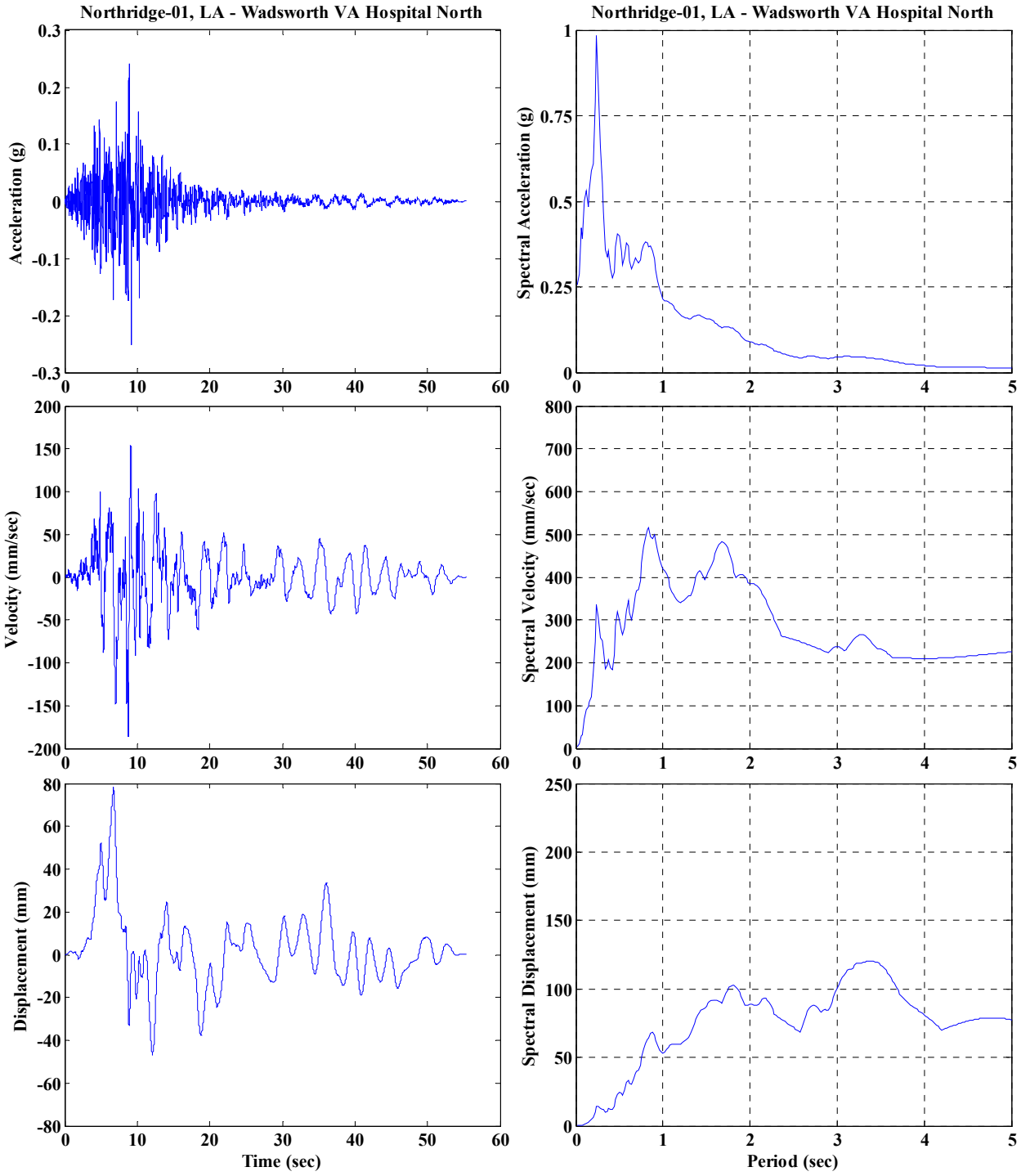

Figure C.10. 75 YRP, Northridge-01, LA - Wadsworth VA Hospital North

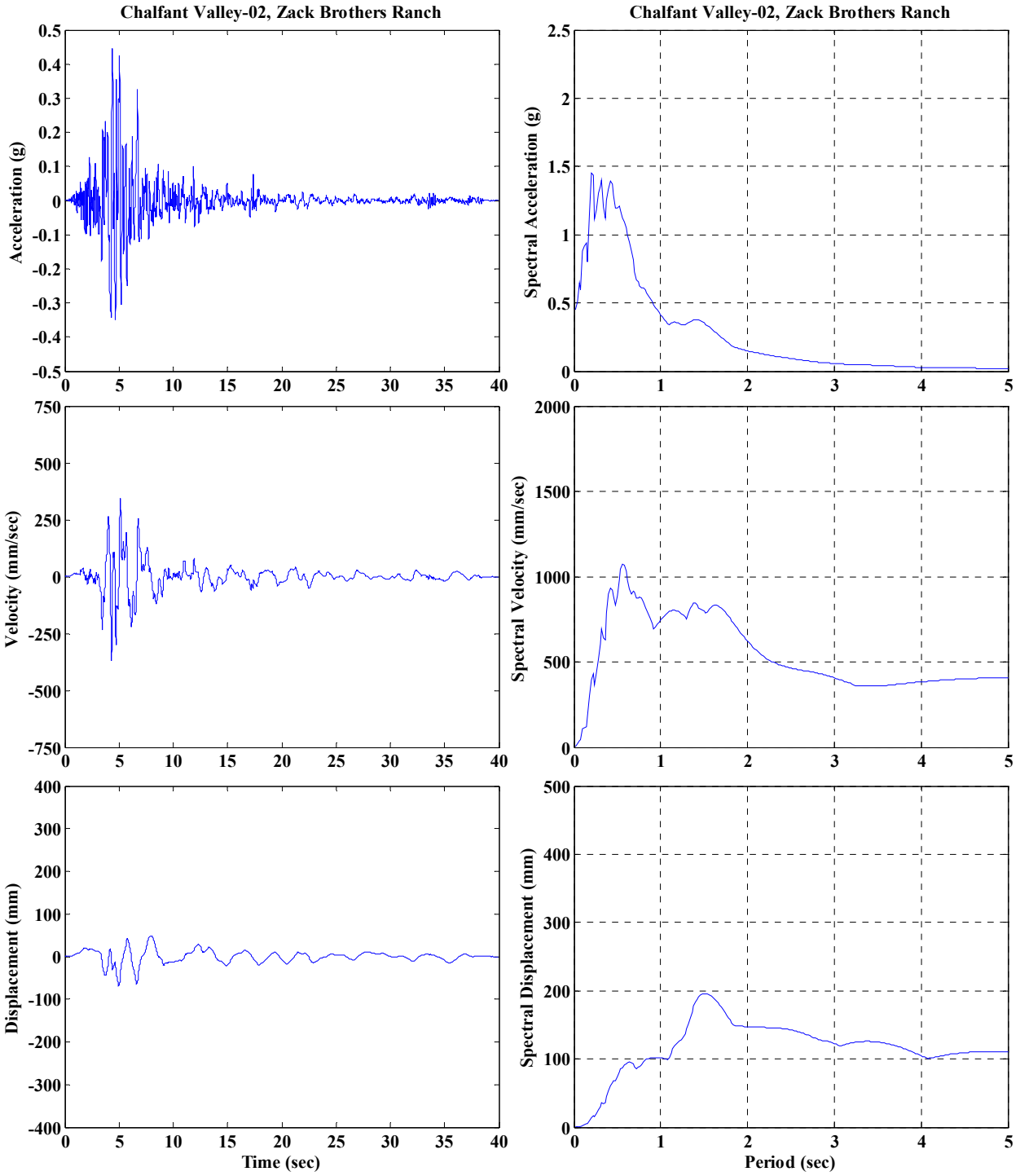

Figure C.11. 475 YRP, Chalfant Valley-02, Zack Brothers Ranch

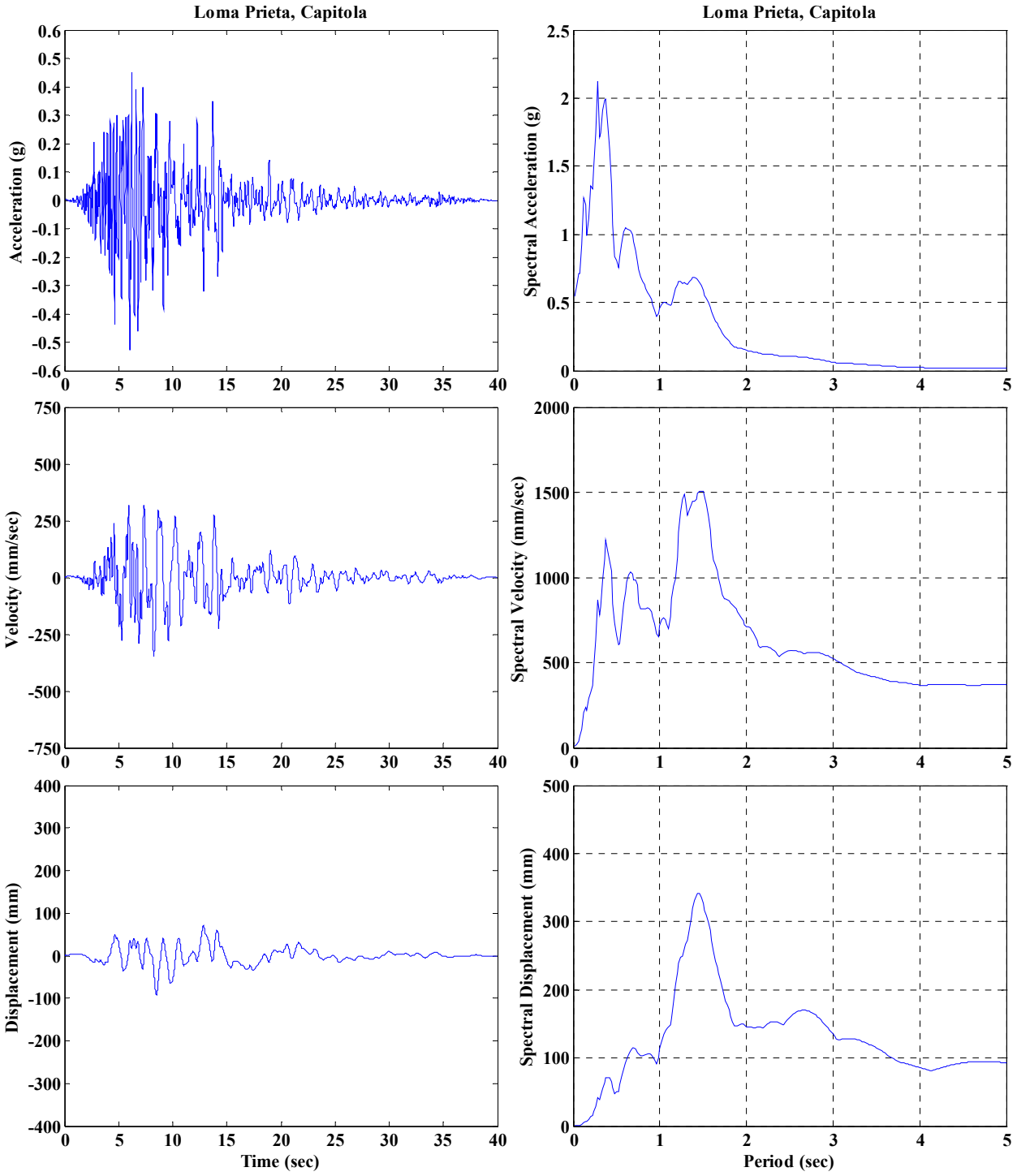

Figure C.12. 475 YRP, Loma Prieta, Capitola

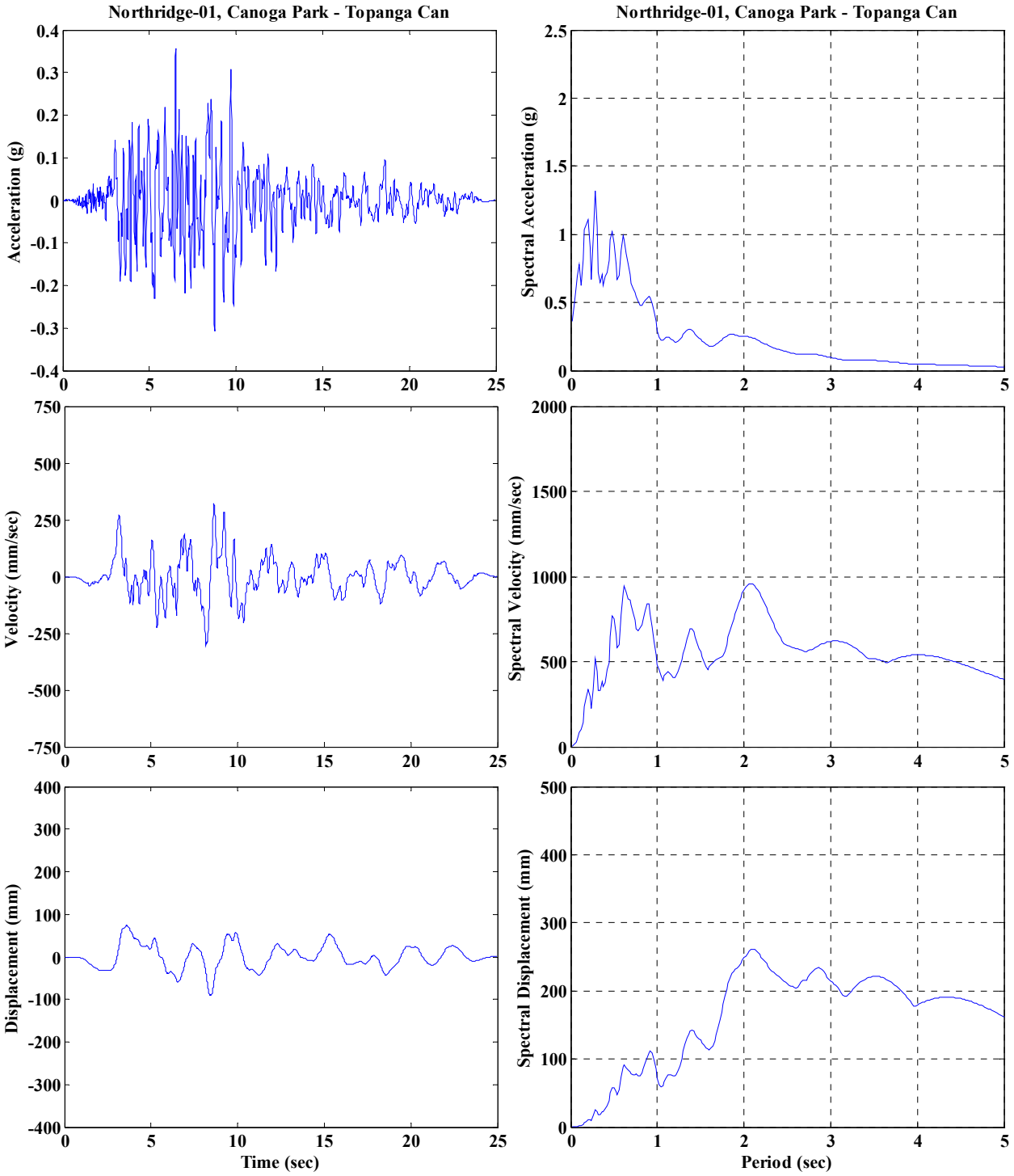

Figure C.13. 475 YRP, Northridge-01, Canoga Park - Topanga Can

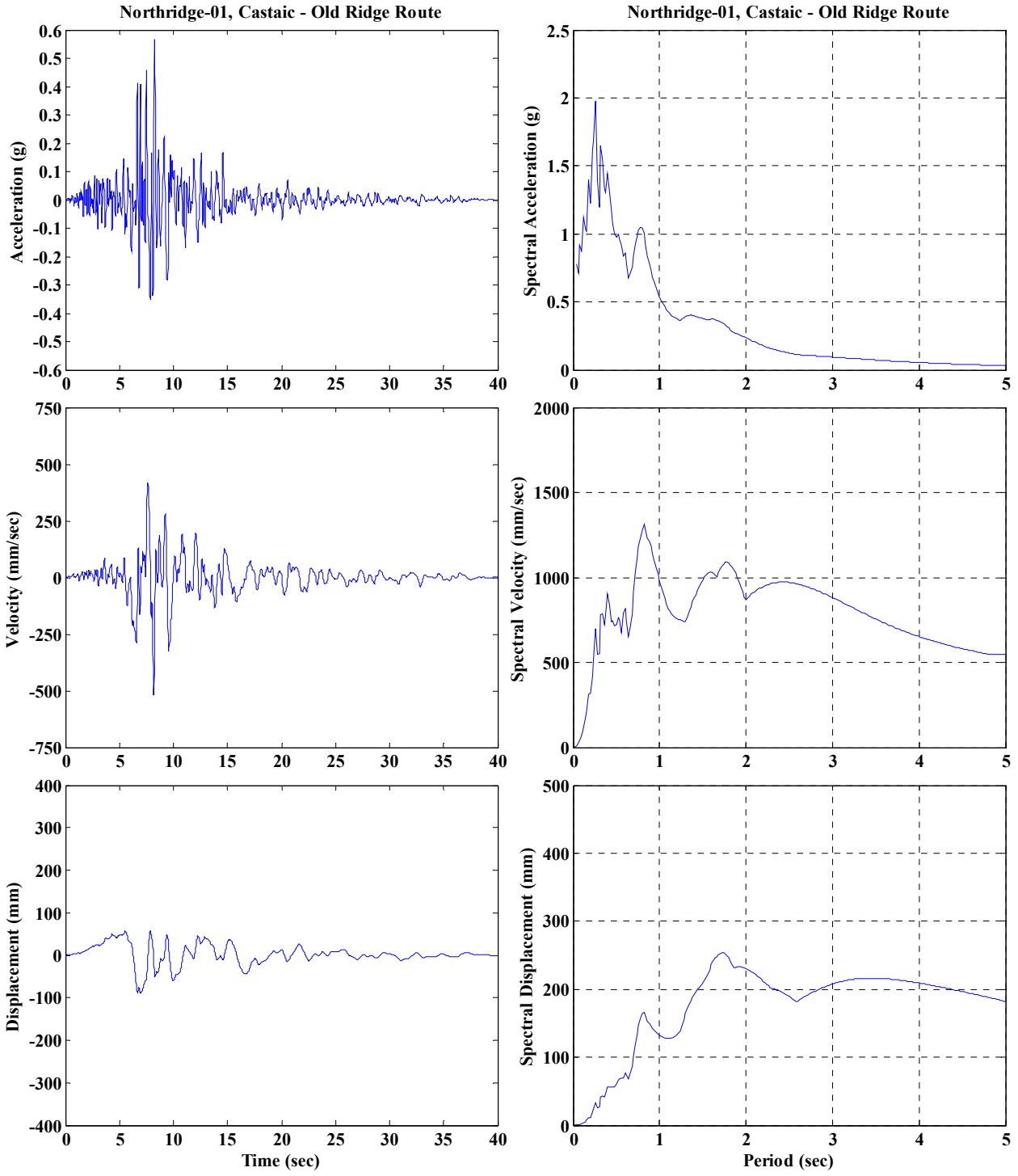

Figure C.14. 475 YRP, Northridge-01, Castaic - Old Ridge Route

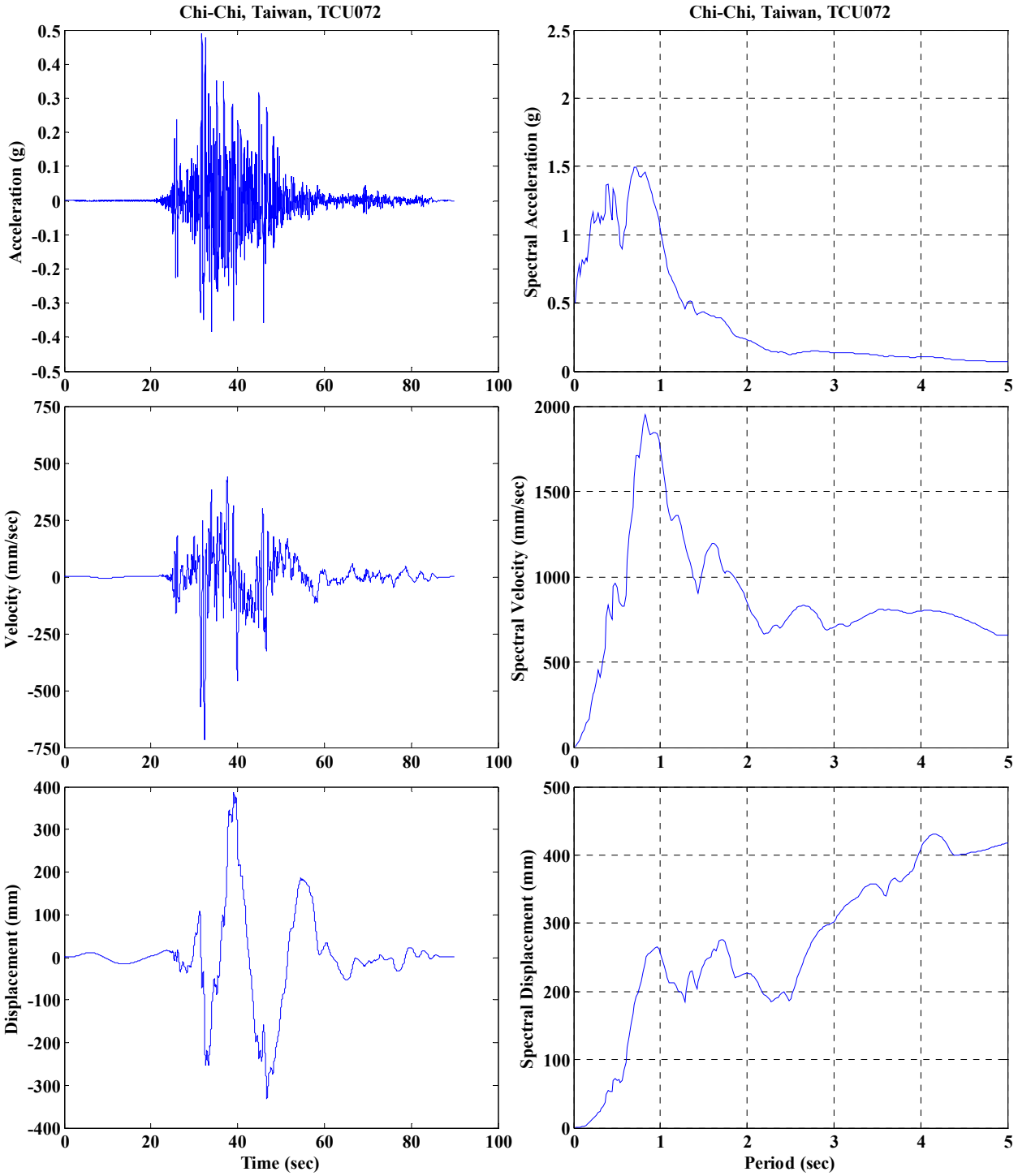

Figure C.15. 475 YRP, Chi-Chi, Taiwan, TCU072

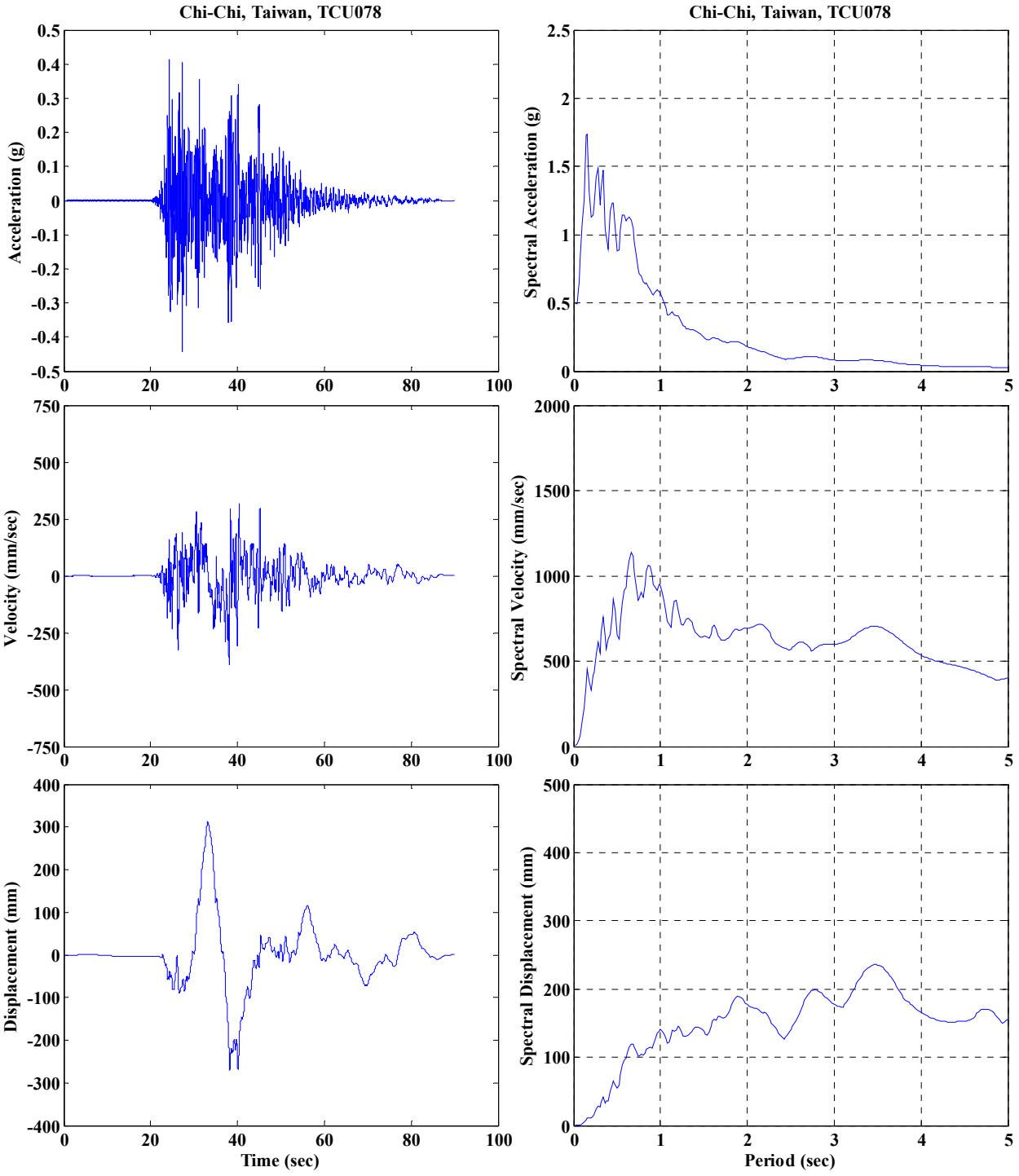

Figure C.16. 475 YRP, Chi-Chi, Taiwan, TCU078

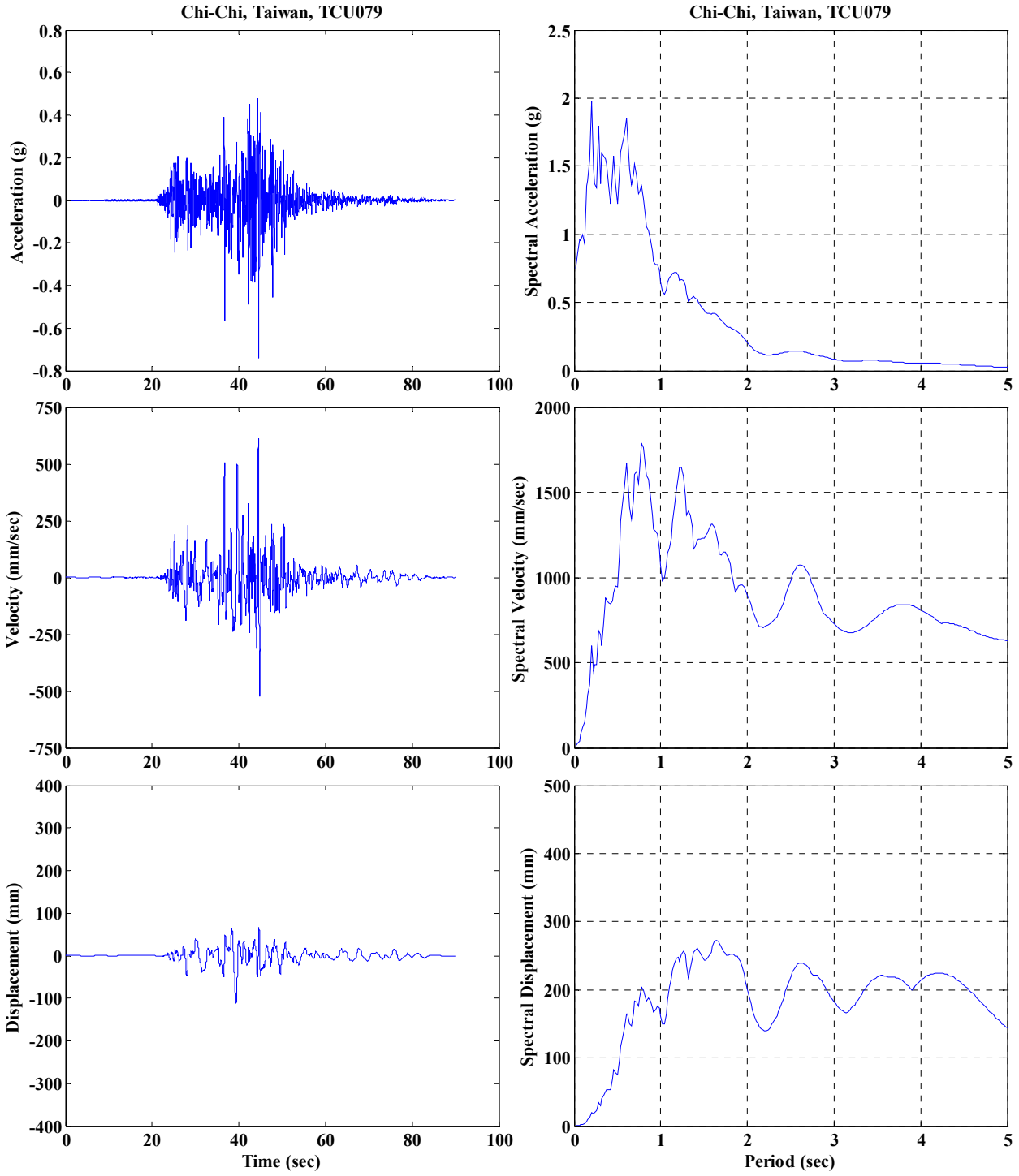

Figure C.17. 475 YRP, Chi-Chi, Taiwan, TCU079

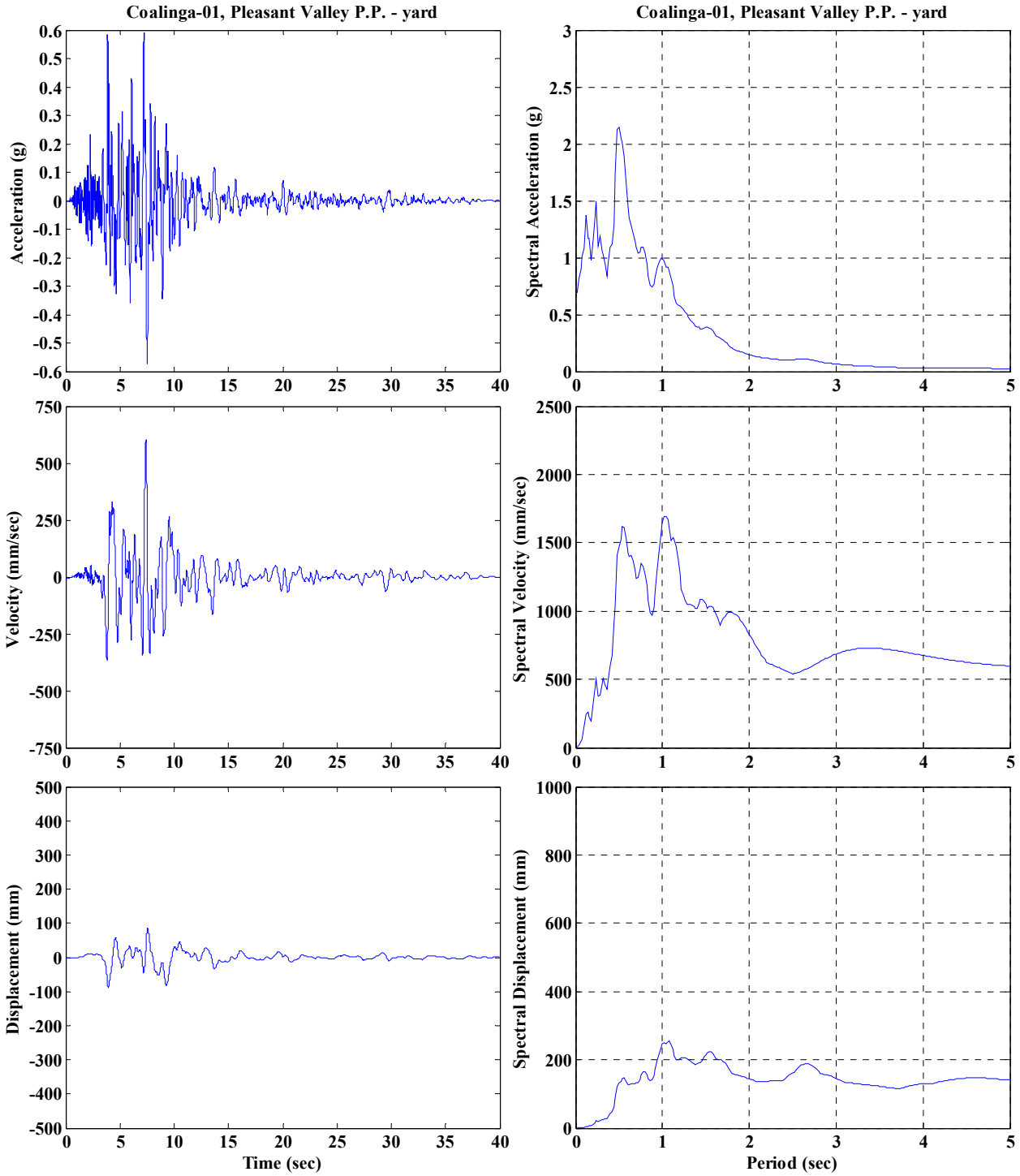

Figure C.18. 2475 YRP, Coalinga-01, Pleasant Valley P.P. - yard

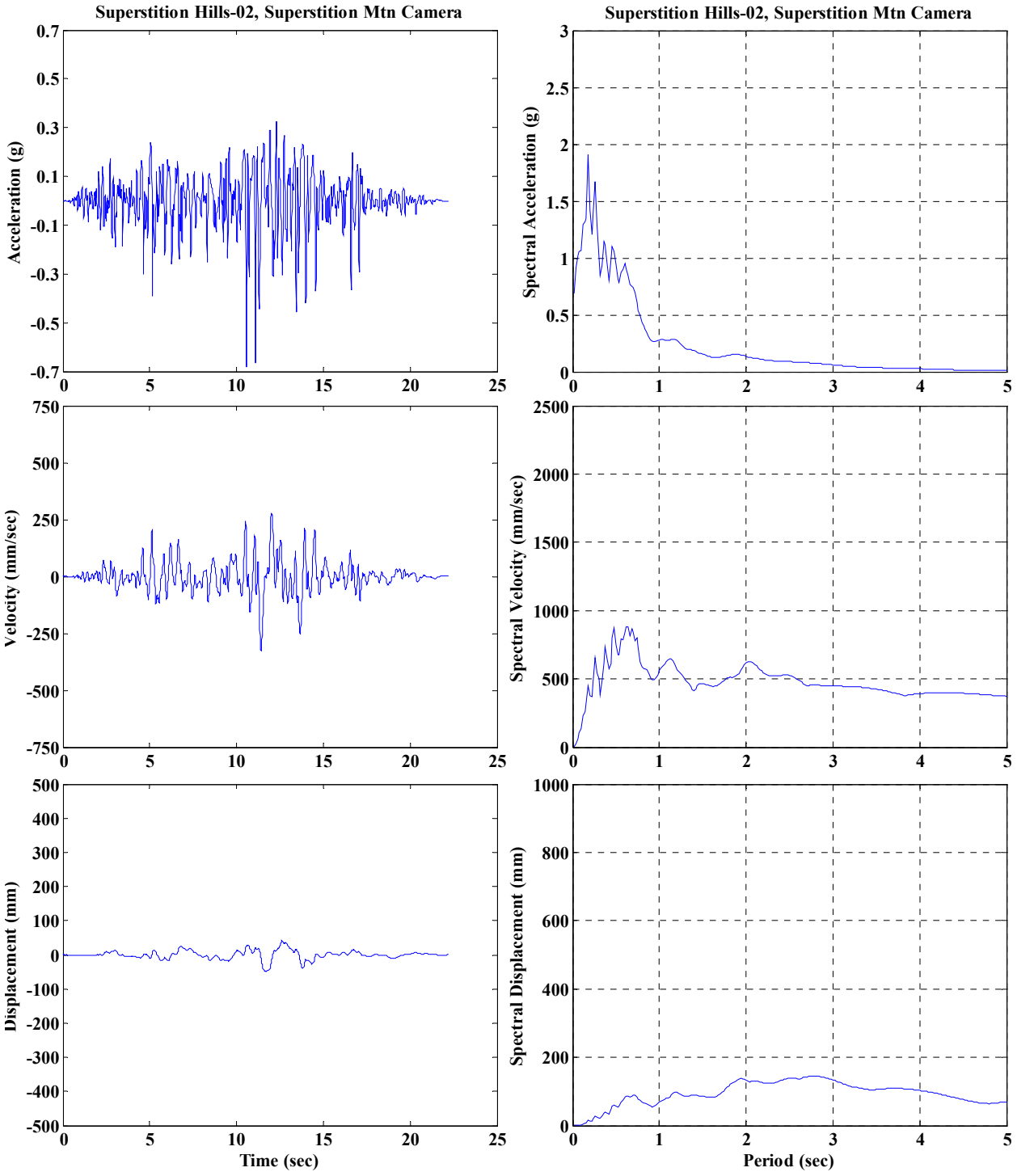

Figure C.19. 2475 YRP, Superstition Hills-02, Superstition Mtn Camera

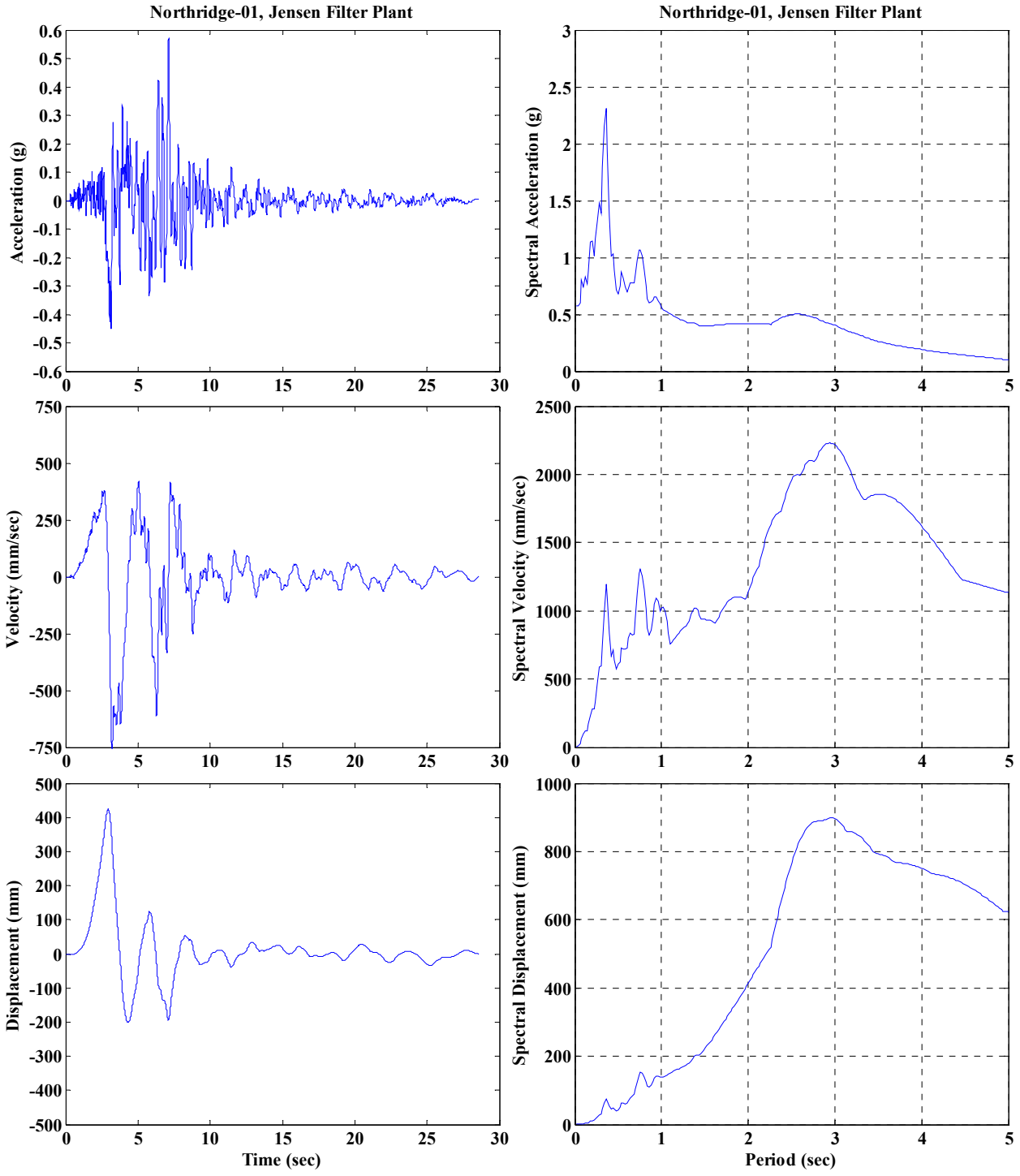

Figure C.20. 2475 YRP, Northridge-01, Jensen Filter Plant

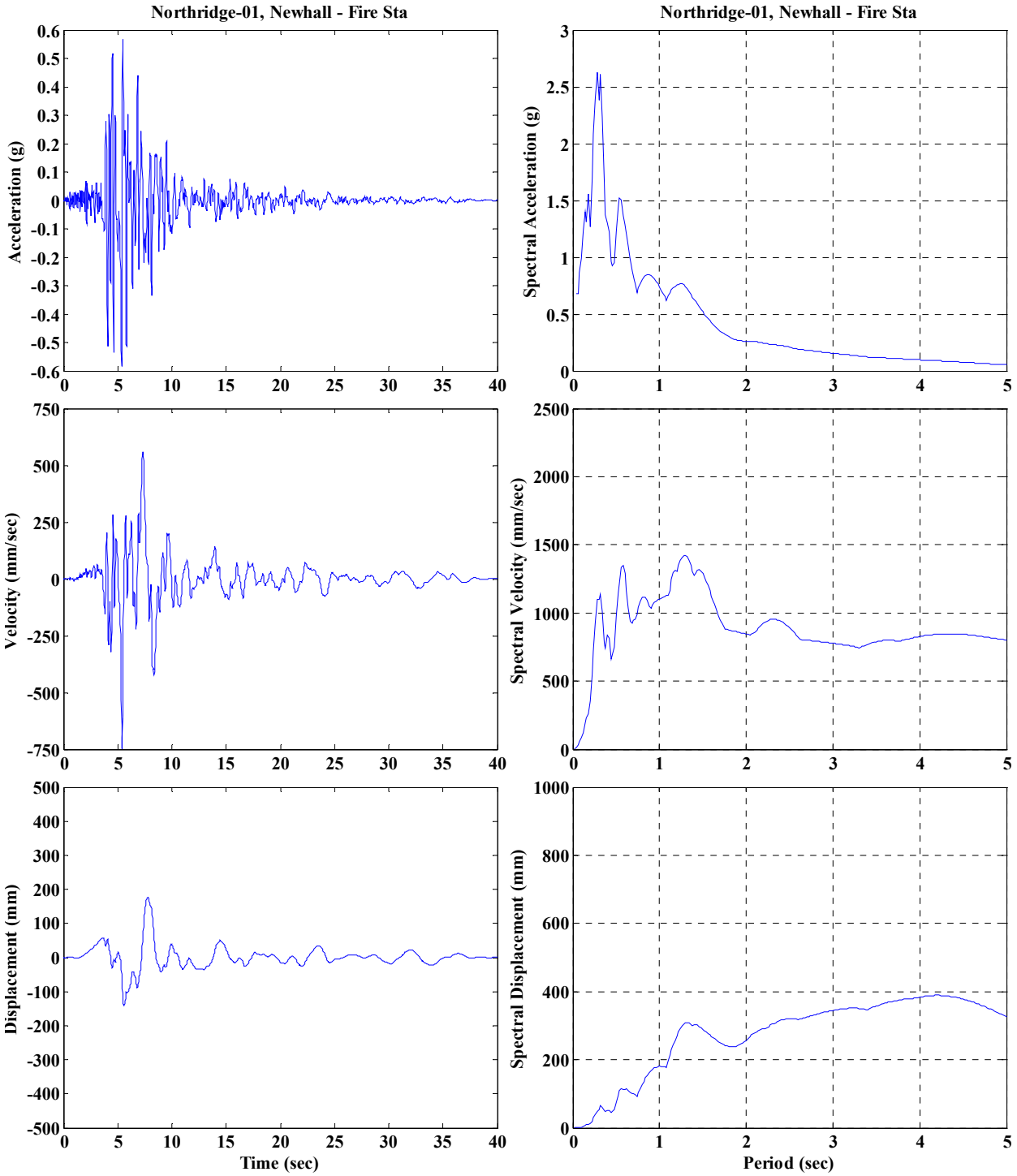

Figure C.21. 2475 YRP, Northridge-01, Newhall - Fire Station

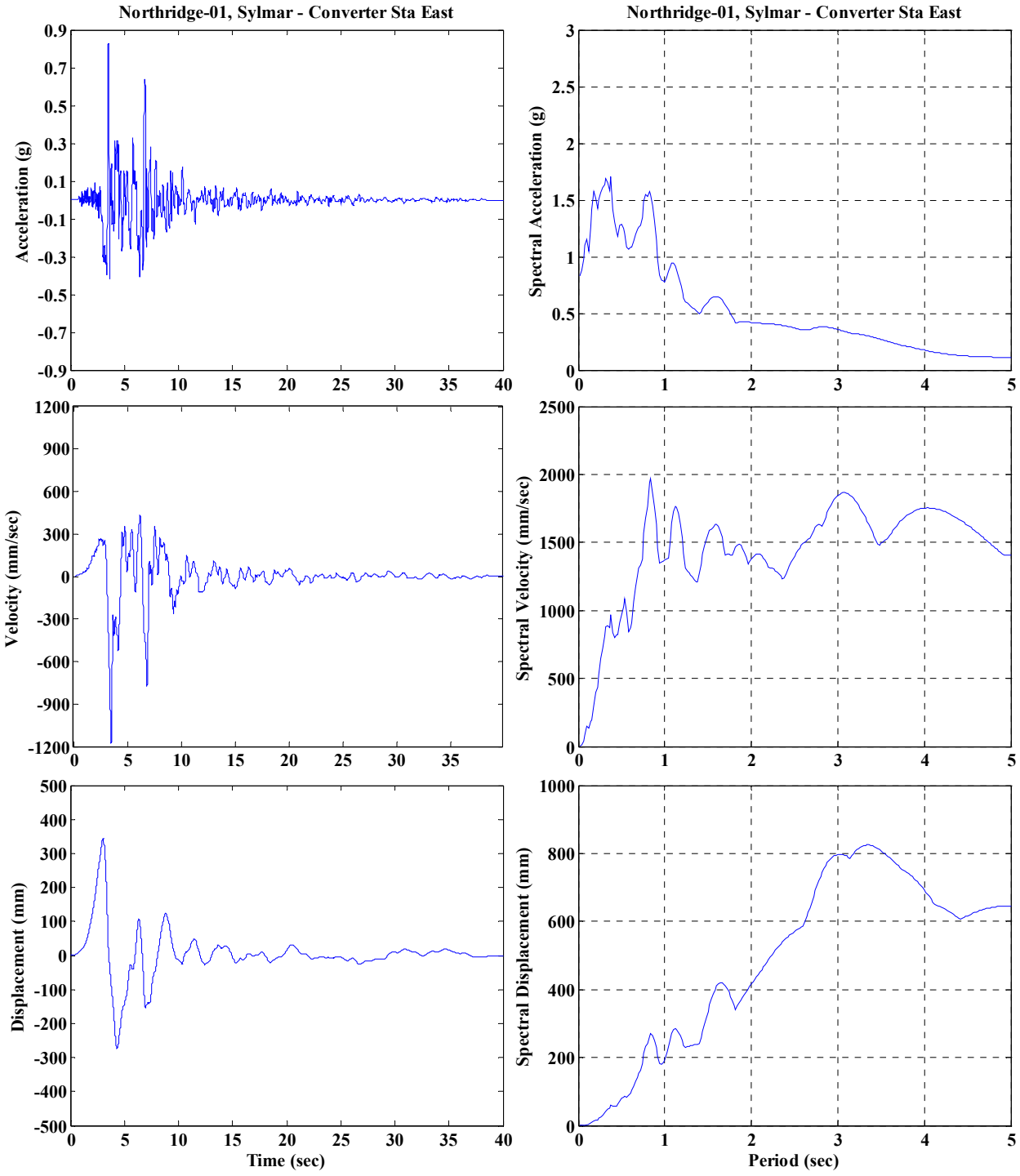

Figure C.22. 2475 YRP, Northridge-01, Sylmar - Converter Sta East

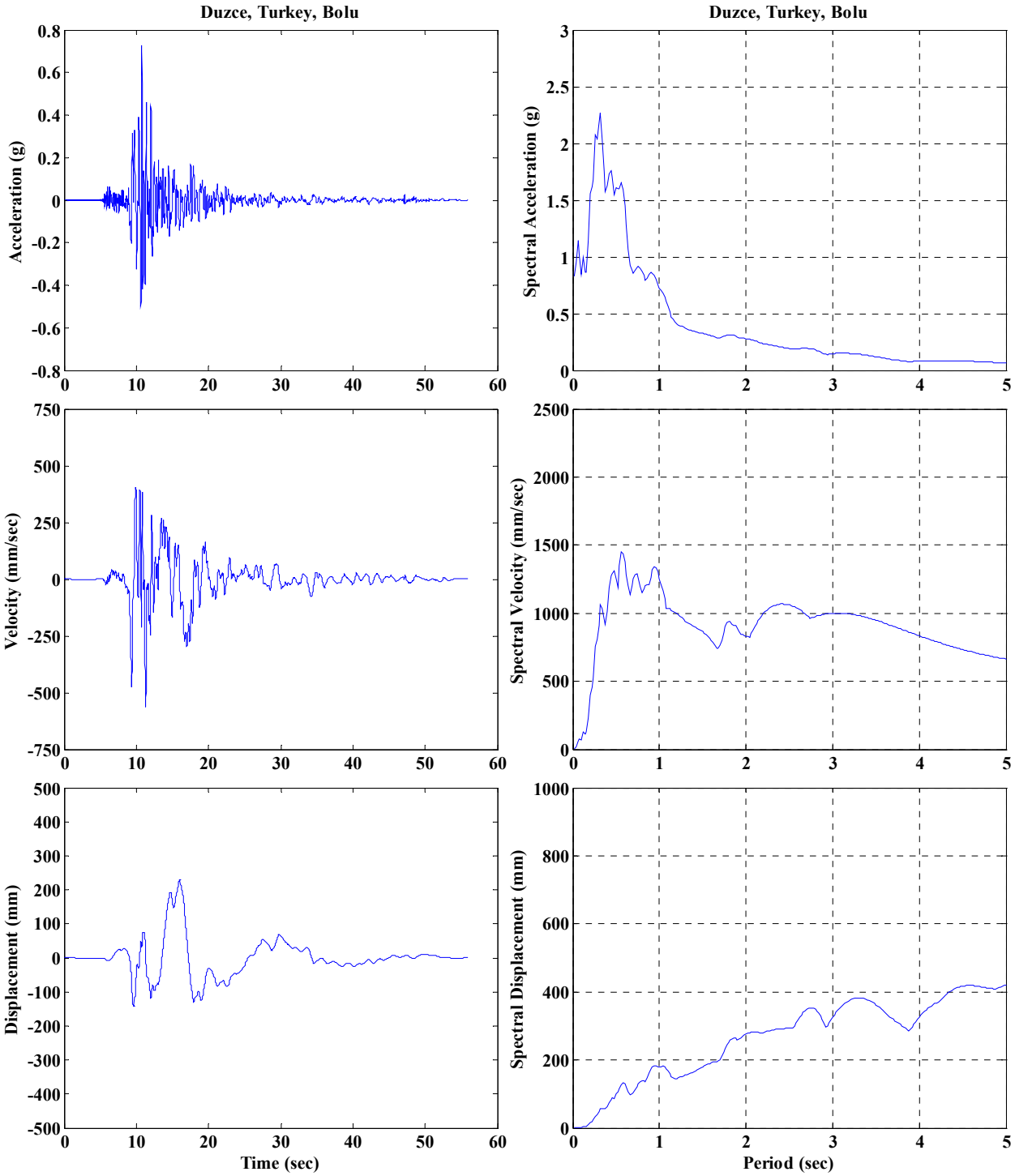

Figure C.23. 2475 YRP, Duzce, Turkey, Bolu

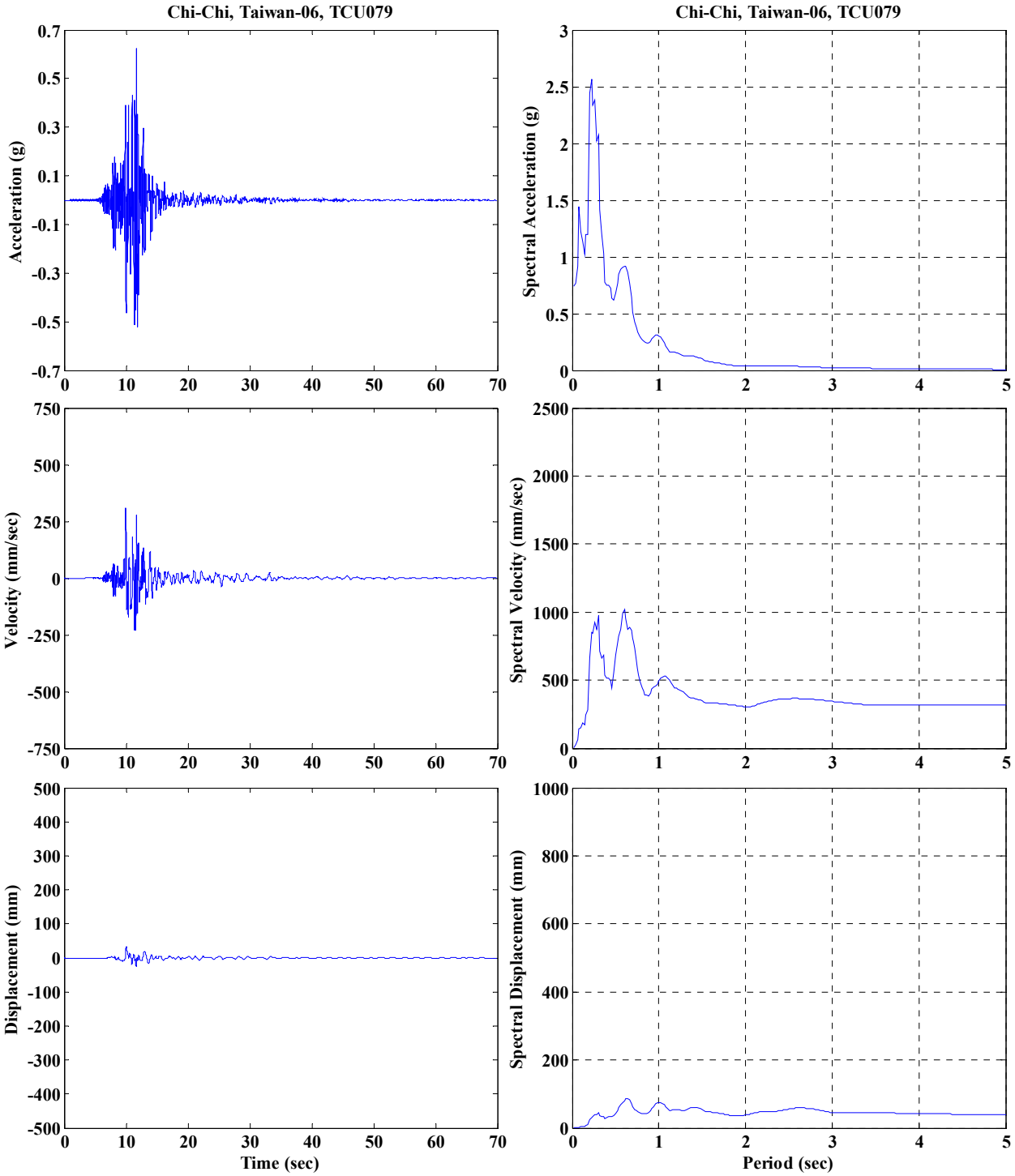

Figure C.24. 2475 YRP, Chi-Chi, Taiwan-06, TCU079